Università di Pisa

Dottorato di Ricerca in Fisica

UNIVERSITÀ DI PISA

Graduate Course in Physics
PhD thesis

High Power fibered optical components for Gravitational Waves detectors

Candidate

Matthieu Gosselin

Supervisor

Dr. Eric Genin

Tutor

Dr. Francesco Fidecaro

July 2018

Ciclo di Dottorato XXX

Contents

Acknowledgments

First of all I would like to thanks my tutor Francesco Fidecaro who has made this work possible and the reviewers of this thesis, Frederic Cleva, Mauro Tonelli and Peter Wessels who accepted to take from their time to read it and gave me useful comments to improve it.

I spent most of the time of this PhD on the Virgo site, lost in the countryside of Cascina but where I met many people that I would like to thanks here. Tatiana and people from the electronics and mechanical departements, for having patiently designed and provided all the things I was needed despite my not so good explanations. To Annalisa, Antonino, Richard and Vis, for having borne me in the office and shared the zenzerini, galette, tea and others dolce! To all the interns that passed by and were always bringing some fresh air to Virgo during summer time. To Magazzu, who helped me in the mess of the lab and through the administrative procedure, and for always having entertaining stories to tell during the breaks. To Fred because he wanted to be cited here and also for his (good?) advice of an old french expatriate in Italy. To Madda, Gary, Heinrich, for their simplicity and good mood and more generally to all the people that I was meeting everyday, during the ping pong time or somewhere else. To Lucia, Julia, Francesco, Giovanni, Jose for having shared our PhD life difficulties and also the good moments.

During my PhD I had the opportunity to spend two periods of one month in Hanover. I really appreciated my time there and I would like to thanks all the people that made my stays very instructive and pleasant at the same time, especially Oliver, Michael and Peter at the LZH and Patrick and Benno at the AEI.

I had the chance to be part of the GraWIToN project funded by the European Commission. It gave me the opportunity to participate to many schools, conferences and workshops where I learned a lot. It also allowed me to meet the other Grawitons fellows, Rudy, Zeno, Gregoire, Dany, Jojo, Imran, Omar, Nini, Justus, Shuba, Gang, Serena and Akshat to cite them all. We spent lot of time together and became much more than simple colleagues. Generally speaking, it has been a pleasure to share these experiences with them and I hope that we will have so many others occasions to meet again. All that would not have been possible without our board that I would like to thank here for their work: Erika, Elena and Michele.

I would like to thanks Camilla, who arrived some months before the end of this PhD, the most difficult part as everybody would agree. She supported me a lot during this period

and helped me to keep an essential balance in my everyday life at a time when it was easy to lose it. For that and for everything, thanks a lot.

I would like to thanks Gabriel who has always been present for me, even and especially, during the toughest moments of this PhD either professional or personal. It has not been easy all the time, I can be stubborn, but with a lot of patience he kept explaining, pushing me forward and sharing his passion for physics. It has been a pleasure to learn by his side, to work while having good time together. We had many good moments, but I think that we will keep a "strictly professional relationship, hein Gabriel!?"

I would like to thanks Eric for his great, almost paternal, support. Everyday, even if he was committed and spent so much time to make advanced Virgo work. Not only he guided me through this PhD from the beginning to the end but was also always available to give me either technical explanation or organizational advice. I may not have been the best at listening them, but it seems that we finally did it!

Finally I would like to dedicate this work to my friends, my family and my parents. I was in Italy while you were in France or in the rest of the world but despite the physical distance you remain close to me. It was important for me to have your unconditional support all that time, whenever I needed it. I also dedicate and have a special thought for my grand father who was very proud of what I was doing.

Introduction

In February 2016, with the first direct detection of gravitational waves [1], the LIGO-Virgo collaboration ended a quest started a century ago when Einstein predicted their existence in his theory of the general relativity. Since then scientists were trying to detect this little ripple of the space-time. The challenge was huge considering that even the biggest astrophysical events induce a very small relative variation of length ($\sim 10^{-18}m$)) when arriving on earth. In order to reach such a sensitivity, very complex giant detectors using laser interferometry have been built and improved over the past years. From the quality of the optical components to the seismic isolation, from the vacuum to the data acquisition, every part is essential and every single improvement is a step towards a better sensitivity.
The work that we are presenting here is part of this desire of decreasing the noises on one hand, and decrease the complexity on the other hand. We were indeed working on the optical components that are used between the laser and the interferometer of the Advanced Virgo detector, namely the injection system. The idea is to prospect for the use of optical fibers to guide the light through this part of the interferometer to try to simplify it as well as avoiding external disturbances which cause among other things laser beam pointing noise [2].

The goal of this work was to realize a fibered version able to withstand 100 W monochromatic light of one of the most critical component of the Injection system, the Faraday isolator. Since we knew this main objective would have been hard to achieve we set some intermediate objectives in the project. First, we had to select and test the best available current optical components and technologies for our applications. Then, we had to work on the optimization and development of very critical components such as water-cooled fiber optic collimators able to evacuate the excess of heat present at the input end of the optical fiber. Finally, the idea was to realize high power fiber optical components (able to withstand laser power higher than 100 W at 1064 nm). In this final part, the idea was to realize in a first moment a fibered electro optic modulator to debug most of the problems in the fibering of optical components at high power. This would have paved the way to the realization of a fibered Faraday isolator which purpose would be to bring the light from the laser system to the vacuum system without introducing beam jitter noise. The second purpose of this isolator is to protect the laser system from the light coming back from the input mode cleaner cavity and the interferometer.

In chapter 1, we will review the astrophysical sources of gravitational waves and briefly derived their propagation equations to see how they perturb the space time. Then we will see how this perturbation can be detected by an interferometer such as Advanced Virgo. We

will see that every part of the detector is critical and we will especially described the laser injection subsystem which is the one we are trying to improve.

The chapter 2 is a theoretical part in which we will investigate the possibility of using optical fibers to guide the laser beam of Advanced Virgo. In a first part, we will describe the characteristics of this laser beam and in a second one we will detail the working principle of different kind of optical fibers. This will allow us to understand the kind of fiber that can be used to guide the laser beam by keeping its properties unchanged. Then we will detail how to pass from the free space propagation of the laser beam to its propagation into an optical fiber and the related difficulties. Especially, we will discuss the issues linked to the high power, both while injecting and while propagating into the fiber.

In chapter 3, we will present the experimental results that we obtained with two different fibers that we selected. Moreover we will review the different improvements that we have done along the experiments that we carried out in order to improve the coupling into these fibers.

The chapter 4 is devoted to the presentation of the fibered Electro-Optic Modulator (EOM) that we developed using the fibers that we presented previously. After having presented its working principle, we will detail its design and its characterization.

Finally in chapter 5, we will detail the issues linked to a high power beam into a Faraday isolator. We are presenting some theoretical and experimental works that we carried out in order to improve their performance. We are also proposing the optical set-up of a fibered FI and its expectation.

Chapter 1

Advanced Virgo gravitational waves detector

In this chapter we will see how Gravitational Waves (GW) produced by massive events are disturbing the space-time and how we try to detect these perturbations in the fabric of the space time thanks to ground based interferometric Gravitational Waves Detectors (GWD). Then the general design of such a detector will be briefly described, and we will see the improvements that have been done in order to reach the sensitivity needed to be able to detect some events. Such a sensitivity can only be achieved by having all the subsystems working together. We will briefly described them in a third section but among all them, one is of particular interest in this thesis: the injection system. The work that we will present here has been done within the frame of this subsystem. We will dedicate the last part of this chapter to explain its role and the issues that have to be faced that motivate the work that we have done.

1.1 Gravitational waves

1.1.1 Equation of propagation

In its theory of special relativity, Einstein described the space-time as a four dimensional manyfold where time and space are related. From this theory he derived an other one, the General Relativity which was a new way to apprehend the gravity. At the same time the presence of masses is bending the space time and the curvature that appears are ruling the displacement of these masses. In this frame we are not using a flat metric anymore but rather:

$$ds^2 = g_{\mu\nu}dx^\mu dx^\nu \tag{1.1}$$

Where $g_{\mu\nu}dx^\mu dx^\nu$ is a non flat metric tensor that is governed by the Einstein fields equations [3]:

$$G_{\mu\nu}(g_{\mu\nu}) = \frac{8\pi G}{c^4} T_{\mu\nu} \tag{1.2}$$

Where $G_{\mu\nu}$ is the Einstein tensor, G is the gravity constant and $T_{\mu\nu}$ is the stress-energy tensor.

Einstein equations, due to their non-linearity are difficult to solve. However, for GW sources far from Earth, one can do the far-field approximation in which the metric is close to the flat metric one and get:

$$g_{\mu\nu} \approx \eta_{\mu\nu} + h_{\mu\nu} \tag{1.3}$$

Where $\eta_{\mu\nu}$ is the Minkowski metric used for a flat space considered without gravitation and $h_{\mu\nu}$ is a small perturbation that verifies $|h_{\mu\nu}| \ll 1$.

Since the choice of the coordinate system is not important in general relativity, it has been shown that by using the Lorenz gauge, one can rewrite the Einstein's equations as follow :

$$\left(\nabla^2 - \frac{1}{c^2}\frac{\partial^2}{\partial t^2}\right) h_{\mu\nu} = -16\pi T_{\mu\nu} \tag{1.4}$$

And since we are working in the far field approximation we have $T_{\mu\nu}$=0 and finally:

$$\left(\nabla^2 - \frac{1}{c^2}\frac{\partial^2}{\partial t^2}\right) h_{\mu\nu} = 0 \tag{1.5}$$

This is the equation of propagation of a gravitational wave and a general solution for this equation is given by the superposition of plane waves:

$$h_{\mu\nu} = \varepsilon_{\mu\nu} e^{i(\omega t - \mathbf{k}.\mathbf{r})} \tag{1.6}$$

where $\mathbf{k}$ is the wave vector, ω its frequency and $\varepsilon_{\mu\nu}$ a tensor that gives the information on its polarization. It is a 4×4 matrix that describes the spatial effects of a passing GW. It has 10 degrees of freedom but by using a gauge called the Transverse Traceless (TT) gauge

and by choosing a wave vector in the z direction, one can rewrite it as follow:

$$\varepsilon_{\mu\nu} = h_{+}\varepsilon^{+}_{\mu\nu} + h_{\times}\varepsilon^{\times}_{\mu\nu} \tag{1.7}$$

Where $\varepsilon^{+}_{\mu\nu}$ and $\varepsilon^{\times}_{\mu\nu}$ are the so-called plus and cross polarizations that are defined by the following matrix:

$$\varepsilon^{+} = \begin{pmatrix} 0 & 0 & 0 & 0 \\ 0 & 1 & 0 & 0 \\ 0 & 0 & -1 & 0 \\ 0 & 0 & 0 & 0 \end{pmatrix} \qquad \text{and} \qquad \varepsilon^{\times} = \begin{pmatrix} 0 & 0 & 0 & 0 \\ 0 & 0 & 1 & 0 \\ 0 & 1 & 0 & 0 \\ 0 & 0 & 0 & 0 \end{pmatrix} \tag{1.8}$$

So finally, the propagation equation of a GW can be written as follow:

$$h^{TT}_{\mu\nu} = \begin{pmatrix} 0 & 0 & 0 & 0 \\ 0 & h^{+} & h^{\times} & 0 \\ 0 & h^{\times} & -h^{+} & 0 \\ 0 & 0 & 0 & 0 \end{pmatrix} e^{i(\omega t - kz)} \tag{1.9}$$

1.1.2 Effect of a gravitational wave

Now that we have a simple propagation equation for a GW, let us evaluate the effects of its passage. To do so, we consider two test masses: A that we placed at the origin of the coordinate system and B (x_B,y_B,z_B) placed at an initial distance L_0 considered infinitely small in the far-field approximation. In the TT coordinates, having $\vec{n}$ as a unit spatial vector, the distance between these two masses is given by:

$$L^2 = g_{\mu\nu}(x^{\mu}_B - x^{\mu}_A)\,(x^{\nu}_B - x^{\nu}_A) = (\delta_{ij} + h^{TT}_{ij})x^{i}_B x^{j}_B \tag{1.10}$$

Where δ_{ij} is the symbol of Kronecker. Since we have $x^{i}_B = L_0 n^{i}$, we can rewrite the equation as follow:

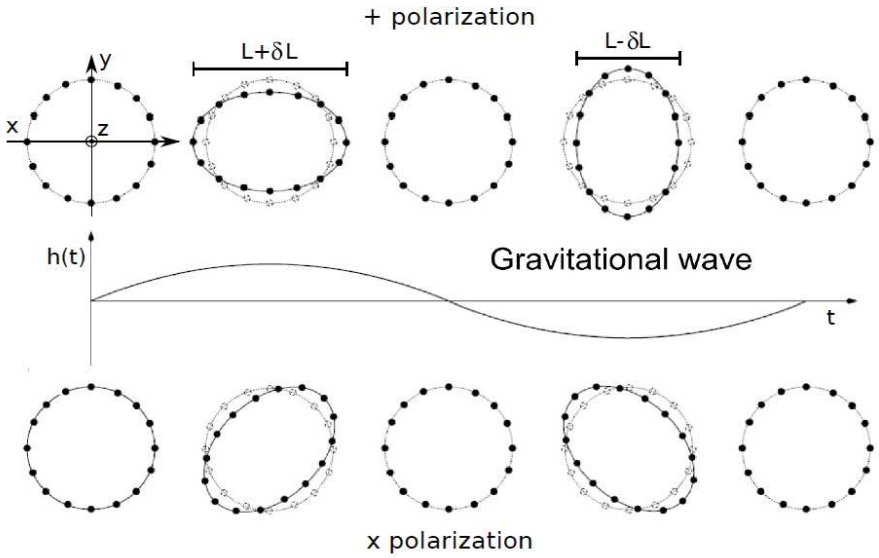

Figure 1.1: Effects of both the plus and cross polarizations of a GW propagating along the z-axis on test masses circularly distributed in a perpendicular plane.

$$\begin{aligned} L &= \sqrt{L_0^2\,(\delta_{ij} + h_{ij}^{TT}) n^i n^j} \\ &= L_0 \sqrt{(1 + h_{ij}^{TT}) n^i n^j} \\ &\approx L_0 (1 + \frac{1}{2} h_{ij}^{TT}) n^i n^j \end{aligned} \tag{1.11}$$

Finally the variation of length is given by $\delta L = L - L_0 = \frac{L_0}{2} h_{ij}^{TT}\ n^i n^j$ and for a well oriented source, the relative change of the length is given by :

$$\frac{\delta_L}{L_0} = \frac{h}{2} \tag{1.12}$$

Two points has to be retained from this equation: the variation of length between two masses depends actually on the initial length that was separating them and that it directly depends on the strain h of the GW. The effects of both cross and plus polarization of a GW on test masses circularly distributed is shown on figure 1.1.

For a long time there has been a debate about the actual existence of these GW, trying to figure out if they were physically existing or were just a mathematical artifact of the theory. Einstein himself changed his mind about it several times. The answer could only come

from an experimental evidence of their existence and that is why people started experiments trying to detect this variation of length. These experiments will be detailed in section 1.2. The challenge was huge, we will indeed see in the next part that even the strain of the GW emitted by the biggest astrophysical events are inducing very small variations of length while reaching the Earth.

1.1.3 Sources of gravitational waves

Every moving masse produces GW however only the biggest and fastest ones are creating GW that have a strain high enough to be detected by Gravitational Waves Detector (GWD). For example in [4], they are considering an experiment that could be conducted in a laboratory: a system of two masses $m_1 = m_2 = 1$ kg, separated by a distance of r = 1 m, turning around their centroid at an angular frequency $\omega = 1$ rad.s^{-1}. The equation that gives the strain of the produced GW when observed in the perpendicular plane at a distance R = 1 m from the centroid of the system, is given by :

$$h_0 = \frac{4G}{Rc^4}\mu r^2\omega^2 \tag{1.13}$$

Where c is the speed of light, G the gravitational constant and μ the reduced mass of the system. A numerical application leads to a strain of $h_0 = 1.6\ 10^{-45}$. Considering that the GWD have a detection sensibility of about 10^{-21} (see the sensitivity curves in figure 1.9), one can easily understand that only cataclysmic astrophysical events have an effect susceptible to be detected on earth. In this section we are detailing the events that are expecting to emit GWs with a strain high enough to be detected by ground-based interferometeric GWD.

1.1.3.1 Burst

Burst are GW that have the particularity of being very short in time. Their sources are not fully known and do not have a well defined wave model. However, the most expected sources of burst are supernovae, when a star collapses to become a neutron star or a black hole. It is expected to have a frequency lower than 1 kHz and an amplitude of:

$$h \approx 9.6 \cdot 10^{-20} \left(\frac{10kpc}{r}\right) \tag{1.14}$$

Since there is no signal a priori, the idea to look for these event is to search for an anomalous higher amount of power in the signal detected by the detectors.

1.1.3.2 Neutron Star

Spinning Neutron Stars (NS) are emitting GW if they present an asymmetry in their mass distribution or if the spin axis is not aligned with their main axis. The emitted GW have a frequency two times higher than the spin frequency of the NS and can be considered constant over a long period of time. The amplitude depends on the momentum of inertia of the star or eccentricity given by the formula :

$$h \approx 1.06 \cdot 10^{-25} \left(\frac{\epsilon}{10^{-6}}\right) \left(\frac{I}{10^{38} kg \cdot m^2}\right) \left(\frac{10kpc}{r}\right) \left(\frac{f}{1kHz}\right)^2 \tag{1.15}$$

I is the quadrupole momentum of the NS. The parameters of this equation have been normalized by their typical expected values.

Some particular NS are also emitting periodic radio pulse, they are then called pulsar. This radio pulse can be measured and thanks to it, one can precisely measure the spin frequency. Then thanks to this frequency we can reconstruct a GW signal a priori and give an upper limit to the expected strain. For example, the Vela pulsar has a spin frequency that is approximately 20Hz. Given the fact that its GW signal has not been evidenced using the data from the first generation of GWD, an upper limit of $h = 2 \times 10^{-24}$ has been given for this pulsar [5].

1.1.3.3 Stochastic background

Approximately 10^{-36} to 10^{-32} seconds after the Big Bang, GW were produced according to the inflation theory. The incoherent sum in time and frequency of all the resulting events is what is called stochastic background. The signal follows a Gaussian distribution that makes it particularly difficult to detect since the most common noises of the detectors also have a Gaussian shape. The idea to evidence such a signal is to use the data from different detectors to try to extract the signal from their uncorrelated noise.

1.1.3.4 Compact Binary Coalescence

The binary systems in which we are interested in, are of three types: Binary Black Holes (BBH), Binary Neutron Stars (BNS) or mixed systems (BH-NS). They are very massive astrophysical objects that produce GW at twice their orbital frequency. While producing these GW the system is losing energy, so the orbital distance is decreasing while the orbital frequency is increasing. Thus such a system can be divided in three steps. The inspiral phase when they get closer to each other, increasing their orbital frequency. At the beginning of this phase, GW that are produced have a frequency too low to be detected by the ground based GWD. The part that can be detected is just before the merger, when the frequency is greater than 10 Hz (see the typical sensitivity curve of ground based interferometric GWD

figure 1.8). Then, when the two objects are at distance comparable to the sum of their radii, we are entering the merging phase whose signal is not well defined since we can not apply the far field approximation anymore. After the merging , we are entering the ring-down phase when the resulting object of the fusion is emitting GW whose signal is a damped sinus. The expected strain of such a signal is given by equation 1.16, where $\mathcal{M} = \mu^{3/5} M^{2/5}$ with $M = m_1 + m_2$ the total mass of the system and $\mu = m_1 m_2 / M$ its reduced mass. $M_\odot$ is the solar mass and r the distance of observation.

$$h \propto 10^{-19} \left(\frac{\mathcal{M}}{M_\odot} \right)^{5/6} \left[\frac{Mpc}{r} \right] \tag{1.16}$$

The GW of the first direct detection were produced by a BBH. We will detail it in the paragraph hereafter.

1.1.4 First direct detections

Before entering into the details of the first direct detections that has been done by interferometric ground bases GWD, let us mention the first indirect proof of the existence of such waves that have been made in 1974 by R.A Hulse and J.H Taylor (Nobel prize in Physics in 1993). The PSR $B_{1913+16}$ is binary pulsar system that has been detected by Hulse and Taylor [6], in the following works Taylor and Weisberg indirectly proved the existence of GW by analyzing the decay of its orbital frequency and proving that the energy loss was in perfect agreement with the prediction of general relativity [7].

1.1.4.1 GW150914: first detection

On September 14^{th}, 2015, about one century after Einstein's prediction, the two LIGO GWD did the first direct detection of a GW. It was a transient signal, called GW150914, coming from the coalescence of two black holes having a mass of about $30 M_\odot$ [1]. The signal that they received can be seen on figure 1.2. One can clearly see the inspiral phase, when both the frequency and the amplitude of the signal are increasing till reaching the merging moment and then the ring-down phase. During this process the equivalent of 2.5 to 3.5 $M_\odot$ were emitted in GW.

This event, not only gave more credit to the theory of the general relativity, but also gave useful information to astrophysicists since the BH are particularly difficult to study with usual instruments. Astrophysicists, for example, were expecting BH to have masses either smaller, around $10 M_\odot$ or greater than $100 M_\odot$. In 2017, for their " decisive contributions to the LIGO detector and the observation of gravitational waves ", Rainer Weiss, Kip Thorne and Barry Barish were rewarded with the Nobel prize of Physics.

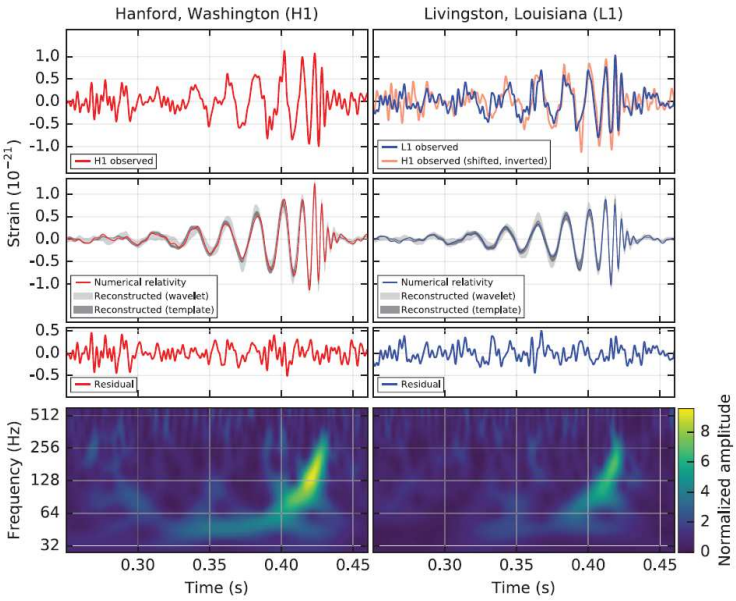

Figure 1.2: GW150914 signals detected by the Ligo detectors.

After this first event, three other BBH coalescences have been detected: GW151226 [8], GW170104 [9] and GW170814 [10]. This last event has been co-jointly detected by the LIGO detectors and Virgo. It was the first event observed by Virgo which started its observation run on August 1^{st}, 2017. Thanks to the contribution of Virgo the credible area at 90% of the sky localization of the event decreased from 1160 deg^2 to 100 deg^2. A graphic summary of these detections is represented in figure 1.3.

1.1.4.2 GW170817: a multimessenger BNS coalescence

On August, 17^{th} 2017, the LIGO-Virgo detector observed the first GW signal from the coalescence of a BNS system: GW170417 [11]. This signal was the longest and loudest observed so far by GWD. The very interesting point about the discovery of this BNS merging system is that 1.7 ± 0.05 seconds after the GW signal, a Short Gamma Ray Burst has been observed by the INTEGRAL detector and the Fermi GMB detector [12]. Both the GW and the Gamma ray signals are presented in figure 1.4.

This very first multimessenger observation allows many measurements such as giving limits on the relative difference between the speed of gravity and the speed of light [13]. Moreover thanks to the three detector network, the event has been very well localized in the sky (31 deg^2) and during the period following this event, electromagnetic data have been acquired from this part of the sky. The results that have been found are in agreement with a BNS coalescence at the inferred distance from the GW data [14]. This allows for example an independent measure of the Hubble constant that appears to be consistent with the estimations that have already been done previously [15].

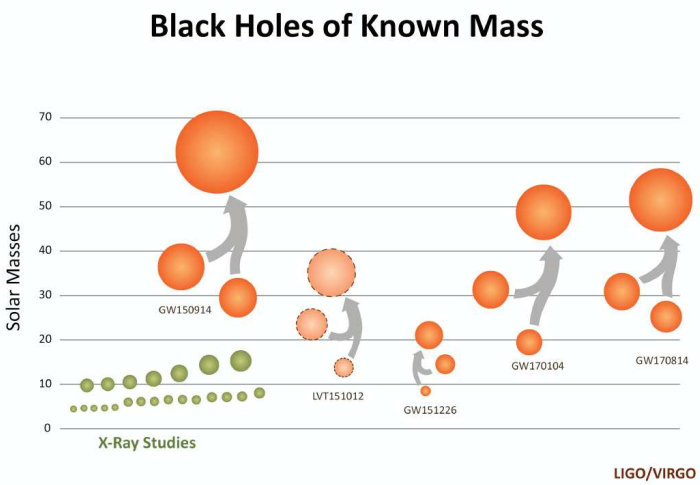

Figure 1.3: Summary of the population of black holes of known mass. In green are represented the ones discovered by X-ray methods while the one discovered by GW signals by the Ligo-Virgo collaboration. (Via LIGO/Caltech/MIT/SonomaSate (Aurore Simonnet))

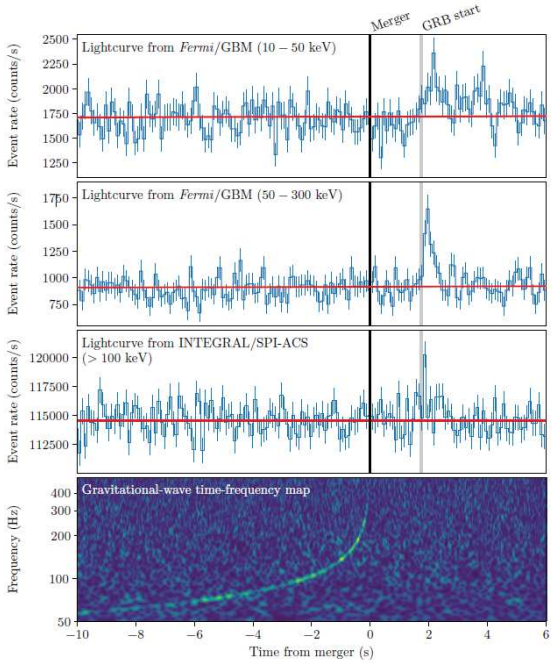

Figure 1.4: Multi messenger signals received from a BNS coalescence. The three graphs on the top are representing the gamma ray bursts that have been observed by three different detectors while the bottom signal represent the reconstructed spectrogram received by the GWD.

1.2 Interferometric gravitational waves detectors

1.2.1 History, current and future generations

In 1960, Weber was the first to set up an experiment to try to detect GW [16]. It consisted in resonant bars made of aluminum having a diameter of 1 meter and a length of 2 meters. When a GW is passing, the bar is vibrating at a resonance frequency of 1660 Hz and induces a voltage through a piezo-electric sensor. The measurement of this voltage could give the information about the GW. However the initial sensitivity was too low to detect any events. Some other experiment were based on the same principle and had a better sensitivity but none of them had results significant enough to claim a detection.

The first mention of an optical interferometric detector for GW has to be given to Gertsenshtein and Pustovoit in a paper of 1962 [17]. However the detailed design of such a detector as well as its limitation has firstly been descibed by Rainer Weiss in 1972 [18]. From this point, propositions for long time projects came up both in Europe with Giazotto and Brillet who proposed the Virgo project [19] and in United States with the LIGO project [20]. This led to the first generation of GWDs that were finally running in the 2000s. However the sensitivity of the detectors of this generation was not high enough and they did not detect any events during their running time. Then they have been improved in the second generation GWD which have a better sensitivity: advanced LIGO and advanced Virgo. More than 40 years after the first proposals, with the success of the first direct detections that we presented in the previous section, this technology proved its ability to detect GW. And even if some others technologies to detect GW are still under study, it seems that the future detectors will be mainly based on interferometry as evidenced by the many projects to come or already started: CLIO (cryogenic, Japan) [21], AIGO [22] (longer arm, US), Einstein Telescope (with a design sensitivity 10 times greater, Europe) [23] or the space based project Lisa [24], Decigo [25], TianQin [**TianQin**], Big bang observer [26]...

1.2.2 Michelson Morlay interferometer

We saw previously that the distance between two test masses is changed while a GW is passing and that the change in the distance is proportional to the amplitude of the GW (equation 1.12). The idea of the Michelson interferometer that we present in figure 1.5, is to suspend the mirrors that are at the end of the arms such as they are behaving like test masses and to measure the differential length between these two arms. To do so a laser beam of wavelength λ is injected, separated into two beam of equal amplitude thanks to a Beam Splitter (BS), the beams are back reflected on the end mirrors and partially recombined on the output photodiode. Because of the interferences that are created while recombining the beams, the power detected on this photodiode depends on the phase shift $\Delta\Phi$ that is introduced between the two arms, which, itself, depends on the differential arm length ΔL of the detector as highlighted by the following equation:

$$\Delta\Phi = \frac{2\pi}{\lambda}\Delta L \tag{1.17}$$

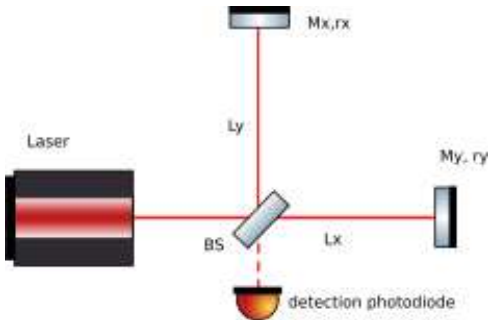

Figure 1.5: Basic scheme of a Michelson interferometer

By deriving the equation of such an interferometer, one can easily show that the power detected on the photodiode is given by [27]:

$$P_{det} = \frac{1}{4} P_0 (r_x^2 + r_y^2)(1 + C\ cos(\Delta\Phi)) \tag{1.18}$$

Where r_x and r_y are the reflectivity of the mirrors and C is the contrast defined as:

$$C = \frac{2 r_x r_y}{r_x^2 + r_y^2} \tag{1.19}$$

In order to get a better SNR, in a first approximation, we can consider that the detector is working in dark fringe. It means that the initial phase $\Delta\Phi$ is set such as the term $1 + C\ cos(\Delta\Phi)$ is equal to zero. Actually in order to get the information on the sign of the variation of $\Delta\Phi$ the working point of the interferometer is slightly shifted from the dark fringe.

Now, let us consider the effect of the passage of a gravitational wave on this power by taking a look at the phase shift. We have :

$$\Delta\Phi = \Delta\Phi_0 + \delta\Phi_{GW} = \Delta\Phi_0 + \frac{2\pi}{\lambda}(\delta l_x - \delta l_y) \tag{1.20}$$

We saw in section 1.1.2 that in the case of a well oriented gravitational wave, we have a maximum length difference between the two arms when $\delta l_x = 1/2hL$ and $\delta l_y = -1/2hL$. Since $|h| \ll 1$ we can approximate $\cos(\delta\Phi_{GW}) = 1$ and $\sin(\delta\Phi_{GW}) = \delta\Phi_{GW}$. And finally get

the power fluctuation at the output of the interferometer while a GW is passing:

$$\delta P_{det} = \frac{1}{4} P_0 \left(r_x^2 + r_y^2\right) C \sin(\Delta\Phi_0) \frac{2\pi}{\lambda} hL \tag{1.21}$$

From this simple equation several points can be noticed. In order to maximize the detected power, one can increase the input power, increase the length of the arms, and having mirrors with a reflectivity as high as possible. The issues about the coating of the mirrors will be quickly reviewed in section 1.3. Since the length of the arms can not physically be infinitely increased, we will see in section 1.2.3 how it can be done optically. Finally, concerning the increase of the power, we will see how it is done in section 2.1.3, but also that a compromise has to be found because of noises that appear at high power.

Concerning the noises, still by looking at the equation 1.21, one can see that the power fluctuation, the variation of the initial length of the arm as well as the frequency noise will affect the measure. The issue with frequency stabilization will be discussed in section 2.1.2.

1.2.3 Michelson interferometer dual recycled cavity design

In this section we are briefly reviewing the improvements that have been done from a basic Michelson interferometer in order to improve its sensitivity. A basic scheme of the optical design of an advanced GWD is presented in figure 1.6.

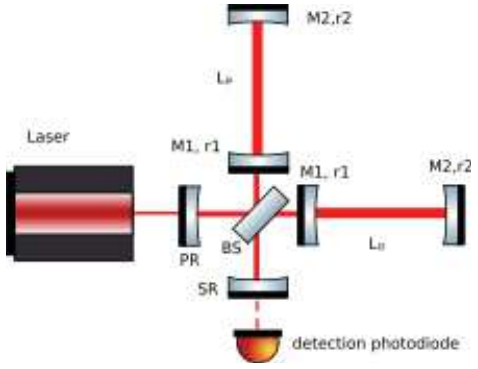

Figure 1.6: Advanced scheme of a Michelson interferometer. The mirrors M1 have been placed in order to optically increase the length of the arms. PR is creating the Power Recycling cavity while SR is a creating the Signal Recycling cavity.

The first point to notice is the insertion of the mirrors M_1. By doing that, one is creating a Fabry-Perot cavity in the arms of the interferometer and thus optically increase the length of the arm. Indeed in such a cavity, the light is resonating back and forth between the two mirrors before going out through the input mirror (more details are given in section B). The

numbers of round trip inside the cavity depends on its finesse defined as:

$$\mathcal{F} = \frac{\pi \sqrt{r_1 r_2}}{1 - r_1 r_2} \tag{1.22}$$

Where r_1 and r_2 are the reflectivities of the mirrors. In turns it allows to defined the gain of the cavity:

$$G_{FP} = \frac{2\mathcal{F}}{\pi} \tag{1.23}$$

In the case of AdV, the FP cavity have a finesse of about 450 and by taking into account their frequency response, this improves the optical length and thus the sensitivity by a factor of approximately 290.

The second point to notice is the mirror called PR, which stands for Power Recycling. Indeed by adding this mirror, the power that is normally sent back to the laser while working in dark fringe (i.e destructive interferences on the photodiode), is reinjected in the interferometer. This increases the power inside the interferometer without having to deal with the problem linked to the increase of the power of the laser.

Finally the last improvement is coming from the Signal Recycling mirror (SR on the figure). This mirror allows to recycle the signal that would come from the passage of a GW and especially to tune the sensibility of the interferometer to the frequencies we are interested in.

By looking at the figure 1.7, one can see the increase in terms of sensitivity that these three improvements are bringing compare to a normal Michelson interferometer. However these sensitivity curves are theoretical and it practice there are some noises that deteriorate it. This noises are detailed in the next section.

1.2.4 Sensitivity and limiting noises

We already briefly spoke about the noises that affect the detected power in section 1.2.2. In practice, considering the very small effect that occurs when a GW is passing, the detectors are subject to many different sources of noise. In figure 1.8, one can find the theoretical sensitivity curve of the dual-recycled interferometer scheme that we described in the previous section and its limiting noises. The main limiting noises are described in the following paragraphs.

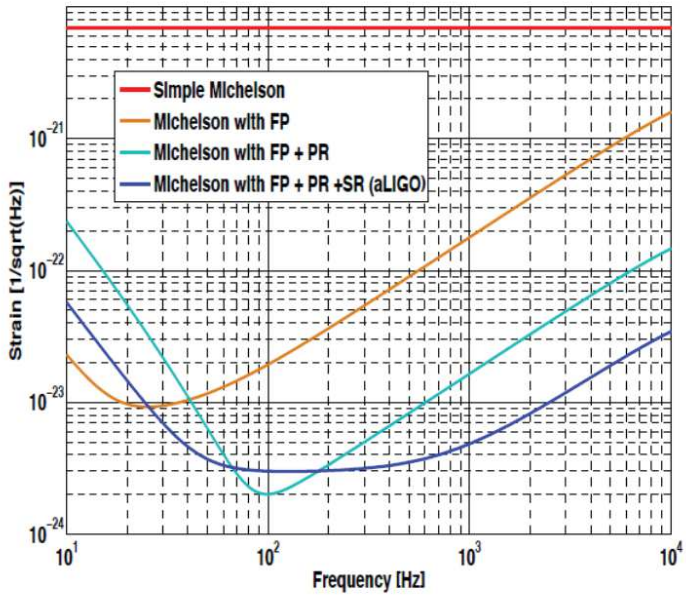

Figure 1.7: Sensitivity improvements by adding resonant cavities to the basic design of a Michelson interferometer. Figure from Stefan Hild's lecture [28]

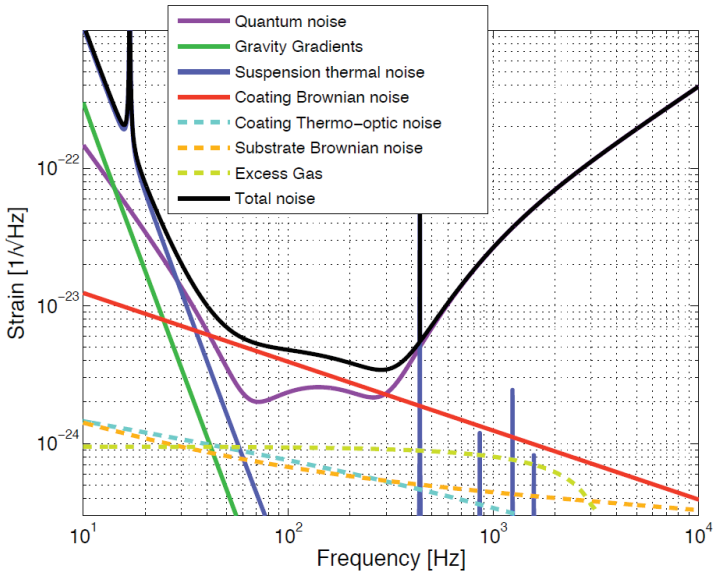

Figure 1.8: Sensitivity curve from the TDR [29]. It has been plotted for a power of 125W with a signal recycling cavity tuned to optimize the inspiral range for coalescing BNS

The Quantum noise is the most limiting one. It is coming from the quantum nature of the light itself. Indeed while detecting the power with the photodiode, the measure of a number N of photons is following a Poisson process that has an uncertainty that grows as $\sqrt{N}$. So the higher the power, the lower is its relative uncertainty. This noise is called the shot noise and is mainly limiting the high frequency band. At low frequencies, however, the noise is due to the radiation pressure that the photons applied on the mirrors while hitting it and it is directly proportional to the power. That is why a compromise has to be found while setting the power of the interferometer. A lower power will increase the sensitivity in the low frequency region while a higher power will increase it in the high frequency one.

The seismic noises are the noises coming from the earth itself. They would limit the low frequency band if they were not attenuated. In order to act as free falling test masses, the mirrors are suspended and these suspensions are compensating for the seismic noise (detail in section 1.3.3). However the main issue that has to be faced with this seismic noises is that it affects the macroscopic position of the mirrors and thus introduces some variations in the working point of the interferometer.

The thermal noise appears in both the coating of the mirrors and in the suspension. It is due to Brownian motion since they are operating at ambient temperature. It is the main contribution at very low frequency. For higher frequencies this noise is attenuated by the suspension. In order to decrease this noise, several solutions are possible. The first one, for the noise coming from the test masses is to increase the size of the beam in order to average its contribution on a bigger surface. The second option that is done in some designs such as KAGRA, is to cryogenically cool down the mirrors and the suspensions.

These are the theoretical expected noises, in practice there are many other sources as it can be seen on the typical sensitivity curves that are plotted in figure 1.9. During the commissioning phase, lots of work is dedicated to this noise hunting.

1.3 Advanced Virgo detector

The Virgo detector was a first generation interferometric detector it ran between 2007 and 2011 but its sensitivity was not good enough to detect any events. It has been improved between 2011 and 2017 in a new version that is called Advanced Virgo (AdV). A general layout of this version is presented in figure 1.10. In August 2017 AdV joined the two other LIGO interferometers and together they detected GW events. Such a complex machine can reach a sensitivity high enough to detect events only if all the subsystems are working properly together. In this section we are briefly describing all these subsystems in order to better understand how the detector is working and especially the interactions with the two subsystems that have been the frame of the work done in this thesis: the injection subsystem and the prestabilized laser subsystem. We will dedicated a full section to describe them (respectively in section 1.4 and section 2.1).

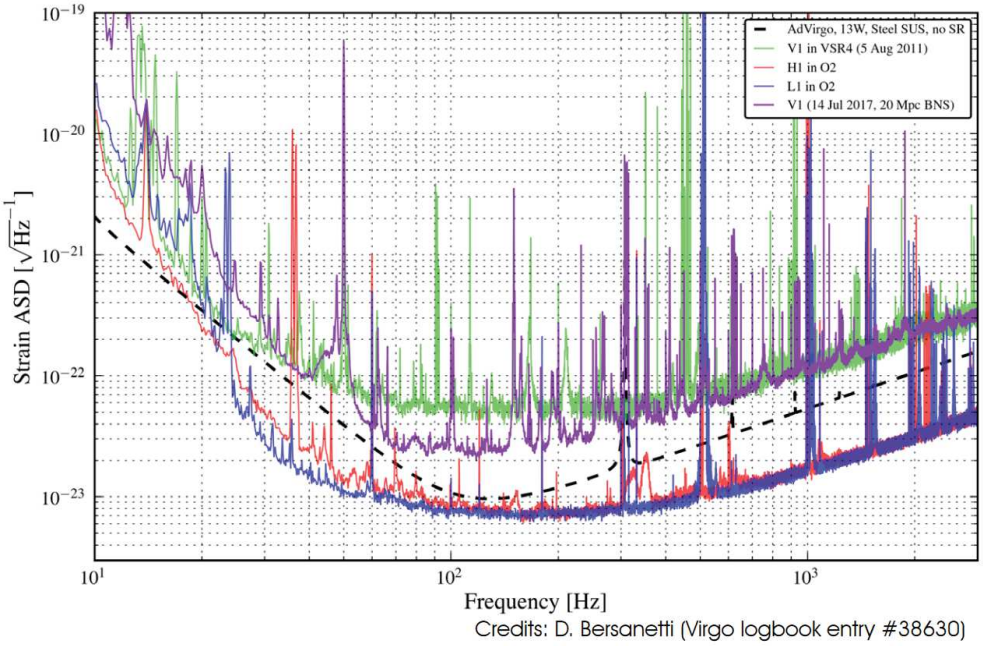

Figure 1.9: Typical sensitivity curves of the three main ground based GW interferometers

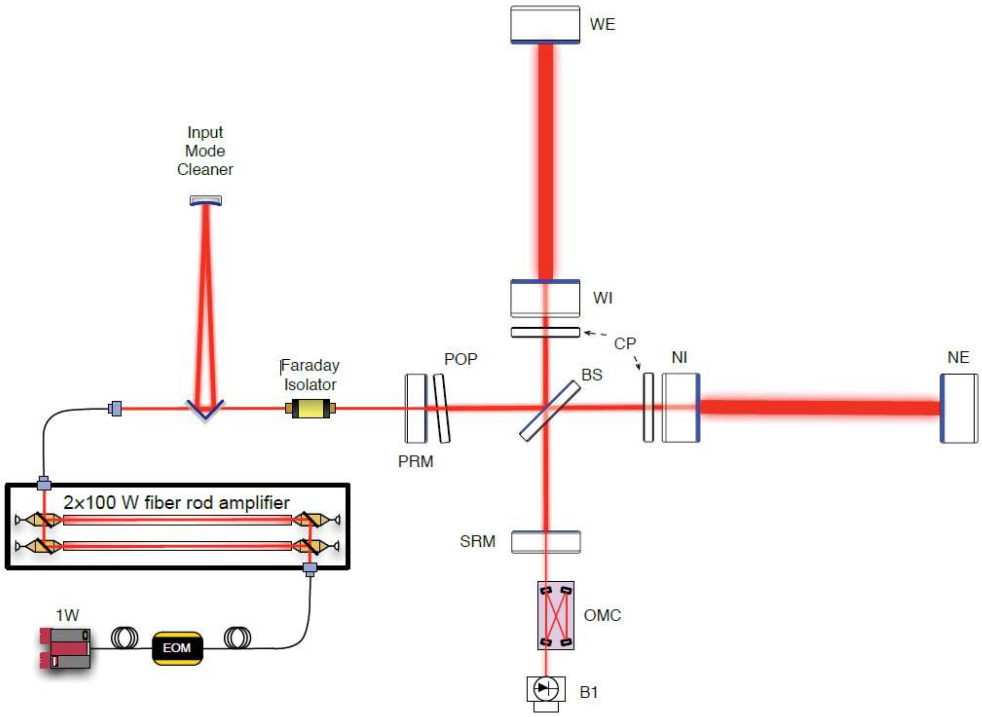

Figure 1.1: AdV optical layout.

Figure 1.10: General layout of the AdV detector as it is presented in the initial technical design report

1.3.1 Optical Simulation and Design

The optical simulation and design is the subsystem in charge of creating the tools needed to simulate the interferometer and used them to define its general layout. It defines the characteristics such as the properties of the mirrors, their position, the geometry of the different cavities. This work is done in order to maximize the sensitivity by keeping coherent parameters with what is concretely feasible. In particular they are in charge of investigating the improvements that would bring the future upgrades. As an example, there is lots of works done on the possibility of using higher order mode or on the squeezed light.

1.3.2 Mirrors and Thermal Compensation System

The subsystem of the mirrors is in charge of the optics that are used in the core of the interferometer: the input mirrors, the end mirrors, the beam splitter but also the pick off plates and the compensation plates. All these optics have very high characteristics in term of dimensions, flatness or coating characteristics that makes them unique and difficult to realize. The pick off plates are placed on the beam path to pick off a small amount of power in order to analyze the different characteristics of the beam. The compensation plates can be seen on the general layout of AdV presented in figure 1.10, they are used to correct the aberrations of the mirrors that arise when they are heated up by the laser beam. These deformations are analyzed thanks to a wavefront sensor and are then corrected either by heating the compensation plates with a CO_2 laser (input mirror) or by using a ring heater (end mirrors).

1.3.3 Suspension system

As we already mentioned in section 1.2.2, the suspension system allows the end mirrors to behave as free falling test masses. In particular it isolates the mirror from the ground motion which is one of the major issue that has to be faced to reach the require sensitivity at low frequencies. The chain used to attenuate the seismic noise is presented in figure 1.11. It consists in a succession of six mechanical filters that are linked together by metallic wires and an inverted pendulum. This part is called *superattenuator* and is attached to the last stage called the *marionetta*. The marionetta as well as the mirror can be controlled thanks to four magnets attached to them and whose position is control by four coils. The whole structure is 9 meters high. The attenuation is obtained thanks to the pendulum phenomena: each stage of the filter is attenuating the frequencies that are above it resonance frequency. In the case of AdV, the resonant frequencies are below 2.5Hz which leads at the end to an attenuation of the seismic noise by 14 orders of magnitude for the frequencies above 10Hz [30].

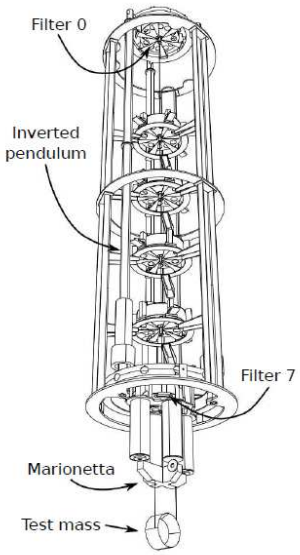

Figure 1.11: Scheme of the attenuation system of AdV. The 7 stages of filters allow to isolate the mirror from the ground motion so that it behaves as a test mass.

1.3.4 Detection system

As we saw in section 1.2.3, the detector is made of many different optical cavities. All these cavities have to be locked thanks to the PDH error signal that is presented in appendix B. The detection subsystem is in charge of acquiring these reflected errors signals thanks to the photodiodes placed on the five optical benches that are shown on the optical design presented in figure 1.12. B1 is the photodiode of the detection port, used to detect a possible GW signal. This signal is going through two output mode cleaner placed in order to give a detection signal as clean as possible. B2 is monitoring the power reflected by the power recycling cavity and B4 is monitoring the power inside the power recycling cavity. B5 is used to monitor the power reflected by the north arm. B7 and B8 are respectively monitoring the power transmitted through the north arm and the west arm. For each of this photodiode there are also two quadrant photodiodes that are used to control the angular degree of liberty of the interferometer.

1.3.5 Stray Light Control

What is called stray light is the uncontrolled diffused light in the interferometer. It can come from the part of the beam that is going out of the clear aperture of the optics, or from their anti-reflective coating which is not perfect. The propagation of this light is not controlled and participates to the noises of the interferometer. The issues linked to stray light have been evidenced during the commissioning of the first generation of gravitational waves detectors. The aim of this subsystem is to control that light in order to make it ten times lower than the target sensitivity. The solution to this problem is to install baffle in

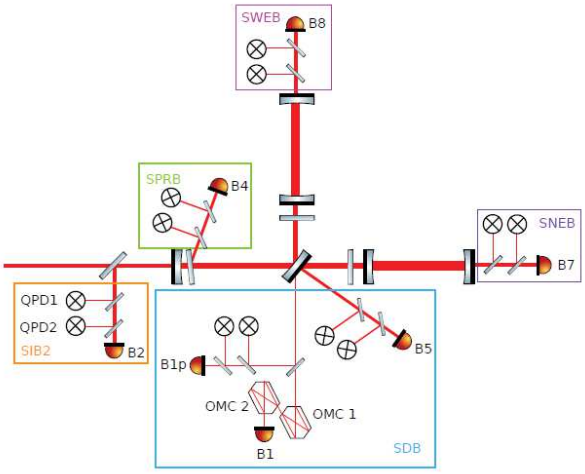

Figure 1.12: Optical scheme of the five detection benches used to acquire and the error signals to lock the cavities as well as their angular and longitudinal position

the vacuum chamber in order to absorb the residual light. These baffles should also have a very low reflectivity and low scattering. Some of them also need to be suspended in order to avoid any power fluctuations that would appear if they are oscillating.

1.3.6 Data Acquisition System

The Data acquisition system is in charge of acquiring, exchanging and processing all the data of the detector. It gives the information on the state of the interferometer that allows to control it. All these data are available online but are also stocked for a different period depending on the sampling frequency: 6 months for the 10 kHz, 1 year for the 50 Hz and 3 years for the 1 Hz. This allows to perform offline analysis of the data to understand the behavior of the detector. A simple overview of its working principle in the case of the actuation of the mirrors is given in figure 1.13. The data are converted from analog to digital signals thanks to the ADC, transported, processed in the RTPC (real time computers), and feedbacks are sent back to the interferometer to apply the correction on the mirrors position thanks to the DAC and the coil of the suspension system.

1.3.7 Interferometer Sensing and Control

Such a complex machine can not entirely works by its own. Even with the different error signals and the different feedback loops, the optics are experiencing residual motions that push them away from their desired position and thus bring the interferometer out of its working point. That is why an active control of the 4 longitudinal and 16 angular degrees of freedom is needed. The aim of this subsystem is to find the optimal working points of the different feedback loops.

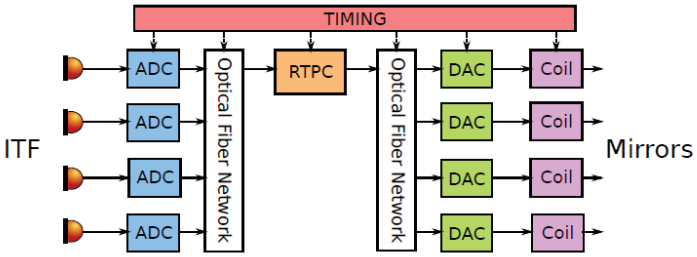

Figure 1.13: Analog-digital chain used to control the mirrors

1.4 Injection subsystem

1.4.1 General requirements

The injection sub-system is taking care of the optical elements that are used to control the different properties of the laser beam before injecting it in the interferometer. It starts at the output of the laser and finishes before the power recycling mirror. The properties of the delivered beam are about the frequency and the angular stabilities, the input power control and the geometrical shape of the beam. The optical layout of this part is presented in figure 1.14, we will detail the important characteristics and components through the development done in the next paragraphs.

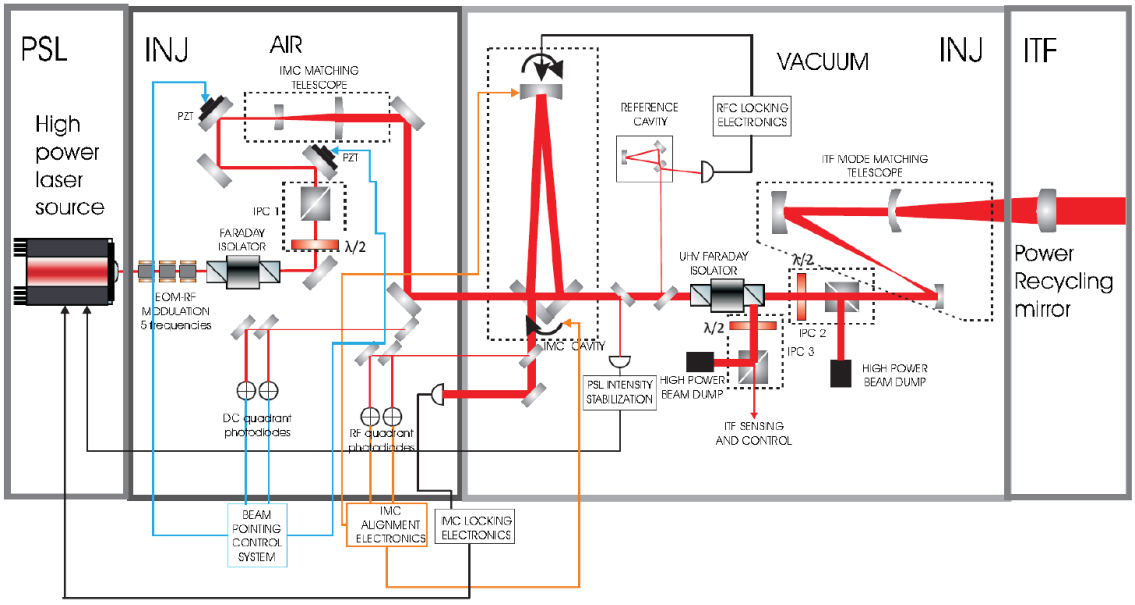

Figure 1.14: Injection optical layout. It is comprised between the Pre-Stabilized Laser and the interferometer itself. There are two main part and in-air one and another under vacuum.

1.4.2 Electro-Optics Modulators

In the injection subsystem there are two optical cavities: the Input Mode Cleaner (IMC) and the reference cavity. They can be seen on the optical layout (figure 1.14). They are used to pre-stabilize the frequency of the laser as we will see in section 2.1.2. Moreover, the interferometer itself, as we saw in section 1.2.3, is made of three different cavities (PR, SR and the two arms). In order to ensure the good functioning of the interferometer, these cavities have to be locked. This means that the frequency of the light that resonates inside the cavities have to match the actual length of these cavities. The detailed working principle of the optical cavities and how they are locked thanks to the PDH error signal, is detailed in appendix B. To create the needed error signal the beam has to be phase modulated thanks to Electro-Optic Modulators (EOM). The working principle of this device will be fully detailed in section 4.1, and especially its modulation depth m. We summarized the different frequencies needed to lock the interferometer in the following table:

Frequency (MHz)	m
6.27	0.22
8.36	0.15
22.3	0.15
56.4	0.25
119	0.15

Table 1.1: Frequencies needed to lock the different cavities of both the injection part and the interferometer

1.4.3 Faraday Isolators

We will enter in the detail of the working principle of a Faraday Isolator (FI) in section 5.1. It is actually used as an optical diode: the light can go through it in the forward direction but is rejected while going through it in the backward direction. There are two of them in the injection subsystem as it can be seen on the figure 1.14. The first one is placed at the beginning to avoid light to be reinjected into the laser subsystem. If it would happen this could cause instabilities in the functioning of the laser or, even worst, could damage it. This FI is the one we are the most interested in for the works that we will present. Since the IMC is a triangular cavity the risks linked to have some power back reflected are actually quite low and the requirement on this FI are not so restrictive. On the contrary the second FI, placed between the interferometer and the IMC has very strong requirements that are presented in table 1.2. This FI is working under vacuum and has to handle both the input power from the laser and the power that is back reflected by the interferometer. Moreover this power back reflected power from the interferometer contains the information needed to create the errors signals used to lock the interferometer.

The requirements on the Faraday in the in-air injection part are similar except for the vacuum compatibility. They are however much more easy to reach due to the fact that it is

Parameter	Requirement
Isolation (at 150W)	>40dB
Total throughput	>95%
Residual thermal lens (at 150W)	> 100 m
Clear Aperture	>20mm
Vaccuum compatibility	$< 10^{-6}$ mbar

Table 1.2: Requirements of the under vaccum FI

easier to cool it down. These points will be discussed in section 5.2.

1.4.4 Beam Pointing Control

The injection subsystem is also in charge of the Beam Pointing Control (BPC) of the interferometer. The method generally used to control the beam pointing in free space and especially used in AdV [29] is a close loop where two quadrant photodiodes (QPD) are used to monitor the position of the beam and create the error signal, the corrections are made thanks to two Piezo Electric Transductors (PZT) which both have a vertical and horizontal degree of freedom. The scheme of the set-up is presented in figure 1.15. BPC_ QN is called the near field quadrant photodiode, there is a telescope between the peak off of the main beam and the QDP which has been designed with a high magnification to make it more sensible to the vertical and horizontal shifts. On the contrary BPC_ QF is called the far field quadrant photodiode and the telescope has been designed with a long focal length in order to make it sensitive to the tilts of the beam. The sensitivity of these QPD is given by the following equation [2]:

$$S = \frac{2\sqrt{2/\pi}}{w} \times a \times i_{dc} \tag{1.24}$$

Where w is the beam size on the quadrant photodiode, i_{dc} is the current response of the photodiode (linked to optical power through the efficiency of the photodiode), the factor a can either be $a = f \times \theta$ for the far field QPD with f the focal length of the telescope and θ the angular jitter in radian, or $a = M \times d$ where M is the magnification of the telescope and d the lateral jitter of the beam in meters.

1.4.5 Motivations and objectives

The works that we will present in the next chapters have been done in the frame of this injection subsystem. We were investigating on possible improvements for the current and next generation of interferometric GWD and especially on the use of optical fibers in the in-air part of the injection system. The use of optical fiber would have several advantages. Firstly

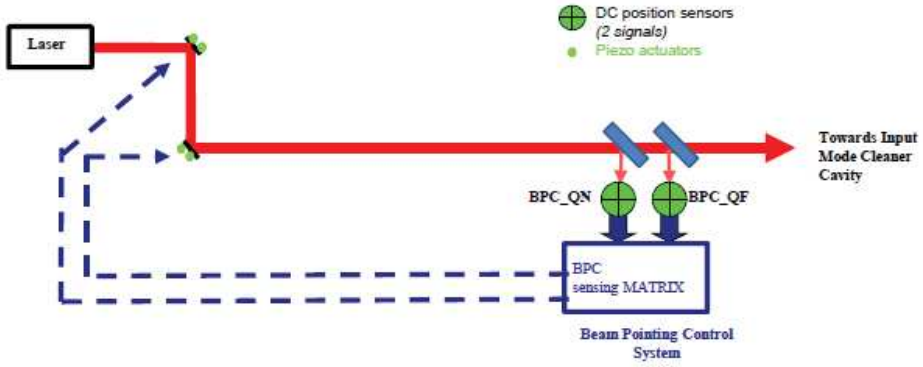

Figure 1.15: Beam pointing control using a near-field and a far-field quadrant photodiodes. The near-field QPD is monitoring the shift of the beam while the far-field QPD is monitoring the tilt. The corrections are applied thanks to two PZT.

it will simplify and ease the maintenance of the injection subsystem by reducing its size and the issues linked to the alignment. Secondly, confining the beam into the fibers will reduce the beam jitter linked to the free space propagation which is one of the limiting problem in the current version of Advanced Virgo. The path between the in-air External Injection Bench (EIB) and the under-vacuum bench Suspended Injection Bench 1 (SIB1) is actually particularly critical since the two benches are seismically isolated with a different system. Thus, there are deviations between them two that complicate the lock of the interferometer. This deviation could be avoided by linking the two benches together with an optical fiber that would bring the beam directly on SIB1. This would however require a fiber of about 20 meters to be able to pass through the different stages of the suspension system and avoid to perturb the seismic isolation. A possible design of what the injection part would look like in this case is presented in figure 1.16. It can be compared to the current design that we presented in figure 1.14. One can notice that, in this case, the IMC mode matching telescope would have to be redesigned to be placed on the Suspended Injection Bench 1 (SIB1).

The objective of this PhD was to gain experience towards that goal. To do so we were considering the development of two components: a high power fibered EOM and a high power fibered FI. We developed the work through different steps. The first one was to understand the difficulties linked to the use of optical fibers in our case (Chapter 2), to try to find solutions and especially to find fibers that could fulfill our needs and test them to confirm their ability to transport the laser beam of Advanced Virgo (Chapter 3). Finally, the idea was to work on the high power EOM (Chapter 4) and the FI (Chapter 5) used in the injection part of Advanced Virgo, and especially, using those fibers, to design new versions of a fibered EOM and FI that could be used in the current and/or next generation of GWD.

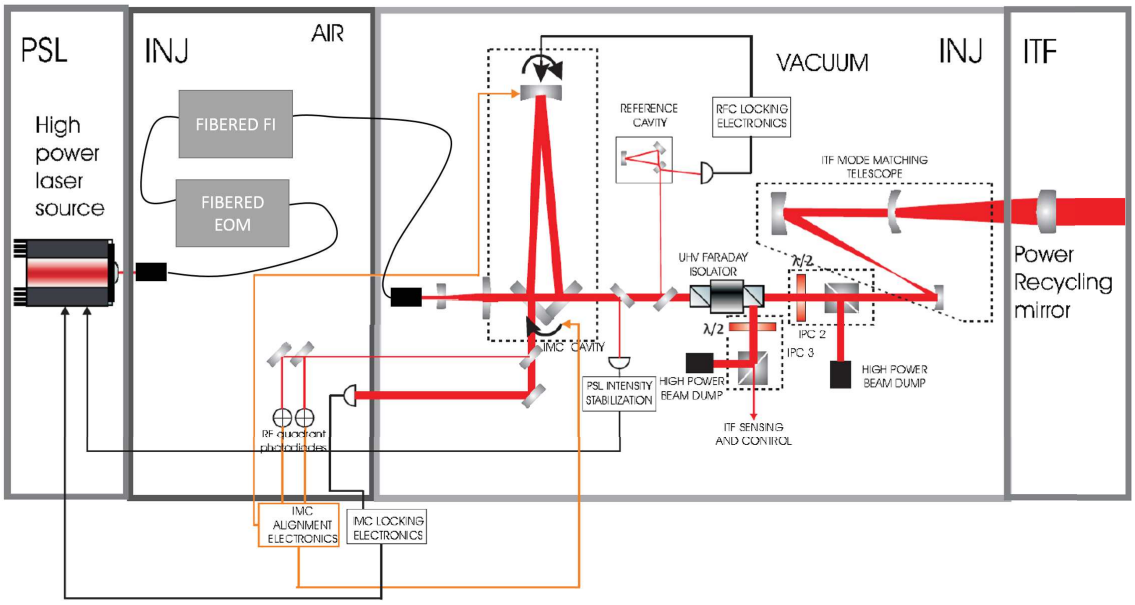

Figure 1.16: Possible design of the injection subsystem using optical fibers.

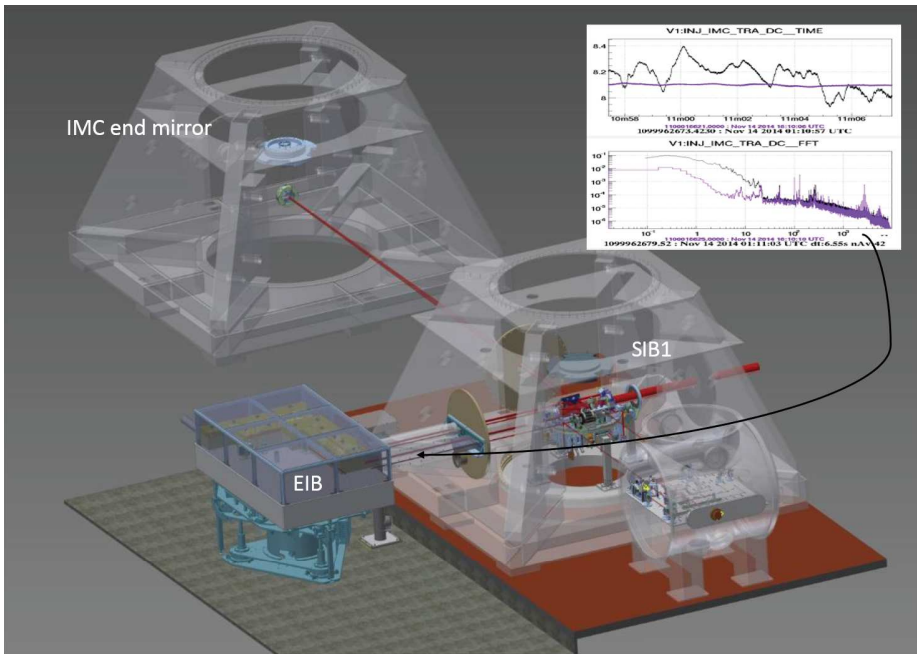

Figure 1.17: Injection subsystem representation. One of the critical part is passage from the in-air EIB bench to the under vacuum one SIB1. Reduction of the power noise due to the beam jitter in this part is already presented. By using an optical fiber this part could be avoid

Chapter 2

High power single frequency Laser beam delivery with optical fibers

The aim of this chapter is to see how optical fibers can be used to deliver a high power single frequency beam instead of having the beam propagating in free space. First we will review the main properties of a laser beam by taking the example of the one we are using in AdV. Then we will detail the working principle of different design of optical fibers to see how they could be used to transport the light by keeping the characteristics of the input beam and fulfill our needs. Then we will investigate the issues linked to the injection of a high power beam from free space into a fiber. Finally we will discuss the non linear effects inside the fibers that are the other critical point of having high power into optical fibers.

2.1 Advanced Virgo Laser beam characteristics

A laser (for "Light Amplification by Stimulated Emission of Radiation") is an optical device that has the particularity of producing light spatially and temporally coherent. The laser effect is obtained thanks to the stimulated emission which is a property of interaction between light and matter that are already theoretically predicted by Einstein in 1917 [31]. Stimulated emission is the process through which an atom in an exited state, hit by a photon, is emitting a photon with the same properties. Many researchers worked on this phenomena, among these works we can cite V.Fabrikant who had the idea of using this emission to amplify electromagnetic waves, W.Lamb and R.C Retherford who firstly experimentally demonstrated stimulated emission or again A.Kastler in 1950 who suggested the technique of optical pumping (Nobel Prize in 1966) that he validated two years later with Winter and Brossel [32]. But the first Maser (amplification of microwaves in gas) was only created in 1953. In the following years people worked on the adaptation of this principle for visible light (Nobel prize for Townes, Bassov, et Prokhorov in 1964). Finally in 1960, Maiman demonstrated the first functioning laser [33]. It was the solution of a long time quest: how to get spatial and temporal coherent light. It opened a new area of physics: photonics. Nowadays, from telecommunication to metrology, from military to medical applications, laser is used everywhere and has been subject to many improvements.

In this section we will not enter into the details of the laser technology, there would be too much to be said. Instead we will review the main characteristics of the very specific laser beam that is used in Advanced Virgo and explain its properties: first we will detail how is obtained a single frequency emission, in a second part how to amplify this laser emission in order to reach the high amount of power we need in our detector. Then we will take a close look to two main properties of a laser beam that are of particular importance while working with optical fiber: the polarization and the spatial shape of that beam. Knowing this characteristics will help us, in the further developments of the thesis, to understand how they could get worse while propagating into an optical fiber.

2.1.1 Characteristics

In table 2.1, you can find the requirements of the Pre-Stabilized Laser as they have been given in the Technical Design Report (TDR) of Advanced Virgo [29]. These characteristics are the target ones that have to be considered for all the work that we have done in the following chapters. The requirements are on the power, the frequency linewidth, but also on the spatial quality of the beam. The Polarization state is not mentioned in the requirements but for our application we considered that it has to be linear with a PER $>$ 20 dB. Moreover it has to be noted that the use of optical fibers could significantly deteriorate the power and frequency noises.

Requirement	Value
Power	175 W on TEM_{00} at the input of INJ
Laser linewidth	< 1 Hz
Power Noise	-172 dB/Hz

Table 2.1: PSL requirements in advanced Virgo

2.1.2 Single frequency emission

The principle of a laser is to have a medium optically pumped so that the atoms are in their excited state and to place this medium in a resonant optical cavity (see appendix B). A photon spontaneously emitted will resonate inside this cavity and will participate to the stimulated emission of the medium. The laser used in Advanced Virgo is made of several stages with growing power. The one which drives the frequency is a 1 W Nd:YAG CW single mode at 1064 nm, based on the Non-Planar Ring Oscillator (NPRO) technology [34]. It is called the master laser. A picture of the laser as well as the NPRO cavity are presented in figure 2.2. This kind of cavity has been developed in the years 1980s by Kane et al [35], and improved few years later by Nillson et al [36]. The front face of such a cavity is highly transmissive for the pump light (red on the figure), the light created by stimulated emission is then circulating inside the crystal by total internal reflection and the same front mirror is used as a coupling mirror to get the laser beam out. The particularity of this cavity is

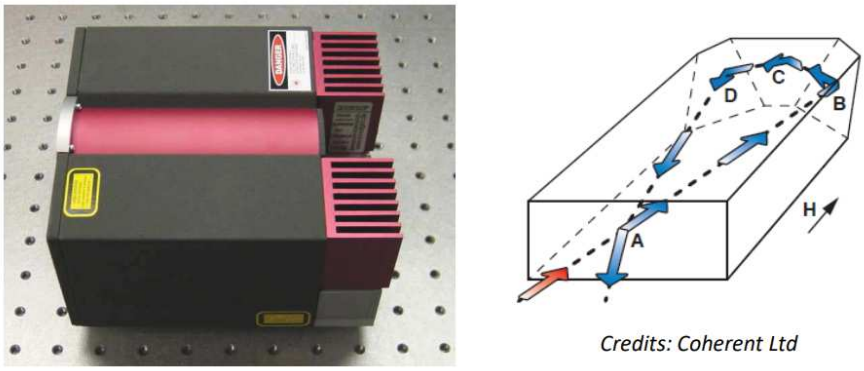

Figure 2.1: The master laser used in Advanced Virgo (left): a 1 Watt Nd:YAG CW single mode at 1064 nm, based on a Non-Planar Ring Oscillator (right). The red arrow corresponds to the injection of the pump light.

coming from the fact that it is a non planar one. Thus for each round trip the polarization is experiencing a small rotation, this rotation combined with a rotation due to the Faraday effect that arise in the crystal because of the magnetic field that is applied on it (see section 5.1). Thus the polarization direction of the light circulating in the clockwise sense and counter clockwise sense are different and since the coating of the front face is slightly polarization dependent, the undesired propagation will experience more losses and thus will not be amplified as well as the other one. Thanks to this unidirectional operation, there are no standing waves, thus no spatial hole burning and thus no gain for a second longitudinal mode. Due to its monolithic design this cavity is very stable, this feature ensure its single frequency operation: it has a linewidth of about 1 kHz over 100 ms. It can be actuated at low frequencies with a change in the temperature of the crystal and at high frequencies with a piezoelectric transducer acting on one of the face of the cavity. This single frequency operation is of main importance for the interferometer but we will see that it is an issue in our application since it will enhance some non-linear effects in optical fibers (section 2.4).

2.1.3 High power amplification

In order to reach the amount of power we are interested in, a two stages scheme is used. It can be seen on figure 2.2. The first stage is a laser whose emission is amplified thanks to two Nd:YVO4 crystals that are optically pumped in a four-mirrors bow-tie optical cavity which is locked thanks to the frequency reference of the master laser. It allows to reach a power of 20 W. These 20 W are then reinjected into a second amplifier. This one is a solid state amplifier made with 4 crystals that allows to reach a power up to 50 W. The advantage of using an amplifier is that it does not need to be locked and thus makes the coupling much simpler.

As one could have noticed, in its current version Advanced Virgo is not working with

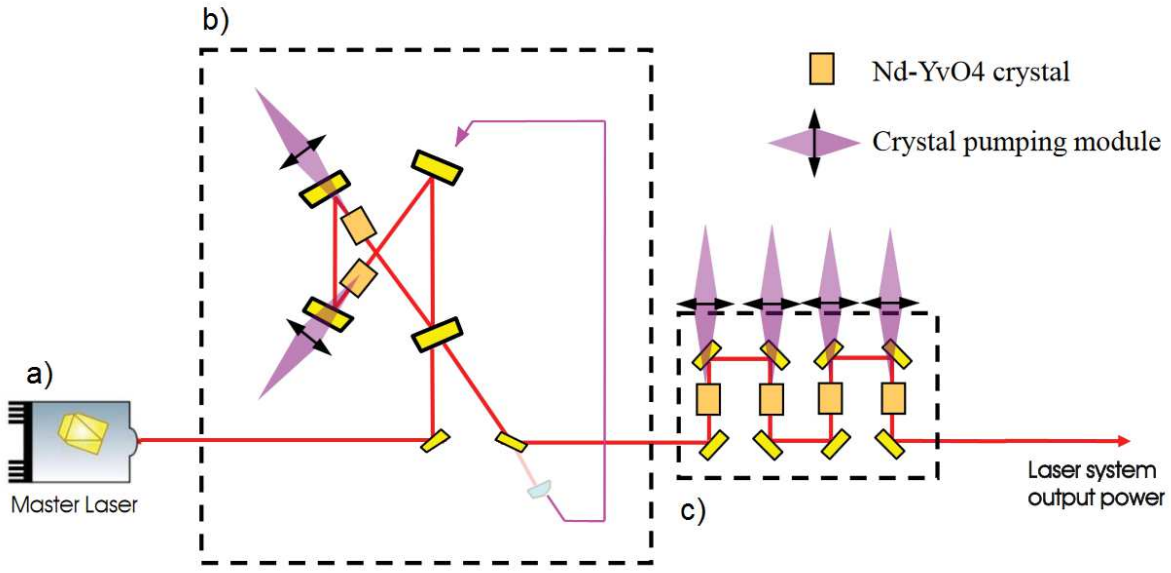

Figure 2.2: The two amplification stages used in Advanced Virgo to increase the power. a) is the master laser that deliver a power up to 1 W, b) is the slave laser that amplify the power till 20 W, c) is a solid state amplifier that allows to reach 60 W

the power of 200 W that was expected in its design. In December 2017 the second stage amplifier will be replaced by an amplifier from Neolase [37] that will allow us to reach an output power of 100 W. In order to reach the needed 200 W some possibilities are under investigation, especially the use of fiber laser. The use of such laser amplifier would make the works that we have done in this thesis even more relevant.

2.1.4 Polarization

The polarization quality of the laser beam of Advanced Virgo, before being injected in the interferometer, is of about 40 dB. In order to understand what is this quality of polarization let us come back to the nature to the electromagnetic model of the light: it is an electromagnetic wave that have two components, the electric and magnetic fields that propagate perpendicularly to each other and that are included in the planes orthogonal to the propagation direction. The polarization state is giving us the information about the electric field. At a given time t, we can indeed decompose the electric field on an orthogonal base ($\vec{\boldsymbol{x}}$,$\vec{\boldsymbol{y}}$) as follow: $\vec{\boldsymbol{E}} = \vec{\boldsymbol{E}}_{\boldsymbol{x}} + \vec{\boldsymbol{E}}_{\boldsymbol{y}}$ where $\vec{\boldsymbol{E}}_{\boldsymbol{x}} = E_{0x}e^{i(\omega t\Phi_x)}\vec{\boldsymbol{x}}$ and $\vec{\boldsymbol{E}}_{\boldsymbol{y}} = E_{0y}e^{i(\omega t\Phi_y)}\vec{\boldsymbol{y}}$. Depending on the amplitude E_{0x} and E_{0y} of these fields and their phase difference $\Delta\Phi = \Phi_y - \Phi_x$, we can classify the polarization states into three categories defined below:

- The elliptical polarization, when there are no distinctive characteristics on E_{0x}, E_{0y} or $\Delta\Phi$ (figure 2.3 a)

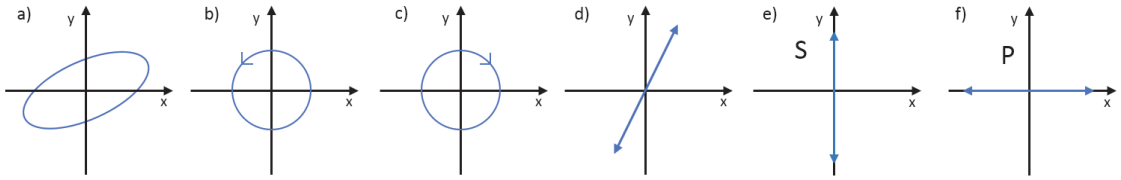

Figure 2.3: x horizontal y vertical polarization states a) elliptical b) left circular c) right circular d) linear polarization e) S-polarized f) P-polarized

- The circular polarization, is a special case of elliptical polarization when the two components of the electric field E_x and E_y have the same amplitude and a phase shift of $\pm\pi/2$. Depending on the sign of the phase shift the polarization is said to be left-hand (figure 2.3 b) or right-hand circularly polarized (figure 2.3 c)
- The linear polarization, is when along its propagation, the electric field is included ina single plan. This means that either there is a phase shift such as $\Delta\Phi = 0\ [\pi]$ (figure 2.3 d) or that the amplitude of one of the component is null ($E_{0x} = 0$ or $E_{0y} = 0$) (figure 2.3 e and f)

Among these polarization states, the most important ones while considering the reflection and transmission on a surface are the so-called S and P polarizations. The polarization is said to be linear P when it is included in the plane of incidence while linear S is when it is included in the perpendicular plane. In figure 2.3, they have been specified for the most usual set-up, i.e when the beam is kept in plane parallel to the optical bench. When giving the polarization properties of an optical component, manufacturers always have to differentiate the behavior of both polarizations. These polarization states are also used to analyze the polarization quality of a beam by analyzing its PER (Polarization Extinction Ratio) (equation 2.1) thanks to a polarizer.

$$PER = 10\ \log\left(\frac{P_S}{P_S + P_P}\right) \tag{2.1}$$

2.1.5 Spatial beam quality

2.1.5.1 Higher order modes

In the characteristics of the laser (table 2.1) we saw that 175 W should be in the TEM_{00} mode. This mode is the fundamental mode of the Hermite-Gauss base. Indeed, every single beam can be decomposed on different basis. The most commonly used are the Hermite-Gauss and the Laguerre-Gauss ones that are presented in figure 2.4, but it does exist some others basis such as Ince-Gaussian, Hypergeometric-Gaussian modes.

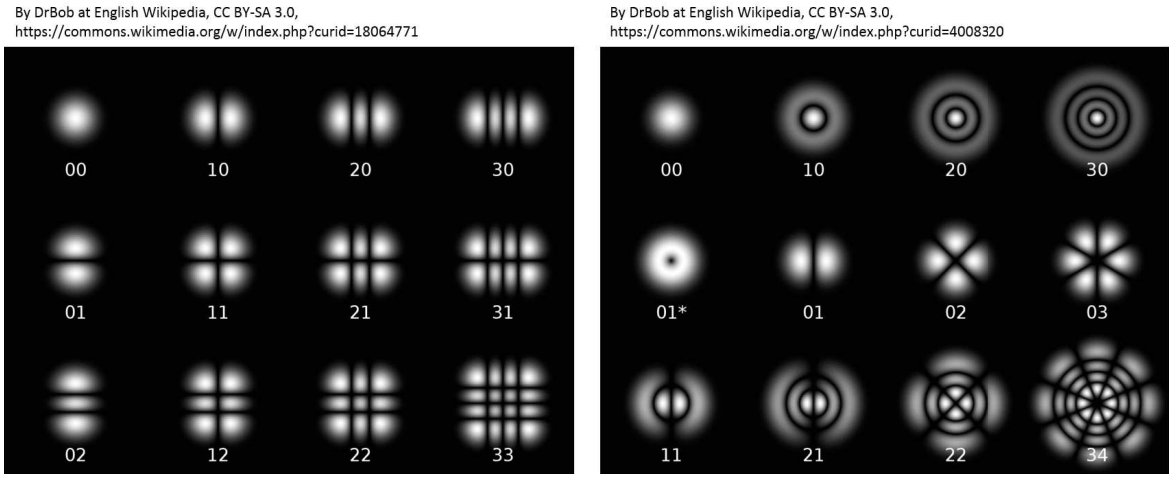

Figure 2.4: Rectangular transverse mode patterns TEM_{mn}) also called HG modes (left) and cylindrical transverse mode patterns TEM_{pl} also called LG modes (right), via wikimedia

Because of its particularities that we will detail in section 2.3.1, this TEM_{00}, also called Gaussian mode, is the most wanted and the most common one at the output of lasers. In practice it is difficult to obtain because of the asymmetries and the imperfection of the bulk medium used for the laser emission, as well as all the others optics used in the set-up. A spatial filtering of the beam in order to keep only the TEM_{00} can be obtained thanks to resonant optical cavities. Indeed depending on its characteristics it is possible to design optical cavities for which only the TEM_{00} is transmitted. However even if one would initially work with a perfect TEM_{00}, every transmittive optical element could introduce aberrations which results in spreading thepower of TEM_{00} into Higher Order Modes (HOM). For example lenses are introducing HOM, the most commonly used ones are spherical lenses because they are cheaper to manufacture and in most of applications the aberrations that they introduce are meaningless. But in some cases where we want to avoid any distortion of the beam it could be useful to use another type of lenses such aspherical lenses or even Positive Best Form Lenses (PBFL).

These HOM are of great importance in our application since cavities and single mode fibers are designed to guide only the fundamental mode. The power contained in the HOM will not be transmitted and will result in power losses or in power fluctuation if it varies in time. In the case of the fibers these losses participate to the heating of the connectors as we will see in section 2.3.3.

2.1.5.2 Beam quality factor

A first way to get information about the HOM content is to look at the beam quality factor. Noted M^2, it is a single value defined by the ISO standard 11146 [38] commonly used to characterize the quality of the output beam of a laser. It gives us the information on how well a beam can be focused compare to the diffracted-limited TEM_{00} beam. Thus a perfect

TEM_{00} mode will have a $M^2 = 1$, lower values are not possible and laser beams with a greater M^2 will diverge faster following the equation:

$$\theta = M^2 \frac{\lambda}{\pi w_0} \tag{2.2}$$

This angle of divergence as well as the propagation of the beam are explained in detail in section 2.3.1. So the value of the M^2 can be computed by measuring the beam width at different distance, computing the divergence and comparing it to the theoretical one. This anomaly in the focusing and the divergence of the beam is actually coming from the HOM that are not propagating like the TEM_{00}. So it gives a first idea of the beam content and a convenient way to compute the propagation. However in the case of a $M^2 \neq 1$ a complete characterization is required in order to define the effective power contained in the HOM of the beam.

2.1.5.3 Higher order modes content analysis

The most common way to measure the mode content of a beam is to scan an optical resonator. The working principle of such cavity is presented in appendix B. The idea here is to scan the cavity over a whole Free Spectral Range (FSR) by displacing a mirror mounted on a piezoelectric transducer. In the case of a non degenerate optical cavity, every mode is resonant for a specific frequency. By scanning the frequency (either the resonant frequency of the cavity or the frequency of the laser) on can select the associated mode. So by knowing the response of the cavity, ie where are the different modes resonating, one can know the mode content of any input beam by measuring the amplitude of the transmitted peaks through the cavity.

2.2 Optical fibers

One of the way to propagate the light without having a beam diverging over the distance and being able to easily bring it to a remote places of interest is to use optical fibers. In this section we will go through the history of optical fibers to see how they evolved from their discovery to the different current designs. We will explain some of these designs to see how they could fulfill our needs: able to withstand a power up to 200 W, keep the polarization state, keep the beam quality (TEM_{00}), have a length of about 20 meters and do not introduce power or phase noises higher than those that have been specified in the injection part of the Technical Design Report of Advanced Virgo [29].

2.2.1 History, from the discovery to the wide current use

An optical fiber is a wave-guide, a wire generally made of glass or plastic which is able to transport the light. The ability of transparent medium to conduct the light was already known in the ancient Greece but it has firstly been scientifically demonstrated in the early 1840s by Colladon and Babinet [39, 40] in a paper in which they were discribing the conduction of light in a stream of water. In further works people extented the principle to the guiding of light into a glass medium. Starting in the 1880s, people were using it to transport light in remote places thanks to reflective pipe in a first time (Wheeler, 1880), and then with glass rods, especially for surgery (Roth and Reuss 1888 and Smith 1898). They were also used to transport images thanks to arrays of fibers in what could be considered as an ancester of television [41]. Works on image transportation have been carried on over the years, by John Logie Baird and Clarence W. Hansell in the 1920s, Heinrich Lamm in 1930s, but the breakthrough came from Abraham Van Heel in 1954 who covered the fiber with a material of lower refractive index to protect the fiber from outside perurbation, and thus started reduce the signal losses [42]. Nowadays fibers are still used for power transportation or direct image transmission either in military, surgery or industrial applications. But its main use is for telecommunication. Compared to copper wires it has indeed several advantages among which the main ones are:

- A larger bandwidth of few thousands of MHz/km
- Speed, telecommunication in optical fibers is faster because it has a greater propagation distance before which a repeater is needed. The use of optical amplifier makes also them faster since the information is repeated without having to encode it.
- Immunity and reliability, since fibers are less sensitive to environmental noises and especially electromagnetic interference.
- Security, it is indeed physically almost impossible to pick up a signal directly on a fiber.

For all these reasons optical fibers have become the most used mean for long distance telecommunication [43]. However optical telecommunication has not been possible for a long time. The first attemp has to be given to Alexander Graham Bell in 1880 with is photophone [44]. It was a device that was converting the sound of voice into a light signal thanks to a vibrating mirror, this signal was then propagating and was read by a detector located in a remote place. However the device was facing too many difficulties, and was especially subject to too many external perturbations, so he did not push his research any further. A link was missing between the emitter and the receiver in order to avoid those perturbations over long distance: an optical fiber. Works on propagation in optical fibers started, but at the beginning they were facing a similar issue, losses inside the material were approximately 1000 dB/km whereas in order to work properly an optical communication needs an attenuation lower than 20 dB/km as it has been theorized by Kao in 1966 [45]. In the years after he designed such a system, using silica fiber, and received a Nobel price in 2009 for this. That was the beginning of many works done over the years to improve the understanding of

optical fibers and to keep improving its performances, especially regarding depolarization, dispersion, attenuation, non linearity, noise sensitivity, which are the main criteria limiting the possible propagation length of a signal inside a fiber. The field is still very active nowadays as it is evidenced for example by the about 60.000 papers, referenced by google scholar, that have been published about or using optical fibers in 2016.

Beyond power and image transmission and telecommunication, the improvement that have been made on optical fibers led to a new field of application, the fiber sensing. There are many different designs that we will not detail here but most of them are based on the sensitivity of fibers to external perturbation. By using an input beam having good characteristics and a good quality fiber, one can measure the distortion brought by an external perturbation by analyzing the beam at the output of the fiber.

In our application the use of optical fibers is at the boundary between power delivery and sensoring/telecommunication. On the one hand, we are indeed using a high quality beam which presents characteristics in term of polarization, spatial mode or spectral width that are comparable or even better than the ones that could be used in optical telecommunications or fiber sensing but on the other hand we are working at a much higher power. So the challenge is to find a fiber that could at the same time withstand high powers and keep a good beam quality.

We already mentioned the huge amount of work which is done every year on optical fibers, there would be a lot to say on them but we will not enter too much into the details. In the next sections we will simply introduce the basic working principle of the very first optical fibers and how the designs have then been improved over the years, leading to new types of optical fibers with different characteristics that make them suitable for different applications.

2.2.2 Main characteristics

Depending on the use for which they have been designed, the characteristics of optical fibers vary a lot from one to another. In order to better understand the designs and the properties of the fibers that we will describe in the next paragraphs, we are reviewing in this part the main characteristics that have to be taken into account while designing and manufacturing them:

- The material that is used in the core and the cladding of the fiber (see figure 2.5) and especially its optical properties. The most common used is silica, but manufacturers are also doping it with ions in order to change the behavior of the fiber. We are then speaking about doped or active fibers.

- The diameter of the core, often subject to compromise: a higher core diameter allows higher power capability but it also modifies the modes that are actually guided by the fiber.

- The mode content, the modes that can propagate inside the fibers. In particular, by opposition to multimode fibers, a fiber is said to be single mode when only the fundamental mode can propagate into it.

- The Mode Field Diameter (MFD), is the diameter of the fundamental mode actually propagating into the fiber. It is particularly relevant for single mode fiber and it has in general a value close to the core diameter.

- The Numerical Aperture (NA) of a fiber is giving the information on the acceptance angle θ_a at which light can be injected into the fiber (see figure 2.7).

- The PER, as it has been defined in equation 2.1, is the quality of the polarization at the output of the fiber. It is especially relevant for Polarization Maintening (PM) fibers and polarizing fibers.

- The attenuation, is giving the ratio of the input light lost along the fiber. Often given in dB/km, it is particularly important for km-scale optical fibers.

- The bending radius is the minimum radius of curvature at which the fiber can be bent keeping its nominal characteristics. For some designs there is also a maximum bending radius.

Obviously most of the value of these parameters are wavelength dependent and are only valid for the one that is provided in the datasheet of the fiber.

2.2.3 Fiber designs

In the next paragraphs we will review and explain the working principle of some fibers. The list is not exhaustive since too many designs exist but we will understand the motivation that led manufacturers to come from basic step index fibers to more complex designs. In particular we will detail the working principle of the fiber types in which we are interested: the Polarization Maintening Fibers (PMF) and the Photonics Crystal Fibers (PCF).

2.2.3.1 Step index fibers

Step index optical fibers were the very first optical fibers that have been manufactured. They are generally made of glass and are based on the Total Intern Reflection (TIR) at the interface between the core of the fiber and its surrounding cladding (figure 2.5). The TIR is a consequence of the Snell-Descartes law (eq 2.3) that describes the behavior of a beam at

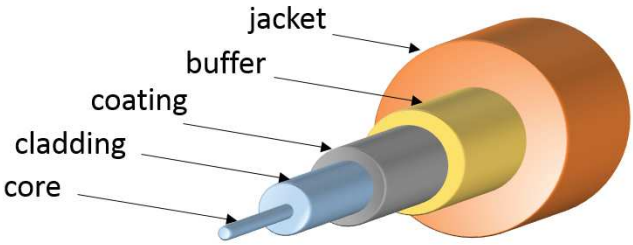

Figure 2.5: Typical structure of an optical fiber: the core is surrounded by the cladding and they are protected by different layers, generally a coating, a buffer and a jacket.

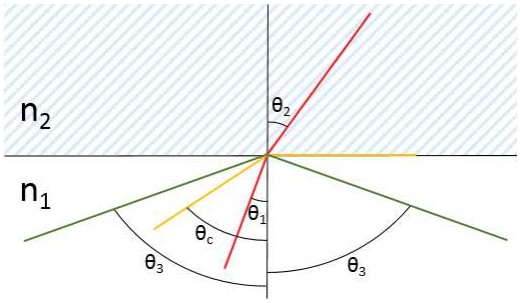

Figure 2.6: Refraction of a beam at the interface between a medium of refractive index n_1 and another one of lower refractive index n_2 according to the Snell-Descartes law. While $\theta_3 > \theta_c$ the beam is reflected with the same angle

the interface between a medium of refractive index n_1 to another one of refractive index n_2 (figure 2.3):

$$n_1 \sin(\theta_1) = n_2 \sin(\theta_2) \tag{2.3}$$

In a step index optical fiber, n_1 the refractive index of the core is greater than n_2 the refractive index of the cladding. Thus for every angle greater than the critical angle $\theta_c = \arcsin(n_2/n_1)$ the light is not refracted anymore but completely reflected on the interface (figure 2.7).

Using the parameters of the fiber we can define the parameter:

$$V = \frac{2\pi}{\lambda} r NA \tag{2.4}$$

Where r is the radius of the core of the fiber and NA is the Numerical Aperture of the fiber defined by the following equation:

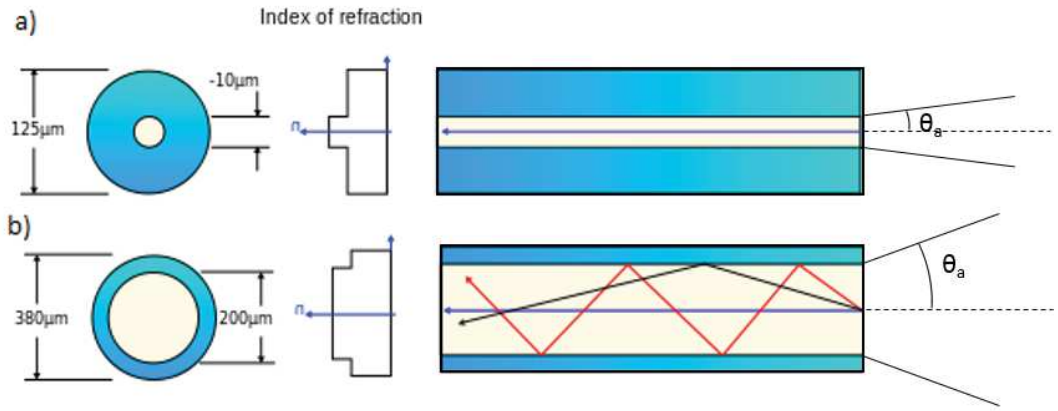

Figure 2.7: Total Internal Reflection into a step index fiber for single mode fiber (a) and multimode fibers (b). θ_a is the acceptance angle of the fibers (Source: adapted from wikimedia picture)

$$NA = \sqrt{n_{core}^2 - n_{cladding}^2} \tag{2.5}$$

The full acceptance angle of the fiber $2\theta_a$, that can be seen on figure 2.7, can be obtained from the value of the NA thanks to the formula $\theta_a = \arcsin(NA)$. When V is smaller than 2.405 only one mode can propagate inside the fiber and it is then considered as a single mode fiber, otherwise the fiber is said to be multimode. One of the challenge with optical fiber is to increase the size of the core by keeping its single mode behavior. Looking at the equation 2.4, the basic idea to do so at a given wavelength would be to reduce the NA, ie reduce the difference between the refractive indices of the core and the cladding. However this can not be done infinitely. Because of manufacturing problems, while fabricating the fibers any defaults in the core or cladding will lead to a change in the refractive index that would modify the guidance properties of the fiber. Moreover, if such a fiber existed there would actually be many pratical problems: any external perturbation such as temperature changes or bending of the fiber would modify the refractive indices and will affect its behavior. In practice even if values down to 0.04 have been reached [46], the usual NA of fibers is greater than 0.06. This leads to a maximum core radius for a single mode step-index fiber of about 6.8 µm , it is even lower in practice in order to reduce the sensitivity to bending losses. That is not enough to increase the power to the range that we are interested in. Moreover fibers do have other drawbacks, for example it does not preserve the input polarization. That is why new kind of fibers have been developed over the years. We will detail hereafter the working principle of the ones that are of interest for our application.

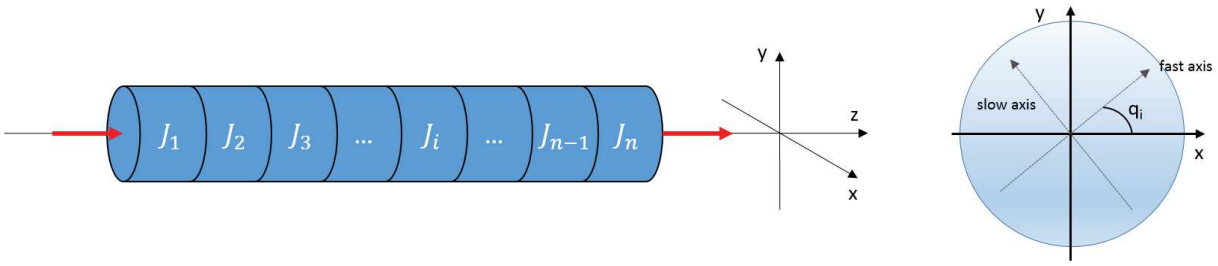

Figure 2.8: Modelling of a fiber as a succession of uniform birefringent segment. Each segment is described by the angle q between its fast axis and the horizontal axis and the phase shift δ that is introduced between the fast and the slow axis

2.2.3.2 Polarizing and Polarization Maintaining fiber

While using a fiber in an optical setup it is also important to keep the polarization state while propagating into it or at least to have a stable state at the output of the fiber. This is not the case with usual optical fibers like the ones that we described before. Indeed every single default in the structure of the fiber will lead to small birefringence which, along the fiber, will depolarized the light and give us a random state of polarization at the output. Polarizing and Polarization Maintaining Fibers (PMF) are fibers that are designed to keep a stable state of polarization at the output. We will hereafter described their behavior by using a segmented model of the fiber.

Let us consider an optical fiber as a succession of uniform birefringent elements as presented in figure 2.8. For a standard optical fiber which is not subject to twist we consider that the induced birefringence is linear and the Jones matrix of the segments can be defined by the matrix 2.6 [47] (see appendix C on the Jones matrix formalism).

$$J_i = \begin{bmatrix} \cos\frac{\delta_i}{2} + j\sin\frac{\delta_i}{2}\cos 2q_i & j\sin\frac{\delta_i}{2}\sin 2q_i \\ j\sin\frac{\delta_i}{2}\sin 2q_i & \cos\frac{\delta_i}{2} - j\sin\frac{\delta_i}{2}\cos 2q_i \end{bmatrix} \tag{2.6}$$

The axis having the smallest effective refractive index is called the fast axis and the orthogonal one is called the slow axis. The parameter q is the angle between the fast axis and a reference axis, the horizontal one ($\vec{\boldsymbol{x}}$) for example, and δ is the phase shift in rad/m between the slow and the fast axis.

An electric field E_{i-1} coming out of the $(i-1)^{th}$ segment can be decomposed in the base of the two main axes of the i^{th} element. It results in two electric fields E_{i1} and E_{i2}, that are experiencing a phase shift δ_i one respecting to the other while propagating into the i^{th} segment. Again, at the output of the i^{th} segment the two electric field can both be decomposed on the base of the $(i+1)^{th}$ segment, and so on till the end of the fiber. The

passage from one segment to another is called the mode coupling. If the characteristics of the segments are relatively similar, the mode coupling is quite low and the characteristics of the input electric field are not varying too much, but if they are very different, it can results in a complete different output. Thus, the electric fields $E_{n1}e^{i\phi_{n1}}$ and $E_{n2}e^{i\phi_{n2}}$, and so the actual polarization state at the output of the fiber, depend on the propagation in every segment and especially on the variation of the parameter q from one segment to another.

A standard fiber has a circular symmetry and does not exhibit any specific birefringence. The small birefringence of a segment is coming from defects inside the fiber itself or from externally applied stresses such as temperature change, mechanical constraint, bending, twist. So every segment has its own main axes, the parameter q is varying a lot and the mode coupling is important. The spatial evolution dq/dz is generally supposed to follow a normal distribution $N(0, \sigma)$ centered in 0 and having a variance σ depending on the characteristics of the fiber. The parameter δ is following a Rayleigh distibution. So in such a fiber the mode coupling is randomly distributed along the fiber and the light at the output of the fiber is depolarized. To characterize the decoupling along the fiber we can define the coupling length L_C, formally defined by equation 2.7, which is the length after which the polarization has changed in a significative way. For standard telecommunication fibers this length varies between 5 m and 500 m [47].

$$\frac{1}{L}\int_0^L \vec{\boldsymbol{\beta}}(z)\vec{\boldsymbol{\beta}}(z+\nu)dz =< \delta(z)^2 > e^{-2\frac{|\nu|}{L_C}} \tag{2.7}$$

Where $\vec{\boldsymbol{\beta}}(z)$ is the birefringent vector that describes the birefringent properties of a medium at a distance z. It points towards the fastest mode of the birefringent element on the Poincare sphere and its size corresponds to the phase delay per length unit between the two eigen modes.

$$\vec{\boldsymbol{\beta}}(z) = \delta(z)\vec{\boldsymbol{u}} = \begin{bmatrix}\beta_1\\ \beta_2\\ \beta_3\end{bmatrix} \tag{2.8}$$

In polarization maintaining fibers manufacturers introduce an artificial high uniform birefringence much larger than the residual birefringence of usual fibers. So δ_i is a constant and the variance σ of the spatial distribution of dq/dz is null. The main axes are constant and linear along the fiber and there is no mode coupling while propagating. So when a linear polarized light is launched into the fiber, aligned on one of the main axis it will remain polarized on the same main axis at the output. A small amount of depolarized light can still arise from the birefringence induced by defects. But this birefringence is negligible in regards to the one artificially added by manufacturers and PMF generally exhibit a PER at

the output of the order of 20 dB.

The higher the birefringence, the less sensitive to external defects is the fiber. A common way to give the information about the birefringence of a fiber is to give its beating length L_B, defined in equation 2.9. It is the length over which the electric fields on both axis are experiencing a phase delay of 2π, which lead to the initial state of polarization.

$$L_B = \frac{2\pi}{\beta_{yx}} \tag{2.9}$$

In table 2.2 is presented a comparison of the different characteristic values that we introduced between standard fibers and PM fibers.

	Standard fiber	Polarization Maintaining Fiber
L_B	5-50 m	few millimeters
σ	4-15 °/m	0
L_C	5-500 m	∞

Table 2.2: Birefringence properties of PMF and standart fibers

There are different ways to introduce this birefringence in the core of the fiber (see figure 2.9). First works started in the late 1970s, with fibers whose core was dumbbell-shape [48], or with elliptical cores. Nowadays the usual way to do it, is to introduce a stress on one of the axis of the fiber. It is done by modifying the cladding on both part of the core, there are three main designs that are shown on figure 2.9: either with an elliptical cladding, with partly circular stress elements (bow-tie design) or with stress rods (PANDA) into the cladding. These elements have a different thermal expansion coefficient and while manufacturing the fiber it induces a mechanical stress on the core which, by photo-elastic effect, modifies the refractive index on its axis and give the needed birefringence to the core of the fiber.

In order to work properly it has to be noticed that linear polarized light has to be launched precisely on one of the main axis of the fiber. If it is not the case, the polarization is split on both the fast and the slow axis and the polarization state on both axis is kept but there will be a phase delay between the two components at the output of the fiber that will depend on its optical length. Thus the fiber behaves like a waveplate whose birefringence will depend on all the external perturbations.

Polarizing fibers, also called single-polarization fibers, are fibers that allow only one linear polarization to propagate. They are based on the same principle than PMF, the core exhibit a high birefringence that avoids any mode coupling, but they also have the particularity of not guiding the polarization on the other main axis. This ability of guiding on one axis but

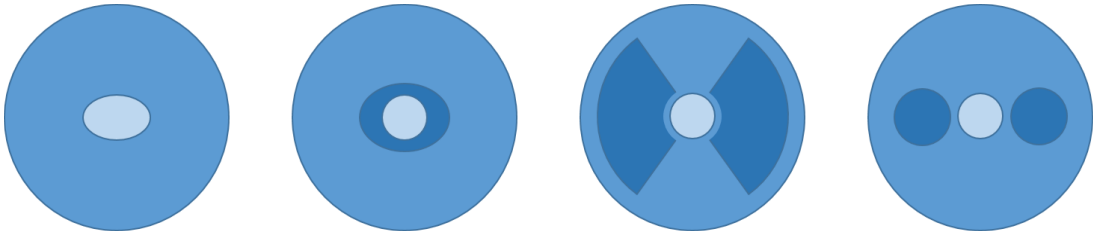

Figure 2.9: Different designs used to induce a birefringence into the core of optical fibers to make them polarization maintening. From left to right: elliptical-core, elliptical cladding, bow-tie fibers, PANDA fibers. The darker part are representing the stress elements that are added in the cladding.

not the other one can be obtained with special cladding designs as we will explain in the next section.

2.2.3.3 Photonic Crystal Fiber

A photonic crystal is a periodic structure of dieletric materials that modifies the behavior of the electro-magnectic waves. In the early 1990s Russel [49] had the idea to use this property in the cladding of optical fibers to confine the light into the core instead of using the usual refractive index difference of step-index fiber. The idea of Photonic Crystal Fiber (PCF) is indeed to create an array of micrometric air holes in the cross section of the fiber that guide the light into the core of the fiber. In 1996, Knight and al report the first fabrication of this type of fiber [50]. That was the beginning of a new area in optical fiber research that rapidly led to new commercial technologies. Indeed, by the various different possible designs, as you can see on the examples shown in figure 2.10, this technology is offering much more possibilities than usual fibers.

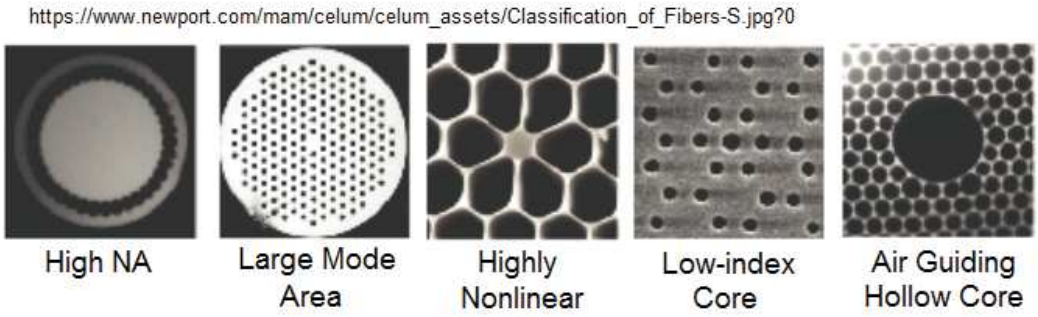

Figure 2.10: Cross sections of index guiding fiber and a PBG fibers

There are two main types of PCF. On one hand there are the ones having a core with a higher refractive index than the cladding, and thus have a behavior similar to the usual step-index fibers, they are called Index-Guiding, High-Index Core, Holey or Hole-assisted

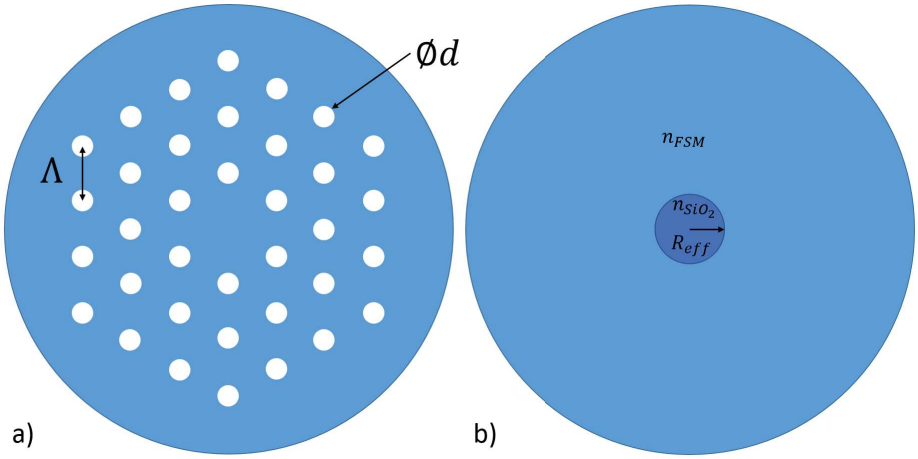

Figure 2.11: Cross section of a simple design of PCF and its equivalent design described by Koshiba model [52]

fibers. On the other hand there are the ones called Photonic Bandgap fibers (PBG fibers) or Bandgap Guiding fibers, using the properties of the microstructured cladding to create a photonic bandgap that can confine the light into a core of lower refractive index.

Index-Guiding fibers

We will here describe the working principle of an index guiding fiber with a simple design (figure 2.11) following the development that Hansen had in his thesis [51]. Such a fiber works thanks to the Total Internal Reflection, like it has been shown in section 2.2.3.1 for step index fiber. This can be demonstrated thanks to a finite element method analysis but Koshiba and Saitoh showed in [52] that it can also be well approximated by a step-index fiber model with the following characteristics:

- An effective core radius $R_{eff} = \Lambda/\sqrt{3}$ where Λ is the pitch of the fiber, ie the distance between the centers of two adjacent holes of the structure.
- An effective refractive index of the core n_{SiO_2} equal to the refractive index of the glass of the fiber.
- An effective refractive index of the cladding n_{FSM}. Where FSM (Fundamental Space-filling Mode) is the fundamental mode that propagates into the microstructure of the cladding. Thus the effective refractive index depends on Λ, d the diameter of the holes and the wavelength λ of the fundamental mode.

As we did before for the step-index fibers it is possible to define the V parameter that gives the information about the single mode behavior of the fiber. If $V_{PCF} < 2.405$, only one mode is propagating into the fiber.

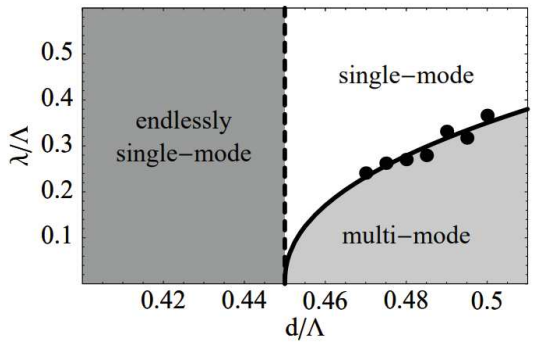

Figure 2.12: Single mode operation of PCF fibers depending on the ratios $d/\Lambda$and λ/Λ from [53]

$$V_{PCF} = \frac{2\pi\Lambda}{\sqrt{3}\lambda}\sqrt{n_{SiO_2}^2 - n_{FSM}^2} \tag{2.10}$$

But the difference with the step-index fibers is coming from the fact that the effective refractive index of the cladding n_{FSM} has a strong dependence on λ. For long wavelengths, when $\lambda/\Lambda \gg 1$ the FSM has a uniform field distribution and thus n_{FSM} tends to an average between the refractive indices of the air holes and the silica. The effective refractive index of the cladding is then lower than the refractive index of the core and the TIR can occur. For short wavelengths, when $\lambda/\Lambda \ll 1$ the FSM is confined in the silica part of the cladding, avoiding the air holes. By using this fundamental cladding mode as a solution for the scalar wave equation it can be shown [51] that $n_{SiO_2}^2 - n_{FSM}^2 \propto \lambda^2$ and so that V_{PCF} is a constant. It has been then shown [53] that this constant depends also on d and especially that the single mode condition is verified when $d/\Lambda \lesssim 0.45$ independently of the wavelength. This value can even be higher under certain conditions on the ratio λ/Λ as illustrated on figure 2.12. This particularity of PCF fibers explains the two main characteristics that make them interesting: firstly the endlessly single-mode guidance, fibers are single mode at all wavelengths, and secondly the possibility to increase the pitch, and thus the core of the fiber, while keeping a single mode behavior. This is how are designed the Large Mode Area (LMA) fibers that are interesting in our application. However in practice one can not infinitely increase the pitch and the mode field diameter of a fiber. Quite rapidely the fibers become much more sensitive to any kind of disturbances such as bending [54].

Photonic Band Gap fibers

Already in 1978, Yeh et al [55] realized a fiber whose cladding was a succession of concentric rings of different refractive indices that allowed the light to propagate only in the core of lower refractive index, that was the first Bragg Fiber. The first development of a PGB fiber using photonic crystals took place later, in 1995, when Birks et al reported a fiber with an air-silica structure in the cladding that creates the needed Photonic Bandgap to guide the

light into a core of lower refractive index [56].

Unlike the index guided fibers and step index fibers, light in PGB fibers is not guided by TIR. Indeed the structure of the photonic crystal of their cladding forms a kind of 2D Bragg mirror (figure 2.10) in the transverse direction which avoids some wavelengths to propagate. For these specific wavelengths, light can only propagate into the core of the fiber, whatever its refractive index. Thus manufacturers can design a fiber whose core have a lower refractive index than the cladding. It can even be an air-hole, we are then speaking about hollowcore fiber, the first one has been developped in 1999 [57]. Hollow core fibers have several advantages compare to usual guidance in silica. First there is almost no interaction with the matter which reduce the non-linear effects that we will detail in section 2.4. On the contrary the core can be filled with highly non linear gas to realize Raman laser [58] or high harmonic generation [59]. They can also be used to guide wavelength that are usually absorbed by silica. However they have quite high propagation losses and they are very few designs that maintain the polarization.

2.3 High Power fiber injection

In this section we are explaining how to pass from a free space propagation of a beam to a propagation in an optical fiber, we will especially take a look at the issues linked to the use of high power. In most cases fibers and so the system used to inject into them are designed for low power.

2.3.1 Gaussian beam propagation

Due to its particular properties, the fundamental mode TEM_{00} is also called a Gaussian beam. The propagation of a Gaussian beam is the propagation of a wave in both time and space. Those physical problems that involves partial differential equations in both time and space are analytically described by the Helmholtz propagation equation :

$$\nabla^2 E + k^2 E = 0 \tag{2.11}$$

Where ∇^2 is the Laplacian, E is the amplitude of the propagating electric field and k is the wave number. The propagation of a Gaussian beam is a particular solution of this equation in the frame of the paraxial approximation. Such an assumption is equivalent to consider that the angle θ between the optical axis and the wave vector $\boldsymbol{k}$ is small: $\theta \ll 1$. It allows to write the amplitude on the following form : $E(x, y, z) = u(x, y, z)e^{-ikz}$, where u a complex scalar function that gives the information on the variation around the plane wave. By reinjecting this prior expression in the general Helmholtz equation, using the approximation that we did

and solving it, we can get the expression of the electric field of a Gaussian beam propagation:

$$\vec{\boldsymbol{E}}(r,z) = \frac{w_0}{w(z)} \exp\left(\frac{-r^2}{w(z)^2}\right) \exp\left(-i(kz + k\frac{r^2}{2R(z)} - \phi(z))\right) E_0\vec{\boldsymbol{x}} \tag{2.12}$$

Where

- $E_0 = E(0,0)$
- $\vec{\boldsymbol{x}}$ is a vector of the plane orthogonal to the propagation direction
- w_0 is the waist radius, arbitrarily placed at $z = 0$
- z is the axial distance from the position of w_0
- r is the radial distance from the beam axis
- $w(z)$ is the width of the intensity profile at the distance z measured at $1/e^2$ of its axial value
- k is the wave number, $k = \dfrac{2\pi}{\lambda}$
- $R(z)$ is the radius of curvature of the beam's wavefront at the distance z
- $\phi(z) = \tan^{-1}(z\lambda/\pi\omega_0^2)$, is the Gouy phase which is the phase difference between the actual beam and a plane wave of same frequency.

This is the fundamental mode, the so-called TEM_{00} (see figure 2.4) that we mentioned in section 2.1.1. It is the most common mode that can be found at the output of lasers due to the fact that it allows the most concentrated spot. It is called Gaussian beam because its transverse electric field is described by a Gaussian function. Giving the properties of Gaussian function, the intensity which is the value of interest in experiments since it can be easily measured with a photometer is also following a Gaussian distribution:

$$I(r,z) = \vec{\boldsymbol{E}}(r,z)\vec{\boldsymbol{E}}^*(r,z) = \frac{2E_0^2}{\pi w(z)^2} \exp\left(-2\frac{r^2}{w(z)^2}\right) \tag{2.13}$$

Its other particularity is that while propagating a Gaussian beam remains Gaussian, its width w(z) and radius of curvature R(z) are following the propagation equations 2.14 and 2.15, where z is the distance from the location of the waist w_0. The value $z_R = \pi w_0^2/\lambda$ is called the Rayleigh range (figure 2.12). This is the range over which the width of the beam increases of a factor $\sqrt{2}$, and thus the peak of intensity is divided by a factor 2. It is generally admitted that a beam is considered collimated (i.e. its width does not vary too much) within a range small in regards to its Rayleigh range. A typical Gaussian propagation as well as all the parameters that we mentioned previously can be seen in figure 2.14.

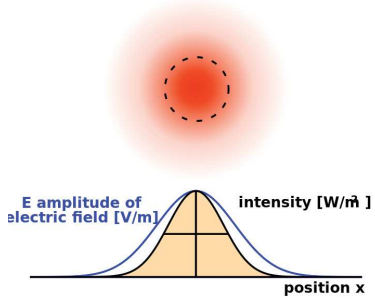

Figure 2.13: Spatial representation of a Gaussian beam (top) and its related transverse Gaussian electric field and intensity. (Via Wikimedia Commons)

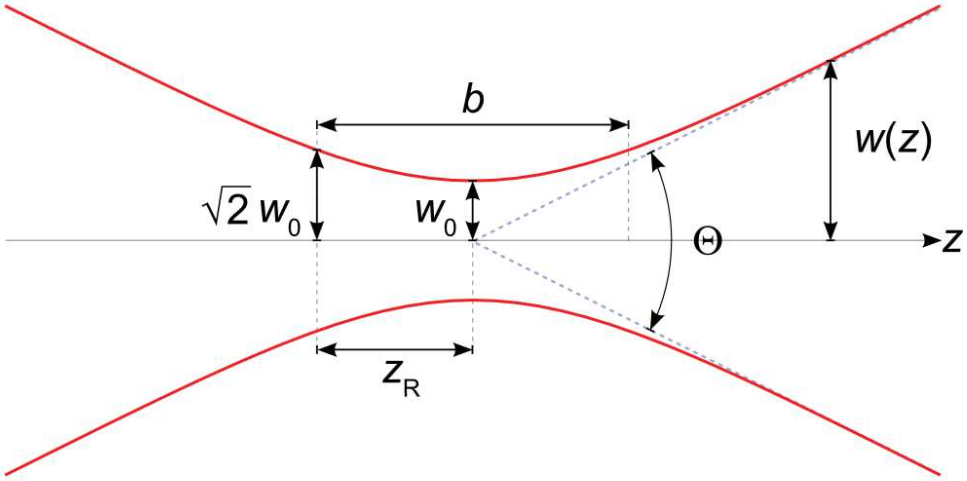

Figure 2.14: Width of a Gaussian beam (red) along the z-axis. w_0: beam waist, $\Theta = 2\theta$ divergence, Z_R Rayleigh range, b depth of focus. Via Wikimedia Commons

$$w(z) = w_0\sqrt{1 + \left(\frac{z}{z_R}\right)^2} \tag{2.14}$$

$$R(z) = z\left(1 + \left(\frac{z_R}{z}\right)^2\right) \tag{2.15}$$

Another value of interest about a Gaussian beam propagation is its divergence θ defined in equation 2.16. Out of the Rayleigh range the increase of the beam width tends to be linear, the divergence give us the angle between that line and the propagation axis. The important

point to be noticed is that, the smaller the waist the greater the divergence, this is of particular importance while injecting light into an optical fiber as we will see in the next sections.

$$\theta \approx \arctan\left(\frac{\lambda}{\pi w_0}\right) \tag{2.16}$$

So the propagation of a perfect Gaussian beam can be defined knowing only the size and the location of its waist w_0 and be computed using the formulas above. At each point z, the width $w(z)$ can be computed and corresponds to the width of the intensity profile when its value went down to $1/e^2 \approx 13.5\%$ of its peak value as you can see in figure 2.13. This value is often the one given to describe the beam, however when designing an optical set-up, considering a Gaussian beam propagation, one has to be careful at the clear aperture of the optical components that are used. It is considered that to avoid any losses, the clear aperture has to be five times larger than the width of the beam at that point. Indeed the power losses are then lower than 50 ppm. Beyond the losses the problem of having a clear aperture which is too small regarding the beam width is that the light is then diffracted and participates to the diffused light of the setup. For most of the applications this is not important, but for an interferometer as sensitive as Virgo, this light can perturb its behavior (section 1.3.5).

We saw that a Gaussian beam remains Gaussian while propagating, this is also the case when passing through a perfect lens. Its new waist size and position can be computed using the equations 2.17 and 2.18:

$$z_0{}' = f\frac{z_0(f+z_0)+z_R^2}{(f+z_0)^2+z_R^2} \tag{2.17}$$

$$\frac{w_0}{w_0'} = \frac{f}{\sqrt{(f+z_0)^2+z_R^2}} \tag{2.18}$$

When designing an optical set-up, the aim is to bring the Gaussian beam to the desired position and size taking care of the clear aperture of the components. This can be done using softwares based on the formulas that we detailed previously. Another practical way to follow the propagation of a beam in the paraxial approximation is to use the ray transfer matrix analysis, also called the ABCD matrix formalism. Every single optical component is described by a matrix $\begin{bmatrix} AB \\ CD \end{bmatrix}$ whose coefficients depend on its characteristics. In this formalism a Gaussian beam is described by $\begin{bmatrix} q_{in} \\ 1 \end{bmatrix}$ with $\frac{1}{q_{in}} = \frac{1}{R} - \frac{i\lambda_0}{\pi n w^2}$. One can then simply multiplying the input matrix of the Gaussian beam by the matrices of the different free space propagations and optical elements of the set-up to get the matrix of the output beam. However the usual and more practical way is too use softwares or Matlab codes that are mainly based on this formalism.

2.3.2 Mode matching

One of the critical part while working with optical fibers is the passage from a free space propagation to the propagation into the fiber. In the further development of this section we are considering the case of the injection of a Gaussian beam into a single mode fiber. In order to do this injection, one has to design an optical set-up that will transfer the power of the input free space modes into the modes that propagate into the fiber. The trivial idea is to design a telescope made of two (or more) lenses that has the magnification needed to bring the input beam into a beam whose waist size is located on the end facet of the fiber and whose waist is equal to the size of the core of the fiber.

The coupling between the input beam and the actual modes of the fibers is given by the overlapping integral 2.19 :

$$\eta = \frac{|\int E_1^* E_2 dA|^2}{\int |E_1|^2 dA \int |E_2|^2 dA} \tag{2.19}$$

where E1 is the electric field of the input beam and E2 is the one that propagates into the fiber. They can be decomposed on the higher order modes bases such as the ones that we presented in section 2.1.5.1. In our case, both electric fields have few higher order modes and most of the power is included in the TEM_{00} mode. The actual mode content of the fibers that we used for our works will be presented in 3.2.2 and 3.3.2.

To have an idea of the importance of the mismatching, in the development below we present a simple approach considering that the fiber's fundamental mode as well as the input beam are the fundamental Gaussian mode TEM_{00}. The coupling into the fiber directly depends on the mismatching between these two beams as it is highlighted in figure 2.15 where we computed the mode matching between two Gaussian beams using the overlapping integral given in equation 2.19. We were making varying both the position and the size of the waist of the input beam (E_1) in regards to the one of the fiber (E_2). In the case of a Gaussian mode with a well located waist and only looking at the dependence of the size of the waist, the equation 2.19 can be simplify as follow:

$$\eta = \left(\frac{2}{\frac{w_1}{w_2} + \frac{w_2}{w_1}} \right)^2 \tag{2.20}$$

If the input waist is too large compare to the required one, light will propagate into the cladding of the fiber. If the waist is smaller than the required one and/or the waist is not well located, the divergence of the beam (eq 2.16) will vary and will not match the NA of the fiber (eq 2.5) anymore. This will lead again to mismatched light that will propagate into the cladding.

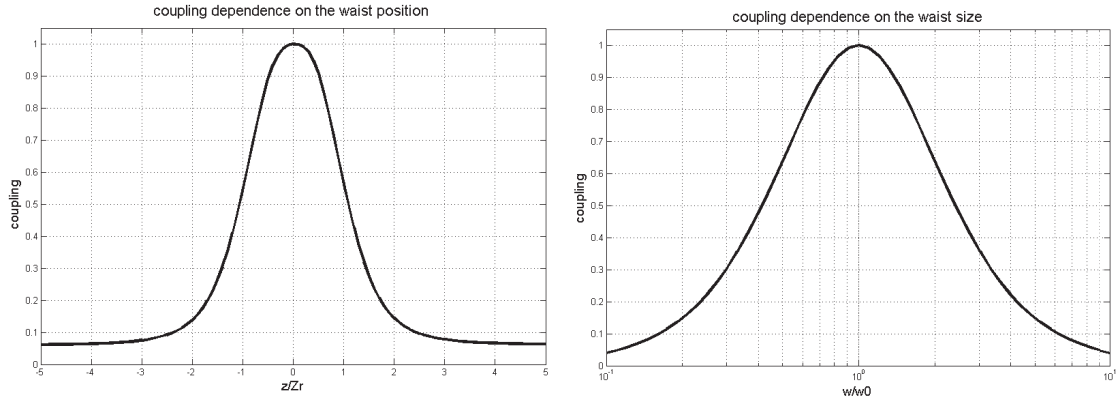

Figure 2.15: Mode matching dependence on the position (left) and size (right) of the waist. They have been computed by looking at the overlapping between a fixed Gaussian beam and another one whose position (left) and size (right) were varying.

What comes out of this two simple graphics is that, as much as possible, it is better to work with bigger waists. Having a bigger waist will increase the Rayleigh range Z_R and reduce the dependence on the position and will also reduce the relative dependence on the waist size. That is why in practice it is convenient to use a collimator attached to the fiber and adapt the beam to the characteristics of the fiber with its collimator. In practice it is difficult to know these characteristics with precision from the datasheets of the components. They can vary because of imperfections of the fiber or because of the actual distance between the lens and the fiber end. A better way to know the needed characteristics of the beam to inject into the fiber is to proceed to a reverse mode matching, coming from the Helmholtz reciprocity principle that states that properties of the beam in the forward and backward direction of propagation are the same (except in the case of moving, non linear or magnetic media). So the idea is actually to inject the beam by the other end of the fiber, even with a non-optimized coupling, and analyzing the output mode on the side we are interested in. Once the output characteristics (size and position of w_0) are perfectly known, one can design an optical setup that would best match the input Gaussian beam to this one.

2.3.3 Mode stripping

Light can be mismatched at the input of the fiber either because it contains HOM that are not guided in the core or because of a difference between the actual and the ideal waist position and size. This mismatched light is injected into the cladding of the fiber. In the best case it results in other modes guided into it and this deteriorates the output beam quality. But in a worst case, it could also go into the protective coating of the fiber which is more generally made of plastic (figure 2.5), locally increase its temperature and damage it. This could lead to the rupture of the fiber or to an effect called fuse effect ignition as André et al detail in [60]. Starting from a local heating point, a defect is created which lead to an increase of the optical absorption which will in turn dramatically increase the temperature.

Thus, once an initial threshold is triggered this phenomena stimulates itself till reaching a temperature high enough to burn and vaporize the core of the optical fiber. Step by step it can propagate through the fiber till its end. So while dealing with high power densities the idea is to strip out this remaining power out of the cladding before it could damage the fiber. To do so, on the first centimeters of the fiber, the manufacturer either remove the coating or chose it so that the light scattered from the cladding can easily be refracted out and then be dumped and absorbed. In order to improve the process, they also create some anomalies, such as an engraved grating that increase the scattering occurring in the cladding.

2.3.4 Critical point of the air/silica interface

2.3.4.1 Laser Induced Damage Threshold

While working with high power beams focused on a spot of some micrometers, we are dealing with very high power densities and one of the problem that has to be faced is about the damage of the fused silica itself. Overheating of the medium is due to its absorption and especially to all its microscopic defects that have a greater absorption. These micro defects are more present on the interfaces than in the bulk medium, this makes the end facets of fibers a critical point while doing the injection. To compute the maximum density of power that is hitting the fiber end facet, we have to evaluate the intensity of the Gaussian beam (equation 2.13) in $r = 0$. It gives us the equation 2.21 which corresponds to twice the average power density of the beam. On figure 2.16 we plotted the peak intensity power received by the fiber end facet versus the size of the mode, which is approximately equal to the size of the core of the fiber. We have to deal with peak power densities of the order of $10^7 - 10^9 W/cm^2$.

$$I(0, z) = \frac{2P_0}{\pi w^2(z)} \tag{2.21}$$

In the litterature, we can find values for Laser Induced Damage Threshold (LIDT) of fused silica that vary a lot. It is indeed difficult to give a precise value since any sample may be different at a microscopic scale and small defects can completely change the value of the LIDT. For instance fiberguide industries, which is company specialized in high power fibers, estimate the LIDT at the interface between air and fused silica to be about 15 MW/cm^2 [61], whereas in an application note from 2014 [62], holo/or, an optical elements manufacturer, is giving a value of about 1200 GW/cm^2. As we pointed out before these values depend a lot on the surface quality they were using while doing the tests. Alley et al investigate this in a paper [63] in which they describe different techniques for finely polishing the fused silica in order to get the best surface quality that would give the greater LIDT. As a result they give values that goes from 50 GW/cm^2 to 500 GW/cm^2.

The important point stressed by these studies is that the densities of power in our application are very close to the LIDT of a clean interface between air and fused silica. The power density of a beam of 200 W over a surface having a radius of 7 µm is indeed of 260

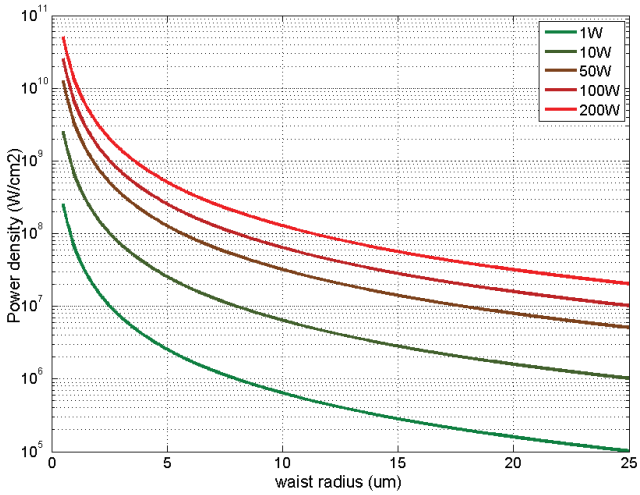

Figure 2.16: Peak power densities on the fiber end facets for different input power plotted versus the size of the beam waist at the interface. The usual single mode fiber have a core radius of about 3 µm while the one that we worked with had a core radius of 6 µm and 15 µm.

MW/cm^2. So special care is required while handling the fiber in order to avoid any dust, any scratch that could significantly lower the LIDT and could damage the fiber while increasing the power.

2.3.4.2 Fibers end caps

One of the problem with microstructured fiber is that its complicated cross section makes it difficult to work on the interface and thus to get a good quality surface. To avoid this problem, the technique used by the companies that connectorize fibers is to add an end cap at the end of the fiber. It consists in splicing a piece of pure fused silica fiber which is then cleaved at the desired length with the desired angle (figure 2.17).

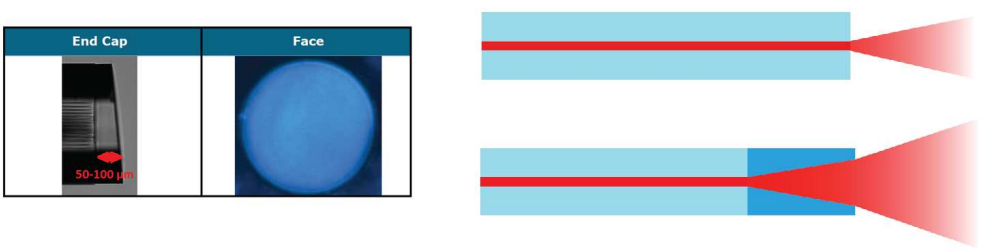

Figure 2.17: Report from Alphanov on an end cap put on a LMA-PM-40-FUD fiber (left), divergence at the output of the fiber with and without end cap (right).

It has also the advantage of avoiding fluids to get into the holes of the structure. If this had to happen it would be hard to remove because of the strong capillary forces into the air holes.

In the end cap the light is not confined into the core anymore. So the beam starts to diverge and has a bigger size when hitting the air/silica interface, and thus a lower intensity peak. This also gives a conditions on the length and the width of the end cap, it has to be short or large enough to avoid light to diverge out of it. This divergence combined with the angle of the end cap avoid the back reflected light on the interface to be recoupled into the fiber.

2.3.4.3 Anti-Reflective coating

In order to avoid these back reflections, one also has to make these end caps coated with an Anti-Reflective coating (AR coating). Indeed, whenever a beam is passing from a medium of refractive index n_1 to a medium of refractive index n_2, it experiences a refraction and a reflection depending on the refractive indices of the media and the angle of the incident beam. The equations describing this phenomena are known as the Fresnel equations (eq 2.22 and eq 2.23). They depend on the polarization state of the incident light, either it is in the plane of incidence (P) or perpendicular to this plan (S) as we detailed in section 2.1.4.

$$R_S = \left[\frac{n_1 \cos\theta_i - n_2 \sqrt{1 - \left(\frac{n_1}{n_2} \sin\theta_i\right)^2}}{n_1 \cos\theta_i + n_2 \sqrt{1 - \left(\frac{n_1}{n_2} \sin\theta_i\right)^2}} \right]^2 \tag{2.22}$$

$$R_P = \left[\frac{n_1 \sqrt{1 - \left(\frac{n_1}{n_2} \sin\theta_i\right)^2} - n_2 \cos\theta_i}{n_1 \sqrt{1 - \left(\frac{n_1}{n_2} \sin\theta_i\right)^2} + n_2 \cos\theta_i} \right]^2 \tag{2.23}$$

If we consider that they are no losses, the transmission can simply be found by using the conservation of the energy : $T_S + R_S = 1$ and $T_P + R_P = 1$

In our case we are working almost at normal incidence, there is a small angle due to the angle of the end facet of the fiber, but we can approximate the Fresnel equations 2.22 and 2.23 by evaluating them for $\theta_i = 0°$. The reflectance is then simply given for both polarizations by equation 2.24.

$$R_S = R_P = \left[\frac{n_1 - n_2}{n_1 + n_2} \right]^2 \tag{2.24}$$

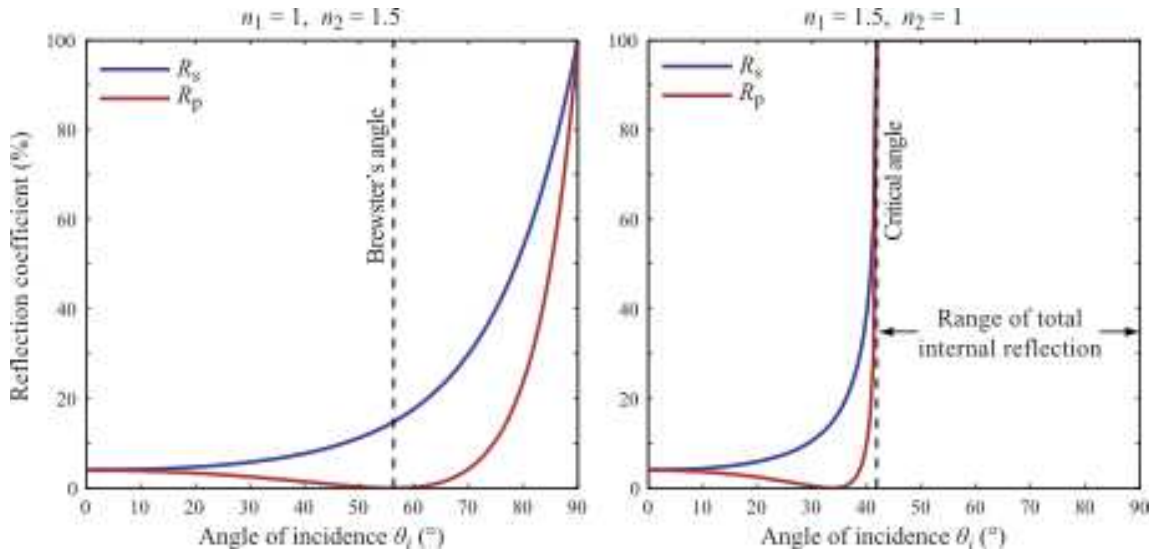

Figure 2.18: Fresnel reflection for both polarizations plotted against the angle of incidence. From air to glass (left) and from glass to air (right). Via Wikimedia Commons

For an interface air-fused silica ($n_1 = 1$ and $n_2 = 1.4496$ at 1064 nm [64]), this leads to approximately 3.4 % of the total power that are reflected. When the end cap has an angle, the reflected light is tilted respecting to the input one and it can be separated and dumped. At the output, the beam is backreflected into the fiber but as we saw in section 2.3.4.2, the backreflected light is not reinjected into the core because of both the divergence into the end cap and the tilt angle of this end facet. Instead, it goes in the cladding and heat up the connector (see section 2.3.3). In total it is about 7% of the input power that would be lost because of these reflections. To avoid these losses an AR coating on the end facets of the fibers is needed.

An AR coating is a succession of dielectric layers applied on the surface that has to be coated. The refractive indices and thickness of these layers are chosen so that the waves back reflected on every surface are destructively interfering. At the same time, the forward reflected light is experiencing constructive interferences. As shown in figure 2.19, the thickness of the layers to create these interferences is chosen to be $\lambda/4$ at the desired incidence. Such a coating will have good performances for a specific wavelength but will be less efficient for the others. In practice in order to have broadband coating or to reach a reflectivity as low as possible for a chosen wavelength, the layout of the coating designed by the manufacturers is much more complex and require numerical simulations. As a result, they can decrease the backreflected light down to tens or hundreds of ppm.

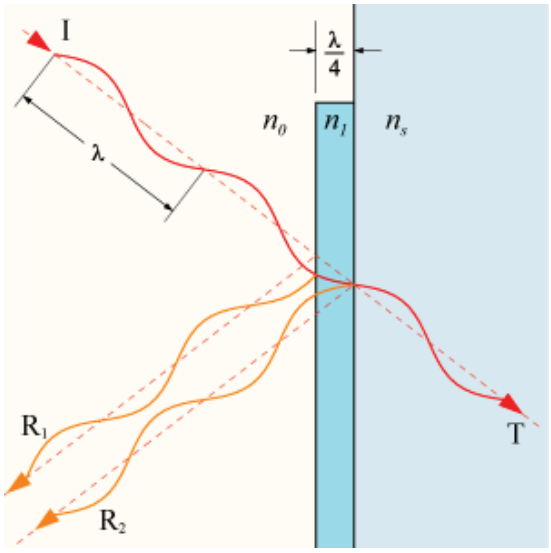

Figure 2.19: Destructive interferences of the AR coating. (Via Wikimedia)

2.4 Non linear effects into optical fibers

While scaling up the power into a medium, non linear effects can occur and optical fibers are particularly subject to these effects. Indeed, the smallness of their core rapidly leads to high density of power and in general they also have very long interaction lengths. There are two main causes for non linear effects. The first one is the intensity dependence of the refractive index of the medium, known as the Kerr effect, and the second one is the inelastic scattering that occurs between the molecules of the medium and the propagating light. In this section, we will briefly detail the processes of the different non linear effects and give some order of magnitude of the power at which they appear in an optical fiber made of fused silica. We will see that the main limiting one in our application is the Stimulated Brillouin Scattering. So in a second step, we will describe this one more in detail.

2.4.1 Kerr effect: non-linear refractive index

The polarization density of a medium is a vector that represents its density of permanent electric dipole moments as well as the moments induced by an external electric field. It is defined by the following equation $P = \epsilon_0 \chi^{(e)} E$, where ϵ_0 is the electric permittivity of vacuum, $\chi^{(e)}$ is the electric susceptibility, and E is the electric field. When the electric field reaches values that are high enough the polarization density starts to saturate and does not follow the equation above, it can then rather be modelled by the equation 2.25. In this equation the $\chi^{(k)}$ are called the k^{th} nonlinear susceptibilities and they are the reasons of the non linear behavior of the medium.

$$P = P_0 + \epsilon_0 \chi^{(1)} E + \epsilon_0 \chi^{(2)} E^2 + \epsilon_0 \chi^{(3)} E^3 + \dots \tag{2.25}$$

Fused silica is not a ferroelectric material, so its initial polarization P_0 is null, $\chi^{(1)}$ corresponds to the linear susceptibility that we described below. Moreover, because of the symmetries of the molecule of silica, the second order susceptibility $\chi^{(2)}$ is also null in optical fibers. The second order non linear effects that could be observed in them are due to defect inside the fiber. The susceptibilities having an order greater than 3 can be neglected compared to the non linearities due to the $\chi^{(3)}$. The third order non linear effect is known as the Kerr effect, it modifies the refractive index of the medium and can lead to the following non linear effect :

- Four Wave Mixing (FWM), is a non linear effect that occurs when two beams of different frequencies (ν_1 and ν_2, considering $\nu_1 < \nu_2$) are launched together in the same optical fiber. The interferences between the two beam modulate the refractive index at a frequency $\Delta\nu = \nu_2 - \nu_1$ and leads to the creation of two additional frequencies $\nu_3 = 2\nu_1 - \nu_2$ and $\nu_4 = \nu_2 - \nu_1$. Since in our application we are working with a single wavelength, this effect is not of our concern.

- Cross Phase Modulation (CPM) appears also when two beams of different wavelength are launched into a fiber. The refractive index varies under the influence of the optical power of one wavelength through the Kerr effect and thus impacts on the phase of the other wavelength. As with FWM, this is not a problem in our application.

- Self Phase Modulation (SPM), is a non linear effect which is particularly relevant for short pulse of light. Indeed in pulses the intensity of the light varies in time, and so is the refractive index. This end up with a negative frequency shift at the front of the pulse and a positive one after the peak on intensity. In our application we use Continuous Wave (CW) whose intensity does not vary consequently in short periods of time, so the effects of SPM are not critical. However it has been shown in [65] that while amplifying an NPRO laser through a double-clad Yb-doped fiber, the intensity noise was broadening the linewidth of the laser. This is something that have to be considered. In order to keep narrow linewidth operation at the output of the fiber, intensity fluctuations at the input have to be as low as possible.

- Self focusing, is the only consequence of Kerr effect that could be an issue. It is due to the intensity profile of the beam, the modified refractive index exhibits a spatial variation, which makes the medium acting like a focusing lens. It can be a stimulated process since the peak intensity in the self focused area will keep increasing, which lead to an even higher intensity peak. If in a way or another the beam is not defocused, this can lead to the destruction of the medium.

However we will see through the development below that the value of this change in the refractive index is not sufficient for the lengths of fiber that we have. To do so we can introduce the electric field $E = E_0 \cos(\omega t - kz)$ in the equation 2.25, the detailed calculation

has been done in [66], by using trigonometric properties and eliminating the higher order mode that are neglected, we can easily obtain the following equation:

$$P = \left(\epsilon_0 \chi^{(1)} + \frac{3}{2}\frac{\chi^{(3)}}{c n_l} I\right) E_0 \cos(\omega t - kz) \tag{2.26}$$

where c is the speed of light, n_l the linear refractive index and I the intensity of the electric field defined as follow: $I = 0.5\ c\epsilon_0 n_l E_0^2$.

To get the effective refractive index with its linear part n_l and nonlinear part n_{nl}, so it can be written as $n_{eff} = n_l + n_{nl} I$. To do that, we can derive the effective susceptibility from equation 2.26, as well as the effective refractive index :

$$\chi_{eff} = \frac{P}{\epsilon_0 E} = \chi^{(1)} + \frac{3}{2}\frac{\chi^{(3)}}{c\epsilon_0 n_l} I \tag{2.27}$$

$$n_{eff} = \sqrt{1 + \chi_{eff}} \tag{2.28}$$

The idea of the development below is to separate the effective refractive index in a non-linear part n_{nl} depending on the intensity and a linear part n_l which by definition is $n_l = \sqrt{1 + \chi^{(1)}}$.

$$\begin{aligned} n_{eff} &= \sqrt{1 + \chi_{eff}} \\ &= \sqrt{1 + \chi^{(1)} + \frac{3}{2}\frac{\chi^{(3)}}{c\epsilon_0 n_l} I} \\ &= \sqrt{1 + \chi^{(1)}}\ \sqrt{1 + \frac{3}{2}\frac{\chi^{(3)}}{c\epsilon_0 n_l (1 + \chi^{(1)})} I} \\ &= n_l \sqrt{1 + \frac{3}{2}\frac{\chi^{(3)}}{c\epsilon_0 n_l^3} I} \end{aligned} \tag{2.29}$$

By doing a Taylor development of the square root, n_{eff} can be approximated under the desired form:

$$n_{eff} = n_l + n_{nl} I \quad \text{with} \quad n_{nl} = \frac{3}{4}\frac{\chi^{(3)}}{c\epsilon_0 n_l^2} \tag{2.30}$$

A review of the measured values of this nonlinear refractive index has been made in [67]. For a wavelength of 1064 nm the value is comprised between 1.92×10^{-16} and 3.3×10^{-16} cm^2/W . If we do a numerical evaluation of the change in the refractive index of the core of a fiber, considering an uniform distribution of the power, taking a average value of 2.5×10^{-16} cm^2/W for n_{nl}, an optical power of 200 W and 15 µm for the diameter of the core of the fiber we get $\Delta n = 2.83 \times 10^{-8}$ which is neglected for the few meters of fibers that we need in our application.

An other approach is to consider the critical power above which self-focusing effect occur, it is defined as follow [68]:

$$P_{cr} = \alpha \frac{\lambda^2}{4\pi n_l n_{nl}} \tag{2.31}$$

Where α is a numerical factor that does not have any analytical expression. For a Gaussian beam it has been evaluated at 1.8962 [69]. The numerical evaluation for fused silica gives: $P_{cr} \sim 5$ MW which is way greater than the power that we are using. This effect is actually particularly relevant for very high power pulses laser.

2.4.2 Stimulated Raman Scattering

The Raman scattering is a non linear effect theoretically predicted by Smekal in 1923 [70] and independently evidenced in 1928 by Raman and Krishnan in liquids [71] and Landsberg and Mandelstam in crystals [72]. It comes from the inelastic interaction of a photon and a molecule of the medium. Usually while propagating into a medium photons are subject to an elastic scattering (Rayleigh scattering), but a tiny amount of them are inelastically scattered on vibrating molecules. There is an energy exchange: either molecules are excited to a higher vibrational level whereas the frequency of the photons is down shifted (Stokes wave) or the molecules lose some energy and a photon of higher energy is emitted (anti-Stokes wave). The typical Raman shift gain depends on the nature of the molecule itself. The one of silica is presented in figure 2.20, it has a maximum around 13 THz and a bandwidth of about 40 THz.

The phenomenon described here above is a spontaneous one, but the probability of having Raman scattering at a given frequency is increased by the presence in the medium of photons already having this frequency. So the more power in the Stoke wave, the higher the probability of having photons scattered at the Stoke frequency, this leads to a point where the system becomes stimulated and we are then speaking about Stimulated Raman Scattering (SRS). An analyzis of the propagating equations in the medium [73] leads to an approximation of this power threshold at that point. The threshold when 50% of the input

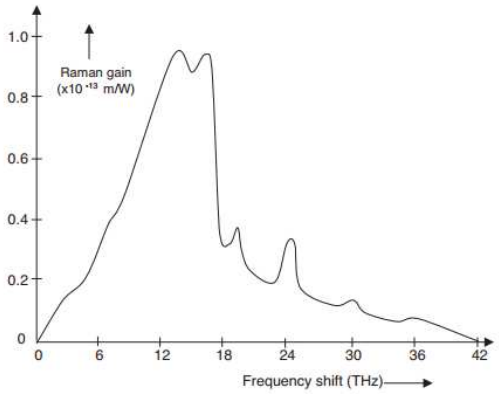

Figure 2.20: Raman gain for silica. The intensity of the scaterred light is plotted in regards to the frequency shift. It has a peak at 13THz and a bandwidth of about 40 THz [73].

signal is in the Raman signal is given by the equation 2.32:

$$P_{th} = \frac{16 A_{eff}}{g_R L_{eff}} \tag{2.32}$$

Where g_R is the value of the Raman gain for the excited frequency (see figure 2.20), it is of the order of 10^{-13} m/W, A_{eff} is the effective area of the mode inside the fiber, L_{eff} is the effective length of the fiber as defined in equation 2.36. This power threshold is given for the forward SRS, for the backward SRS a higher power threshold can be computed by replacing the numerical factor 16 by 20.

If we make a numerical evaluation of this power threshold for a fiber whose core diameter is 15 µm and having an effective length of 5 m, we get $P_{th} = 1800$ W. This value is less than an order of magnitude higher than the power that we plan to use. So this is a non linear effect that we could eventually take into consideration, however we will see in the next section that the threshold for Stimulated Brillouin Scaterring is much lower than this one and is an issue that we have to deal with before having to face the SRS.

2.4.3 Stimulated Brillouin Scattering

2.4.3.1 Theory

The Brillouin Scattering comes from the interaction between light and the molecules of the medium in which it propagates. It has been predicted in theory by Leon Brillouin in 1922 [74], but has first been observed only in 1964 while working with laser [75]. The difference between the Raman scattering that we detailed previously is that in this case, the created phonons are not incoherent optical ones anymore but coherent acoustic ones. As we will

explain hereafter, this give rise to a macroscopic acoustic wave in the fiber that alter its behavior. The spontaneous Brillouin scattering appears when an input photon, interacting with a molecule of the medium, is converted into an acoustic phonon and a photon of lower frequency. This scattered light is called the Stokes wave and while appearing in an optical fiber it can only propagate either in the forward or backward direction. This spontaneous phenomena is always present but when reaching a certain amount of power it becomes stimulated. Indeed the backscattered light is interfering with the input light and by a phenomena of electrostriction it locally creates a variation in the refractive index of the medium. The acoustic wave created this way is then propagating in the medium and results in a moving Bragg grating on which the input light is reflected. Thus the downshifted frequency of the Stokes wave can also be seen as a Doppler effect induced by the displacement of the grating. So one can easily understand that the more power in the Stokes wave, the stronger the interferences and thus the more power is backreflected (figure 2.21), the phenomena becomes Stimulated and we can then speak about the Stimulated Brillouin Scaterring (SBS). To initiate this stimulated process it requires an initial Stoke wave with a certain intensity. The power in this Stoke wave increases by spontaneous effect with the input power and with interaction length with the medium. That is why optical fibers that have a particularly long interaction length without too much attenuation are particularly subject to this non linear effect. Another point that has to be pointed out is that while the process becomes stimulated, even before clearly observed any power in the Stokes wave, the relative intensity noise of the output power is increasing.

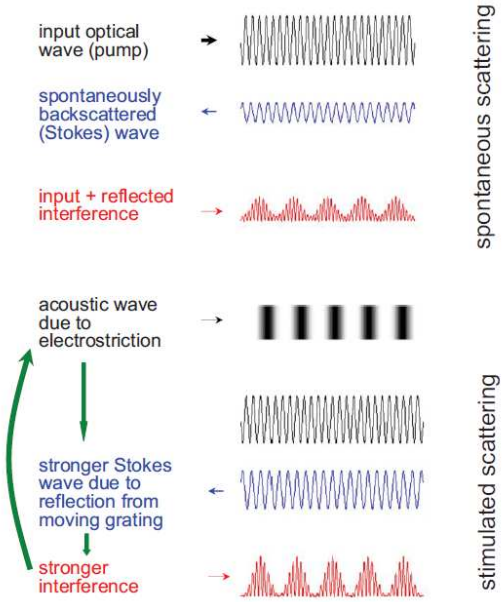

Figure 2.21: Spontaneous and Stimulated Brillouin Scattering in optical fibers [76]. The back scattered Stokes wave interfers with the input signal, by electrostriction this create an acoustic wave propagating along the fiber which reflects the input light and thus further enhance the interferences

2.4.3.2 SBS Threshold

The Stimulated Brilllouin Scattering Threshold (SBST) is the power threshold Pth at which the SBS is initializing. It can be detected by measuring the power of the Stokes wave back reflected from the fiber and compare it to a certain amount of the input power. To do so we abitrarely set a value μ such as $P_R = \mu Pin$ where P_R is the power back reflected. Often μ is taken equal to 0.01, 0.1 or even 1. There are no easy formula that gives a precise value for the SBST but usually a good approximation when half of the input power is backreflected is given by the following equation [73]:

$$P_{th} = \frac{21 b A_{eff}}{g_B L_{eff}} \tag{2.33}$$

where

- A_{eff} is the effective area of the mode propagating into the fiber
- b is a polarization factor
- g_b is the effective peak Brillouin gain
- L_{eff} is the effective length of the fiber

In the development here after we will describe and explain the different parameters that appear in this equation.

The factor 21 is a numerical factor that can be computed from the numerical evaluation of the equation of the spectral density of the backscattered light with the usual parameters of the fibers as Kobyakov et al explained in [76].

The effective area A_{eff} is often approximated as the mode field diameter of the fiber, this approximation is accurate with standard step-index fibers but can lead to some variations in the SBST when working with fibers whose structure is more complex. Indeed, what has to be considered is actually the effective area of the acousto-optic interaction, and when working with optical fibers with more complex cross section, the acoustic modes that are excited and able to propagate through the fiber can be different than the usual longitudinal one. This interaction has been better studied in various paper [77] [78] and it has even been shown in [79] [80] that this can lead to a higher SBST for smaller optical effective area.

The polarization factor b is a factor that varies between 1 and 2 according to the input polarization state [81]. If the fiber is not birefringent, then we have $b = 1$ but when there is a birefringence then b is varying. It is equal to 1 when the input linear polarization is sent on one of the main axis of the fiber and equal to 2 when sent at 45° of the axis. This makes it particularly relevant for polarization maintaining fibers.

The peak Brillouin gain g_{B0} is the maximum value of gain spectrum of the excited acoustic mode. This spectral profile, presented in figure 2.22, has a Lorentzian shape described

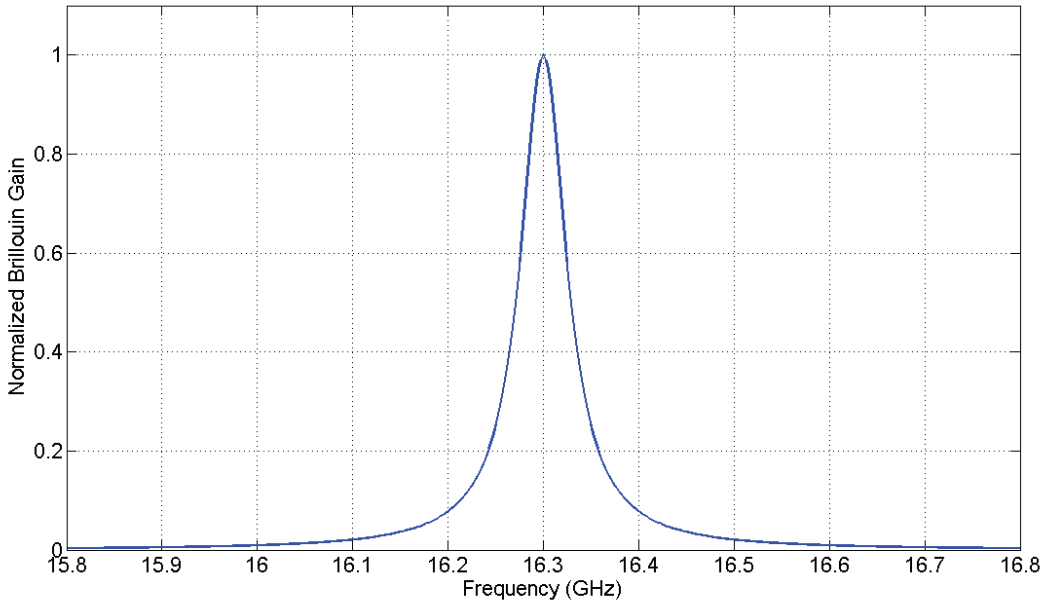

Figure 2.22: Lorentzian shape of the normalized Brillouin gain profile, computed with usual values for single mode step index fiber $\nu_{B0} = 16.3$ GHz, $\Delta\nu_B = 58$ MHz. These values can differ according to the physical properties of the fiber

by the equation 2.34:

$$g_B(\nu) = g_{B0}\frac{(\Delta\nu_B/2)^2}{(\nu - \nu_{B0})^2 + (\Delta\nu_B/2)^2} \tag{2.34}$$

Where g_{B0} is the peak Brillouin gain, ν_{B0} is the central frequency of the profile and $\Delta\nu_B$ its FWHM. The values depend on the wavelength, the material and the structure of the fiber and also the acoustic mode that is excited. Typical values at 1064 nm for the silica for the fundamental longitudinal acoustic mode are $\nu_{B0} = 16.3$ GHz, $\Delta\nu_B = 58$ MHz and $g_{B0} = 2.4 \times 10^{-11}$ m/W [82].

This value of the peak Brillouin gain can be taken as it is to calculate the SBST for narrow linewidth lasers. However, when it comes to laser with a broader bandwidth, one has to take into account the FWHM $\Delta\nu_{laser}$ of the laser that mitigates the effective peak Brillouin gain as follow [83]:

$$g_B = \frac{g_{B0}}{1 + \Delta\nu_{laser}/\Delta\nu_B} \tag{2.35}$$

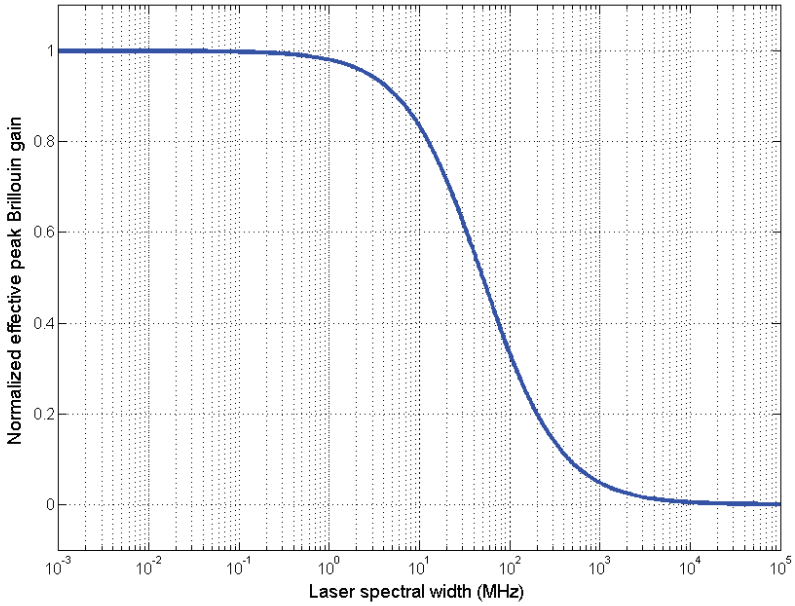

Figure 2.23: Normalized effective Brillouin peak gain dependence on the bandwidth of the input beam, computed with a FWHM of the Brillouin gain spectrum of $\Delta\nu_B = 50$ MHz

This equation, whose dependence on the laser linewidth has been plotted in figure 2.23, explains why SBS is only relevant for single frequency laser.

The effective length of the fiber, defined in equation 2.36, is a way to take into account the attenuation of the fiber. Calculated from the distribution of the power inside the fiber, it corresponds to the length of a fiber that would not have any losses (see explanations figure 2.24).

$$L_{eff} = \frac{1 - e^{-\alpha L}}{\alpha} \tag{2.36}$$

where α is the attenuation of the fiber. Two cases can then be distinguished:

- $\alpha L \ll 1$ which leads to $L_{eff} = L$
- $\alpha L \gg 1$ which leads to $L_{eff} = 1/\alpha$

In our case, the typical attenuation in the fibers that we are using is about $\alpha < 0.1$ dB/m [84], considering the relatively small length of fiber that we need (few meters) we can consider that $L_{eff} = L$.

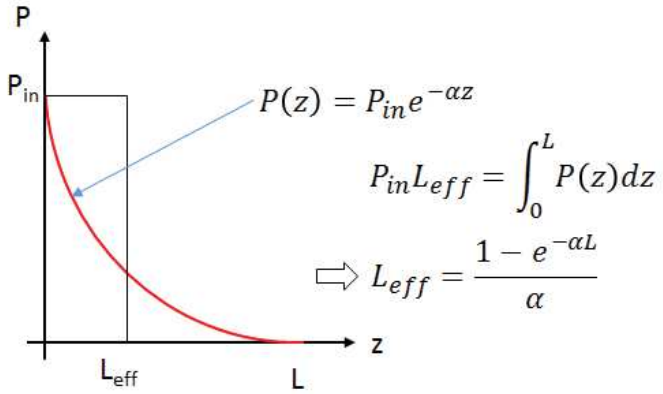

Figure 2.24: Effective length of a fiber having an attenuation α. It represents the length that would have the fiber without attenuation, ie with a uniform power distribution.

2.4.3.3 SBS in photonics fibers

The model that we described in the previous section is a good approximation for usual step-index fibers, but we saw that the SBST depends on the acousto-optic effective area. Due to their complex structure and hard boundaries, PCF fibers exhibit strong acoustic reflections that lead to a mix of shear and longitudinal acoustic resonance in the core of the fibers. This can result in an increased number of exited modes in a small core PCF fiber as it has been shown by Dainese et al in [85]. The peaks of these excited modes were in the range of 10 GHz and leads to a SBST five time greater that the one that was computed thanks to the equation 2.33. In an other study, Beugnot et al [86] highlighted a Brillouin gain spectrum 3 times broader than the one usualy observed in step index fiber and as a consequence observed a SBST 3 times larger than the theoretical one. In these two cases, the complex propagation of the acoustic waves in the structure lead to an improvement in the SBST but for example in [87] they observed an increase of the Brillouin gain of a factor of 100 in a microstructured sulfite glass based PCF compare to the expected one in fused silica.

So there is no simple way to compute the SBST in PCF fibers, every single structure will have a different behavior which can be understood thanks to a finite element method analysis to define what are the excited acoustic mode inside the fiber. Using these methods manufacturers can also design fibers with structures that guide acoustic waves differently in order to have the desire effect: either increase the SBST for most of fibers or decrease it in some other cases such as non-linear fibers.

In our case, to the best of our knowledge, the fibers that we were using, LMA-PM-15 and LMA-PM-40-FUD (see chapter 3), have not been studied theoretically. We do not have the software and the ability to carry such a theoretical study but we did experimental tests. They are described in their respective sections 3.2 and 3.3.

2.4.3.4 Ways to increase the SBS threshold

Giving the equation of the SBST (2.33), for a given length of fiber in an application where we want to increase it, one can act on the following parameters: the polarization factor b, the effective area A_{eff} and the Brillouin gain g_B. We are reviewing hereafter the influence of these parameters.

We saw in section 2.4.3.2 that the polarization factor is relevant only in PM fibers and can increase the SBST by 3 dB while splitting the polarization on the two axis of the fibers. This has been investigated theoretically and experimentally in many works such as [88] and [89] respectively for small core PCF fibers and for PCF fibers whose core is of the order of 6 µm . They both found the 3 dB increase. We investigated this characteristic for the LMA-PM-15 from NKT photonics and present the results in section 3.2.5.

The second parameter that can be modified in order to increase the SBST is the acousto-optic effective area A_{eff}. This area can be computed by analyzing the propagation of both the acoustic waves and the electromagnetic ones inside the fiber. However in a first approximation, the trivial idea is to use fibers having a greater core diameter. That is what motivated our choice of using LMA-PM-40-FUD fibers instead of the LMA-PM-15.

Finally the last parameter influencing the SBST is the Brillouin gain g_b. This gain is itself influenced by many parameters such as temperature or bending of the fiber. The influence of the temperature as been used in [90] or in [91] where they coiled the fiber on two reels having different temperature. This shifts the peak Brillouin gain and creates two Stokes waves of different frequency. These two Stokes waves are not enhancing each other through the stimulated process and so the SBST is decreased. This method is more relevant for active fibers, where the deployment of the fiber is not of interest. With a passive fiber used to transport a beam the deployment of the fiber is actually a constraint and not a degree of freedom. A control of the temperature over the length of the fiber would be difficult to realize.

An other approach that has been demonstrated to work for an active fiber is to phase modulate the beam at low power in order to spread the power in different frequency peak in the fiber [92]. This is exciting different Stokes waves in the fiber and so increase the SBST. At the output of the fiber they were using a high power phase modulator having the same modulation frequencies than the input one but with a phase shift of $\pi/2$ in order to bring the power back in the carrier. This could eventually mitigate the SBS in our application. However, it would required two high power EOM having a high modulation depth. They were indeed doing the experiment with a modulation of 1.33 and get an improvement of a factor 1.5 on the SBST.

Finally an other idea is to choose another material for the core of the fiber or to doped that core in order to lower Brillouin gain. This last point has been done in several works such as [93], but is not relevant for our passive fibers. What would be relevant is to use an hollow core fiber. In such a fiber the light is propagating into the air which avoids the interaction between the light and the molecules. Recent works have been conducted in order

to characterize non linear effects in hollow core fibers and it seems that the main limiting effect is the forward Brillouin scattering [94] [95].

2.5 Conclusion

In this chapter, we saw that the Advanced Virgo laser has very high demanding specification in term of linewidth, power, polarization quality and spatial beam quality. These characteristics makes it almost unique and it requires very specific optical fibers to be able to transport it and not worsens its properties. We also saw that the two critical points while injecting a high power single frequency laser in an optical fiber are the injection, because of the high power densities that can easily damage the fiber, and the single frequency operation that makes the fiber particularly subject to the Stimulated Brillouin Scattering. In order to mitigate these effects, we need a fiber with a core as large as possible that would, at the same time, keep the optical properties of the beam. However usual fibers are designed either to keep a good output beam quality or to deliver high power beam. By detailing the working principle of different design of fibers we came to the conclusion that Photonic Crystal Fiber having a structure that maintain the polarization are the best candidate for our application. In the next chapter, we will give the results on our investigation on this kind of fibers.

Chapter 3

Polarization Maintaining Large Mode Area fibers for high power single frequency beam transportation

In this chapter we are investigating the ability of the LMA-PM-15 and the LMA-PM-40-FUD to transport a high power single frequency beam. In the first part we are reviewing the improvements that we brought throughout our experiment in order to increase the coupling into the fibers. The experiments that we carried out on the fibers are presented in the sections 3.2 and 3.3.

3.1 Investigation on the improvement of the coupling

In chapter 2, we saw that the injection was a critical point of the experiments that we carried out on the fibers. Throughout the experiments, we improved our methods to couple into the fibers. In the following sections we detail these different improvements.

3.1.1 High power connectors and cooling down

The interface air/silica of the end facet of the fiber is a critical point and working on it requires specific facilities that we do not have in our laboratories. So one way to make the fibers usable, easy to handle and able to withstand higher power densities was to make them connectorized by a company expert in that field. On figure 3.1, you can see the two connectors that we were using in our experiments: a high power SMA-905 and a SMA-6 from Alphanov. They both have end caps and mode strippers in order to manage the power densities and the heating due to mismatching. They also gave us the possibility to use commercial components such as collimators as we will see in section 3.1.2.

The temperature in the SMA-905 rise by 7°C by Watt lost whereas the new generation, the SMA-6, has a temperature elevation of the order of 1°C by Watt lost. This later has

Figure 3.1: The two high power connectors that were used in our experiments. The high power SMA-905 connector on the left furnished with the fibers from NKT photonics and the SMA-6 connector developed by Alphanov.

been designed to dissipate power up to 6W according to the manufacturer [96]. However considering an input power of 200W, 6W of losses due to mismatching correspond to a coupling greater than 97% and such a coupling is difficult to reach in practice, especially because of the HOM of both the laser and the fiber. Moreover while the temperature increases, mechanical constraints arise and can decrease the coupling. An initial miscoupling that would bring only few watts of losses could be enough to increase the temperature of the connector that would modify its properties and bring even more losses. Hence the need to cool down the connectors to keep their temperature as low as possible while increasing the power. We first tried to cool them down by accelerating the convection that occurs at the interface between the copper part of the connector and the surrounding air by using a fan. However this technique is not the most efficient one and presents the drawback of inducing molecular and dust agitation which is something that we want to avoid on an optical bench. That is why we designed a water cooling system for both connectors. The one for the SMA-6 connector will be detailed in section 3.1.2 since it is part of a whole homemade collimator. The one for the SMA-905, based on the design of a similar one that is used at the Albert Einstein Institute in Hanover, is presented in figure 3.2. It consists on a piece of copper surrounding the connector, the thermal contact is ensured thanks to a sheet of graphite. The piece of copper is cooled down by water coming from a chiller and flowing inside. Thus by conduction, the whole structure is kept at a lower temperature. Along the experiments that we were conducting, and that we will detail later in the thesis, we were monitoring the temperature of the connector used to inject the laser beam into the fiber. For 40W injected with a coupling efficiency of 80%, knowing that about 4% were reflected on the input end facet of the fiber, we had 6.4W lost in the connector that were heating it. From room temperature of 22°C, the connector reached a temperature of 36°C while being cooling down by the fan and only 31°C while using the water cooling system.

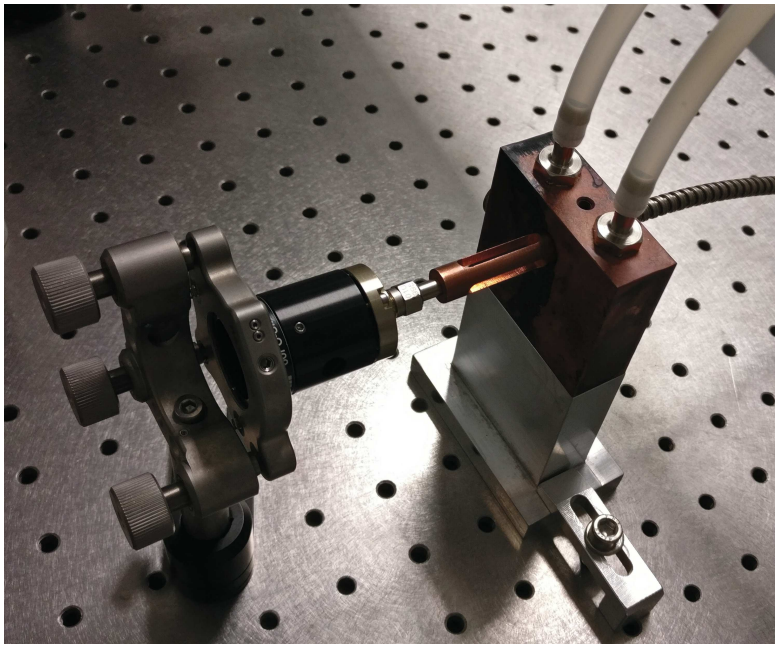

Figure 3.2: SMA-905 Water cooling system, the surrounding piece of copper is water cooled, keeping the whole structure at a lower temperature.

3.1.2 Home made collimators

In the first experiments that we were carrying out, we were using commercial collimators from Schäfter und Kirschhoff which can be directly connected to our high power connectors (see figure 3.2. The lenses can be translated inside the tube and allows us to reach different values of waist size and position as you can see on figure 3.3. However although these collimators are very compact and convenient for first experiments, it is complicated to precisely set the position of the lens inside the tube. Moreover they did not give us the needed liberty on the position of the lens in the transverse directions.

In order to improve the coupling, we designed our own collimators with more degrees of freedom on the position of the lens regarding the fiber. The design is presented in figure 3.4, it is used for a fiber connectorized with a SMA-6 from Alphanov. The connector is squeezed between two pieces of copper. The thermal contact is ensured by a sheet of silicon. The bottom part is soldered to a third copper piece that has been machined such as water can flow inside. The coil shape of the dug part maximizes the contact surface between the copper and the flowing water. The temperature of the water is regulated by a chiller and thus by convection it can evacuate the heat from the system and keep it a lower temperature. The beam coming out of the fiber is then collimated through a lens, carefully chosen to avoid any spherical aberrations. Thanks to a translation stage and a 5-axis kinematic mount we do have 5 degrees of freedom (tilt X and Y, shift X, Y, Z) needed to well align this lens.

The first advantage of these collimators is the water cooling system that keep the con-

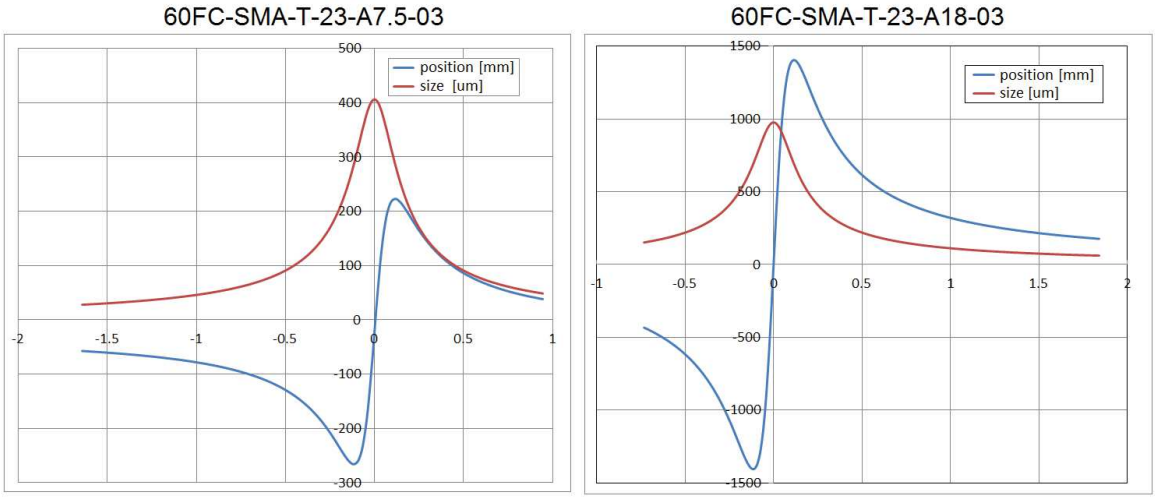

Figure 3.3: Waist position and size for two collimators from Schäfter + Kirschhoff of focal length 7.5 mm and 18 mm used with a LMA-PM-15 fiber. They are plotted against the distance between the focal plane of the lens and the end facet of the fiber. They do not give us all the needed degrees of freedom to properly couple into the fibers.

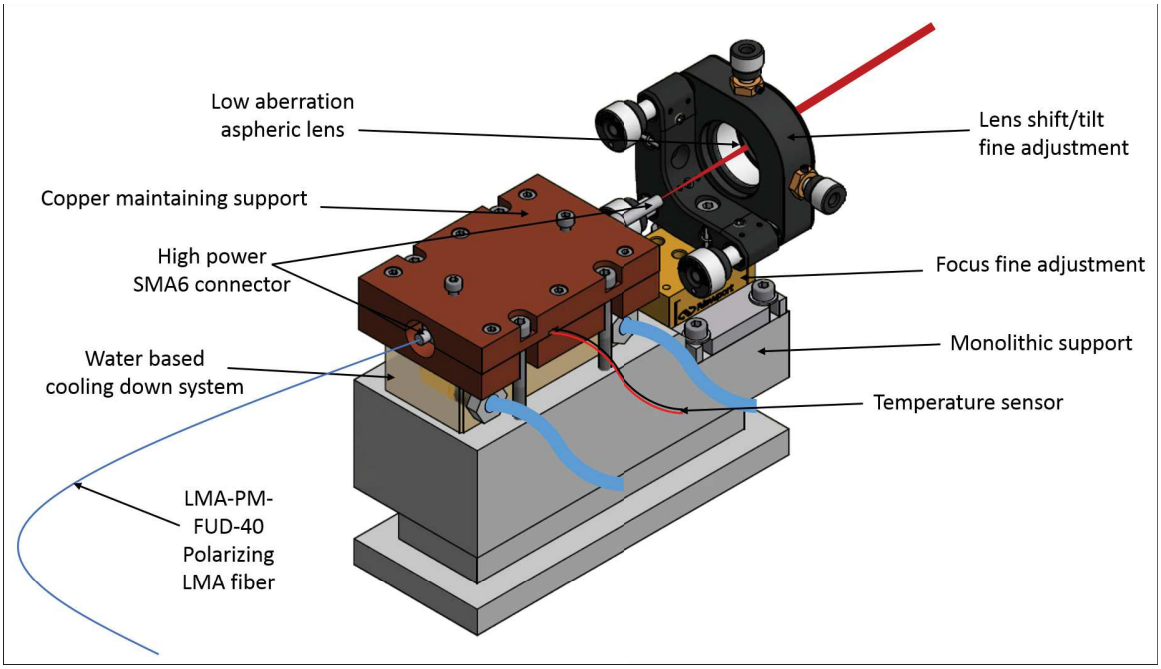

Figure 3.4: Home made collimators. The connector is squeezed between two plates of copper that are water cooled. The lens is precisely set thanks to the 5-axis mount.

nectors at a quite low temperature. They give us the possibility of choosing the lens with the focal length adapted to the waist needed for our set-ups. It also allows us to tilt and shift the lens (5-axis kinematic mount from Thorlabs Pitch/Yaw: ± 4 °, X/Y translation: ± 1 mm, Z translation ± 3.2 mm) to have a perfectly centered beam and avoid any aberration that would be caused by a misaligned beam.

This freedom on the position of the lens was specially needed for the LMA-PM-40-FUD fiber (see section 3.3) that we are using since they are still under development and the characteristics of their output beam can slightly vary from one fiber to another.

3.1.3 Anti-Reflective coating on fiber end facets

We saw in section 2.3.4 that in order to maximize the coupling, an AR coating was needed on the end facets of the fibers. Considering the way the manufacturers were adding the end cap to the fiber (splice a long one and then cleave it to the desire length) we had to make these end caps coat after the connectorization. This was a problem because the usual methods are heating the substrate while deposing the successive layers of the coating and heating the fiber was not possible for us because of the outer protections of the fiber made of acrylate (see figure 2.5).

While investigating on the possibility of doing such a coating on our fibers, one of the company (Thin Metal Film) told us that they could do it using Ion Beam Assisted Deposition (IBAD) which does not require any heating. They also insured us that the coating will have a better LIDT than usual methods used to coat the substrates. In figure 3.5, you can see the measured reflectivity of one of the run that they did on our fibers. We measured it ourselves and found a reflectivity of about 200 ppm. Qualitatively we also observed an increase of the coupling of about 10%. This is of the order of the expected 6.7%. The difference between the theoretical and the experimental value can be explained by the difficulty of doing a repeatable measurement of coupling efficiency. Indeed, since the coupling depends on too many different parameters, it is difficult to realize the exact same experiment, with and without coating.

However, despite the fact that the manufacturer told us that such a coating has a better LIDT, we encountered some problems while using the fibers at high power (about 40 W). In figure 3.6, you can see the end cap of a LMA-PM-40-FUD that has been AR coated and used at high power. One can clearly see the damages and especially that the AR coating is cracked. It is however difficult to estimate the actual consequences of these damages. The two end caps of the fibers presented similar damages and yet it was still possible to inject light into that fiber and reach coupling similar to the usual ones for this fiber without coating.

From the moment we realized the problem of these damaged AR coating, we tried to find a solution and decided to stop the tests at high power in the mean time. We contacted the company, they said that it must come from the quality of the surface before coating. Some new solutions are under investigation. A promising one is to use a bigger end cap, such as the one presented in figure 3.7, that will have been properly AR coated previously. This, however, is incompatible with the high power connectors that we were using since then and

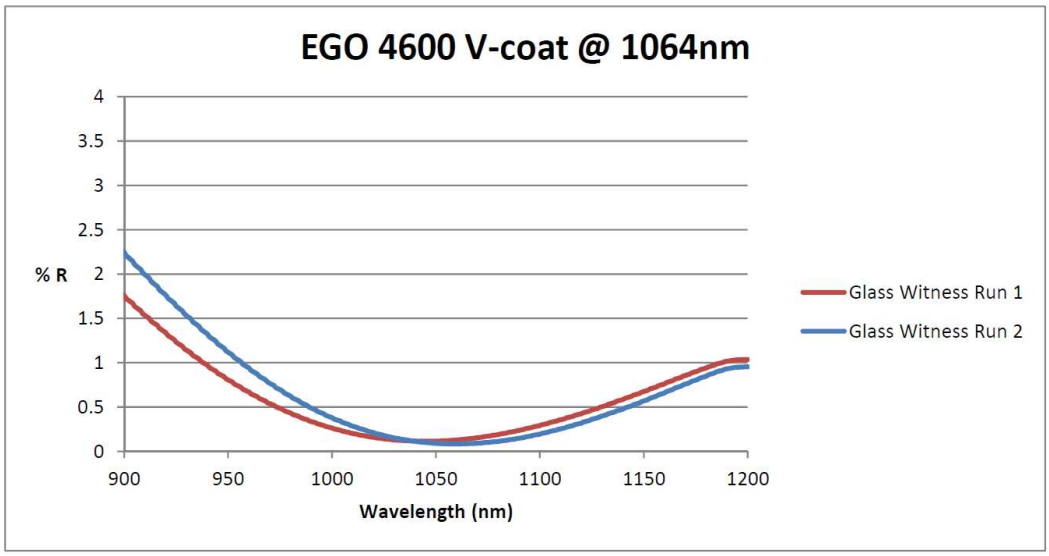

Figure 3.5: Characterization of the AR coating at 1064 nm done by the company Thin Metal Film

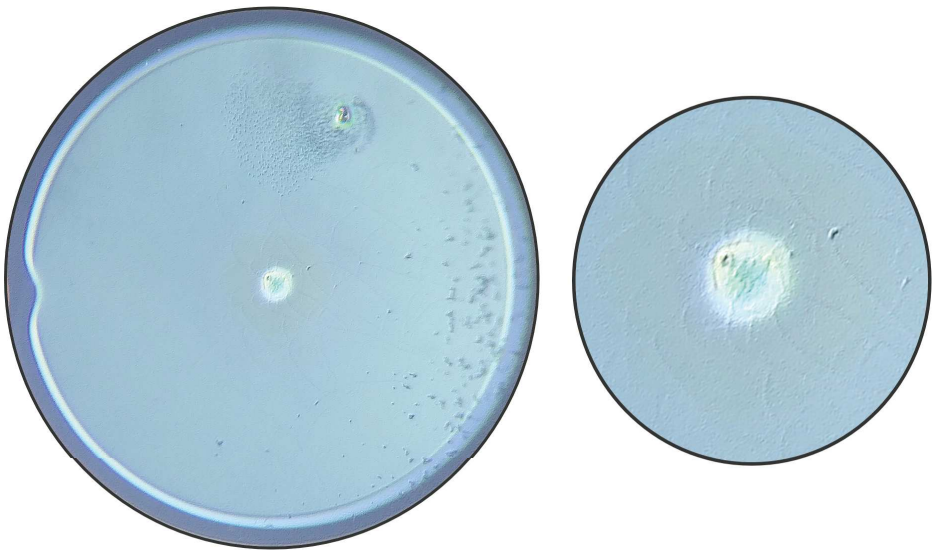

Figure 3.6: Endcap of a SMA-6 connector that has been damaged while increasing the power. One can see on the zoom presented on the right that the AR coating is cracked.

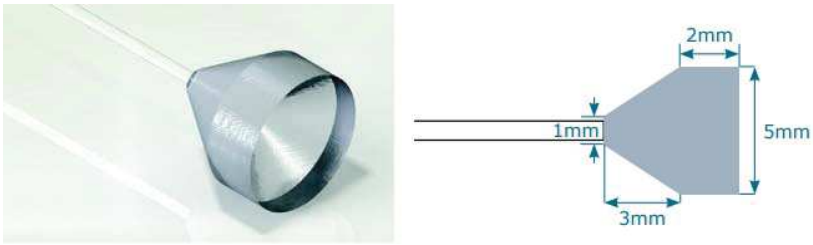

Figure 3.7: End cap from Alphanov, the bigger air/silica interface would allow to applied an AR coating before connectorizing it on the fiber. It also allows to decrease the power densities on this interface.

the injecting system will have to be redesigned.

3.1.4 Automatic alignment

While working with single mode fibers whose core is about few micrometers and considering the high magnification of the collimators that we are using, the power couple into the fibers is strongly dependent on the alignment of the beam and especially the tilt as you can see on figure 3.8 where we computed the tilt dependency of the coupling of a Gaussian beam into a single mode fiber. This miscoupling is critical in our case, since we are dealing with densities of power of several MW/cm^2, a misalignment can rapidly lead to the destruction of the fiber. That is why it was necessary to find an efficient way to keep the alignment of the beam with respect to the core of the fiber.

The usual method to control the alignment of a beam is the one using two quadrant photodides that we presented in section 1.4.4. However this technique can not correct the slow drift that could appear between the reference QPDs and the fiber in which we have to inject the power.

In this section, we are presenting another method that allows us to keep the beam aligned on the fiber without having the two drawbacks mentioned previously. It consists in using the core of the fiber as the reference instead of the two QPD. Indeed, the transmitted power at the output of the fiber directly depends on the position of the beam in regards to the core of the fiber as it is highlighted on figure 3.8. We realized afterwards that a similar method is also used in the product FiberLock commercialized by TEM-messtechnik [97].

The idea of this method is to induce a sinusoidal displacement of the beam on the core of the fiber at a given frequency f_1 thanks to a PZT. This displacement will be seen in the spectrum of the output power by a line at the frequency f_1. The particularity of this AC power is that its phase depends on the actual position of the beam on the core of the fiber as it is explain for an horizontal displacement on figure 3.9. When the position of the beam is changing in respect to the center of the core of fiber, the phase of the AC signal is flipping. So by demodulating this signal thanks to the reference oscillator used to control the PZT

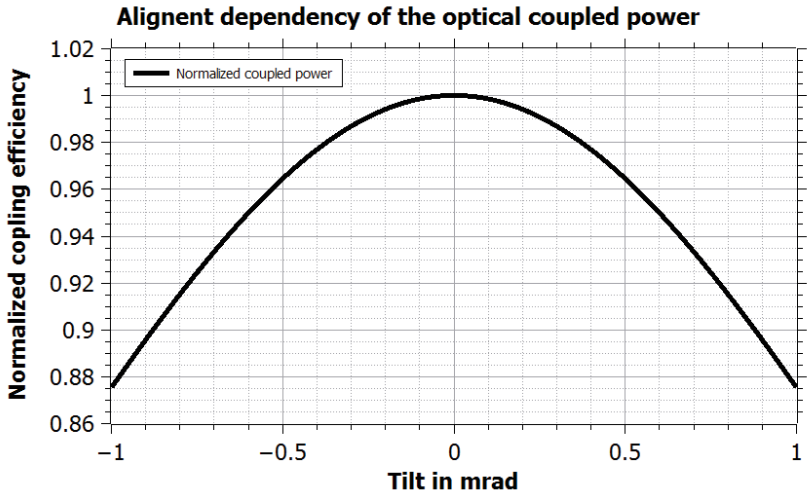

Figure 3.8: Zemax simulation - Normalized Coupling efficiency of a free space beam into a single-mode optical fiber with a tilt of a mirror of ± 1 mrad at 10 cm from the input collimator. The 1064 nm input beam is 900μm radius @ 1/e^2 for a collimator lens of 11 mm focal length. The diameter of the core of the optical fiber is 6 µm (the maximum coupling efficiency is 80% in this configuration)

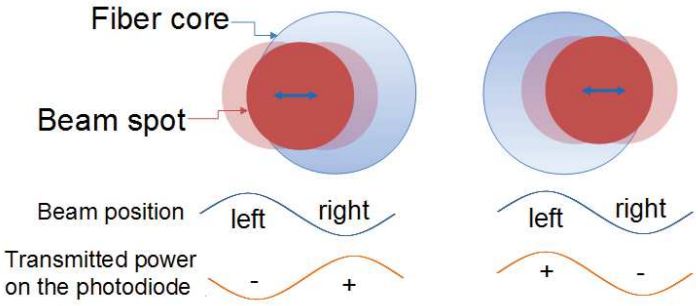

Figure 3.9: While the beam is scanning the core of the fiber, depending on the position of the beam, the phase of the oscillation that can be seen in the output power is flipping. This characteristics is used to generate an error signal to lock the beam on the center of the fiber.

at the frequency f_1, we create an error signal whose sign is changing when passing by the center of the fiber. This error signal is then shaped into a control loop that we will detail later and then added to the initial sinusoidal excitation as a DC value to bring the beam back on the center of the fiber.

Analytically this can be derived from the spatial overlapping between two Gaussian beam, E_1 at a position x_1 which is the one centered on the core of the fiber that maximizes the coupling and the actual beam E_2 at a shifted value x_2. The overlapping integral between these two beams can be computed thanks to the following formula [98]:

$$P = P_0 \ \exp\left(-\frac{(x_1 - x_2)^2}{\omega_0^2}\right) \tag{3.1}$$

In our case, by taking the center of the fiber as the reference for the x axis, we have $x_1 = 0$ and $x_2 = x_0 + \Delta x \ \cos(f_1 t)$, where x_0 is the shift of a misaligned beam and Δx is the amplitude of the displacement induced by the PZT. Thus at the output of the fiber we have :

$$\begin{aligned} P_{out} &= P_0 \ \exp\left(-\frac{(-x_0 - \Delta x \ \cos(f_1 t))^2}{\omega_0^2}\right) \\ &= P_0 \ \exp\left(-\frac{1}{\omega_0^2}(x_0^2 + \Delta x^2 \ \cos^2(f_1 t) + 2x_0 \Delta x \ \cos(f_1 t))\right) \\ &= P_0 \ \exp\left(-\frac{1}{\omega_0^2}(x_0^2 + \Delta x^2 \ \frac{1 + \cos(2f_1 t)}{2} + 2x_0 \Delta x \ \cos(f_1 t))\right) \end{aligned} \tag{3.2}$$

By considering small variation of x_2 we can do the approximation $e^x \sim 1 + x$.

$$\begin{aligned} P_{out} = P_0 \ &\left(1 - \frac{1}{\omega_0^2}(x_0^2 + \frac{\Delta x^2}{2})\right) \\ &+ P_0 \ \frac{2x_0 \Delta x}{\omega_0^2} \cos(f_1 t) \\ &+ P_0 \ \frac{\Delta x^2}{2\omega_0^2} \cos(2f_1 t) \end{aligned} \tag{3.3}$$

This expression makes appear the power fluctuation at the frequencies f_1 and $2f_1$. By demodulating this expression at the modulation frequency f_1, carefully checking that there is no phase shift, and using a low pass filter to keep only the DC value of the signal we can

keep only the contribution of the signal at the frequency f_1 and we have :

$$V_{demod} = -\frac{2AP_0\Delta x}{\omega_0^2}x_0 \tag{3.4}$$

where A is a factor that depends on the response of the photodiode and on the amplitude of the electric power used to demodulate. The important point to be noticed is that this value directly depends on x_0 so it can be used as an error signal to correct this misalignment by applying a DC value on the PZT.

In a first time, we validated the principle of this method thanks to the experiment presented in figure 3.10. We were acquiring the error signal in open loop by inducing a linear displacement on the core of the fiber. The results are shown in figure 3.11, they are in good agreements with the computed ones.

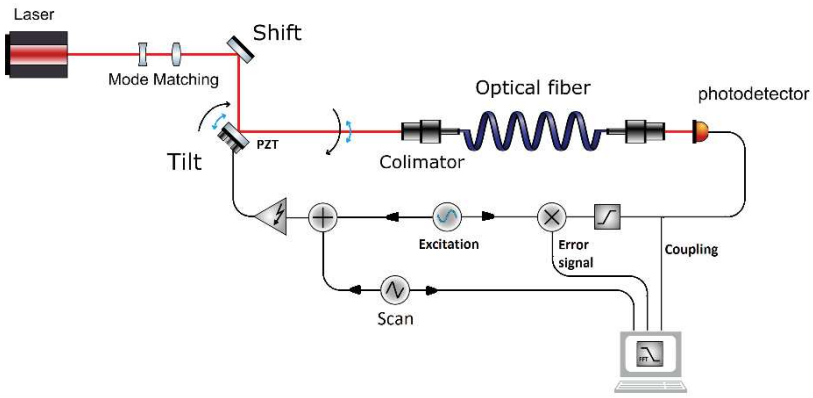

Figure 3.10: Setup used to confirm the feasibility of using this error signal to lock the coupling at its maximum. The signal on the PZT is composed by the oscillating excitation added to a DC ramp. The error signal is generated by demodulating the coupling with the oscillation. The scan, the coupling and the error signal are acquired and results are presented in figure 3.11

In close loop, this error signal can be used to correct the shift of the input beam so that the coupled light into the optical fiber is at its maximum for this degree of liberty. The control loop can simply be a lowpass filter or a more complex loop as shown in figure 3.12 where we present a analogical design of the set-up in which we were setting different parameters for the PID thanks to the configurable analogical filter FALC110 [99].

This set-up can also be used to align the fiber from the beginning. Considering for example the horizontal degrees of freedom. Once the loop is engaged for the horizontal tilt, it is possible to maximize the output optical power by using the shift mirror. With this method

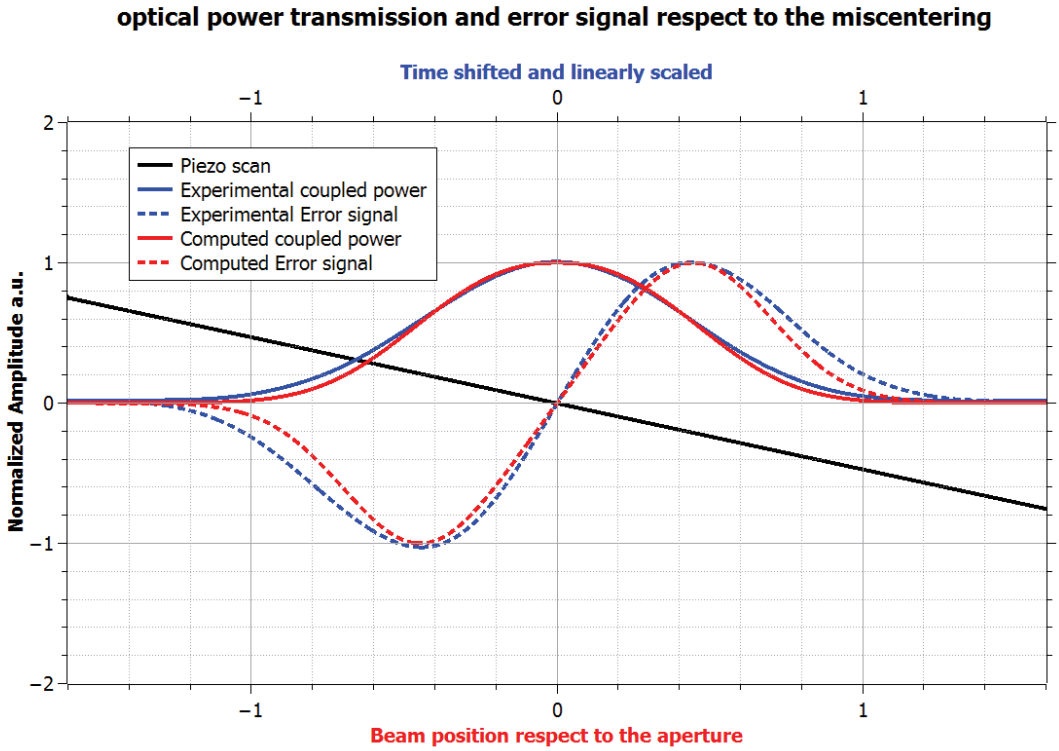

Figure 3.11: Numerical simulation computed with the following parameters: Aperture and Gaussian beam of unity radius ($1/e^2$ for the beam size), amplitude of the excitation of 10^{-2}, compared with the experimental values obtained with the setup presented in figure 3.10, the experimental data were numerically low pass filtered and an offset was added to the amplitude for the error signal and the scan.

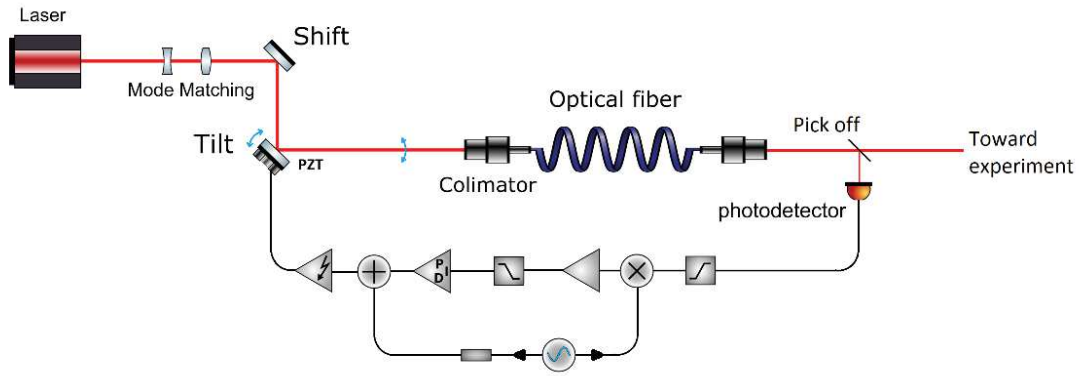

Figure 3.12: All-analog setup to keep the beam locked on the core of the fiber for one degree of liberty

we can reach the maximum of the coupling efficiency on one degree of freedom. Switching the active control on the other degree of freedom, the maximum output power is quickly find. This method could be extended for the two degrees of freedom (shift and tilt) and optimized by using low noise electronic in order to minimize the residual amplitude modulation at the frequency excitation and the harmonics in transmission of the optical fiber. These frequencies have to be chosen high enough to be out of the detection band of Virgo (figure 1.8). Moreover, if there is a power control at the output of the fiber, these fluctuations can easily be corrected and the error signal generated to do so would also contain the information on the amplitude of the f_1 and $2f_1$ lines. Thus, it contains the information on the position of the beam, and so it can be used to create the needed error signal of the lock. Actually, at low power, instead of locking the alignment on the maximum coupling, it is also possible to slightly detune the error signal in order to lock the alignment not on the maximum of coupling but on a specific power and used this technique for power stabilization. However, this would induce some losses in the input connector of the fiber that we want to avoid. Finally another point of interest, for our future work, is on the possibility to use the beam jitter induced by an EOM as the exciting signal. We will explain this interesting feature of an EOM in section 4.3.1.

3.2 LMA-PM-15

3.2.1 Description and characteristics

The LMA-PM-15 is a PCF fiber that has been developped by NKT Photonics [84] and whose main characteristics are detailed in table 3.1. In this section, we will detail the experiments that we carried out on a 5m-long patchcord of this fiber. It was connectorized on both end by a high power SMA-905 connector that we presented in figure 3.1, and protected by a metallic jacket. Pictures of its cross section as well as its output mode are shown in figure 3.13. In the structure of its cladding we can see the air hole patern, each air capillary has a diameter $d = 4.5\mu m$ and the pitch between two of them is $\Lambda = 9.6\mu m$ [100]. This gives us a ratio $d/\Lambda \sim 0.47$. So according to the theory that we saw in section 2.2.3.3, we are at the edge of the single mode behavior, the ratio is indeed slightly larger than the condition for a single mode propagation that we specified before. However this value is a numerical evaluation that also depend on the wavelength and the fiber is said to be single mode at 1064nm by the designer [84].

Commercially available since 2008, this fiber has already been used in many application. In [101], they were using this fiber to keep the pointing instabilities to its minimum while transporting a 12W laser beam in a bose einstein condensate. In [102], they were using it at a power up to 18W with a coupling efficiency of 86%. Finally, in [103], four of these fibers were used to transport the power from laser amplifiers and recombine them into a single waveguide in order to do the coherent sum of the beams and obtained an output power of about 100 W. Their length is not specified but each fibers was transporting a single frequency beam whose power was between 30 W and 50 W. Although not so many details are given on

Optical properties	
Attenuation 1064 nm	< 10 dB/km
MFD @ 1064 nm ($1/e^2$)	12.6 ± 1.5 µm
NA @ 1064 nm (5%)	0.07 ± 0.02
Birefringence Δn @ 1064 nm	$\geq 1.3 \times 10^{-4}$
Polarization Extinction Ratio	≥ 18 dB
Mechanical properties	
Core diameter	14.8 ± 0.8 µm
Outer cladding diameter	230 ± 5 µm
Coating diameter	350 ± 10 µm
Core and cladding material	Pure silica
Coating material	single layer Acrylate

Table 3.1: Main characteristics of the LMA-PM-15 fiber from NKT Photonics

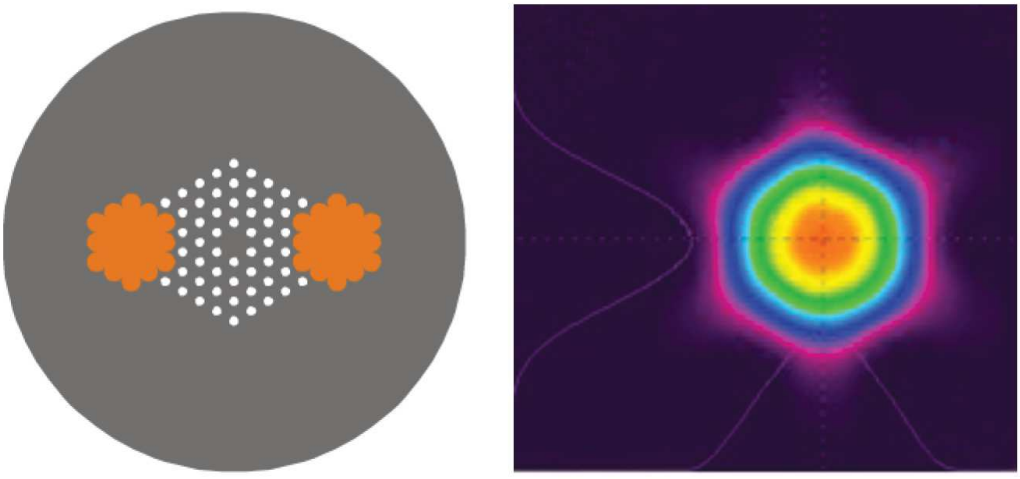

Figure 3.13: LMA-PM-15: structure of the cross section (left) and output mode shape (right) as given in the datasheet.

how it was used, the properties highlighted in these papers, made of this fiber, an interesting candidate as a first step in our aim of transporting high power single frequency beam.

3.2.2 Output beam characterization

In this section we are investigating the characteristics of the output beam of the LMA-PM-15: its Mode Field Diameter, the M^2 associated to its propagation and the HOM content. To do so we used the set-up presented in figure 3.14. The laser was protected from backreflection thanks to a Faraday Isolator, a first lens was then used to avoid the beam to diverge too much while propagating. We were monitoring the power used for the injection thanks to the HWP2 and PBS1. The mode of the beam was then shaped thanks to a telescope made of a divergent lens and a convergent one. The polarization before injecting was set thanks to HWP3 and the collimator used for the injection was one having a 18 mm focal length that we presented before (section 3.1.2). At the output of the fiber, the PBS2 was used to clean the polarization and insure that it was not fluctuating because of the fiber. The HWP4 was used to maximized the transmission through this PBS2 while HWP5 was used to precisely set the polarization of the beam that was analyzed. The beam was then either sent into the cavity in order to analyze the mode content or sent onto another line thanks to a flip mirror to be analyzed its propagation thanks to a beam scan. The cavity that we used was the Pre-Mode Cleaner (PMC) that was used during the first phase of Advanced Virgo (2014-2017). It is a triangular cavity having a FSR of 1.063 GHz that we were scanning thanks to the curved end mirror mounted on a PZT. Due to its asymetric configuration the vertical and horizontal higherorder modes are not resonating at the same place : while the successive vertical modes are resonating with an interval δ_ν from where the TEM_{00} is resonating, the horizontal modes are shifted in freqeuncy by $\Delta_\nu = FSR/2$ [104]. One could see this cavity on the picture of the set-up (figure 3.15) and find its main characteristics in table 3.2 [105]. The transmission through the cavity was analyzed thanks to the photodiode PD2. We also set up a CCD camera that allows us to look at the different resonating modes. The photodiode PD1 was giving us the information about the reflected light. In order to maximize the transmission through the cavity one has to match the waist size and position given by the documentation: an horizontal waist $w_{0x} = 508$ µm and a vertical one $w_{0y} = 519$ µm both located between the input and output mirror. In the set-up that we were using, this corresponds to a distance of 1440 mm from the output collimator. The mode matching was done by translating the lens into this collimator.

The first results that we are presenting in figure 3.16 is about the propagation of the beam. We measured the width of the beam before entering into the cavity, the X direction correspond to the horizontal axis while Y is the vertical. This gave us an horizontal waist of 451 µm situated at 1280 mm from the collimator with an associated M^2 of 1.09 and a vertical one of 444 µm located at 1241 mm with an M^2 of 1.1. Thanks to a Zemax simulation using this values and the lens that is used in the collimator we get back to the MFD of the fiber: 6.19 µm in the horizontal direction and 6.09 µm in the vertical one.

Using the values of the waists at the output of the collimator, we did a Zemax simulation

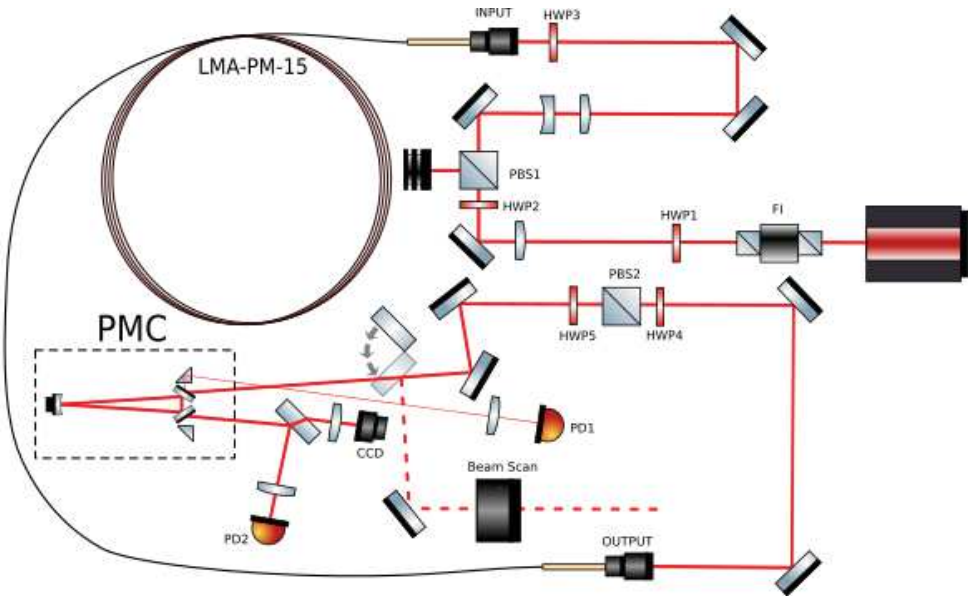

Figure 3.14: Scheme of the setup used to characterized the output mode of the LMA-PM-15

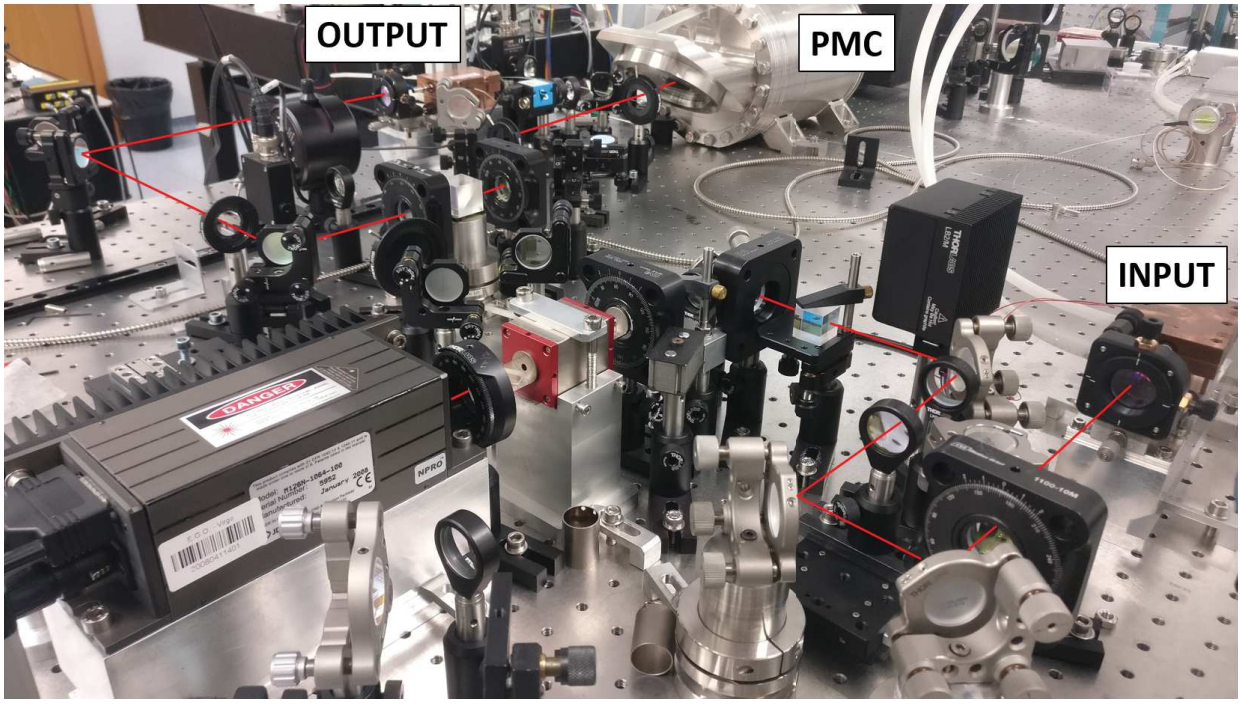

Figure 3.15: Picture of the set-up used to characterized the fiber. In particular, one can see the triangular cavity that was used to analyzed the HOM content of the fibers.

Cavity length	0.282 m ± 2 mm
FSR	1063 MHz ± 7 MHz
Finesse	490
Reflection contrast	89.7%
Transmission contrast	89.7%
Pole	1.085 MHz
Vertical waist (4 W)	519 µm
Horizontal waist (4 W)	508 µm
PMC length changes	0.7 FSR/°

Table 3.2: Main characteristics of the triangular cavity used to analyzed the mode content of the fibers

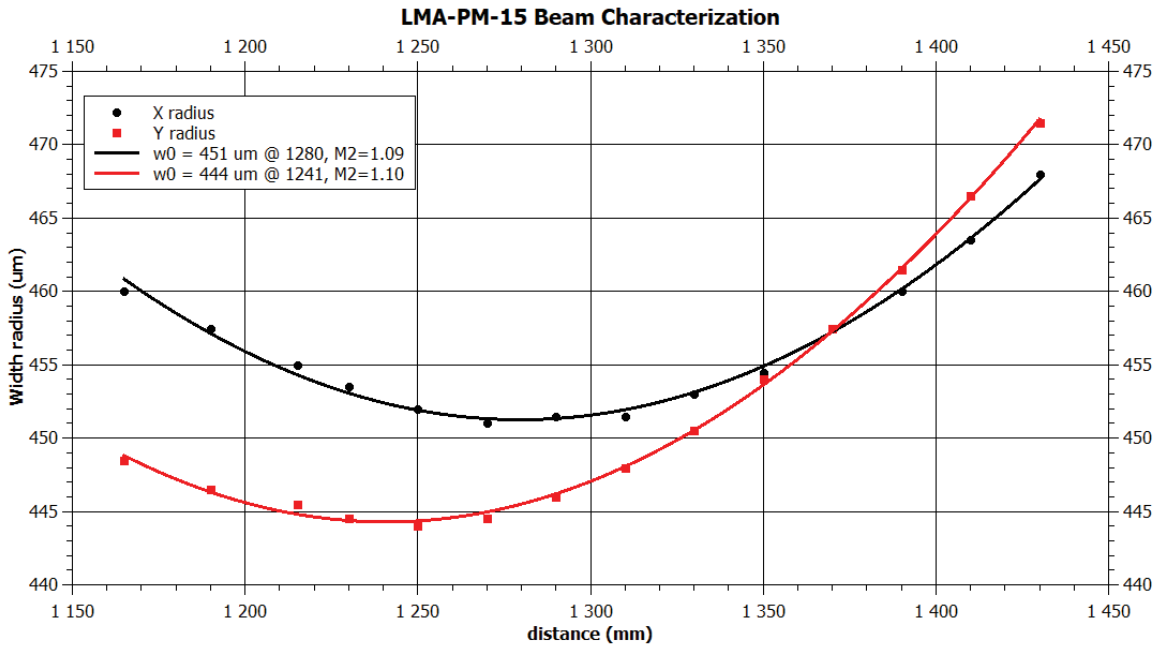

Figure 3.16: Measured beam width at the output of the LMA-PM-15, collimated with a collimator having a focal length of 18.4mm. The fit is done using the propagation equation of a Gaussian fundamental mode (eq 2.12)

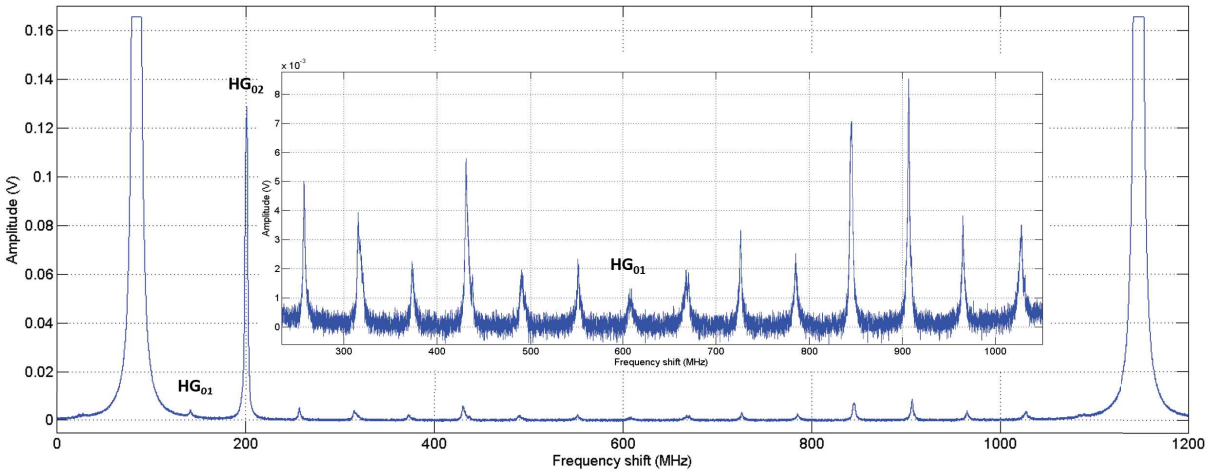

Figure 3.17: Scan of the cavity over one FSR in order to get the HOM content of the LMA-PM-15. The modes HG_{01} and HG_{10} are respectively due to vertical and horizontal misalignment of the beam with respect to the cavity. The high amount of power in the HG_{02} is due to the mismatching.

that gave us a theoretical mismatch of 2.4% while injecting into the cavity. The results of this injection are presented in figure 3.17, as expected the HOM content is dominated by the HG_{20}. Nevertheless we measured the amplitude of the different peaks (without considering the misalignement modes HG_{10} and HG_{01} and found a total of 195.4±0.7 mV while the peak of the TEM_{00} has been measured to be 4.36±0.02 V. The ratio between the amount of power in the HOM peaks and the total power gives 4.29±0.57%. By subtracting the 2.4% of mismatch given by the Zemax simulation this ends with 1.89±0.57% of the total amount of power that is contained in HOM. The error bars have been set by taking the standard deviation of the electronic noise of the measurements.

In a second attempt we set the collimator in order to better match the specifications of the cavity. We had an horizontal waist of 502 µm at 1432 mm and a vertical one of 483 µm at 1292 mm. According to the Zemax simulation this reduces the mismatch into the cavity to 0.7%. In figure 3.18 we present the results of the scan of the FSR in this case as well as the pictures of the different resonating modes taken thanks to the CCD camera. We measured 89.9±0.7 mV in that case for at TEM_{00} measured at 3.14±0.01 V. By subtracting the mismatch, this finally leads to an HOM content of 2.08±0.84%.

We added the images of the modes that we observed. Some of them can be recognized and clearly identified but most of them are a mix of vertical and horizontal modes of large order. Due to a small shift between the horizontal and vertical modes this ends in some double peaks as it can be seen on the figure. We took it into again in our calculation.

Through this two analysis we found coherent results for the HOM of the LMA-PM-15 fiber: 1.89±0.57% and 2.08±0.84%. Considering that the two measurements are independent

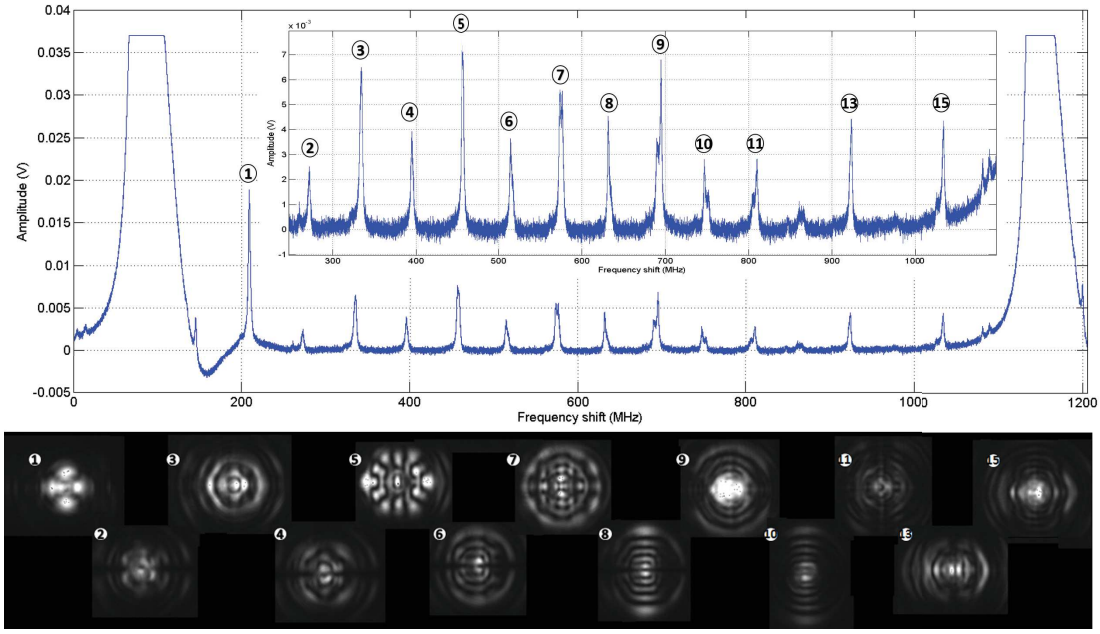

Figure 3.18: Scan of the cavity over one FSR in order to get the HOM content of the LMA-PM-15. This attempt has been done with a better matching and alignment than the previous one. In the bottom part of the figure one can see the modes corresponding to the different peaks.

this leads to a HOM content of 1.98±0.51%. This also in good agreement with an experiment that is carried out at the Cote d'Azur Observatory in Nice, in the characterization of the new laser amplifier system for Advanced Virgo. A LMA-PM-15 patchcord has been set up at the output of a slave laser similar to the one used in Advanced Virgo (presented in section 2.1.3) and was then injected into a mode cleaner cavity. The transmission through this cavity was of 98.2%.

3.2.3 Coupling efficiency at low power

After having made the fibers AR coated, we tried to maximize the coupling into it at low power. The laser used was a boostik 5W amplifier from NKT photonics [106] seeded by a NPRO laser. The waist size and position at the output of this fibered amplifier were as followed : w_{0X}=290µm at 222mm and w_{0Y}=324µm at 226 mm (respectively the horizontal and vertical values). We designed a telescope made of two lenses and a collimator to reach the desired sizes and positions for the waist. The simulation of this telescope is presented in figure 3.19. It has been designed thanks to a Matlab code based on the ABCD matrix formalism. With this set-up we reached 39.7 mW at the output for 42.9 mW at the input. Considering an uncertainty of 1% for both measurements, this leads to a coupling of 92.54 ± 1.4%. Let us investigate hereafter where these looses could come from.

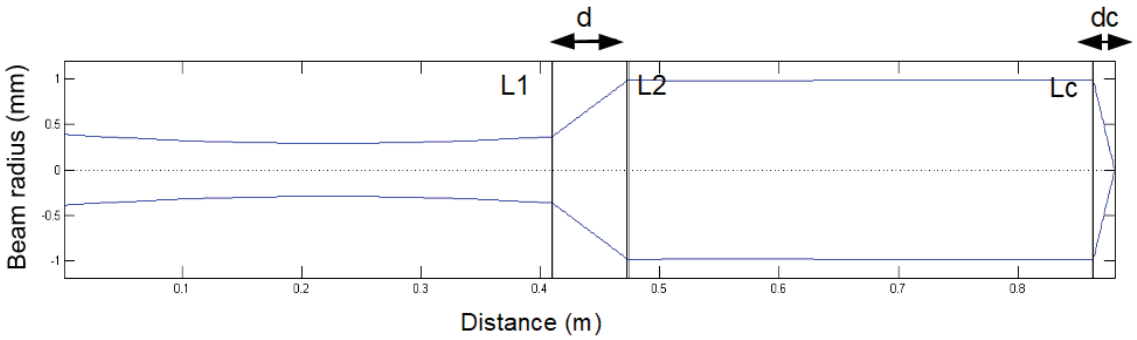

Figure 3.19: Telescope used to couple into the LMA-PM-15. L1: PLCC-19.1-20.6-UV (EFL=-39.92 mm), L2: PLCX-25.4-51.5-C (EFL=99.98 mm), Lc: A280-C (EFL=18.4 mm)

The first point that we checked afterwards was the actual efficiency of the telescope that we designed thanks to the matlab code. We did it thanks to a Zemax simulation of the set-up as accurate as possible: we were using the real lenses imported from the catalog of the manufacturers, we considered the astigmatism of the beam as well as the tilt angle of the end facet of the fiber. In order to maximize the coupling efficiency into the fiber we were making the distance d between L1 and L2 varying as it has been done in the lab with the lens L2 that was mounted on a translation stage. We get an optimum of 98.75%. This result has been obtained for a collimator perfectly set: with a distance dc of 17.317 mm (obtained by Zemax simulation) between the surface of the lens and the fiber. However we saw previously that these collimators were particularly difficult to set (section 3.1.2). Despite the efforts made to set it correctly, it is likely that the collimator was slightly detuned. To take this detuning into account, we performed the same simulation considering a variation of $\pm$ 0.1 mm of this distance. The results are presented in figure 3.20. These measurements leads to a mean of 98.51% and a standard deviation of $\pm$ 0.70%.

The fibers were AR coated with a coating similar to the one that we presented in figure 3.5. So, according to the data of the manufacturer and considering the fact the beam is injected with an angle 7.2° because of the 5° angle of the end facet, this leads to 0.19% $\pm$ 0.05% lost at each interface.

Then we have to consider the coating of the aspheric lenses used in the collimators at each end of the fiber. This coating has a typical reflectivity of 0.15% $\pm$ 0.05% [107]. Considering the four interfaces, this leads to 0.60% $\pm$ 0.10%.

According to the datasheet, the fiber has an attenuation of $\alpha = 10$ dB/km. Using the formula 3.5 which links the losses to the length of the fiber and its attenuation α in dB/km we have 1.15% $\pm$ 0.12% lost inside the fiber.

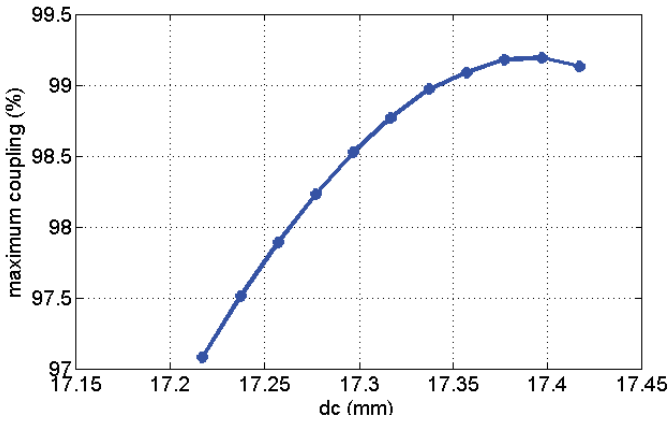

Figure 3.20: Maximum coupling reachable for a distance dc varying of ± 0.1 mm around its initial position

$$Ł_a = 1 - 10^{-\frac{\alpha L}{10 \times 1000}} \tag{3.5}$$

Finally the last cause of losses that we identified is the overlapping difference between the ideal TEM_{00} of the beam and the actual mode of the fiber. This has been studied in section 3.2.2 and we found 1.98± 0.51 %.

Here after is a summary table of the different losses and the associated error bars.

Mode Matching	1.49 %	± 0.7
Reflections end caps	0.38 %	± 0.07
Reflections collimators lenses	0.60 %	± 0.10
Attenuation	1.15 %	± 0.12
HOM fiber	1.98 %	± 0.57
Total	**5.60 %**	± 0.92

Table 3.3: Contributions to the coupling losses while coupling

So finally we had a coupling of 92.54±1.4 % for 5.60±0.92 % losses. There are still about 1.86% of the power missing. Part of this 1.86% could be explained by the mismatching which is quite critical. Moreover in the analysis that we just have done, because of a lack of measurements about it, we did not analyze the actual mode content of the laser. We just considered the coupling losses calculated with the overlapping of the modes of the fiber and a perfect TEM_{00} but there might be HOM in the laser beam, coming either from the laser itself or from its propagation through the set-up (misalignment, spherical lenses).

3.2.4 Broadband laser injection: power handling capacity

In the laboratory, the only laser that we had at our disposal to carry on some high power experiments was the fiber laser YLR-200-LP from IPG photonics [108]. It can reach power up to 200 W, has a $M^2 < 1.1$ and a polarization quality of 50 dB but the problem is that it is not a single frequency laser. Thus, in a first time, the idea of the experiments that we are presenting in the following paragraphs was to investigate the power handling capacity of the fiber by increasing it step by step and solving the eventual problems when they appeared.

To increase the power step by step, we were using the simple setup presented in figure 3.21. The waist of the laser beam is located at the output of the collimator and has been measured at 1.11mm on the horizontal axis and 1.15 mm on the vertical one [109]. In order to couple the light into the fiber we were using a telescope made of a diverging lens (f=-143 mm) located at 600 mm from the FI, a converging lens (f=229 mm) at 82 mm from the first one and finally a collimator from Schäfter und Kirchhoff at 420 mm from the second lens. We were monitoring both the output power and the temperature of the first connector.

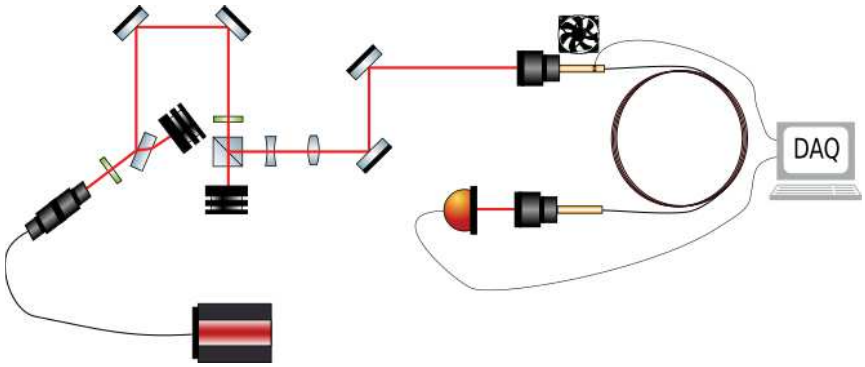

Figure 3.21: Scheme of the set-up used to inject a high power broadband laserbeam in a LMA-PM-15 fiber.

Thanks to this set-up we reached a coupling efficiency of 80%. The losses can be explained by the lack of AR coating on the end facets of the fibers (6.7% for the two facets), reflections on the lenses of the collimators (0.6%), attenuation of the fiber (1.15%). This means that 11.55% were lost while injecting into the fiber and participate to the temperature elevation of the connector. Among these 11.55%, about 2% are due to the mode of the fiber, the rest is due to the telescope that was used as well as the modes of the laser that we were using. Indeed, even if the manufacturer specified a $M^2 < 1.1$, it has actually been measured to be 1.25 in a previous experiment [110]. Despite the coupling losses we started to scale up the power as you can see in figure 3.22 (red and orange curve). While reaching 10 W, about 2 W were lost in the connector and we started to observe a slow decrease of the coupling as well as an increase of the temperature of the connector. We wait to see if it would reach a stable point but the temperature started to exponentially increase, we stopped the experiment at that moment.

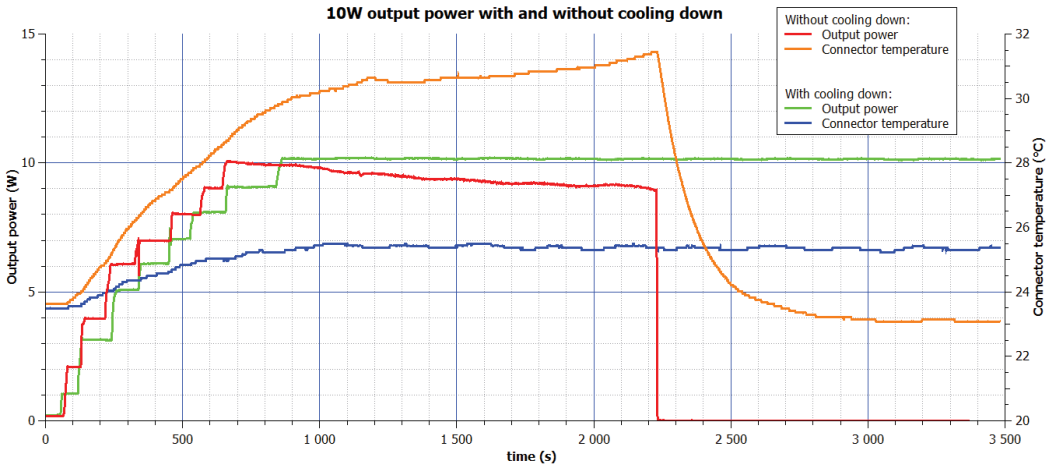

Figure 3.22: Monitor of the power (red) and the temperature (orange) of the first attempt of HP injection in the LMA-PM-15. Second attempt in green (power) and blue (temperature) with a cooling down system.

In order to cool down the connector we added a fan to increase the heat transfer with the surrounding air. We scaled up the power again and reach a stable injection for 10 W with almost no temperature increase in the connector (blue and green curve of the figure 3.22).

Using the same set-up than previously, we kept increasing the power until we reached 15 W and checked the stability over half an hour. The results are presented in figure 3.23. The temperature of the connector was 26.4°C. The statistics of the data gave us a mean of 15.11 W and a standard deviation of 0.01 over more than half an hour for the output power. This confirmed the stability of the coupling.

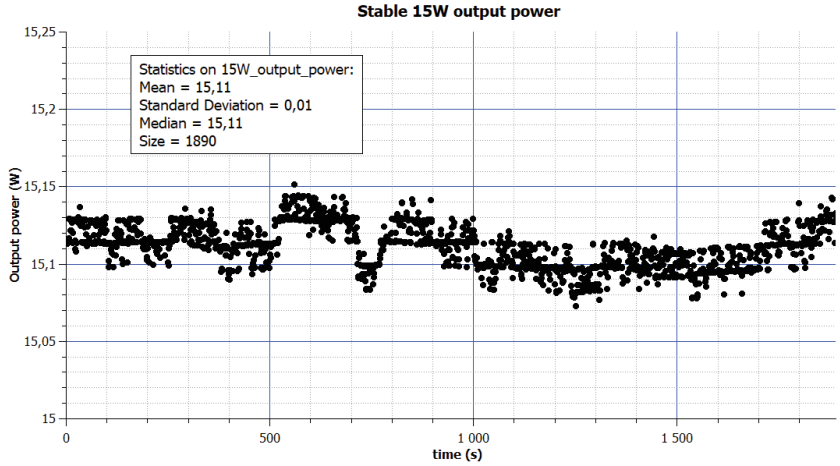

Figure 3.23: Stability of a power of 15 W at the output of the fiber over 30 minutes.

We kept increasing the power, up to 30 W at the output (see figure 3.24). At that point we also reached a temperature of 31°C, which was the point at which the temperature started to increase exponentially when there were no cooling down. We checked the stability over half an hour and did not see the exponential increase as before. However, we observed a very slow decrease in the output power.

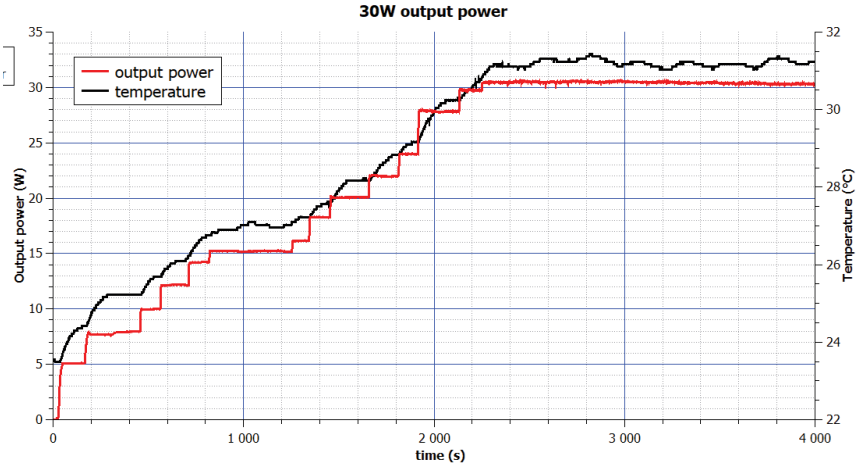

Figure 3.24: Monitor of the power (red) and the temperature of the connector (black) for 30W output power in the LMA-PM-15. Stability over more than 30min.

We did not push the test any further to avoid damaging the fiber. Moreover, we will see in the next section that this is the maximum amount of power that can be sent into this fiber with a single frequency laser because of the SBS effect. In the mean time, we have developed the water cooling system that we presented in figure 3.2 to try to increase the power even further without any temperature elevation. Moreover, while characterizing the EOM that we are presenting in the next chapter, we used the LMA-PM-15 in a similar set-up than this one and get 40 W output power (section 4.4.2). So the power at the input was about 50 W, the connector reached a temperature of 39°C and we did not observe any specific problems.

In table 3.4, we summed up the temperature elevation by Watt lost of the SMA905 connector for the different experiments that we presented in this section. Without any cooling down we have a temperature elevation of 6.23 °C/W which is close to the 7 °C/W that are given by the manufacturer (section 3.1.1). While cooling it down with the fan, it went down to 1.5-1.7 °C/W for low power. We can finally notice that for higher power this method becomes less efficient.

Output (W)	Input (W)	Mismatched (W)	Temp (°C)	Heating coeff (°C/W)
10	12.5	1.44	32	6.23
10	12.5	1.44	25.4	1.66
15.1	18.88	2.18	26.4	1.56
30.5	38.13	4.40	31.2	1.86
40	50	5.78	39	2.77

Table 3.4: Temperature elevation of SMA-905 connectors. The output power is computed using the global coupling of 80% while the mismatched power is obtained by using the 11.55% coefficient that we detailed previously. The initial temperature of the connector was 23°C. Inthe first case the connecor was not cooled down

3.2.5 Single frequency laser injection: investigation on the SBST

3.2.5.1 Injection on the fiber axis: 20W output power and measurement of the SBST

We saw in section 2.4.3 that in order to compute the SBST one has to know the acousto-optic effective area of the fiber. However, the analysis of the propagating acoustic waves is not easy to determine in practice and requires a complex finite elements method analysis. Thus in a first theoretical approach, we computed the SBST with the equation 2.33, using the peak gain value of the usual single mode step-index fiber (2.4×10^{-11} m/W) and by taking the effective area of the fiber equal to its optical effective area. $Aeff = \pi(MFD)^2/4$. Considering both the low attenuation and the small length of the fiber, the effective length was equal to the physical length, 5 meters. This gave us $P_{th} = 21.5W$ for a polarization factor b=1.

The high power laser that we used to do the experiments of the previous section does not have a bandwidth narrow enough to observe SBS and the most powerful narrow linewidth laser that we had at our disposal could not reach the needed 21.5 W. So we moved the experiment to the Albert Einstein Institute in Hannover. They provided us with 40 W from the spare Pre Stabilized Laser (PSL) from LIGO locked on a mode cleaner cavity. The linewidth was narrow enough ($\sim 1kHz$ over 100 ms) to have SBS and the power high enough to reach the SBST that we computed before. On figure 3.25, you can see the set-up used to characterize the fiber. The input power was set thanks to the Input Power Control (IPC) made of the first half waveplate and the Polarized Beam Splitter (PBS), it was monitored by the photodiode PD1. The second half waveplate was used to rotate the linear polarization at the input of the fiber. The photodiode PD2 was used to measured the counterpropagative light coming especially from SBS. Thanks to the angle of the end facet of the fiber, there is an angle difference between the light coming from SBS and the one backreflected on the interface. So the separation between the two is easy to do. Then, at the output of the 5 meters of fiber we were measuring the coupling thanks to the photodiode PD3 and the PER thanks to photodiodes PD4 and PD5. The coupling through the fiber was about 82%. In order to avoid any coupling losses due to the heating up of the connector we were cooling it down thanks to a water-based system similar to the one that we presented in section 3.1.2.

The initial temperature of 22.3°C reached a maximum of 30°C during the experiment. The 18% of losses can be decomposed as follow: reflection on collimator lenses (0.6%), reflection on the end facets of the fiber (6.7%), laser-fiber mismatch (9.55%), fiber attenuation (1.15%).

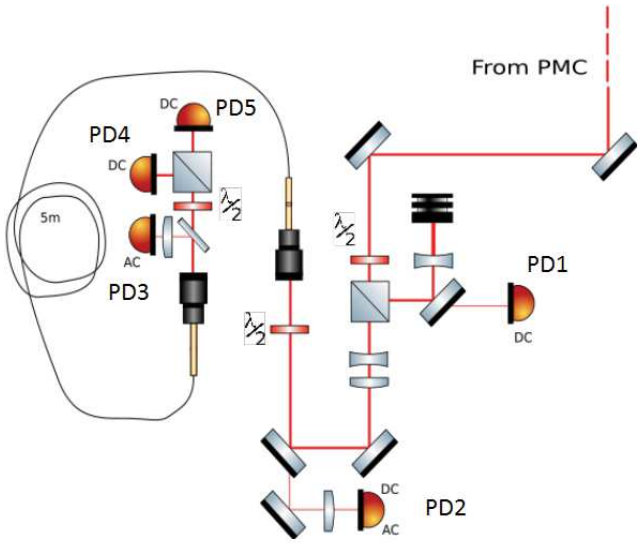

Figure 3.25: Scheme of the experiment used to characterize the SBS in the LMA-PM-15. Input power was monitored thanks to PD1, PD2 measured the power reflected by SBS, PD3 the output power, PD4 and PD5 were used to analyze the output polarization.

In a first experiment we measured the power backreflected by the fiber in order to highlight the SBS, the results are presented in figure 3.26. Because of the different losses that arise along the path we had to scale the input power by a factor of 0.868 to get the effective power participating in the SBS process. Similarly the measured SBS power has to be scaled by a factor 0.964 to get the effective back reflected power.

In our case, we set a value $\mu = 0.01$ for which 1% of the power is backreflected (see section 2.4.3.2). This is a reasonable value considering our requirement in term of power losses. The experimental results give us a $SBST_1$ of about 19.1W.(see figure 3.26). The theoretical expected one that we computed before has not been reached because it would require much more power but we can notice that for 21.5 W only 2.8% of the power is backreflected. This suggests that the actual SBST of this fiber is much larger, which is coherent with the case of enhance SBST in PCF fiber that we detailed in section 2.4.3.3.

We tested the stability of this coupling over 1000 s (figure 3.27). We can not take any clear conclusion with this measurement because of the relatively small amount of time but the coupling was relatively stable over that period.

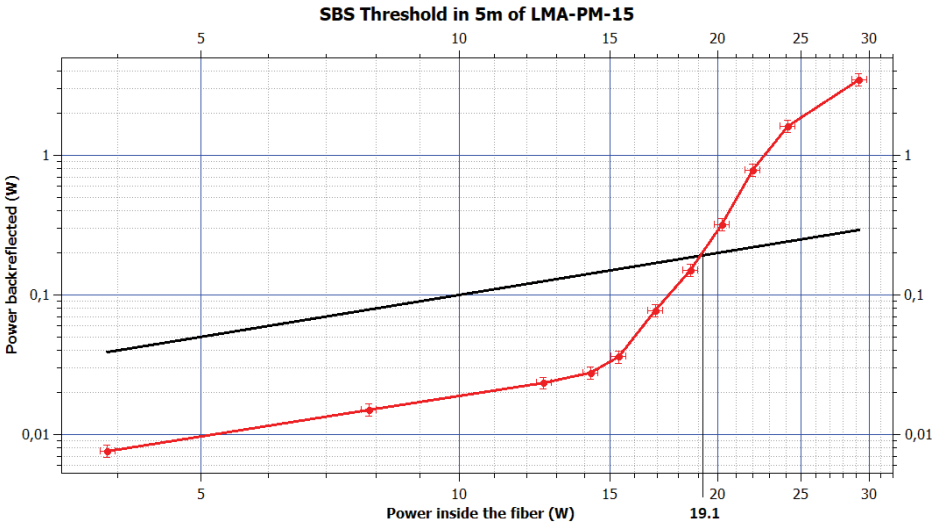

Figure 3.26: The experimental values are plotted in red. It is the amount of power in the Stokes wave back reflected from the LMA-PM-15 fiber by SBS. The black line has been plotted following the equation $P_R = \mu Pin$ for $\mu = 0.01$. The intersection of the two curves gives us a $SBST_1$ of 19.1 W

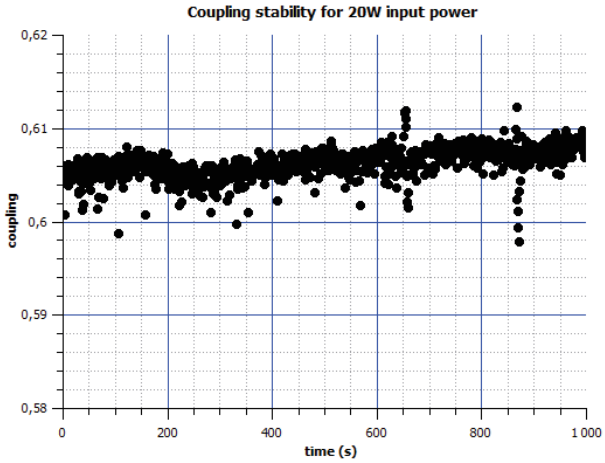

Figure 3.27: Stability of the coupling for 20 W output power in the LMA-PM-15. The input power was about 34 W with an initial coupling of 82% but 7 W were reflected by SBS.

3.2.5.2 Injection out of the fiber axis: 28W output power and measure of the SBST

With the same set-up than before, we characterized the influence of the polarization factor b that appear in the equation of the SBST 2.33. As we saw in section 2.4.3.2, by setting the linear polarization between the two axes, one should get a polarization factor of 2 and double the SBST. To do that, we rotated the polarization at the entrance of the fiber at 45° from the main axes (figure 3.28). Due to the birefringence of the fiber, the electric field is splitted into two components that are propagating on both the fast and the slow axis at a different velocity. Each component is experiencing its own Brillouin scattering and has a threshold equal to the SBST that we computed before. So the effective SBST of the fiber for this polarization state should be twice the one that we had while setting the polarization on a main axis. The results of the experience confirmed this doubling in the SBST as you can see on figure 3.28. We did not have enough power available to get to the theoretical SBST of 43 W but the behavior of the curves let clearly appear the doubling of the SBST.

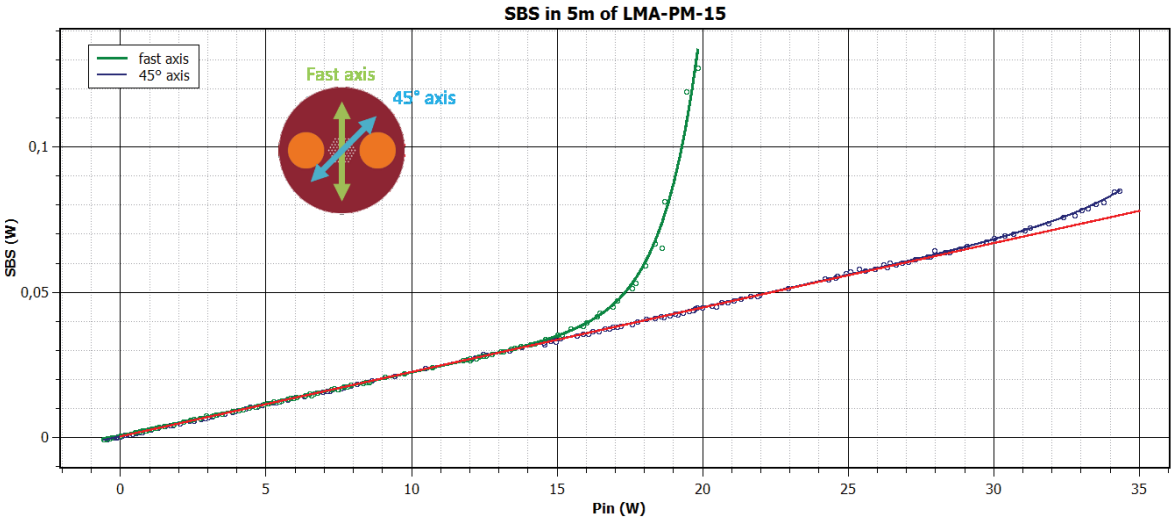

Figure 3.28: Power of the Stokes wave back reflected by SBS function of the input power. It has been plotted for two different states of polarization, in green when the polarization was set on the main axis of he fiber, in blue when the polarization was set at 45° from the main axes. While setting the polarization between the two axis the SBST is doubled.

However, as we saw in section 2.2.3.2, by setting the polarization between the two axis, the fiber becomes much more sensitive to all kind of mechanical stress. Thanks to a half waveplate and quarter waveplate it is however possible to get back to the PER of 18 dB that is specified in the datasheet of the fiber. Thanks to the relative mechanical stability of the fiber, the variation of the output polarization were quite low over the short time of the experiment (few minutes). However while heating up the fiber, as expected, the output polarization was varying a lot (see figure 3.29).

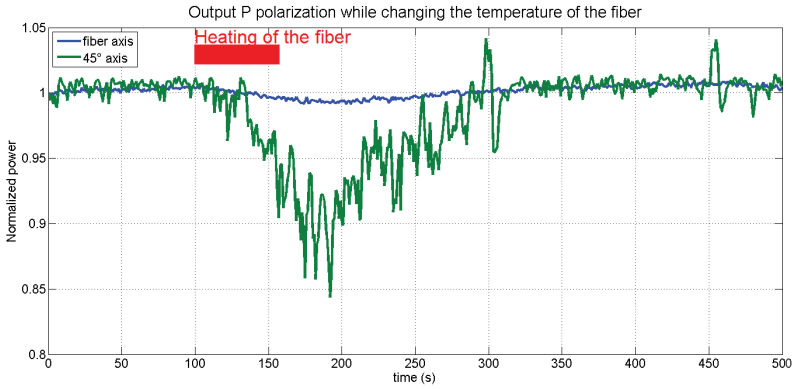

Figure 3.29: Normalized monitor of the P-polarization at the output of the fiber. Started from a stable state we heated the fiber and observed the influence on the output polarization. While set between the two main axis the output polarization is very sensitive to external constraints.

We summarized the results in table 3.5. However, one should keep in mind that in the second case the output power is much more noisy and the output polarization is very sensitive to external perturbations.

	Fast axis	45° axis
Theoretical SBST	21.5 W	43 W
Measured SBST	19.1 W	>30.4 W

Table 3.5: Comparison of two polarization configurations at the input of the fiber

3.2.5.3 Detection of the SBST looking at the power fluctuation in the MHz-range

In order to detect the appearance of SBS one can measure the power that is back reflected and determine when it reaches the SBST (eq 2.33). However, a simple and more efficient way to detect it, is to look at the power noise in the MHz-range. Indeed it has been seen that in active fibers there is a sudden increase of the power noise when the stimulated process starts [83]. Thanks to the same optical setup than before (figure 3.25), we analyzed the power fluctuations at the output of the fiber with a spectrometer connected to the AC output port of the photodiode. The measurements are presented in figure 3.30, we confirmed that this high frequency noise is appearing also in passive fiber .

This noise was present both in the reflected power and in the transmitted one. However while the SBS is starting, the DC power is much less important in the backreflected power

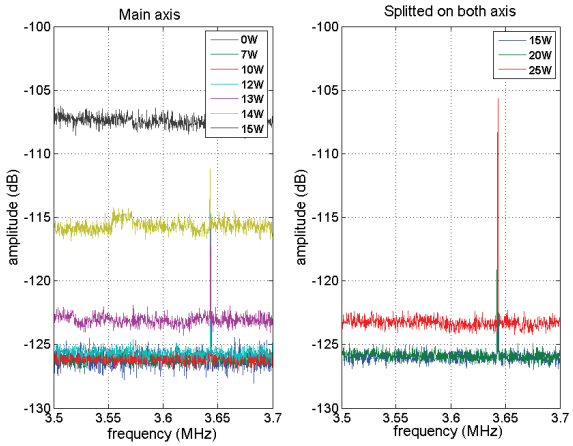

Figure 3.30: Power noise in the MHz range of the Stokes wave reflected by Brillouin Scattering in 5m of LMA-PM-15 fiber with a linear polarization set on a main axis (left) and at 45° from the main axes (right) for different input power. When the process becomes stimulated (see the measure done figure 3.28), an increase in the power noise can be noticed. The peak that can be seen was due to an electronic environmental noise.

than in the transmitted one, this leads to a better SNR in the backreflected. So by demodulating the power reflected by Brillouin scattering at a certain frequency in the MHz-range one can stop increasing the input power before it could get to the point where SBS exponentially increases and when the output power becomes more noisy.

3.3 LMA-PM-40-FUD

The LMA-PM-40-FUD is a PCF fiber from NKT Photonics having a core diameter of 40 µm . It is not polarization maintaining but a polarizing fiber, which means that only one polarization is propagating into it. Contrary to the LMA-PM-15 that we presented in the previous section, it is not yet commercially available. In this section, we are presenting the results of the experiments that we conducted in order to confirm its ability to transport a high power single frequency laser beam.

3.3.1 Description and characteristics

The main characteristics of the fiber as they are given in the datasheet are presented in table 3.6, its structure can be seen on the picture of its cross section on figure 3.31. Since the fiber is still under development the manufacturer did not give any details on the values of the capillaries diameter d and the pitch Λ of the structure but it is said to be single mode at 1064 nm. Moreover, we can see on the picture that it has the usual hexagonal structure and that there are the two rods of constraints that insure its polarizing effect.

Optical properties	
MFD @ 1060 nm ($1/e^2$)	$\sim$ 32 µm
NA @ 1060 nm (5%)	not provided
Birefringence Δn @ 1060 nm	$\sim 1.6 \times 10^{-4}$
Polarization properties	Polarizing
Recommanded coil diameter	$\geq$ 34 cm
Mechanical properties	
Core diameter	40 µm
Outer cladding diameter	450 µm
Coating diameter	540 µm
Core material	F doped silica
Cladding material	Pure silica
Coating material	High temperature acrylate

Table 3.6: Main characteristics of the LMA-PM-40-FUD fiber from NKT Photonics as given in the datasheet

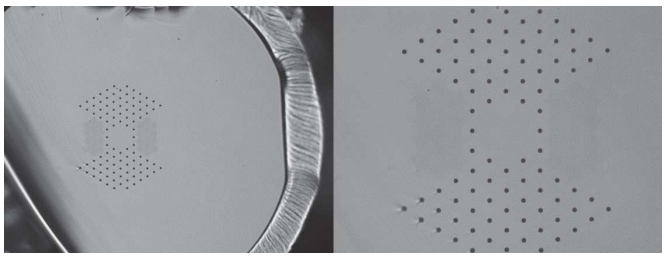

Figure 3.31: Structure of the LMA-PM-40-FUD as presented in the datasheet furnished by NKT photonics. We can see the usual hexagonal pattern of PCF fibers as well as the two constraints that ensure the polarizing properties of the fiber.

First we ordered 10 meters of this fiber to be able to carry out experiments on the SBST without having to increase the power above the values where SBS is not the main problem anymore. We make this piece of fiber connectorized with the high power connectors SMA-6 from Alphanov that are presented in figure 3.1 and AR-coated with the same coating than the one presented in section 3.1.3. The first version was also protected with a metallic jacket in order to reduce the influence of the external perturbations. However, as expected for PCF with such a large core, it is very sensitive to bending, and it appeared that the jacket was actually introducing mechanical constraints on the fiber. These constraints were avoiding the light from propagating properly and made the fiber very sensitive to all external mechanical stress. This issue came from the fact that when being coiled, there is a difference between the inner diameter of the jacket and the outer one. Over 10 meters, this difference of length constraints the fiber inside the jacket when it is deployed. Speaking with the manufacturers we decided to remove the metallic protection in order to be able uncoil the fiber and having the needed liberty on its path.

After having validated some characteristics of the fiber with the 10m-patchcord we ordered two other patchcords of 1.5 meter. These two are indeed much easier to handle to carry out experiments and have a theoretical SBST at 1064 nm above 200 W. They have been connectorized and AR-coated like the other one. In the next section, we are detailing the experiments that we have done to confirm the behavior of the fiber and validate its ability to transport a high power single frequency beam. For each experiment, we precise if we were using either the 10 meters patchcord or the 1.5 meter ones.

3.3.2 Output beam characterization

In this part we analyzed in details the characteristics of the output beam of the LMA-PM-40-FUD fiber. The first test that we did was to look at the beam profile directly at the output of the fiber thanks to a camera. In this case we can consider that we were in a far field condition. The results are presented in figure 3.32. The beam looks perfectly Gaussian, however while taking an overexposed picture of the output beam (figure 3.33) one can notice that light is also propagating into the structure of the fiber.

So in a second experiment we imaged the fiber end thanks to the home made collimators that we presented in section 3.1.2 and analyzed it thanks to a CCD camera, a beam scan and a analyzing optical cavity. The scheme of the set-up is presented in figure 3.34. The details of this set-up can be found in section 3.2.2, where it has also been used to characterized the LMA-PM-15. The fiber that we used was a 1.5 meter long patchcord.

The first point that we investigated was to measure the beam width along the path of the beam in order to determine the waist size and position as well as the associated M^2. Considering the asymmetry of the beam regarding the horizontal/vertical axes, we tilted the beam scan by an angle of 30° in order to be on the axis of the structure of the fiber. The results of this measure are presented in figure 3.35. Despite the relatively strange behavior in the waist region, the regression gave us a M^2=1 along the Y-axis while it was of M^2=1.11 along the X-axis which corresponds to the axis where the light spots of the structure have

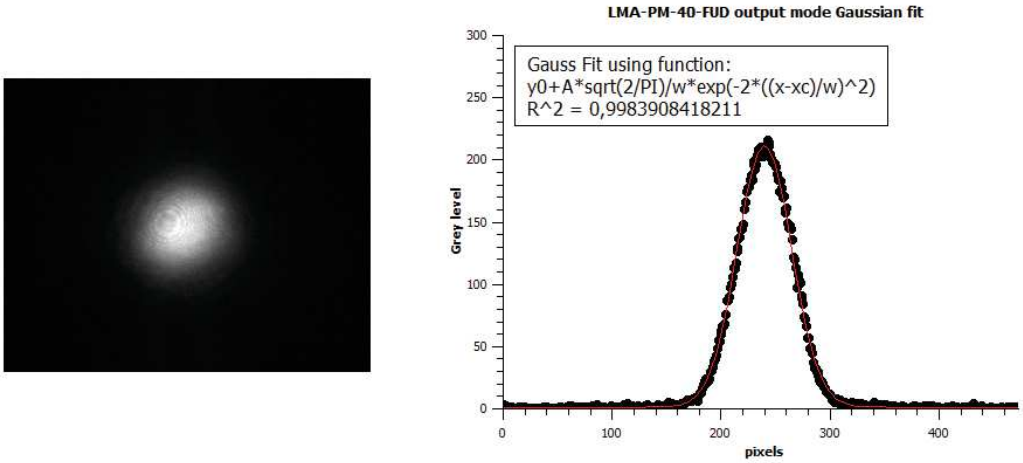

Figure 3.32: LMA-PM-40-FUD output mode. The interferences that can be seen are due to a window in front of the sensor of the camera that does not have AR coating for 1064 nm. The Gaussian fit has been done on the grey level of the pixels of a diameter of the spot

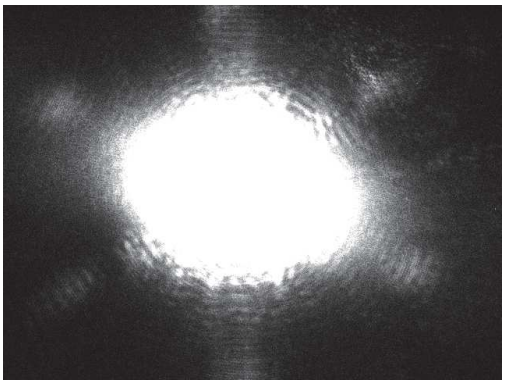

Figure 3.33: Overexposed picture of the LMA-PM-40-FUD output mode that makes appear light in the structure

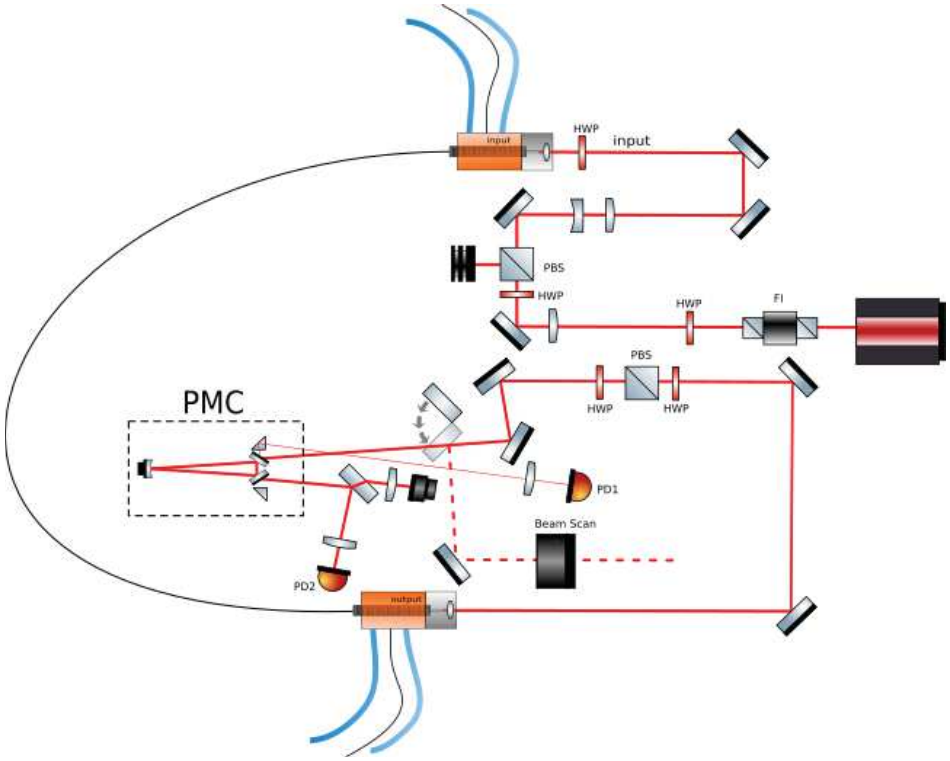

Figure 3.34: Scheme of the setup used to characterized the output mode of the LMA-PM-40-FUD

been observed before. By doing a Zemax simulation using the lens of the collimator and the values of the regression that has been found, we were able to get back to the MFD of the fiber. We get a waist $w_{0X} = 15.1 \pm 0.1$ µm and $w_{0Y} = 14.1 \pm 0.1$ µm. The apparent astigmatism of the fiber as well as the greater M^2 in the X direction can be explained by the light propagating into the structure of the fiber.

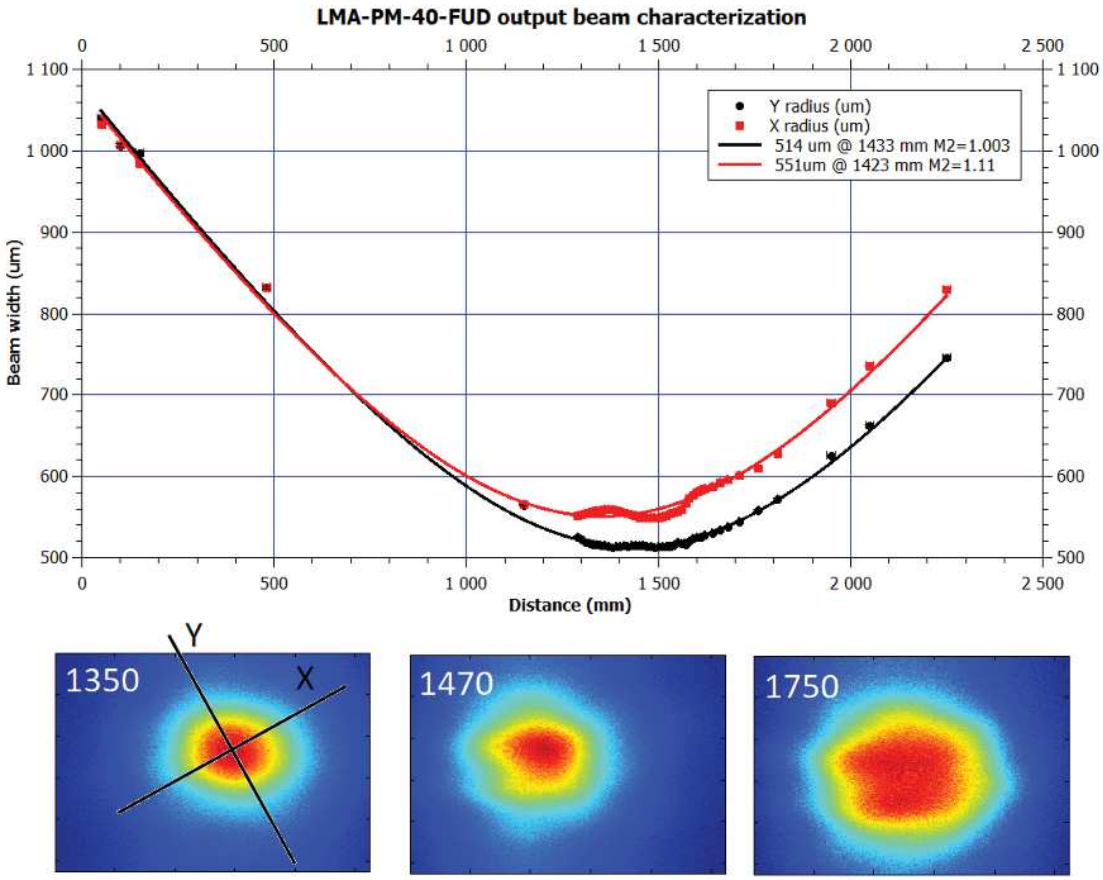

Figure 3.35: Measured beam width at the output of the LMA-PM-15, collimated with an aspheric lens having a focal length of 40 mm. The fit is done using the propagation equation of a Gaussian beam (eq 2.12. On the bottom part of the figure one can see the actual shape of the beam taken at three different distance. The hexagonal structure of the fiber can be recognized.

The second point that we investigated was the actual mode content of the fiber, that would especially be caused by that light propagating into the structure. To measure this HOM content we used the cavity that can be seen on the scheme of the set-up (figure 3.34) and whose characteristics have been detailed in section 3.2.2. By doing a Zemax simulation

of the coupling between the cavity and the beam previously measured we get a miscoupling of 0.54%. The results of the scan of an FSR can be seen on figure 3.36.

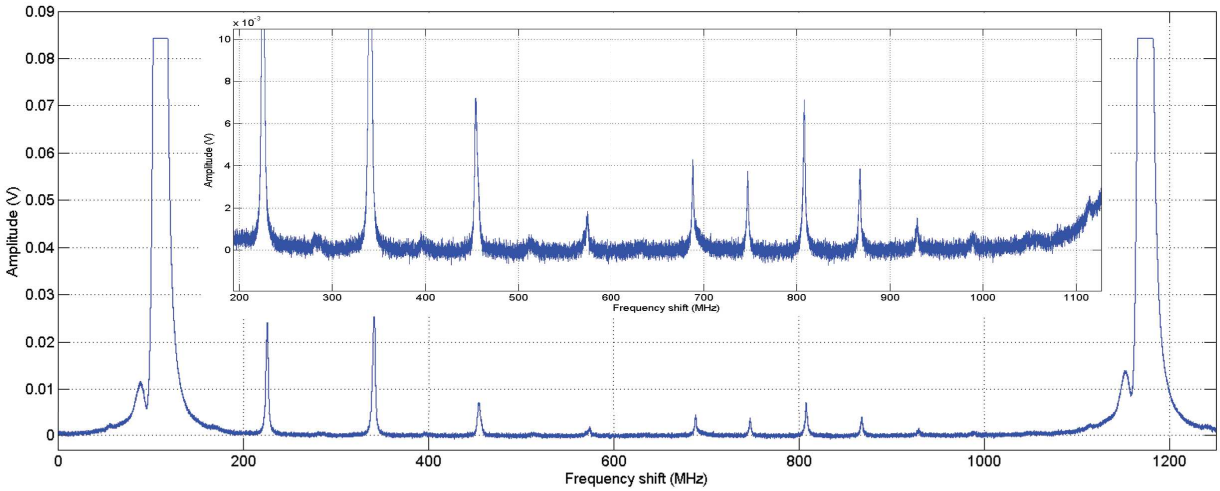

Figure 3.36: Scan of the cavity over one FSR in order to get the HOM content of the LMA-PM-40-FUD. The peak that can be seen just before the TEM_{00} is not an HOM but is actually due to the saturation of the oscilloscope.

We found a total amount of power in the HOM of 87.6±0.56 mV for a TEM_{00} that has been measured at 2.92±0.005 V. This results in an HOM content of 2.91±0.66%. By subtracting the mismatch that we have computed thanks to Zemax we have 2.47±0.66% of HOM for the LMA-PM-40-FUD. The error bars have been set by taking the standard deviation of the electronic noise of the measurements.

3.3.3 Effects of mechanical constraints, sensibility to the twist

We already mentioned in section 3.3.1 that the fiber was sensitive to mechanical constraints. In this section we are presenting our investigations on the effects of the mechanical constraints on the fiber.

In a first approach we did not carry out any quantitative tests. Qualitatively, we observed that the fiber rods inside the fiber introduce a pre-stress in the fiber that makes it quite rigid and difficult to handle. If let free, the fiber will come back to its initial unstress state. This makes it sensitive to the bending when it is applied out of the rods plane. On the contrary, the fiber did not exhibit any strong dependence on the bending radius when it was applied in the rods plane. However in order to avoid any damages, we did not bend it to radius of curvature smaller than the one given in the datasheet (34 cm).

It appeared that the most critical point of this fiber is actually the twist along its propagation axis. In the experiment that we are presenting here we investigated its influence. To do

so, we set the input connector such as the propagation axis of the fiber was in the horizontal plan, made sure that there were no initial twist, and then rotate the output connector. The results are presented in figure 3.37. The input power was set at 30 mW and we were using a 1.5m-long patchcord. During the investigation we also took a look at the evolution of the beam profile for different angle of rotation. Some of the pictures are presented on the graphic.

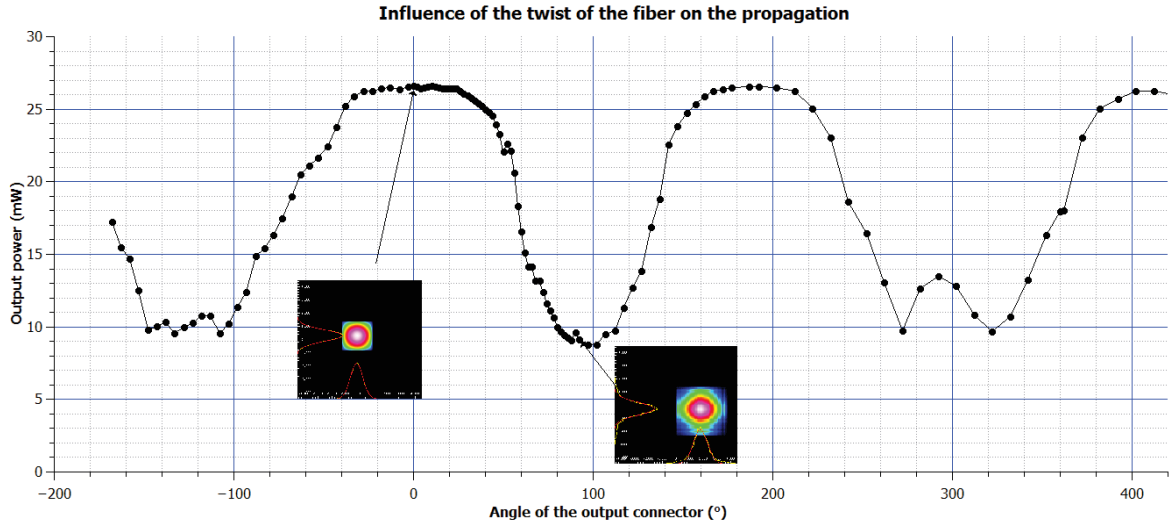

Figure 3.37: Influence of the twist of the fiber on the output power and output beam. The input power was 30 mW and the untwisted state was set to 0°

We observed that there is a range of about 20° around the untwisted state where the fiber is behaving normally. Then the output power is going down to a non-zero value but the analysis of the output beam confirmed that even if there is some power at the output, the spatial mode was deteriorated and the fiber was not working properly. Around 190° the fiber was then going back to a value close to the maximum. Even if this increase is not explained, one could have expect a 180° symmetry. But this shift seemed to be confirmed by a third maximum that was obtained around 410°. There was also a strange behavior also around 300°. We conducted the same experiment with the 10m-long patchcord that was coiled on the bench. We found back a maximum for the untwisted state and some other local maxima, but the behavior of the fiber between those states was pretty chaotic. Moreover except from the maximum of the untwisted state, the behavior of the fiber was not repeatable.

These observations are still not explained but what has to be retained from these experiments is that, while deploying the fiber, one has to be careful to not twist it. The untwisted state is easy to find since the fiber naturally goes back to it when it is let free.

3.3.4 Polarizing effect

In this section we will detail the polarizing effect of the LMA-PM-40-FUD. The theory of polarizing fiber is explain in section 2.2.3.2, the fiber is actually behaving as a polarizer. The scheme of the set-up used to test these characteristics is similar to the one presented in figure 3.39. In the first part of the set-up the beam is shaped and aligned in order to maximize the coupling in the fiber. A pick-off gives us the input power, the rotation of the linear polarization is made possible thanks to the half waveplate placed in front of the fiber. We were using a 1.5m-long patchcord and for both connectors, the propagation axis was placed in the vertical plane by making sure that the fiber was not twisted. We measured the content in S and P polarization at the output for both S and P polarization at the input. The input power was set at 30 mW with a polarization quality of 30 dB. The coupling of about 85 % gives us an output power of 25.66 mW. The results are presented in the table 3.7.

input polarization	Output S	Output P
$\parallel$ to the propagation axis	25.4	0.20
$\perp$ to the propagation axis	0.31	0.20

Table 3.7: Polarizing effect of the LMA-PM-40-FUD fiber from NKT Photonics. Power are given in mW for 30mW at the input with a coupling of about 85%

Thanks to these values we can compute the usual characteristics of the polarizers. We get T_S = **85%** , mainly limited by the coupling itself, T_P = **0.7%** and the **PER** = -10log(0.2/25.4) = **21 dB**. Another effect to be noticed is that because of the guiding properties of the fiber there is also about 1% of S polarization transmitted even while launching the light on the wrong axis.

The deployment of a polarizing fiber influences a lot its performance. Indeed, in theory, while coiling it, one could increase the PER of the fiber thanks to both higher losses on the fast axis and higher attenuation for the HOM. That is why we performed another test, similar to the previous one but with the 10m-patchcord that was coiled on a reel whose diameter is 34 cm (set-up figure 3.38). The input power was also higher, about 500 mW. We found that the PER was 20 dB which is slightly less than what we found for the 1.5m-patchcord uncoiled. So there was no particular improvement.

In conclusion there are two main points to remember from these experiments. First, when launching the light into the fiber on the main axis of the fiber, the actual PER at the output slightly depends on the deployment of the fiber and one could try to find an optimum. However in our application, this is not a degree of freedom that we have and it would not make sense to coil a fiber used to transport light. So the exact PER has to be measured and optimized in the final set-up, once the fiber is deployed. The second point is that there is no need to have a PER greater than 21 dB at the input of the fiber, since the polarization quality will be deteriorated anyway. However one has to be aware that the amount of power that is not polarized along the slow axis of the fiber will participate to the heating of the

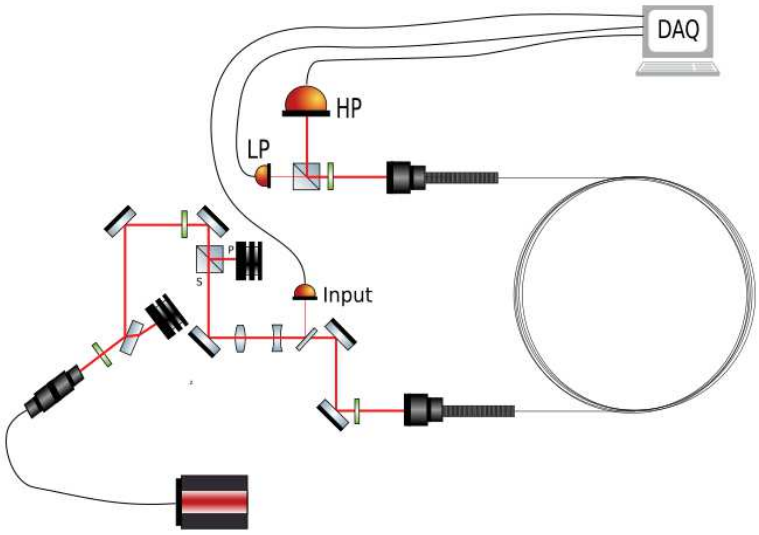

Figure 3.38: Scheme of the set-up used to characterize the polarizing effect of the 10m-long LMA-PM-40-FUD fiber. The input power was set to 500 mW with a coupling of 70%, the polarization was rotated at the input of the fiber thanks to a HWP. We were monitoring the input power, and both S and P polarization at the output

fiber. These considerations are of particular interest in the case of the Faraday Isolator that we will present in the chapter 5.

3.3.5 5W single frequency laser injection and long term stability

Using the set-up presented in figure 3.39, we performed a test on the stability of the properties of the fiber over 7 hours. In order to have access to the daily fluctuation it would have been interesting to extend the test to a period of 24h but we did not have any safety optical shutter in case of dysfunction while being away. The seed laser was power stabilized and the amplifier (boostik [106]), was delivering a single frequency power up to 5.2 W. We were monitoring the input power as well as the two polarization at the output. The fiber used was a 1.5m-long patchord. It was AR coated and we reached a coupling greater than 87.43±0.22%. In a same way that we did for the LMA-PM-15 in section 3.2.3, we are investigating hereafter the possible reasons for the 13% losses that are observed here.

The coating on the lenses of the collimator and on the end facets of the fibers introduce respectively 0.6±0.1% and 0.38±0.07%. The HOM mode content of the fiber has been measured in section 3.3.2: 2.44±0.54%. We did a Zemax simulation of the telescope that was used and maximized the coupling into the fiber for different positions of the lens of the collimator (procedure detailed in section 3.2.3). We found a mismatching of 2.44±0.86%. Finally the last known contribution for the losses is the polarizing effect of the fiber. Knowing that the polarization quality was 30dB and by considering that it has been set with a

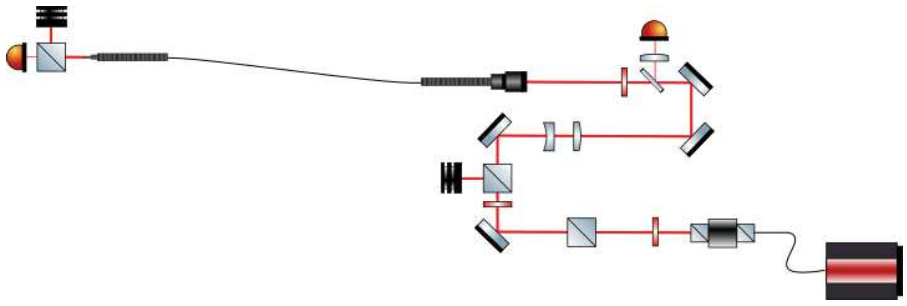

Figure 3.39: Set-up used to test the long term stability of the LMA-PM-40-FUD with 5W injected with a coupling of 87.4% over 7 hours.

precision of $\pm 1°$, it introduces 0.12% of losses. The results are summarize in table 3.8.

Mode Matching	2.44 %	± 0.54
Reflections end caps	0.38 %	± 0.07
Reflections collimators lenses	0.60 %	± 0.10
HOM fiber	2.47 %	± 0.66
Polarization	0.12	± 0.02
Total	**6.01 %**	± 0.86

Table 3.8: Known contributions to the coupling losses in the LMA-PM-40-FUD

So with losses of 6.01% and a coupling of 87.43% there are still 6.56% of the input power that is missing. Some of this power may come from the spatial beam quality of the laser beam that is used to inject into the fiber, since we were only considering its astigmatism to do the Zemax simulation. But most of it may come from the attenuation of the fiber that is not given by the manufacturer. A further experiment that we will carry out will be to estimate it by perfectly measuring the know losses (in particular the mismatch) and see the coupling difference between the 10 meter long patchcord and one of 1.5 meter.

On figure 3.40, we plotted the temporal evolution of the coupling. With this set of data we get an average coupling of 87.43% with a standard deviation of 0.22. The stability was even higher in the second part of the experiment when there were less activities in the laboratory.

3.3.6 40W single frequency laser injection and investigation on the SBST

In the experiment that we are describing hereafter we were investigating the SBST in the 10 m patchcord of LMA-PM-40-FUD. The difficulties of this measurement are coming from the high power needed to reach the threshold. As we did for the LMA-PM-15 (see section

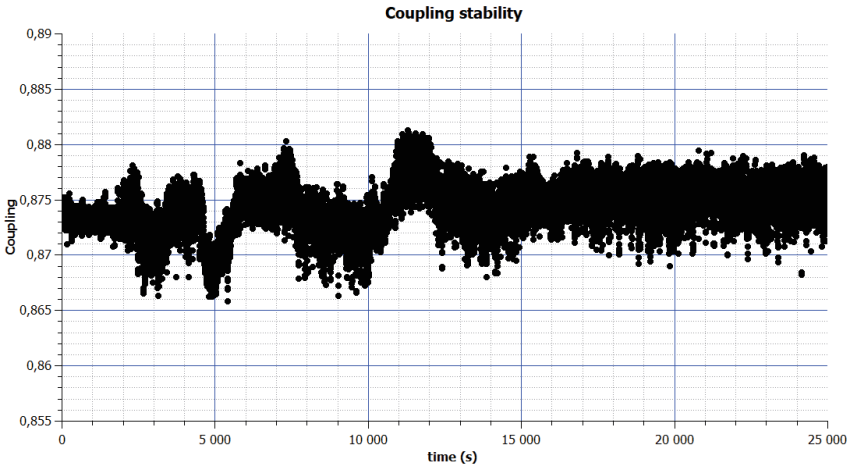

Figure 3.40: Coupling stability of the LMA-PM-40-FUD over 7 hours. The figure on the top is giving the temporal evolution. The figure in the middle is a Gaussian fit done on the data. The figure on the bottom shows the normalized spectral power density of both the input and the output signal

3.2.5), we computed the theoretical SBST using the formula 2.33 given previously. The acousto-optic effective area was taken equal to the optical effective area ($7 \times 10^{-10} m^2$), considering the relatively small length of the fiber the effective length was taken equal to the physical length of the fiber (10 m), and the peak Brillouin gain equal to the usual one used in silica step-index fibers (2.4×10^{-11} m/W). Moreover given that only one polarization is propagating into this fiber, we have a polarization coefficient $b = 1$. With these parameters the numerical evaluation of the theoretical SBST is about 62.3 W.

Initially we did not have at our disposal in the laboratory any single frequency laser with a power high enough to carry out that test. The laser that we had was indeed a laser amplifier *Koheras Boostik* from NKT photonics [106] seeded by the Koheras Adjustik laser also from NKT photonics [111]. This system is totally fibered and give us a single frequency laser power with power up to 5W. Then we get a laser amplifier from Neolase [37], and we seeded it with the 5 W of the adjustik/boostik system. This gave us 42 W at the output of the laser but among these 42 W, 5 W are lost along the set-up presented in figure 3.41 and so only 37 W are available at the input of the fiber. This is too low to reach the SBST that we computed before. However, if we do the analogy with the experiment that we conducted to measure the SBST for the LMA-PM-15 (section 3.2.5), there is a factor of 5.46 between the effective areas of the fibers (by taking 6.25 µm for the LMA-PM-15 and an average waist 14.6 µm for the LMA-PM-40-FUD). There is a factor 2 on the effective length of the fiber (5 meters for the LMA-PM-15 with respect to the 10 meters of the LMA-PM-40-FUD). This finally leads to a factor of 2.73 for the measured SBST. For the LMA-PM-15, it has been measured at 19.1 W for μ =0.01. So in this approximation the SBST of the LMA-PM-40-FUD for μ=0.01 could be of the order of 52.1 W. This still seems to be too high to be measured, but by taking a look at the results for the LMA-PM-15 (figure 3.26), one can see

the effects of the stimulated process can be seen before reaching the SBST, around 14 W. If we keep the previous parallel between the two fibers, we could expect to see some effects around 38.2 W.

We installed a set-up anyway to investigate the high power injection into the fiber and were monitoring the backreflected light coming from the fiber. This set-up is described in figure 3.41, 5W are coming from the Koheras boostik laser amplifier, a telescope is adjusting the size of the beam in order to match the one required inside the amplifier, and another is reshaping it to increase the size of the waist and thus avoiding a too big divergence. 42 W are at the output of the amplifier, and the power in the whole set-up can be set thanks to PBS1 associated with the half waveplate. The flip mirror is used to choose to inject either by the input or the output port of the fiber. Indeed considering the difficulties while injecting into a fiber this gave us the possibility to always keep an alignment at the input by roughly injecting light by the output port. Thus we were able to work on the input port and especially on the characterization of the settings of the home made collimator (presented in section 3.1.2. Then we set up a Faraday Isolator in order to avoid any back reflection, and especially the one coming from SBS, to be reinjected into the amplifier. The crystal used in the Faraday Rotator has a relatively high absorption and while working at high power there is thermal lensing effect that arise (see section 5.2.4). Thus in order to avoid any miscoupling into the fiber arising from this effect we were always working with the maximum power inside the FI. This power was then set to the desirable value thanks to a second IPC formed by the half waveplate and PBS3. PBS4 was used to clean the polarization at the output of the IPC, we will see its importance hereafter. The waist of the beam was then set to theoretical desire value thanks to a telescope. The lens were in fused silica and are not subject of noticeable thermal lensing. A set of three mirror was then used to perfectly aligned the beam on the core of the fiber. Through second mirror about 0.2% of the power is transmitted. This allow us to get pick-offs to both monitor the input power that was send into the fiber (PD1) and the power that was backscattered by the fiber (PD2). Finally we put a half waveplate in front of the collimator to perfectly align the linear polarization on the axis of the fiber. We were measuring the power at the output of the fiber thanks to a high power calorimeter. Given that it has a quite low time response we were also monitoring it in a more qualitative but rapid way by imaging the light that was diffused from the calorimeter on a low power powermeter.

We set up everything at relatively low power (300 mW), get a coupling of about 80%. It is not easy to state where the losses are coming from as we did in the previous section. Indeed there are many unknowns such as the HOM content of the beam at the output of the amplifier that decrease the matching into the fiber, the attenuation of the 10 meters of fiber, the actual reflectivity of the damaged end facets. With this coupling we started to increase the power step by step (figure 3.42). The coupling was slightly decreasing without any temperature increase. While reaching 27 W at the input, we had about 17 W at the output. About 10 W were lost in the connector, the coupling brutally dropped without any noticeable temperature increase of the connector. We stopped everything and tried to carefully increased the power again. The coupling start to drop again but around 20 W at the input. Speaking with the manufacturers of the connectors they confirm that the mode

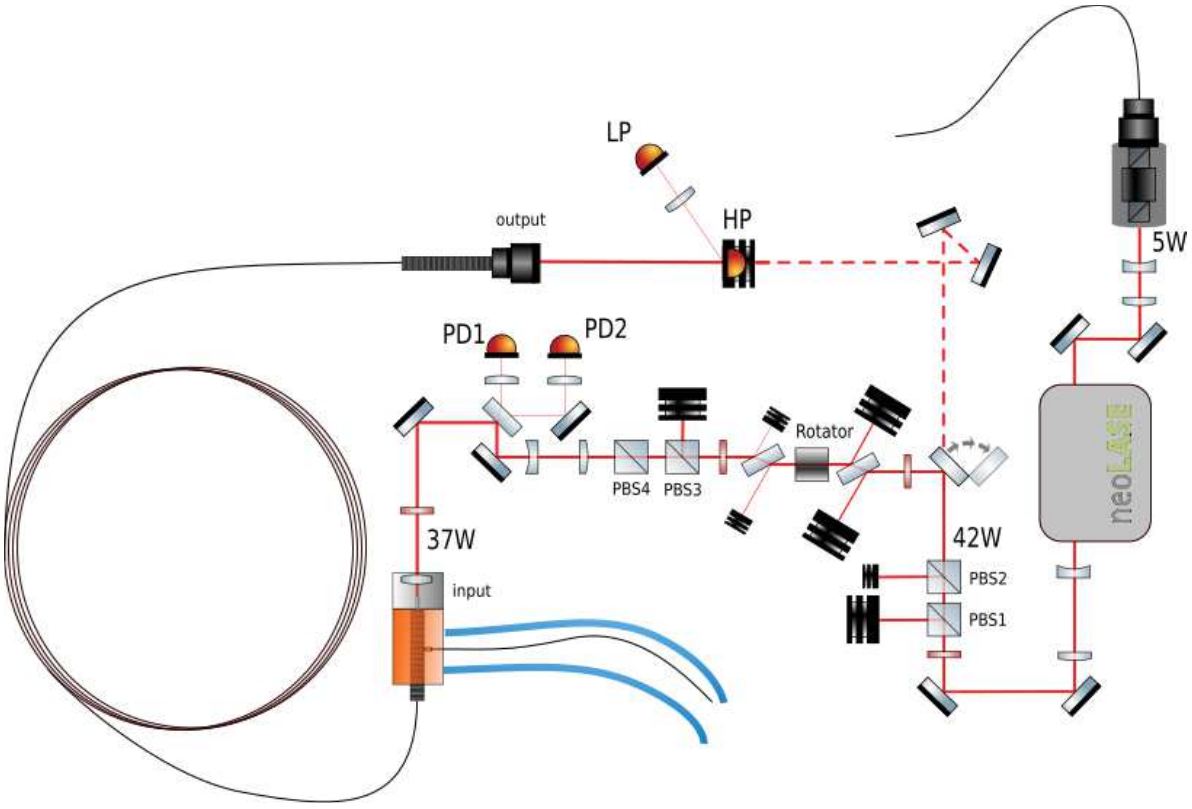

Figure 3.41: Scheme of the set-up used to measure the SBST in the LMA-PM-40-FUD. 5 W from a first laser are amplified through a second amplifier to get 42 W. The power was set thanks to the PBS1 and PBS3. The flip mirror was used to have a low power injection through the output collimator in order to keep a reference while working on the input collimator. The input power is monitored by PD1, the backreflected light by PD2 and the output power by HP and LP.

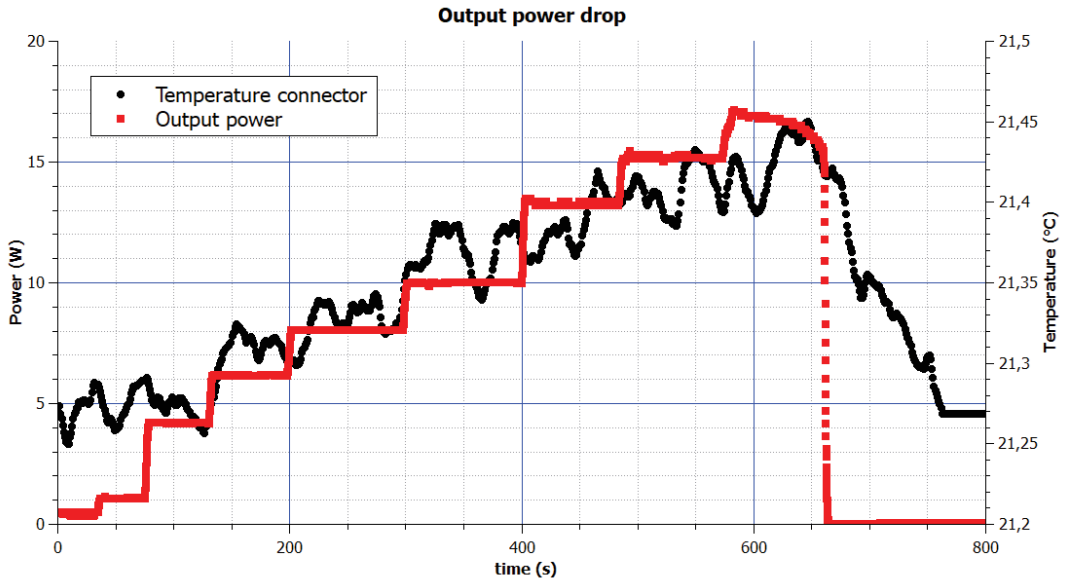

Figure 3.42: Increase of the power in the LMA-PM-40-FUD. The output power suddenly decrease without any temperature increase.

stripper of the connector was probably damaged, and that this can happen even before seeing any heating up of the connector.

In parallel, the results of our investigation on the slow decrease of the coupling brought us to the conclusion that it was a problem of polarization. We had not placed the PBS4 to clean the polarization at the output of the IPC and it appeared that the relatively bad quality of polarization after the IPC used in extinction was leading to a mistunning of the axis of the half waveplate. We placed the PBS4 to solve this problem, and since the input connector was damaged we reverse the fiber and placed the output connector at the input. The coupling was a bit less efficient (about 70%) but was not decreasing anymore while increasing the power. The results of this experiment are presented in figure 3.43. The 37 W available at the input of the fiber, with a coupling of 70%, led to a maximum of 26 W at the output of the fiber.

As predicted by the theoretical value of the SBST the power available is not enough to clearly see any SBS. However, we fitted the data points with a linear function and the two last points are clearly above the linear fit. The SNR is not enough to draw any conclusion but it can be seen as the beginning of the process. In order to confirm it, it would be necessary to have a single frequency laser which would allow us to increase the power even further. An other solution that we are considering is to buy a 20m-long patchcord in order to decrease the SBST, measure it and validate that we could reach 200 W in the 1.5m-long patchcord without having to deal with SBS. In the mean time, thanks to this experiment, we already set a lower value for the SBST in 10 meters of fiber and confirm its ability to transport at least 26 W from a single frequency laser.

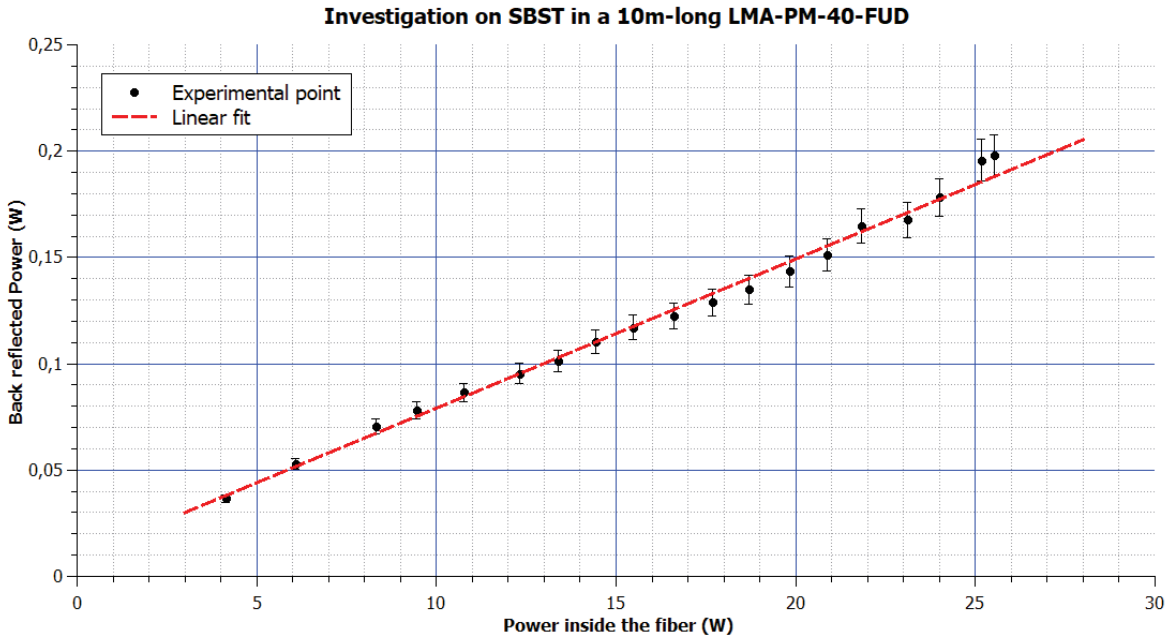

Figure 3.43: Power back reflected from the LMA-PM-40-FUD function of the power inside the fiber in order to see some SBS. The power could not be increase further due to the limited input power available.

3.4 Conclusion

Through the experiments we have been describing in this chapter, we improved our experience in coupling into fibers and managing high power densities. We presented some of these solutions in a first time, however we still have some problems, especially with the AR coating on the end facets of the fibers. New solutions are still under investigation in order to increase the power even further. Despite these problems we managed to carry out some experiments on two fibers: the LMA-PM-15 and the LMA-PM-40-FUD from NKT photonics. This last one is still under development and was particularly difficult to set up. You can find a summary of the interesting characteristics of those fibers in table 3.9.

The 5m-long LMA-PM-15 was used with power as high as 50 W with a broadband laser and was limited to 20 W output power with a single frequency laser due to SBS effect. We reached 28 W by setting the polarization between the two axis and could in theory increase it till 40 W but in that case the output power becomes more noisy and the output polarization becomes very sensitive to external perturbations. The 10m-long LMA-PM-40-FUD has been tested with a single frequency laser up to 37 W at the input and did not exhibit any SBS effects.

In parallel we are investigating the possibilities of using different fibers. A promising idea would be to use a hollow core fiber. Indeed, due to the absence of interaction between light

Fiber	LMA-PM-15	LMA-PM-40-FUD
HOM content	1.98±0.51%	2.47±0.66%
Maximum coupling without coating	89%	81%
Maximum coupling with coating	92.5%	87%
Maximum injected power	50 W	37 W
Maximum single frequency output power	20 W	26 W
Theoretical SBST at 50%	21.5 W	62.3 W
SBST at 1%	95.5 W.m	$>$ 260 W.m
Measured PER	18 dB	21 dB

Table 3.9: Comparison of the characteristics of the two fibers, 5 meters for the LMA-PM-15 and 10 meters for the LMA-PM-40-FUD. For the LMA-PM-15 we considered only the case when the polarization was set on the axis of the fiber

and matter in the core, it exhibits a much higher threshold for non-linear effects. However there are some drawbacks such as a very high attenuation (tens of dB/km) and difficulties to maintain the polarization. The technology is not mature yet and many works are currently done to improve the designs and get all the features together (single-mode, low-loss, polarization maintaining). We could for example cite the commercaly available HC-1060 from NKT-photonics [112] which has about 95% of the power in the TEM_{00} at 1064 nm, a PER of about 15 dB but an attenuation of 85 dB/km. Another considered solution is the PRISM technology for hollowcore fiber (Perturbed Resonance for Improved Single Modedness) which aims at stripping away the unwanted modes. The higher order modes have an attenuation of thousands of dB/km while the one of the fundamental mode is only of few dB/km. This technology allows to have single mode operation and a low attenuation but does not maintain the polarization [113]. However a design of hollow core fiber that unify these three criteria and operating at a wavelength of 1064 nm does not exist for the moment. We are discussing with manufacturers about the possibility of designing such a fiber for our application.

Chapter 4

Fibered Electro Optic Modulator for High Power single frequency lasers

In this chapter we will describe the high power fibered Electro Optic Modulator (EOM) prototype that we designed using the LMA-PM-15 fibers presented in the previous chapter. In a first section, we will present the working principle of an EOM. In the second part we will detail the requirements for Advanced Virgo and see through the review of the characteristics of different modulators that those requirements are not achieved yet for a fibered EOM. In a third part we will present the design of our prototype and the choices that have been made. Finally in the last section we will present the characterization of that prototype.

4.1 Working principle

4.1.1 Pockels cell

An Electro-Optic Modulator (EOM) is a device that can be used to electrically control some properties of a laser beam such as its polarization, its power or its phase. It is based on the Pockels effect, that has been discovered and described by Pockels in 1906 [114]. This effect characterizes the interaction of light with a crystal whose refractive index can be electrically modified. Indeed while applying a voltage on such a crystal, its refractive indices will be modified proportionally to the strength of the electric field. This modification can be described using the model of the index ellipsoid of the crystal defined by the equation 4.1:

$$\left(\frac{1}{n^2}\right)_1 x^2 + \left(\frac{1}{n^2}\right)_2 y^2 + \left(\frac{1}{n^2}\right)_3 z^2 + \left(\frac{1}{n^2}\right)_4 yz + \left(\frac{1}{n^2}\right)_5 xz + \left(\frac{1}{n^2}\right)_6 xy = 1 \qquad (4.1)$$

When applying an electric field $\vec{\boldsymbol{E}} = E_x\vec{\boldsymbol{x}} + E_y\vec{\boldsymbol{y}} + E_z\vec{\boldsymbol{z}}$, the coefficients of the ellipsoid will vary of an amount $\Delta\left(\frac{1}{n^2}\right)_i$ defined by the equations 4.3.

$$\begin{pmatrix} \Delta(1/n^2)_1 \\ \Delta(1/n^2)_2 \\ \Delta(1/n^2)_3 \\ \Delta(1/n^2)_4 \\ \Delta(1/n^2)_5 \\ \Delta(1/n^2)_6 \end{pmatrix} = \begin{pmatrix} r_{11} & r_{12} & r_{13} \\ r_{21} & r_{22} & r_{23} \\ r_{31} & r_{32} & r_{33} \\ r_{41} & r_{42} & r_{43} \\ r_{51} & r_{52} & r_{53} \\ r_{51} & r_{62} & r_{63} \end{pmatrix} \begin{pmatrix} E_x \\ E_y \\ E_z \end{pmatrix} \tag{4.2}$$

Which can be resumed by the following equation :

$$\Delta \left(\frac{1}{n^2} \right)_i = \sum_{j=1}^{3} r_{ij} E_j \quad \text{for i=1..6} \tag{4.3}$$

The r_{ij} are the coefficients of the electro-optic tensor which characterize the material. Generally, due to symmetries in the structure of the crystal and its orientation regarding the axis of the coordinate system, most of these coefficients are equal to zero. For the rest of the development on the Pockels effect, let us consider the crystal that we are using in the electro-optic modulator that we designed: a Rubidium Tantanyle Phosphate $RbTiOPO_4$ crystal also called RTP. We will enter into the detail of its characteristics in section 4.3.1, but let just notice for the moment that it has an orthorombic structure whose electro-optic tensor has the following form:

$$\begin{pmatrix} 0 & 0 & r_{13} \\ 0 & 0 & r_{23} \\ 0 & 0 & r_{33} \\ 0 & r_{42} & 0 \\ r_{51} & 0 & 0 \\ 0 & 0 & 0 \end{pmatrix} \tag{4.4}$$

Usually, and that will be the case in the prototype that we will present in section 4.3 the electric field is induced along the z direction and we have:

$$E = \begin{pmatrix} 0 \\ 0 \\ E_z \end{pmatrix} \tag{4.5}$$

By doing the matrix computation of equation 4.2, the change in the refractive indices of our crystal can be described by equations 4.6, 4.7 and 4.8.

$$\Delta(1/n^2)_1 = r_{13}E_z \tag{4.6}$$
$$\Delta(1/n^2)_2 = r_{23}E_z \tag{4.7}$$
$$\Delta(1/n^2)_3 = r_{33}E_z \tag{4.8}$$

Usually changes in the refractive indices are small, this allows us to make the following approximation:

$$\Delta\left(\frac{1}{n^2}\right) \approx -2n^{-3}\Delta_n \Rightarrow \Delta_n \approx \frac{-n^3}{2}\Delta\left(\frac{1}{n^2}\right) \tag{4.9}$$

Which finally leads to the following equations for the dependence of the refractive indices to the strength of the electric field:

$$n_x = n_{x0} - 0.5n_x^3 r_{13}E_z \tag{4.10}$$
$$n_y = n_{y0} - 0.5n_y^3 r_{23}E_z \tag{4.11}$$
$$n_z = n_{z0} - 0.5n_z^3 r_{33}E_z \tag{4.12}$$

4.1.2 Phase modulation

So we have seen how the Pockels effect was affecting the refractive index of the crystal, in the development below, based on the works of Riehle [115], we will see how this variation can be used to phase modulate the light.

Let us consider the electric field of a single frequency laser beam at ω_0 polarized on the z direction : $\vec{\boldsymbol{E}}(t) = E_0 e^{i(\omega_0 t)}\vec{\boldsymbol{z}}$. The z direction is chosen in order to maximize the effects since the coefficient r_{33} is larger than the two other ones (see table 4.3). While passing through the crystal this electric field will experience a phase shift Φ defined in equation 4.13 depending on the refractive index n_z, the length of the crystal L and the wavelength of the laser beam λ_0.

$$\Phi = \frac{2\pi L n_z}{\lambda_0} \tag{4.13}$$

In equation 4.12, we have seen that the refractive index n_z depends on the voltage applied on the crystal. If we apply an electric signal $U(t) = U_0\ \sin(\omega_m t)$ on the electrodes the electric field inside the crystal will be $E_z(t) = U(t)/d$, with d the distance between the two electrodes

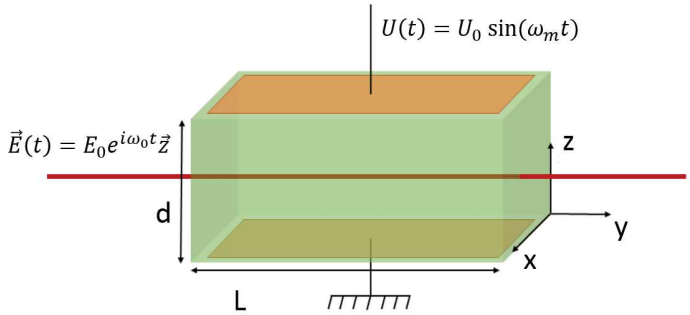

Figure 4.1: Modulation of the crystal by applying a voltage along the z direction

(see figure 4.1). The phase shift will then be time dependent and will have the following form:

$$\Phi = \frac{2\pi L}{\lambda_0}\left(n_e - 0.5 n_z^3 r_{33}\frac{U(t)}{d}\right) \tag{4.14}$$

If we define

$$\Phi_0 = \frac{2\pi L n_e}{\lambda_0} \tag{4.15}$$

and the modulation depth

$$m = \frac{\pi\ L\ n_z^3\ r_{33}\ U_0}{\lambda_0 d} \tag{4.16}$$

We can then write the electric field of the laser beam at the output of the crystal as follow :

$$E_{out}(t) = E_0 e^{i\Phi_0} e^{i(\omega_0 t - m\sin(\omega_m t))} \tag{4.17}$$

Using the Bessel functions $J_k(m)$, we could properly expend the term $e^{i(m\sin(\omega_m t))}$ as follow:

$e^{i(m\sin(\omega_m t))} = J_0(m) + \sum_{k=1}^{\infty} J_k(m) e^{ik\omega_m t} + \sum_{k=1}^{\infty}(-1)^k J_k(m) e^{-ik\omega_m t}$

However in order to lock the different cavities of the interferometer, we know that a maximum modulation depth of 0.2 is needed [29]. This value is relatively small and in this frame we can consider that only the Bessel function of the first order has to be taken into

account. While doing the evaluation of the two first Bessel functions for m=0.2, we have indeed $J_1(m) = 0.0995$ and $J_2(m) = 0.005$, this leads to a ratio for the corresponding powers of $(J_2(m)/J_1(m))^2 = 2.5 \times 10^{-3}$. Thus we consider only the contribution of the Bessel function of the first order and this is finally the same than doing the usual approximation $e^x \approx 1 + x$. Thus we can write equation 4.19:

$$E_{out}(t) = E_0 e^{i(\omega_0 t + \Phi_0)}(1 - im\sin(\omega_m t)) \tag{4.18}$$

$$E_{out}(t) = E_0 e^{i\Phi_0}(e^{i\omega_0 t} + \frac{m}{2}e^{i(\omega_0 - \omega_m)t)} - \frac{m}{2}e^{i(\omega_0 + \omega_m)t)}) \tag{4.19}$$

This expression makes clearly appear the two sidebands at $\omega_0 - \omega_m$ and $\omega_0 + \omega_m$. The spectrum of such a modulated beam that we experimentally obtained can be seen on figure 4.15.

4.2 State of the art

4.2.1 Expected characteristics for Advanced Virgo

As we have seen in the first chapter, in order to lock the different cavities of AdV five modulation frequencies are needed, their values are given in the TDR [29] : $f_1 = 6\,270\,777$ Hz, $f_2 = 56\,436\,993$ Hz, $f_3 = 8\,361\,036$ Hz, used to control the interferometer, $f_4 = 131\,686\,317$ Hz is used for the lock acquisition but it is not used afterwards when the detector is in science mode and finally $f_5 = 22.304$ MHz is used to lock the IMC. Amplitude and phase noises can affect the modulation and thus the stability of the lock and the sensitivity of the interferometer. The most restrictive requirements on these noises are for the modulation frequencies f_1, f_2 and f_3. The different values that those noises should not exceed have been obtained thanks to simulation, they are given in table 4.1. Moreover with these simulations it has been shown that in order to get the desire power in the PDH error signal (see appendix B), a modulation depth of 0.1 is required. However in order to get some margin it has been decided that a modulation depth of 0.2 should be reachable.

Name	Frequency (Hz)	Phase noise (rad/$\sqrt{Hz}$)	Amplitude noise($1/\sqrt{Hz}$)
f_1	6 270 777	1.8×10^{-6}	1.7×10^{-7}
f_2	56 436 993	1.1×10^{-6}	1.1×10^{-6}
f_3	8 361 036	0.27	1.7×10^{-7}

Table 4.1: Requirements on the EOM noises for f>10Hz

These modulation frequencies should be obtained thanks to an EOM that has to be able to withstand an optical power up to 200W without introducing too large thermal effects such as wavefront abberations or changes in the refractive indices. It should also not introduce optical power losses greater than 3% according to the initial design described in the TDR [29]. In practice this last point is not critical as far as the laser is not used at his highest potential value and that power losses do not participate to any kind of heating that would increase the noises or the non-linear effects. The optics group of EGO already developed free space EOMs able to fulfill these needs [116]. The idea is to use the previous experience, further improve the design and to study the possibilities of adding optical fibers to the design.

4.2.2 Commercial modulators and prototypes

In this section we are reviewing the available EOMs and comparing some of their characteristics (table 4.2) to show that none of them fulfill the desired characteristics that we detailed in the previous section and so motivate the design of a new prototype that would do it. In the four EOMs that we have chosen, two of them are commercially available (1) and (2) whereas (3) and (4) are prototypes that have been developed in different laboratories. The pictures of these EOM can be seen in figure 4.2 and we are giving a brief description here below:

- (1) is an EOM developped by the company AdvR which is a leading company in developping photonics component. The device presented, called HPFC electro-optic phase modulator, is fully fibered and has been developped with the aim of improving the power handling of usual fibered modulator [117]. It has indeed a maximum optical power of about 500mW [118] which is greater than the usual ones but still far from what we need.

- (2) is a high power free space EOM developped by Qioptiq under the name PM-C-BB using a Brewster-cut MgO-$LiNbO_3$ crystal. There are many free space EOM available, we chose this one among the others because of its high power density damage threshold of $100 W/cm^2$ [119]. It has a clear aperture of about 2 mm, which is a value common to most of the EOM. By taking a beam with a waist of 400 µm to avoid any spatial mode distortion inside the modulator, this leads to approximately 50 W of power handling.

- (3) is a prototype developped by the company Nova Write INC that was specialized in development and manufacture of directly modulable fiber lasers [120]. However the company does not give so much detail about it and does not exist anymore. The device is fully fibered with a total throughput of about 70% and was said to be able to handle power up to 5 W.

- (4) is the free space high power EOM usinga RTP crystal that has been developped by the optics group of the European Gravitational Observatory in collaboration with

the other departments. It is used in the injection system of Advanced Virgo and can withstand power up to 200W [29, 109] .

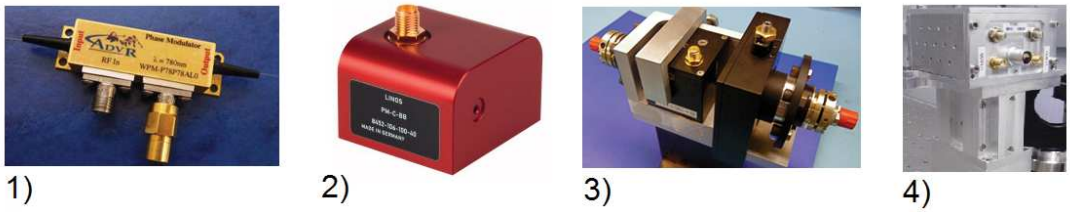

Figure 4.2: State of the art of EOM, 1 and 2 are commercially available and present quite good characteristics, 3 and 4 are two prototypes that are closer to what we are expecting but still do not fulfill our requirements

EOM	(1)	(2)	(3)	(4)	**(5)**
CW power (W)	0.5	50	5	200	**200**
Transmission (%)	~ 30	> 98	~ 70	99.87	$>$ **95** ?
Propagation	fully fibered	free space	fully fibered	free space	**fully fibered**
m	NA	NA	NA	0.2	**0.2**
Vπ (V)	6	500	NA	200	200
clear aperture (mm)	NA	2	NA	5	**NA**

Table 4.2: Comparision of the characteristics of the 4 severals EOM that we are previously to the expected values of the one we would like to develop (5).

What comes out from this comparison is that, as usual when designing a component that will be commercially available, manufacturers have to find compromises between the cost and the different characteristics of the device. These different characteristics will make them more suitable for different applications. For example the EOM from AdvR (1) has been designed to be inserted in a telecommunication network, its losses of around 5 dB are quite usual for these types of application whereas free space components such as (2) exhibit very low losses and can withstand much higher power. Some compromise between these two have been found through the realization of prototypes. The one from Nova Write (3) is using a crystal between two collimators. On one side the beam is expanded out of the fiber, going through the crystal and is then recoupled into another fiber thanks to the other collimator. That is what is actually done in telecom EOM as well but their low cost and very compact integration leads to much lower specifications. This prototype has a design similar to the one that we want to develop but the maximum input power that it can handle is about 5 W and about 30% of the input power is lost through the device because of the lack of degrees of freedom on the beam alignment. The second prototype, free space device used in Advanced Virgo (4), can withstand power up to 200 W with very low power losses. The fully fibered prototype that we developed and that we present in the next sections is based on the design of this prototype.

4.3 Design of the new prototype

4.3.1 Arrangement of the crystals and beam jitter

The crystals that we use to modulate the light are made of RTP (Rubidium Tantanyle Phosphate - $RBTiOPO_4$) from Raicol. A comparison is done in [109] between the crystals generally used to modulate the light. We chose RTP because it is the one that exhibits the lowest absorption at 1064 nm, <50 ppm/cm. Such a low absorption is important for high power application in order to minimize the heating of the crystal that would results in issues such as thermal lens, thermally induced birefringence or depolarization. The main properties of the RTP at 1064 nm, as they have been given by the manufacturer, are presented in table 4.3.

n_x	1.7652
n_y	1.7751
n_z	1.8536
r_{13}	12.5 pm/V
r_{23}	17.1 pm/V
r_{33}	39.6 pm/V

Table 4.3: RTP optical properties at 1064nm [116]

In order to decrease the thermal effects, the other point that has to be considered is the cross section of the crystal. On one hand a larger cross section would allow a larger beam and thus would reduce the power densities in the crystal but on the other hand, it can not be increased to too large values because the required voltage to reach the desired modulation depth would be too high. A compromise has been found with d = 5 mm, it allows a beam waist inside the crystal of 500 µm and a voltage of about 150 V for the needed modulation depth. With such a waist, the focal length of the induced thermal lens is of the order of 20 m that does not affect the coupling in the fiber. With this crystal lower waist are also possible, but one has to check both the induced thermal lens is not too high (7.5m for 300 µm) and that the beam is not diverging too much inside the EOM. The length L has been chosen to be 20 mm so that two modulation frequencies can be applied on the same crystal, this reduces the number of interfaces. Furthermore each of these interfaces has an angle of 1° to avoid any back reflections and to avoid any cavity effects inside the crystal itself that could lead to unwanted effects such has Residual Amplitude Modulation (RAM) (see section 4.4.4) as it was suspected in [121]. The surfaces have then been coated with an AR coating for 1064 nm. We measured the characteristics of this coating for the interfaces of two crystals, for S and P-polarization. The results are presented in table 4.4. The requirement was 500 ppm, that is what we have for the S-polarization and it is even going down to 50 ppm for the P-polarization. However we saw in section 4.1 that in order to get the best modulation depth efficiency from the crystal, light is polarized along the z axis, so it is S-polarized. The tests have been conducted with an Angle Of Incidence (AOI) close to 0° and at normal inci-

dence an AR coating should not be polarization dependent. However this difference can be explained by the birefringence of the crystal, its higher refractive index on the z-axis makes the AR coating less efficient.

	Reflectivity S (ppm)	Reflectivity P (ppm)
crystal 3 face 1	612	52
crystal 3 face 2	538	40
crystal 4 face 1	575	57
crystal 4 face 2	503	30

Table 4.4: AR coating specification on the crystals used in the modulator. They have been measured with an AOI of about 4°. Taking an uncertainty of 2% on each measurements, the reflectivities are given with an uncertainty of 2.8%

In the design we chose to use two crystals and set their respective angles such as the whole optical path seen by the beam is actually equivalent to a plate with parallel faces as you can see on figure 4.3. In this configuration the second crystal is correcting the astigmatism introduced by the first one. Moreover the beam is only slightly shifted and not tilted. This simplifies the whole optical set-up by avoiding the problems linked to the long propagation of a tilted beam. Moreover while using a single crystal, because of a prism effect, any tilt at the input is increased at the output. This is not the case for the configuration with two crystals. To check this effect, as well as the beam jitter induced by the modulation of the refractive index of the crystal, we performed some Matlab simulations of the two configurations. The relation between the angles can easily be found with the Snell-Descartes law (eq 2.6), the only point is to take care of the rotation of the coordinate system at each interface because of the angle of the face of the crystals.

In a first simulation we compared the relative dependence of the output tilt regarding the input one. As expected in the configuration with two crystals the output tilt stays the same while passing the modulator. In the case of one crystal, the tilt is slightly increasing. However, considering the relative small angles of incidence this increase is only of a factor of about 1.0007 which is relatively small and does not motivate by its own the choice of using two crystals. The main advantage of using these two crystals is finally about the correction of the astigmatism and its compactness. In particular, it reduces the distance l_e between the two crystals, especially if two modulators were mounted separately. We also took a look at how the beam is shifted through the two crystals. The total shift is the sum of the shift that occurs in the two crystals and also in between. As expected the shift occurring in the two crystals is the same (about 160 µm), and the main contribution arises in between (about 300 µm). Thus at the output of the two crystal, the beam is shifted by an amount of 600 µm . This is not critical considering the beam size of about 400 µm and the aperture of 5 mm.

These tests have been conducted without considering any modulation inside the crystal. The second parameter that we made varying was the voltage applied on the electrodes used

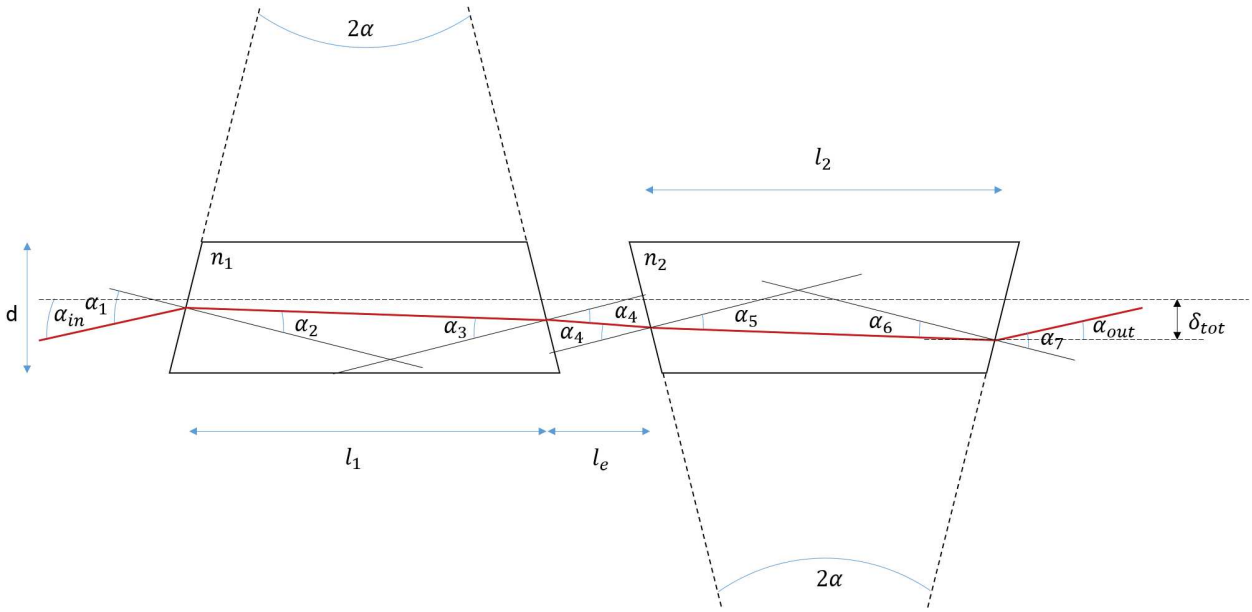

Figure 4.3: Scheme of the crystals used in the EOM. With such a design the beam pointing is less sensible to tilt.

to modulate the refractive index (eq 4.12). We were making varying V_1 and V_2 the voltages applied on crystal 1 on 2, and check their influence on the output beam jitter and beam shift around the initial position ($V_1 = 0$ $V_2 = 0$). The results are presented in figure 4.4. We were making the voltages varying between -150 and +150 V, according to the numerical evaluation done in section 4.3.3. The worst cases are obtained when the applied voltages are maximum and opposite. However this leads to a maximum beam shift of $\pm 4 \times 10^{-9}$ m and to a maximum beam jitter of the order of $\pm 3 \times 10^{-7}$ rad.

In our case, we decided to have two different modulation frequencies per crystal. This slightly modifies the simulation that we have been previously by adding one more refraction inside the crystal. We have done the simulation using the actual modulation depth used in Advanced Virgo (m_1=0.22 at 6.27 MHz, m_2=0.15 at 8.36 MHz, m_3=0.12 at 22.30 MHz, m_4=0.25 at 56.43 MHz). This results in a maximum beam shift of $\pm 5 \times 10^{-9}$ m and to a maximum beam jitter of $\pm 8 \times 10^{-7}$ rad that can be neglected in our set-up as we will show in section 4.3.4.

4.3.2 Mechanical design

In this section, based on the previous experience of the optics group, we present a new mechanical design of a free space modulator having four different modulation frequencies and a thermal control. This modulator will then be inserted in the fully fibered design of the EOM (section 4.3.4). The most relevant views of the drawing of the mechanical design are presented in figure 4.5 and a picture of its assembling in figure 4.6.

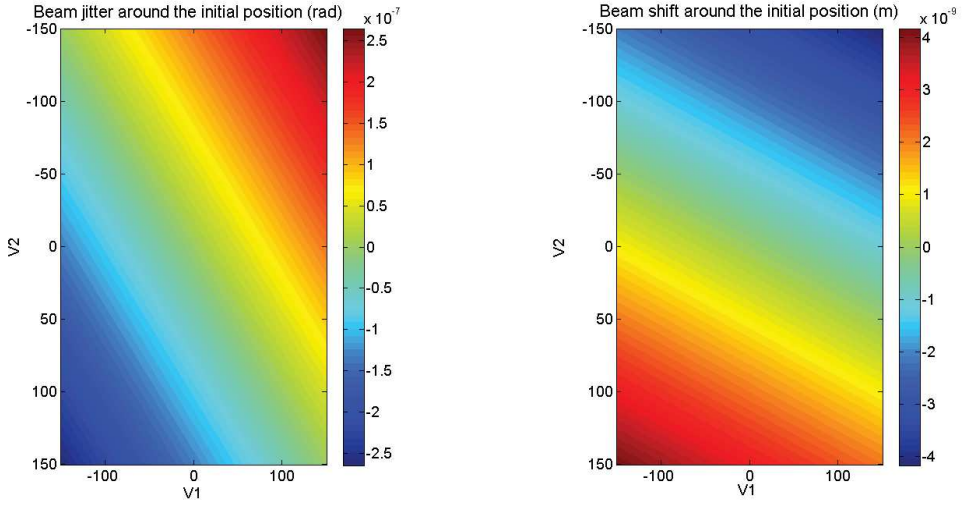

Figure 4.4: Beam jitter and beam shift around the initial position while modulating the two crystals

The two crystals (7) are set between the electric ground electrode (2) on the bottom and two electrodes (3) each on their top. Under the copper plate used as the ground we placed two peltier modules (9) that are used to change the temperature of the crystals. In order to monitor these temperatures, we placed two Resistance Temperature Detectors of 100Ω (RTD100) on the crystals (not visible on the drawings). One with the other, Peltier modules and RTD 100 give us the possibility to design a servo loop in order to keep a stable crystal temperature. It has indeed been shown in [116] that the temperature of the crystal has an effect on the Residual Amplitude Modulation. The thermal contact between the Peltier modules and the copper plate, and the fine adjustment of the structure height is done thanks to sheets of Indium of 125µm . This whole structure is then compressed between two pieces of Teflon (1) and (4) which presents the advantage of having a low electrical permittivity and a high mechanical flexibility. This whole structure is then fixed in a box in order to minimize dust contamination. On each side of the box there is a 5 mm diameter clear aperture which allows the optical beam to go in and out. On the top of that box, there is a DB15 connector on which are connectorized: the Peltier modules, the RTD 100, the electrodes and the ground. This connector makes the optical part of the modulator independent from the electronics one. This one is indeed set-up in a box that we will detail in section 4.3.3 and can be removed and modify without having to touch to the optical part of the modulator. Everything is then screwed on a base plate and a translation stage in order to have the whole set-up at a height of 100 mm and being able to finely set the transverse position of the modulator.

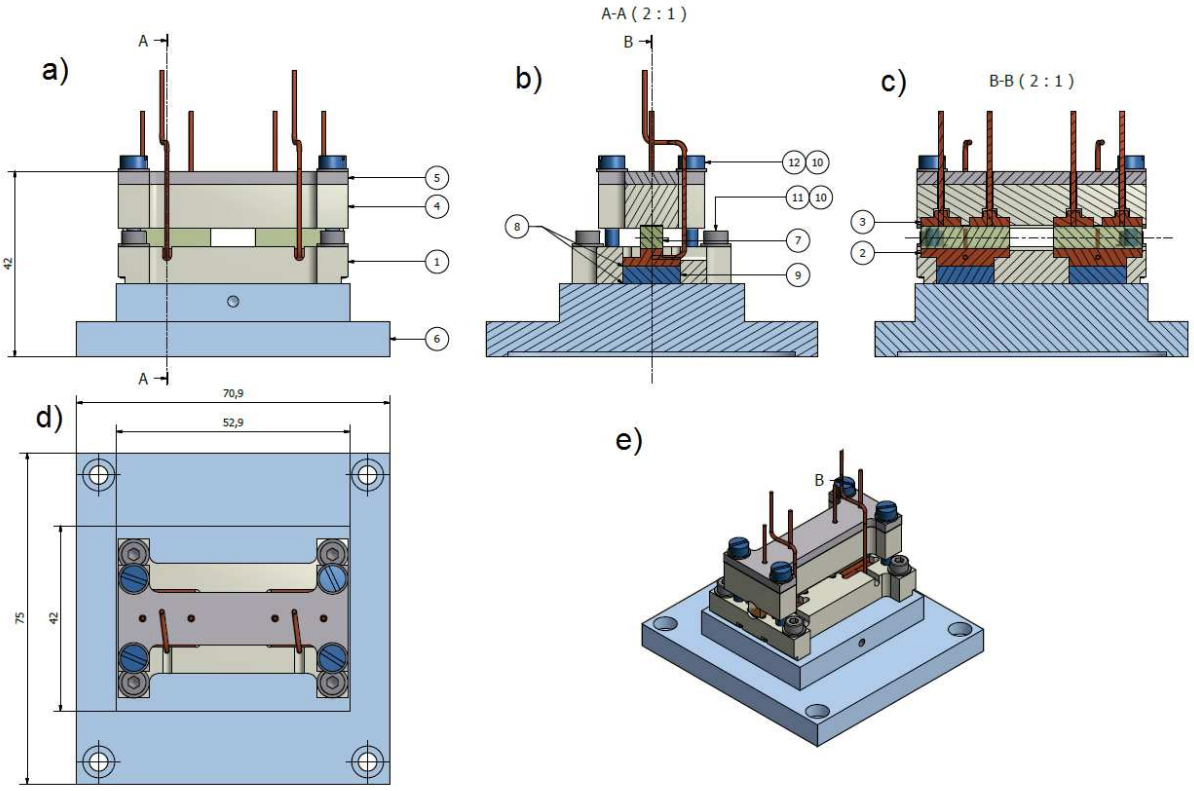

Figure 4.5: Mechanical drawing of the EOM ; a) side view b) front view c) Cut side view d) Top view e) General view part // 1) bottom teflon part, 2) Ground copper plate, 3) Electrodes, 4) Top teflon part, 9) Peltier modules

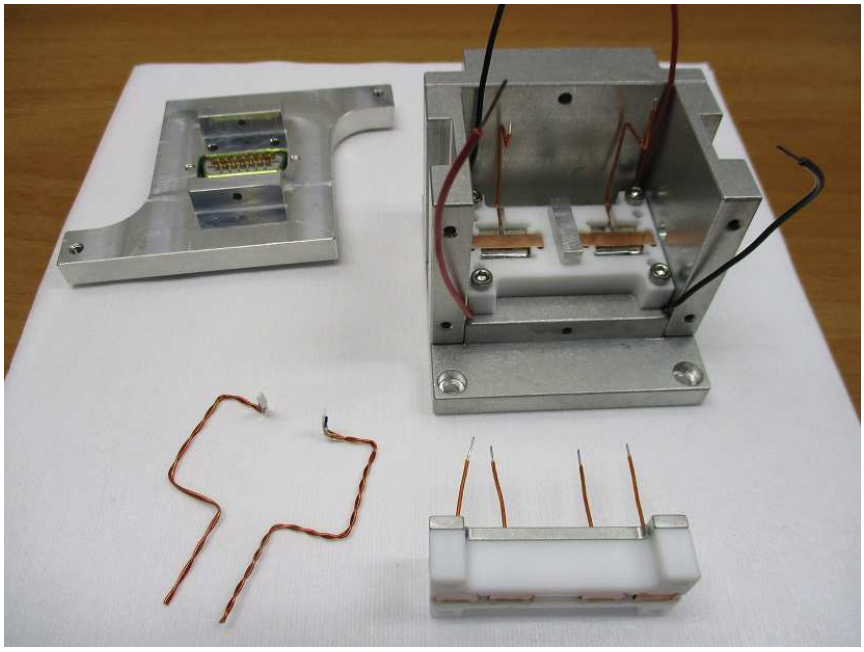

Figure 4.6: Mechanical assembly of the EOM

4.3.3 Modulation electronics

In this section we detail the design of the electronics part of the modulator that is connectorized on top of the crystal box thanks to the DB15 connector as we saw previously. The aim of this electronics part is to have the needed voltage along the z axis of the crystal to reach the desired modulation depth. The crystal, placed between the electrodes and the ground, is acting as a plane capacitor whose capacitance is given by the following equation:

$$C = \epsilon_0 \epsilon_r \frac{A}{d} \tag{4.20}$$

Where ϵ_0 is the vacuum permittivity (8.85 $\times 10^{-12}$ F/m), ϵ_r is the dielectric constant of the material between the electrodes, A is the common surface between the electrode used to modulate and the ground, and d is the distance between them two. Knowing that the dimensions of the electrodes are 5x9mm, the crystal has a thickness of 5mm and the dielectric constant of the RTP is 13, a numerical evaluation leads to a capacitance of about 1pF.

One could simply do the modulation by applying the voltage on the crystal. However for a modulation depth of 0.2, using the parameters of the crystals and the formula 4.21 derived from the equation 4.16, the numerical evaluation leads us to a peak voltage of 150 V.

$$U_0 = \frac{m\lambda_0 d}{\pi L n_z^3 r_{33}} \tag{4.21}$$

So a direct modulation leads to very high electric powers, and this is something we would like to avoid. The guidelines of the electronics design is indeed to keep the electronics simple, with a power as low as possible in order to minimize the room and avoid any heating point that could affect both the electronics and the optics in the set-up. The second point is to maximize the efficiency in order to minimize the effective length of the crystals. A higher number of crystals would indeed introduce more interfaces and a longer crystal would increase unwanted non linear effects such as thermal lensing.

The trivial idea would be to use a transformer to scale the voltage up, but this would create LC serie circuit with both the inductance of the transformer and the capacitance of the crystal. Such a circuit would be difficult to tune and would make high resonant frequencies difficult to reach since the inductance of the transformer increase with the square of the converting ratio of the transformer. So the other idea is to use a transformer to scale down the voltage and use an LC serie circuit afterwards by adding an inductance in serie with the capacitance of the crystal [110]. Indeed with such a design, higher voltages across the crystal are obtained for higher currents into the circuit. The transformer has been designed in order to keep the losses low and to match the 50Ω input impedance of usual RF generators. For the RLC series circuit we chose an inductance of about 2 μH that has been obtained by coiling a wire on a toroid. We added a variable capacitor in parallel to the crystal. This was indeed necessary to be able to finely tune the resonance frequency of the circuit since the overall resistance and capacitance of the circuit depend on many parameters such as the wires that are used, the modulation frequency or any kind of defaults that can appear in the crystal or in the welds. For this prototype we designed such a resonant circuit for 20 MHz with a quality factor Q of 50. This frequency is not one of the frequencies used in the interferometer that we specified before, but we chose it to do some tests because it is easily obtained with the common RF generator and high enough to be easily separated from the carrier while analyzing the sidebands.

4.3.4 Fibered version

The basic idea is to bring the input fiber on one side of a breadboard, use a collimator to get the desired beam characteristics, pass through the modulator and use another collimator on the other side of the breadboard to recouple into the output fiber (see figure 4.8). In this version that we designed we were using the LMA-PM-15 from NKT photonics that we presented and characterized in section 3.2. It was 5 meters long and did not have any AR coating on the end facets of the fiber. The collimators were the ones from Schäfter und Kirchhoff whose focal length is 7.5 mm presented in section 3.1.2. By using these collimators as they have been set by the manufacturer, ie in order to maximize the waist of the output beam and so its Rayleigh range, we have a theoretical beam waist of 406 μm at a distance

of 7.5 mm from the lens. This gives us a Rayleigh range of about 500mm. However there is an optical distance of about 340 mm between the two collimators. By computing the mode matching between these two beams, one can find that there is a loss by miscoupling of about 10%.

To solve this problem the idea is to change the position of the lens inside the collimators to set them so that they have an output beam having the same waist at a distance of 170 mm. Two configurations are theoretically possible as it can be seen on figure 3.3 presenting the reachable waist and position of the collimator. By slightly moving forward the lens of 0.056 mm inside the collimator we have a waist of 366 µm situated at 170 mm from the collimator and by moving it by 0.238 mm we could get a waist of 177 µm situated at 170 mm. The second configuration has a smaller waist, and this has different disadvantages, it would lead to higher density of power inside the crystal and in term of coupling a smaller waist is more sensible to variations. The decrease of the beam waist in the first configuration is not critical in term of power density. The characterization of the beam at the output of the collimator is shown in figure 4.7. As we already highlighted in the dedicated section 3.1.2, these collimators are particularly difficult to set in the desire position, thus the practical parameters of the output beam that we obtained slightly differ from the theoretical ones. However this allowed us to reach good coupling efficiency as we will see in section 4.4.1.

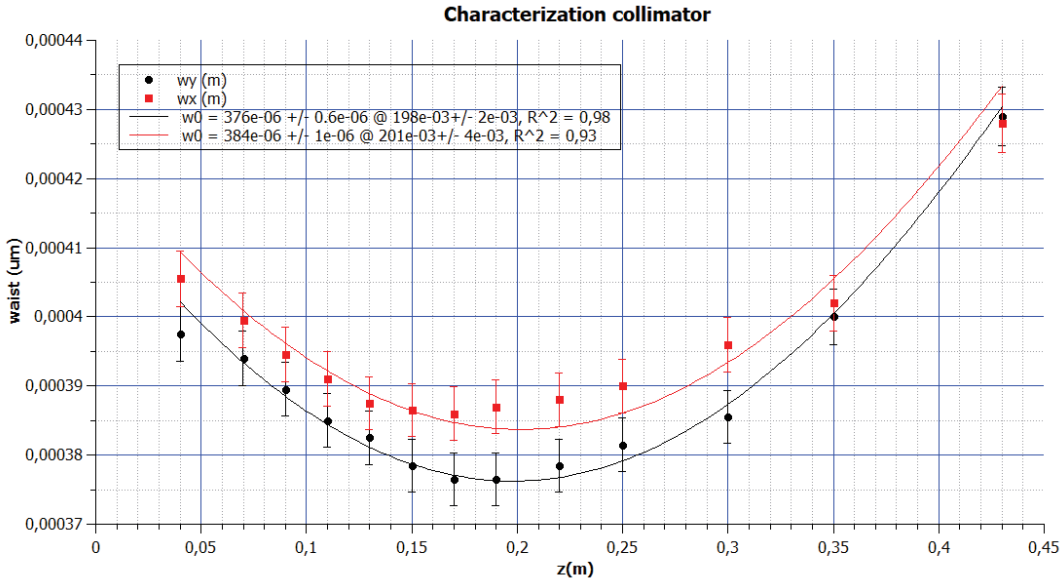

Figure 4.7: Characterization of the beam at the output of a LMA-PM-15 used with a collimator of focal length 7.5mm. The lens is slightly moved inside the collimator in order to have a waist at the desire position.

The needed degrees of freedom to reach this coupling are given by the output collimator that is fixed in a mirror mount (tilts) and this mount is fixed on a 3-axis translation stage (shifts). The input collimator was set on a fixed base in order to avoid mechanical noise

as much as possible. Between the input collimator and the EOM we added a polarizer and a half waveplate, to perfectly set the polarization inside the crystal and thus reduce the Residual Amplitude Modulation (RAM) as we will explain later in section 4.4.4. It has not been implemented yet but the space between the EOM and the output collimator has been kept to be able to set up a high speed shutter that would dump the beam before injecting into the fiber in case of losses in the coupling. On top of the whole breadboard, we placed a box made of Plexiglas in order to avoid air to flow inside and eventually bring dust on the path of the high power beam, especially the interfaces of the crystal that are particularly critical.

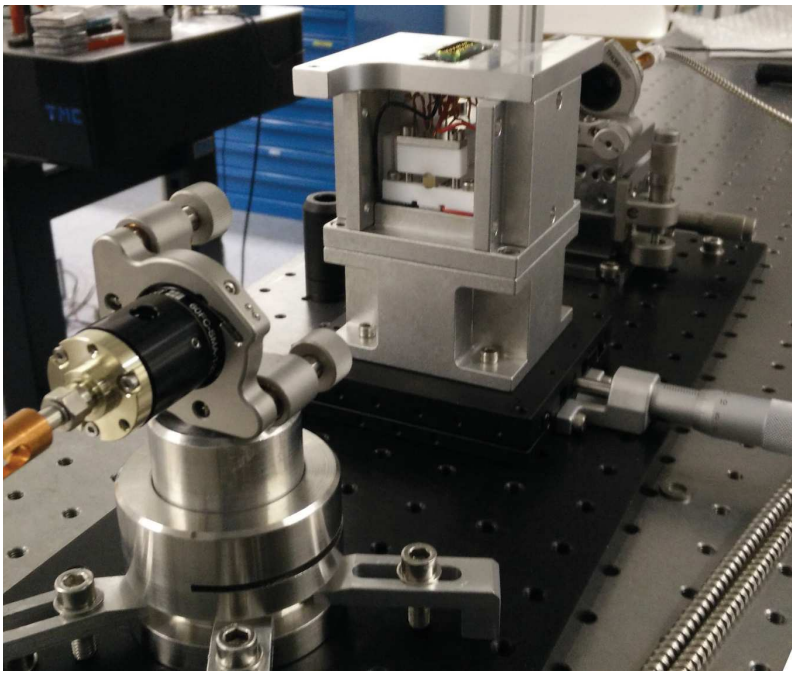

Figure 4.8: Picture of the fibered EOM. To be noted that the box containing the crystals has been opened to show the inside part. The box containing the electronics part that can be plugged on the top has also been removed, and so was the plexiglass box covering the whole set-up in order to avoid dust to flow inside.

The distance of 340 mm between the two collimators that we mentioned previously has been chosen so that other optical elements can be inserted between the collimators and the EOM. Considering the size of the modulator itself and the size of the mirror mounts that are used (see picture 4.8) this let us about 100 mm on each side. We will especially see in section 4.4.4 that this place is needed before the EOM to clean and properly set the polarization at the input of the modulator. In a further version a high speed shutter could be inserted between the EOM and the second collimator. We took a look at the influence of the beam jitter and beam shift induced by the modulator on the coupling into the fiber over this distance. In section 4.3.1 we computed Δ_x the maximum beam shift at the output of the crystal (5×10^{-9} m) and Δ_θ the maximum beam jitter (8×10^{-7} rad). Thanks to the ABCD formalism, we can propagate the vector $(\Delta_x, \Delta_\theta)$ through the set-up and get the actual beam

shift and beam jitter at the input of the fiber $(\Delta'_x, \Delta'_\theta)$ (equation 4.22). d_1 is the distance between the crystal and the lens of the collimator, f is the focal length of the lens of the collimator (7.5 mm) and d_2 is the distance between the lens and the end facet of the fiber (7.5 mm).

$$\begin{pmatrix} \Delta'_x \\ \Delta'_\theta \end{pmatrix} = \begin{pmatrix} 1 & d_2 \\ 0 & 1 \end{pmatrix} \begin{pmatrix} 1 & 0 \\ -1/f & 1 \end{pmatrix} \begin{pmatrix} 1 & d_1 \\ 0 & 1 \end{pmatrix} \begin{pmatrix} \Delta_x \\ \Delta_\theta \end{pmatrix} \tag{4.22}$$

When having the beam jitter and beam shift at the input of the fiber, one can evaluate the losses due to these deviations by, respectively, evaluating equations 4.23 and 4.24, where w_0 is the waist of the beam at the input of the fiber and lambda the wavelength. This leads to a miscoupling of 2×10^{-8} for the tilt and 4×10^{-6} for the shift. It can be neglected.

$$L_\theta = 1 - \exp\left(-\left(\frac{\Delta'_\theta \pi w_0}{\lambda}\right)^2\right) \tag{4.23}$$

$$L_x = 1 - \exp\left(-\left(\frac{\Delta'_x}{w_0}\right)^2\right) \tag{4.24}$$

4.4 Characterization

4.4.1 Low power coupling

The first experiment that we carried out with this fibered EOM was to characterize the coupling at low power. To do so we used the set-up presented in figure 4.9 and measured the powers P_1, P_2 and P_3 . A quarter waveplate and a half waveplate were used to correct the polarization of the beam at the output of the laser and a wedged plate was used to correct its astigmatism. The pair half waveplate - Polarized Beam Splitter was used to set the input power and the fine alignment of the beam in the input collimator was obtained thanks to a pair of HR mirrors. Considering the characteristics of the beam, we managed to design a telescope using only one lens before injecting into the fiber through the collimator. For this injection we reached a stable coupling up to 89% for power of few hundreds of mW. Considering the lack of AR coating on the end facets of the fibers for this experiment, 6.7% where lost because of the reflections. Moreover 3.75% were lost due to the HOM of the fiber (2%), its attenuation (1.15%) and the reflections on the lens of the collimators (0.6%) (see table 3.3). So finally, 89.55% was the maximum theoretical reachable coupling. However this coupling is not the one of interest in our experiment since it will change from one laser to another. The coupling we were interested in was the one between the two collimators on the breadboard, having a focal length of 7.5 mm. We tested it for the two configurations that we detailed in the previous section: either a waist of about 366 µm (configuration 1) or a waist of 177 µm (configuration 2) in the middle of the breadboard.

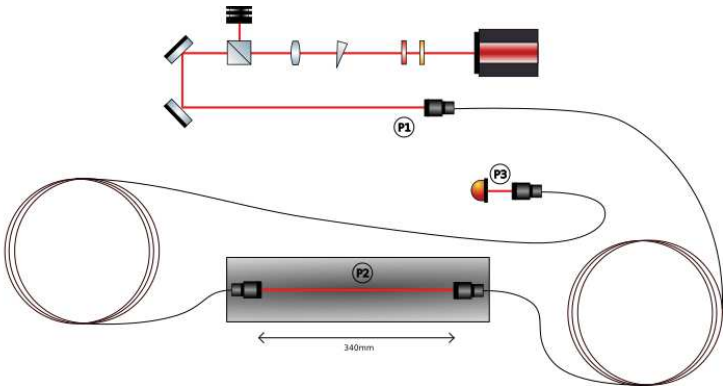

Figure 4.9: Setup used to characterize the coupling between the two collimators at low power

Despite configurations that were slightly varying from the theoretical ones, due to the difficulties to precisely set the lens inside these collimators, we managed to obtain a coupling efficiency of about 87% in the first configuration and 84% in the second one. By adding the EOM we had a global coupling between the collimators of 82%. In this configuration we moved the fibered EOM on the high power bench to perform some test at high power and see how is the coupling behaving when increasing the power.

To be noticed that in a test that has been conducted later, with a 1.5 meter long fiber that had one end facet coated and that was cleaved on the other end, we reached a coupling efficiency in the first configuration that we mentioned of 92.9%. The sum of the known coupling losses in that configuration are 4.19% (attenuation 0.35%, lens collimator 0.3%, non coated end facet 3.35%, coated en facet 0.19%). So the maximum theoretical coupling is 97.09%. The remaining losses of 2.91% are coming from the coupling fiber to fiber. Considering a perfect matching, the coupling between the 98% of TEM_{00} of the input beam and the 98% of TEM_{00} of the mode of the fiber gives us 96.04% of TEM_{00} at the output. This means that among the 2% of HOM in the input beam, 1.05% has been coupled in the fiber.

In table 4.5, we summarized all the losses that arise along the path of the fibered EOM in its design version, considering a TEM_{00} at the input and at the output

4.4.2 High power coupling

In order to test the coupling efficiency of the fibered EOM for high power we used the set-up presented in figure 4.10. The laser was a fiber laser YLR-200-LP from IPG photonics [108], whose power can be increased till 200 W. Its central wavelength is 1070 nm and it is not single frequency. Thus we did not have any problems of SBS and were able to increase the power above the SBST of the LMA-PM-15. We monitored the power at the input, at the output and the temperatures of both input connectors. The coupling efficiency was measured at low power, we had about 80% through the first fiber and 82% through the EOM and the second one, which leads to a global coupling of 66%. This coupling could have been further

Lens reflection	0.3%
End facet reflection	0.19%
TEM_{00} to fiber	2%
Attenuation (5 m)	1.15%
End facet reflection	0.19%
Lens reflection	0.3%
EOM	0.24%
Lens reflection	0.3%
End facet reflection	0.19%
Fiber to fiber	2.91%
Attenuation (5 m)	1.15%
End facet reflection	0.19%
Lens reflection	0.3%
Fiber to TEM_{00}	2%
Total	11.41%

Table 4.5: Losses of the fibered version of the EOM

improved by finely set the collimators but we kept it like that for the first experiments that we were carrying out.

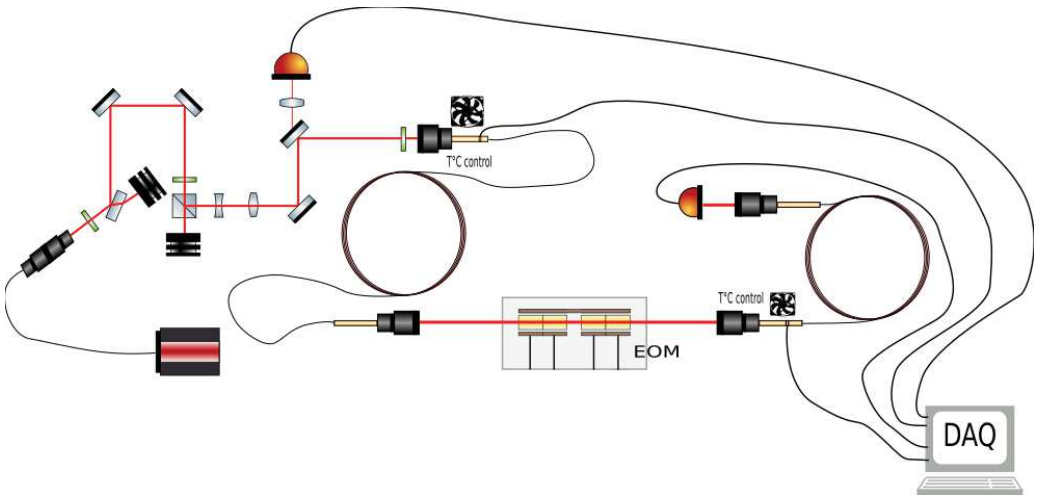

Figure 4.10: Scheme of the set-up used to characterize the EOM at high power. The input and the output power were monitored. The temperatures of the two connectors used for the injection were also monitored.

Then we scaled up the power step by step, checking that no problem were arising. In the first attempt, while reaching 40 W at the input, even if there was no coupling losses, we observed a sudden increase of the temperature of the first connector as it can be seen on figure 4.11. We stopped and decided to replace the fan used to cool down the first connector

with a more powerful one in order to increase the convection around the connector. This was a temporary solution that we set up, waiting for a more permanent one: the water cool down system that we presented previously in figure 3.2. However, thanks to this solution we managed to inject more than 50 W in the fibered EOM (see figures 4.12).

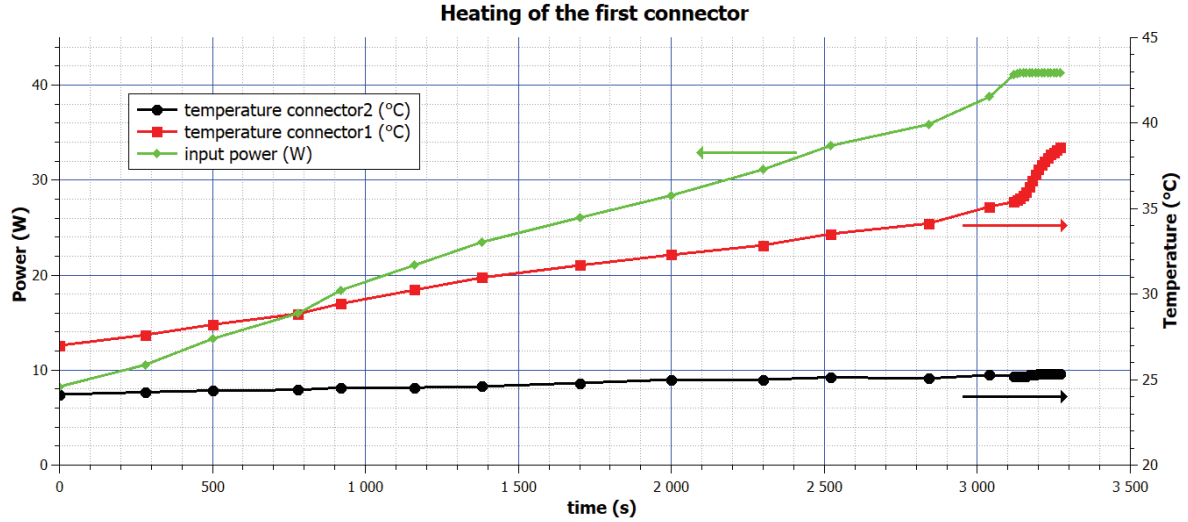

Figure 4.11: Increasing of the injected power, thanks to the set-up presented in figure 4.10 used a simple fan. We noticed the sudden increase of the temperature of the input connector while reaching 41 W

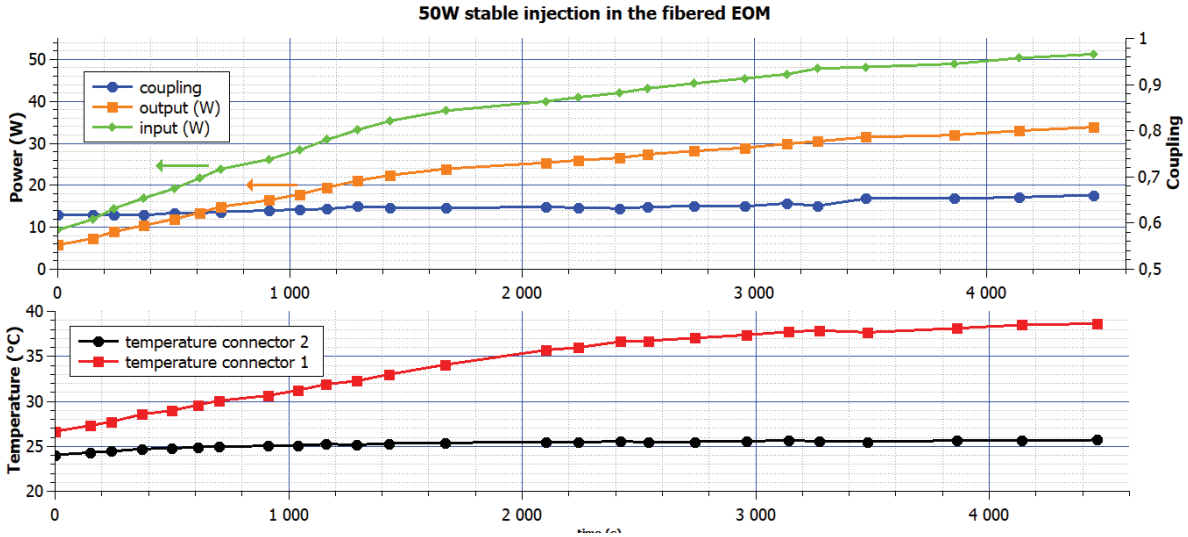

Figure 4.12: Increase of the power at the input of the fibered EOM (set-up presented in figure 4.10 used with a more powerful fan). Until 50 W input power the temperature of the connectors as well as the overall coupling are behaving normally.

Different points have to be noticed in these two attempts. First the difference between the temperatures of the first and second input connectors is not explained. It might come from a difference in the manufacturing of the connectors themselves. Secondly one can notice that there is almost no temperature difference between the first and the second attempt, around 36°C for an input power of 40 W. However, in the second case, there was no sudden increase of the temperature. Moreover, we did not monitor the temperature of the output connectors but it appeared that it was increasing as well. This is due to the light backreflected on the output end facet which is badly recoupled into the fiber. We did not increase the power any further for the moment to avoid any degradation of the fiber.

Before reaching the 50 W at the input, we performed a stability test over more than 2000 seconds. The results can be seen on the figure 4.13. The Gaussian fit on the count of the occurrences of the values of coupling is giving a mean value of 0.645 with a standard deviation $\sigma^2 = 6.84 \times 10^{-3}$. We can see that the coupling was slightly improving over time and the temperature of the first connector was slightly decreasing. We did not investigate this small improvement but we saw while injecting 50 W that the coupling was not decreasing while the temperature of the connector was increasing. Thus this improvement might be caused by a change in the input beam that could come from the laser itself or by any thermal effects in the optics.

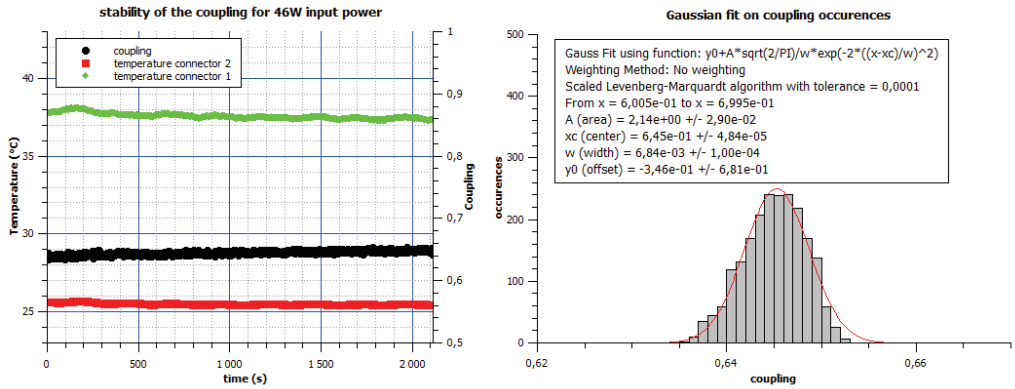

Figure 4.13: Stability of the coupling and the temperature of the connectors of the fibered EOM for 46 W input power

4.4.3 Modulation depth

The modulation depth is the coefficient m defined in equation 4.16, it gives the information on how deep the signal is modulated by looking at the ratio between the power into the sidebands and the one in the carrier.

However a perfect phase modulation can not be seen on a photodiode since the detected intensity does not vary in time as it can be seen in equation 4.25. In order to measure this

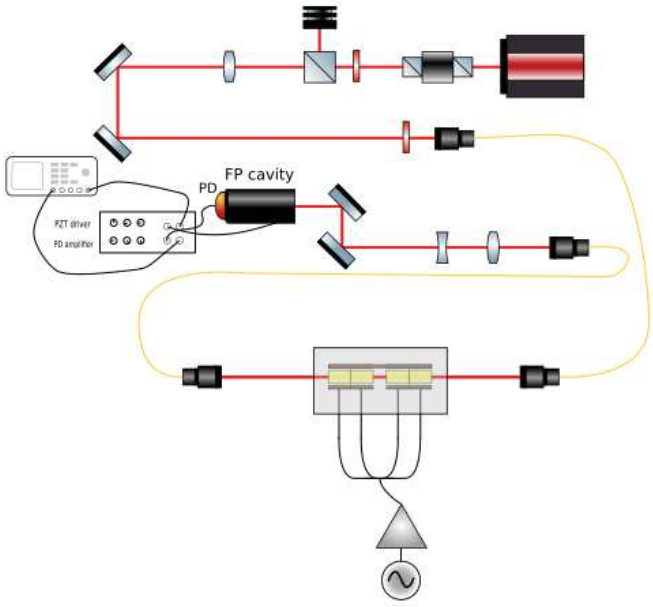

Figure 4.14: Setup used to measure the modulation depth of the two sidebands at 131 MHz thanks to the FPI100 scanning Fabry Pérot cavity from Toptica [122]

coefficient one has to use a SFP cavity to successively make resonate the sidebands and the carrier and analyze them at the output of the cavity (see appendix B).

$$I(t) = E_{out}\ (t)E^*_{out}(t) = E_0 e^{i\Phi_0} e^{i(\omega_0 t - m\sin(\omega_m t))}\ E_0 e^{-i\Phi_0} e^{-i(\omega_0 t - m\sin(\omega_m t))} = E_0^2 \tag{4.25}$$

The modulation depth of the previous prototype (with the same type of crystal and a similar electronics) has already been well investigated in [116], so we did not push the test any further than checking the proper functionning of the modulator by setting up the experiment presented in figure 4.14. The SFP cavity used was the FPI 100 from Toptica [122]. It is a 75 mm confocal cavity with a FSR of 1 GHz and a finesse of about 500 according to the datasheet. The EOM was modulated at a frequency of 131 MHz. The optical electric field E_m in a sideband can be derived from equation 4.19, and the related optical power P_m that we get is given by the equation 4.26:

$$P_m = E_m(t)\ E^*_m(t) = \frac{m}{2} E_0 e^{i(\omega_0+\omega_m)t)}\ \frac{m}{2} E_0 e^{-i(\omega_0-\omega_m)t)} = \frac{m^2}{4} E_0^2 \tag{4.26}$$

The power in the carrier is simply $P_0 = E_0^2$. Thus we have $m = 2\sqrt{P_m/P_0}$.

On the results presented in figure 4.15, we measured the following voltages: $Ve_{m1} = Ve_{m2} = 108$ mV, $Ve_0 = 5.02$ V. Considering a linear answer of the photodiode we can assume that these voltages are directly proportional to the optical power and can be divided to get back to the modulation depth. It gives us a modulation depth of 0.29 which is in agreement with the characteristics of the RTP crystal and the few electric Watts that were applied on the four electrodes, considering the modulation frequency of 131 Mhz and the about 4pF capacitance of the crystals.

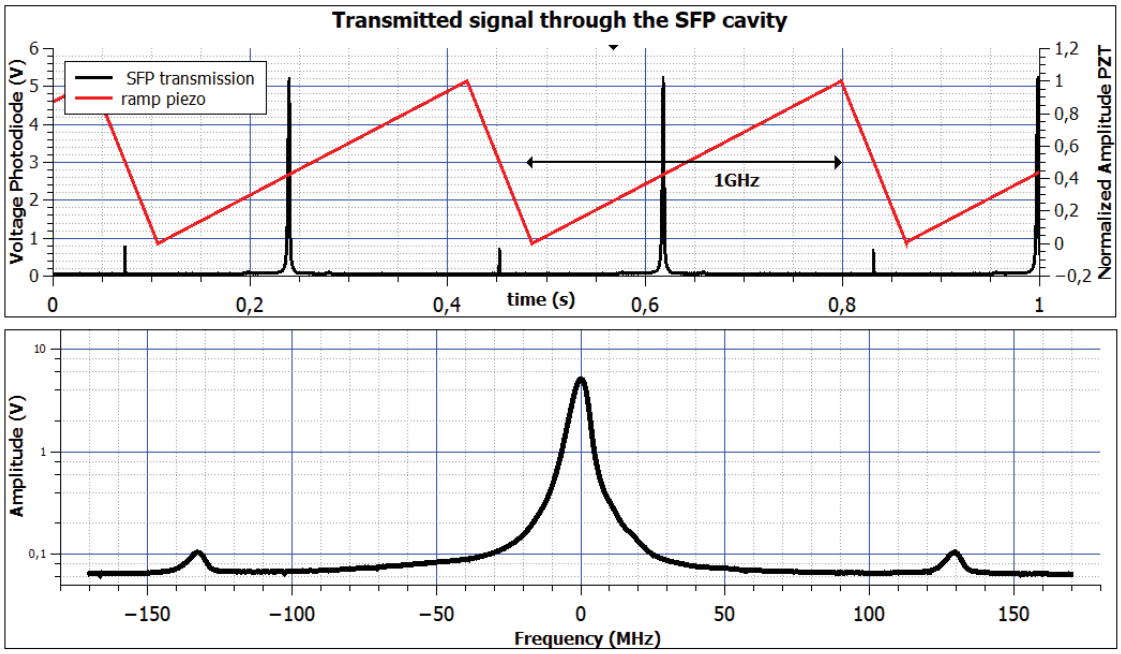

Figure 4.15: Phase modulation at 131 MHz. Two symmetric sidebands were measured that allowed us to measure a modulation depth of about 0.29

4.4.4 Residual Amplitude Modulation

Residual Amplitude Modulation (RAM) is a typical noise that arises in EOM at the same frequency than the one used for the phase modulation. This noise is of great importance in GW detector, indeed it has for effects to unbalance the sidebands of the phase modulation and so to add an offset to the PDH error signal used to lock the interferometer. Since this error signal is set to zero, such an offset can change the length of the different cavities and so deteriorate the sensitivity of the detector. In [123], they studied the influence of the RAM-to-PM ratio in the sensitivity of LIGO. It is the ratio between the modulation depth of the amplitude modulation and the one of the phase modulation. For a realistic ratio of 10^{-4} rad^{-1} that they measured previously, they concluded that it was not deteriorating the sensitivity of the interferometer. However there are some effects that modifies its optomechanical response and could bring some instabilities that we want to avoid.

Various studies have been conducted to understand the causes of this effect. The first reason is a Fabry-Perot cavity effect that can occur inside the crystal itself because of the non-zero reflectivity of its end facets [124]. Since the refractive index of the crystal is modulated, the optical path of this cavity is modulated as well and so is the amplitude of the electric field at the output. This output electric field is given by (see appendix B):

$$E_{out} = \frac{t_1 t_2 e^{-i\phi}}{1 - r_1 r_2 e^{-i\phi}} E_{in} \tag{4.27}$$

Where t_1 and t_2 are the transmission coefficients of the facets and r_1 and r_2 are the reflective ones. $\phi = 2\pi nL/\lambda$ is the phase that depends on the optical path. This phase is modulated at the modulation frequency ω_m, which leads to:

$$E_{out} = \frac{t_1 t_2 e^{-i(\phi_0 + m\sin(\omega_m t))}}{1 - r_1 r_2 e^{-i(\phi_0 + m\sin(\omega_m t))}} E_{in} \tag{4.28}$$

So to avoid this effect it is necessary to have very good AR coatings on the facets of the crystal. In table 4.4, we reported the measured reflectivity of the facets, it was of the order of 600 ppm. This reflectance (r) holds for the ratio of the powers, it is linked to the ones of the electric fields (R) through the relation: $R = r^2$. So the modulation depth of the resulting amplitude modulation is of the order of magnitude of the reflectance of the facets: 6×10^{-4}. This is slightly greater to what would be acceptable, and better coating performances are difficult to reach. So the second idea is to have an angle between the two facets of the crystal in order to mitigate this FP cavity effect. On our crystals, we have an angle of 1° for each facets as it can be seen on the scheme figure 4.3. By comparing it to the divergence of the beam inside the crystal ($\approx$ 500 µm) this leads to an overlap of modes of 4×10^{-4}. So the RAM is theoretically decreased by this amount thanks to the angle of the end facets of the Electro-optic crystal.

The second cause for RAM is a misalignement between the input polarization and the axis of the crystal. When this happens, the input polarization can be projected on the axis of the crystal and we saw previously (table 4.3) that this crystal is birefringent. So both component will experience a different phase shift while going through the crystal and the output polarization state will depend on that phase difference. Moreover we have a modulation of that phase on only one of these axes. So this will finally result in a polarization modulation at the same frequency used for the phase modulation. This polarization modulation will be transformed in RAM while passing through any kind of polarization dependent component such as polarizers.

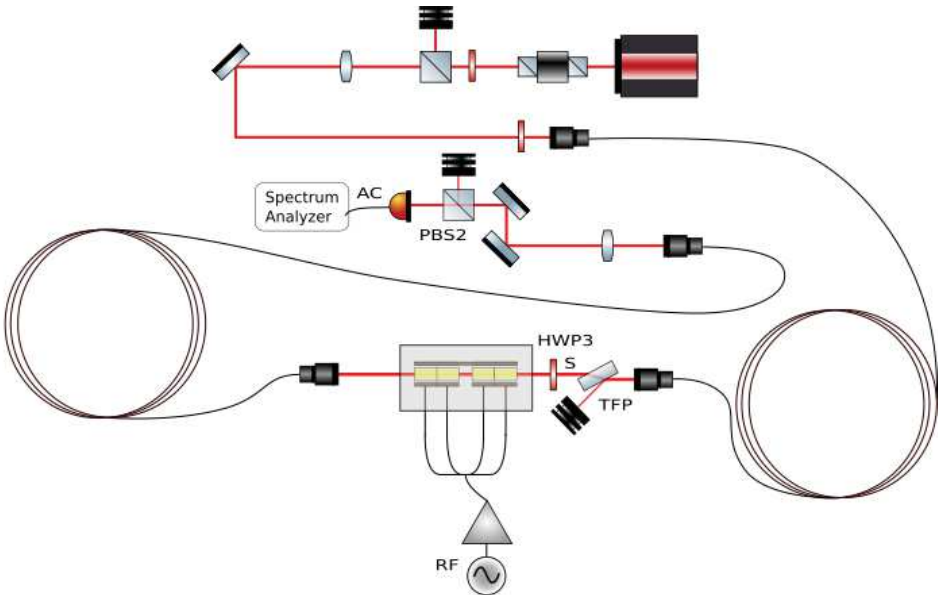

Figure 4.16: Scheme of the setup used to measure the RAM of the fibered EOM. The polarization was clean before the modulator in order to mitigate the effects of RAM. The answer was analyzed after the PBS2 tin order to see the effects of the polarization modulation as well.

In order to see the influence of the polarization on the RAM in the EOM we set up an experiment presented in figure 4.16. The EOM was modulating at a frequency $\omega_m = 3.14$ MHz and we were analyzing the output beam thanks to an AC fast photodiode and a spectrum analyzer. By measuring the peak at the modulation frequency we could get back to the optical power in the sideband through the following equation:

$$Pf_{opt} = \frac{\sqrt{R}}{G} \times 10^{\frac{Pf_{dBm} - 30}{20}} \tag{4.29}$$

With R=50 Ω the impedance of the Spectrum Analyzer and G= 775V/W the gain of the photodiode. In parallel we were also measuring the total output power P_0. The RAM was then obtained by taking the ratio of these two values: $RAM = Pf_{opt}/P_0$. Such a way to do it presents the advantage to be set up very fast, however to do an accurate measurement of the RAM, one should demodulate the signal of the photodiode $E = E_0 + E_m \cos(\omega_m t + \phi)$ into two channels that are in phase and quadrature to be insensitive to the phase variation of the demodulated signal as shown in figure 4.17. The obtained electric fields $E_1 = E_m \cos(\phi)$ and $E_2 = E_m \sin(\phi)$ can then be numerically processed to compute an accurate value of the RAM. This has been done previously in [116] for a similar EOM and a RAM of the order of 10^{-6} has been measured.

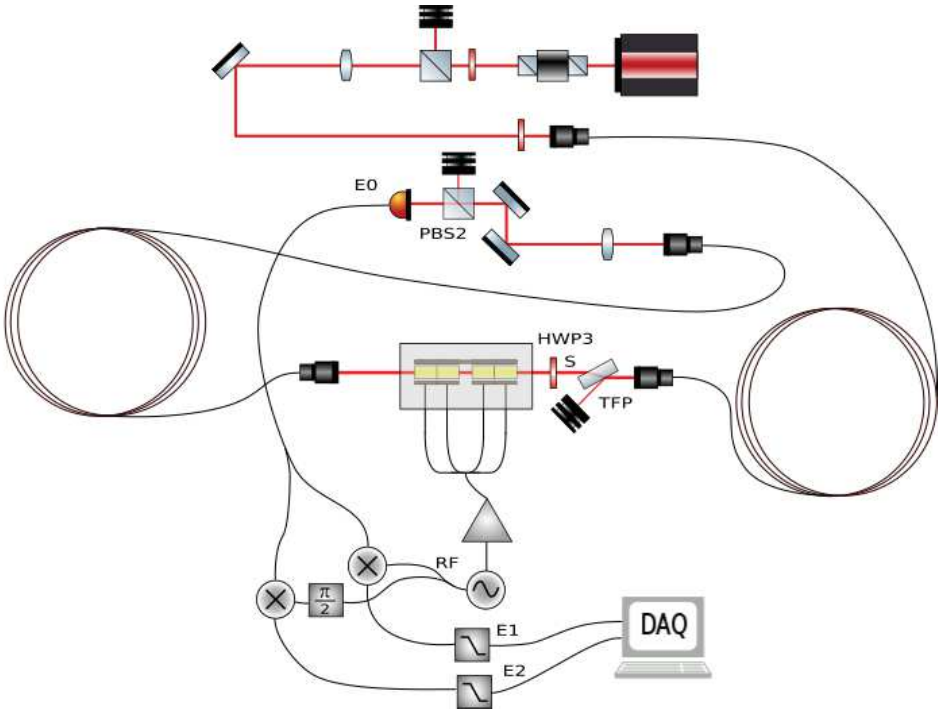

Figure 4.17: Setup used to properly measure the RAM of the fibered EOM. The response of the photodiode is demodulated at the frequency modulation both in phase and quadrature to be able to numerically get back to the total amount power independently to its phase.

However in this experiment we were investigating the influence of the polarization and a differential measurement was enough to characterize it. In a first place, we measure the RAM without the TFP, HWP and PBS2 that can be seen on the scheme of the set-up. We measure a RAM of 4.86×10^{-5}. The reason for intrinsic RAM while modulating a crystal are not clearly identified, they must come from defects of the crystal itself such as its cut. Here we could supposed that it is due to the induced beam jitter that modulates the coupling into the fiber but it has to be noticed that in theory the RAM induced by beam jitter for a well aligned beam should be seen at frequency f=2f$_m$. Then, by adding the PBS2 in front of the photodiode, we measured a RAM of 2.20×10^{-4}. This confirm that the RAM was dominated by polarization modulation. Because of the intrinsic depolarization inside the fiber the polarization quality at its output is around 20dB, we placed the TFP to clean the polarization and a half waveplate to be able to evaluate the influence of the polarization and being able to precisely set the input polarization to minimize the RAM. The results of this investigation are presented in figure 4.18.

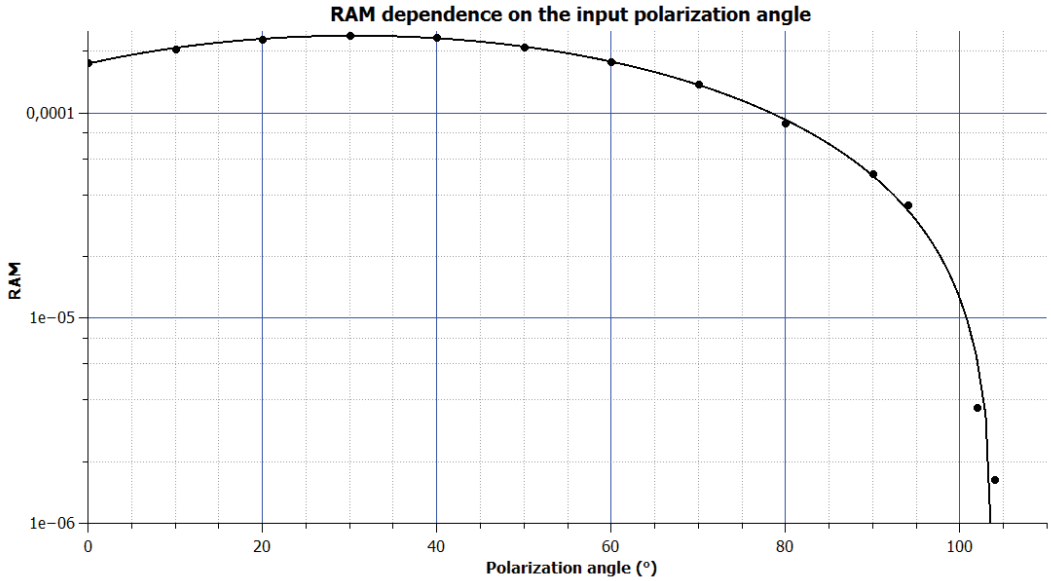

Figure 4.18: RAM when changing the angle of the linear polarization at the input of the EOM. A minimum of 10^{-6} is reached while setting very precisely on the axis of the crystal

The interesting point of this experiment is that when we set very precisely the input polarization we decreased the RAM by two order of magnitude and reached values down to 10^{-6}. Moreover these values are coherent with the ones that had been measured previously.

Another parameter that has been identified to play an important role in the RAM is the temperature of the crystal. It has been evidenced by Wong and Hall in [125], and studied in various paper. For a modulator similar to the one that we are using, a similar behavior has been observed in [116] where the variation of the RAM as well as the temperature of the crystal has been monitored for an input optical power of 105W. The results are shown in

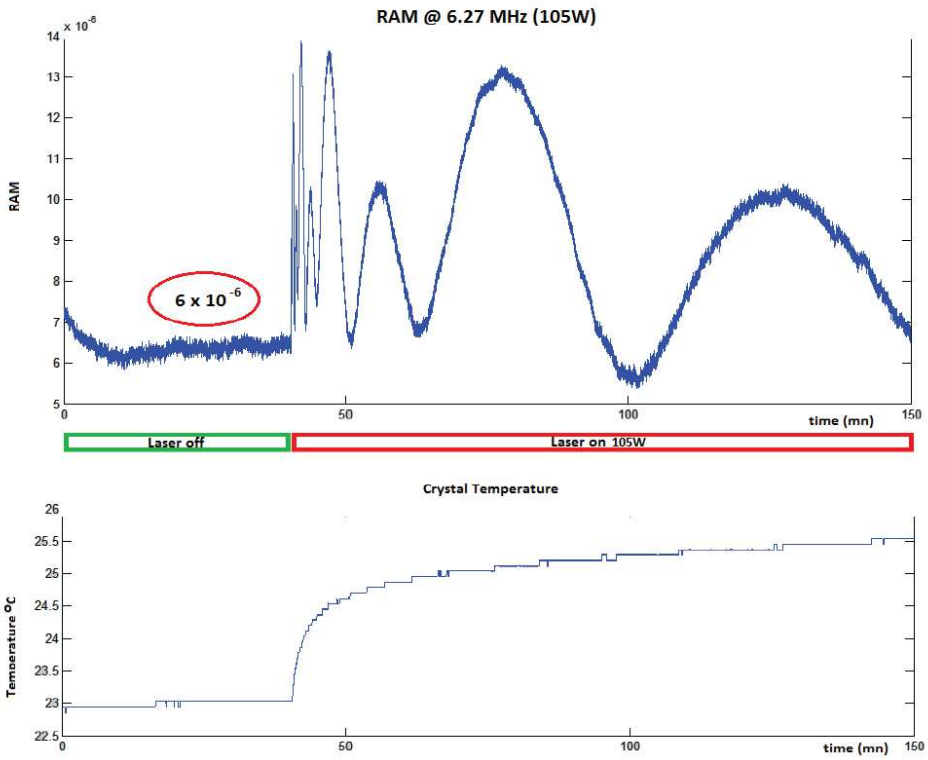

Figure 4.19: Dependence of the RAM on the temperature of the crystal while being heated by a laser beam of 105W [116].

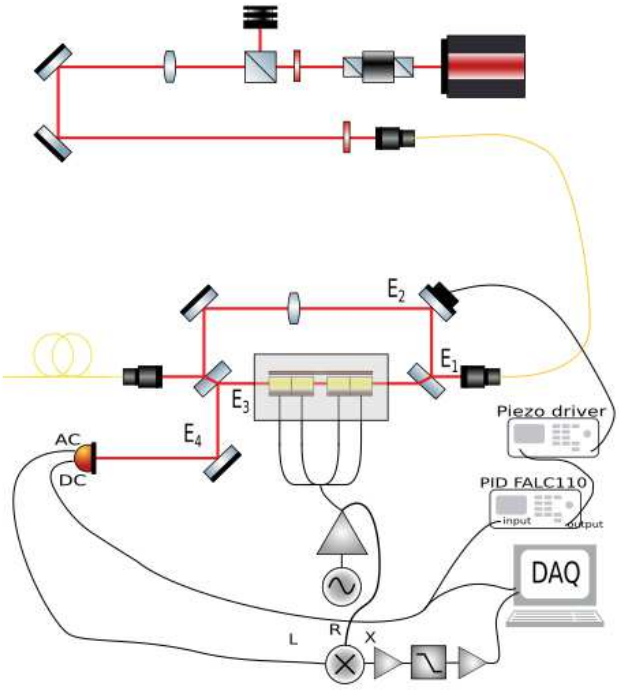

Figure 4.20: Setup to measure the phase noise induced by the modulator

figure 4.19. In the design of our EOM, we added two peltier modules and two temperature probes on the crystal in order to be able to set an active control on the temperature of the crystals to keep it at a stable value that would minimize the RAM. Such a loop has been implemented with success in [126] and will be used in the future version of our prototype, when we will scale the power up.

4.4.5 Phase noise

In order to characterize the phase noise that could be induced by the modulator we set up a Mach Zender Interferometer (MZI) presented on the scheme of the experimental set-up (figure 4.20).

In the first part of the set-up, the power of the light going out of the laser is set to a desired value thanks to a PBS and a HWP and is then injected on the axis of a LMA-PM-15 thanks to a matching lens, two HR mirrors and a HWP. At the output of the fiber, in order to set-up a Mach-Zender Interferometer (MZI), the electric field (E_1) is split in two thanks to a 50:50 BS. One of the split beam will be the reference of the interferometer (E_2) whereas the other one will be modulated in the EOM. For this experience, we were doing a direct modulation on the four electrodes. On the reference arm we placed a lens which helps in matching the characteristics of the two beams that have to interfere. The two beams are recombined thanks to a second beam splitter and we were analyzing the output port E_4 that

was not couple into the fiber to get the information on the phase noise. Here below we detail the calculation of the interference phenomena and how we can get an evaluation of the phase noise.

Let us consider the electric field at the input of the MZI: $E_1 = A_1 e^{j(\omega_0 t + \psi(t))}$ where A_1 is the amplitude of the electric field, ω_0 the optical frequency of the laser, and $\psi(t)$ the common noise before the beam splitter. After the beam splitter we have: $E_2 = A_2 e^{j(\omega_0 t + \psi(t) + \Phi(t))}$ and $E_3 = A_3 e^{j(\omega_0 t + \psi(t) + m\sin(\omega_m t + \varphi(t)))}$ where $\Phi(t)$ is the phase shift between the two electric fields, m is the modulation depth, ω_m is the modulation frequency, $\varphi(t)$ the noise induced by the modulation of the EOM and A_2 and A_3 are the respective amplitudes of E_2 and E_3 such as $A_2^2 + A_3^2 = 1$. In order to maximize the contrast of the interferometer we chose $A_2 \approx A_3 \approx \sqrt{0.5}$. At the output port of the interferometer the two electric fields E_2 and E_3 are interfering and we have $E_4 = E_2 + E_3$. On the photodiode we measure the power P_4 whose expression is given in equation 4.30.

$$P_4 = E_4 E_4^* = (E_2 + E_3)(E_2 + E_3)^* = A_2^2 + A_3^2 + E_2 E_3^* + E_2^* E_3 \tag{4.30}$$

With

$$E_2 E_3^* + E_2^* E_3 = A_2 A_3 (e^{j(\Phi(t) - m\sin(\omega_m t + \varphi(t)))} + e^{-j(\Phi(t) - m\sin(\omega_m t + \varphi(t)))}) \tag{4.31}$$

By using the approximation $e^{jx} \simeq 1 + jx$ for x relatively small we finally have :

$$P_4 = A_2^2 + A_3^2 + 2A_2 A_3 \cos(\Phi(t)) + 2A_2 A_3 \sin(\Phi(t)) \sin(\omega_m t + \varphi(t)) \tag{4.32}$$

From this expression we can separate the DC and AC power of the interfering beam :

$$P_{4DC} = A_2^2 + A_3^2 + 2A_2 A_3 \cos(\Phi(t)) \tag{4.33}$$

$$P_{4AC} = 2A_2 A_3 \sin(\Phi(t)) \sin(\omega_m t + \varphi(t)) \tag{4.34}$$

Having these two measurements the aim was to get back to the value of the phase noise of the EOM $\varphi(t)$. However the measurement of P_{4AC} was dominated by the differential noise $\Phi(t)$ between the two arms. So we used the DC power to create an error signal to lock the interferometer and keep $\Phi(t)$ constant. The actuator of the loop was the PZT that can be seen on the scheme of the set-up, the filter was a pur PID experimentaly designed thanks to the modulable locking electronics FALC110 [99]. We locked it in the middle of a fringe, so that $\cos(\Phi(t)) = 0$ and $\sin(\Phi(t)) = \pm 1$. By doing this we also maximized the AC signal in which we are interested in equation 4.34. Having this AC signal, we demodulated it to get

back to the value of the phase noise induce by the EOM. Let us consider for that V_{4AC} the voltage given by the photodiode, it is directly proportional to the optical power:

$$V_{4AC} = P_{4AC}G = 2GA_2A_3\sin(\Phi(t))\sin(\omega_m t + \varphi(t)) \tag{4.35}$$

Where G is the gain of the photodiode in Volts/Watts. By mixing this response with the input electrics signal that was used to modulate the EOM $V_{mix} = A_m\cos(\omega_m t)$ we get:

$$V = V_{4AC}V_{mix} = 2GA_mA_2A_3\sin(\Phi(t))\sin(\omega_m t + \varphi(t))\cos(\omega_m t) \tag{4.36}$$

By using usual trigonometric formulas we can develop the equation 4.36 and reorganize the terms in order to obtain a DC and a 2ω terms as follow:

$$V = A_2A_3A_mG\sin(\Phi(t))\sin(\varphi(t)) + A_2A_3A_mG\sin(2\omega_m t + \varphi(t)) \tag{4.37}$$

To be noticed that, by doing the calculation in a more rigorous way there would also be a signal of frequency ω_m that would appear in equation 4.37, coming from a term in $2\omega_m$ that has previously been neglected while doing the approximation $e^{jx} = 1 + jx$. Anyway, by choosing a low pass filter whose cutoff frequency is lower than ω_m we keep only the DC value of the demodulated signal:

$$V_{LP} = A_2A_3A_mG\sin(\Phi(t))\sin(\varphi(t)) \tag{4.38}$$

Since $\Phi(t)$ is kept constant with the lock of the interferometer, the temporal variation of V_{LP} are proportional to the variation of $\sin(\varphi(t))$.

In order to do calibrate the measurement, we scanned the interferometer over several fringes thanks to the PZT to get a numerical evaluation of the term $A_2A_3A_mG$ of equation 4.38 and get back to a value in rad/$\sqrt{Hz}$. The calibrated results of the phase noise are presented in figure 4.21. The phase noise is lower than 10^{-6} as required, and we have a trend curve in 1/f. We can also observed some peaks between 50 Hz and 500 Hz, they are also present in the DC value. This is evidenced in figure 4.22 where we plotted the coherence between the AC value (eq 4.34) and the DC value (eq 4.36). They must be due to the power fluctuations that affect the quality of the lock. That correction of the power noise will be seen in the AC signal as well. So the measure of the phase noise that we made is limited by these power fluctuations and what we are presenting here is actually a maximum value of the phase noise.

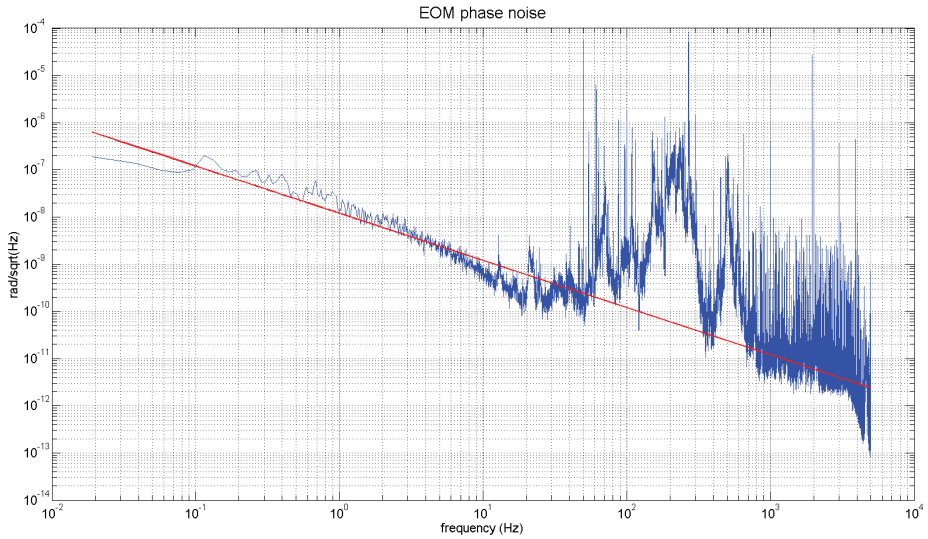

Figure 4.21: Calibrated Phase noise measurements

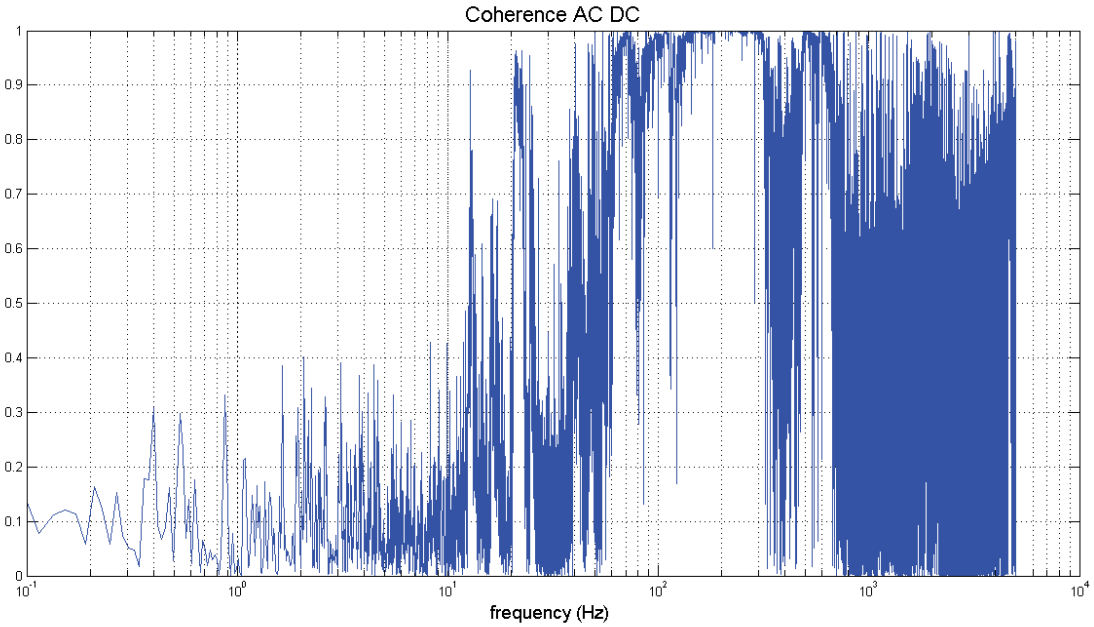

Figure 4.22: Coherence between the AC and DC values measured at the output of the MZI. They are almost fully coherent between 50 Hz and 500 Hz, this suggests that this band is dominated by power noise

4.5 Conclusion

This work was a preparatory task to highlight the problems linked to the fibering of high power components and in particular prepare the improvements needed for the more complex version of a fibered Faraday Isolator that we will present in the next section. Starting from the design of an EOM used in advanced Virgo, we brought some modifications and set it up with LMA-PM-15 fibers from NKT photonics and collimators from Schäfter und Kirchhoff to get a fibered version of this EOM. We validated the proper functioning of this prototype at low power in term of phase modulation, Residual Amplitude Modulation and phase noise. At high power, we demonstrated that in the current version there is no problem in term of coupling for input power up to 50 W. This does not fulfill our expected characteristic yet, but from the best of our knowledge, it does not exist fibered EOM that can withstand that amount of power. The problems in this fibered version are coming from the fibers themselves, especially the heating of the connector and the introduced HOM. Indeed, as one can notice in table 4.5, this is the main contribution to the losses: about three times 2%. Moreover for a single frequency laser, this version can not be used for power greater than 20 W because of the SBS effect. More tests will be conducted with a broadband high power laser in the coming version that will have a water cool down system and AR coating on the end facets of the fibers. However with these fibers the characteristics that we specified can not be reached.

Chapter 5

Faraday Isolator for High Power single frequency lasers, improvements investigation and fibering expectations

In this chapter we are presenting the work that have been done in order to improve the performance of high power Faraday Isolator, and especially the one that could be used in a fibered version. In a first part, we are explaining the working principle of a FI and its characteristics. Then in a second part, we are detailing the main issues linked to the use of high power in FI. In a third part, we are exploring the possibility of mitigating these issues by adding a mechanical stress on the crystal. Both experimental works and simulation have been done to better understand this effect. Finally in a last part, using the experience that we gain on high power FI, we present the design of a fibered version of a Faraday Isolator.

5.1 Faraday Isolator working principle

5.1.1 Faraday effect

The Faraday effect, discovered by Michael Faraday in 1845, is an interaction between light and a magneto-optic material in presence of an external magnetic field. While going through this kind of medium the plane of polarization of the light is rotated by an angle which depends on the properties of the material and on the strengh of the magnetic field (see equation 5.1). The magnetic field is actually inducing a circular birefringence that will affect the polarization state of the beam. If we consider a linear polarization at the input, it can be decomposed into two cicurlar polarizations of same amplitude, one left-hand polarized and the other one righ-hand polarized. Due to the circular birefringence there is a phase velocity difference between these two components and while propagating through the medium a phase shift appears. When being recombined at the output of the medium it leads to a rotated linear polarization. The angle of rotation depends on this phase shift and it can

be formally defined by analyzing the motion equation in the medium of a single electron of the electric field of the beam, and how the propagation constants of this medium are modified by the longitudinal magnetic field [127]. However the usual way to give the information on the rotation angle β is to use the Verdet constant V of the material defined such as:

$$\beta = VBL \tag{5.1}$$

Where B is the strength of the magnetic field, considered longitudinal and invariant in space, L is the length of the magneto optic material. In practice the Verdet constant in $rad/(T.m)$ is experimentally defined and reported in tables for different material, at different wavelengths and temperatures. All materials have a Verdet constant but for most of them it is extremely small, the difficulty consists in finding a magneto optic material that has both a high Verdet constant and good optical properties. A high Verdet constant allows to keep the interaction length as small as possible for a given magnetic field and the good optical properties are needed to avoid any losses, depolarization into the material or also other non-linear effects that can appear especially while working with intense lasers. The most common crystal, which actually also the one that we are using in our prototype, is the Terbium Gallium Garnet (TGG).

The basic design of a Faraday rotator is to surround this crystal by circular magnets which are creating the longitudinal magnetic field and to set its characteristics such as β=45°. Indeed the particularity of a Faraday rotator is that it has a non reciprocal behavior. Contrary to a half waveplate that rotates the polarization thanks to the properties of linear birefringence, in the case of a Faraday Rotator, the sense of rotation of the polarization plane does not depend on the sense of propagation of the light. So the light that eventually is back reflected from the set-up is experiencing a second rotation of 45° while passing through the Faraday Rotator. Thus the back reflected light has a polarization perpendicular to the input one and it becomes easy to separate them thanks to a polarizer. The set-up of a Faraday isolator with the corresponding polarization state is presented in figure 5.1. On the forward direction the input polarizer clean the polarization in order to get a linear polarization going through the Faraday rotator and the output polarizer is cleaning the polarization from the depolarization that could appear in the crystal (details in section 5.2). On the backward direction of propagation the output polarizer is cleaning the polarization to ensure that only a 45° linear polaization is going through the rotator and the input polarizer is reflecting the light which over the whole round trip has experienced a rotation of 90°.

5.1.2 Characteristics of Faraday isolators: isolation and throughput

The FI that we described in the previous section is a theoretical perfect one. In practice the ratios of depolarized light γ and γ_1 (see figure 5.1) are of great importance. They determined the two mains characteristics of a FI: its throughput and its isolation. γ is defined as the ratio

of depolarized light passing through the input polarizer on the backward direction (P_{depol}) and the incident power P_0:

$$\gamma = \frac{P_{depol}}{P_0} \tag{5.2}$$

We call it the depolarization of the FI and when expressed in decibel it gives us the isolation of the FI:

$$I = -10log(\gamma) \tag{5.3}$$

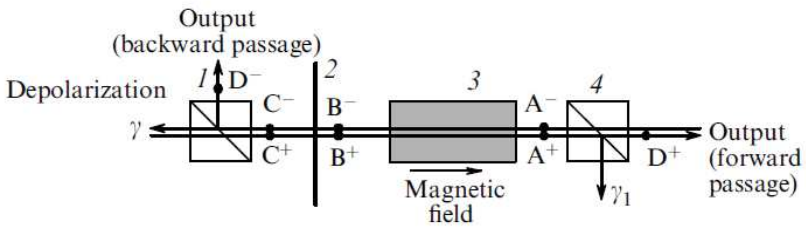

Figure 5.1: Typical design of a Faraday Isolator. A magneto optic crystal is placed in a magnetic field and they are surrounded by two polarizer. An optional half waveplate can be placed in order to finely tune the FI. (Figure from [128])

γ_1 is the ratio of depolarized light reflected on the output polarizer on the forward direction and the input power:

$$\gamma_1 = \frac{P_{depol1}}{P_0} \tag{5.4}$$

If we consider a perfectly longitudinal magnetic field with a crystal that does not introduce any depolarized light, we would have a precise rotation angle of 45° and the properties of the FI would only depend on the properties of the polarizers. The isolation ratio of the first one will indeed set the reachable isolation of the whole FI and their transmission are of great importance in the overall throughput.

But in practice crystal and magnetic field are no perfect and the depolarized light arising in the crystal is generally more important than the characteristics of the polarizers. The first default that we can speak about is a global mistuning, if the induced rotation in the rotator is not exactly 45° and the second polarizer is kept fixed, the throughput is deteriorated. One

could then think about adjusting the output polarizer to maximize the throughput, by doing that the isolation would be worsened. So special care has to be taken while setting the crystal into the magnet in order to avoid any mistuning. The deterioration of the characteristics are presented in figure 5.2.

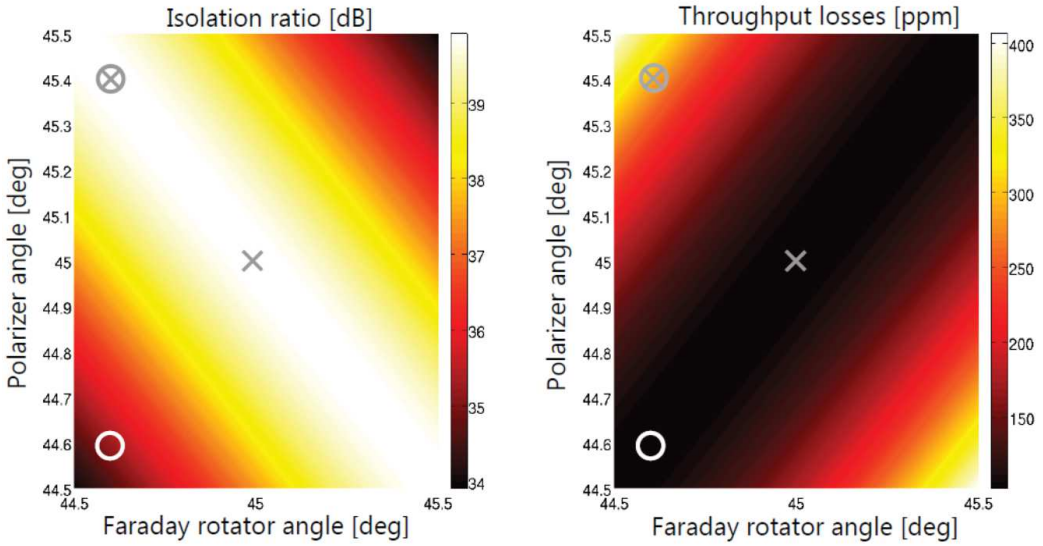

Figure 5.2: Effects of a variation of the angle of rotation of the crystal on the isolation and throughput of the FI.

Any non uniformity in the magnetic field will also contribute in the global depolarization, the macroscopic defects of the crystal will bring losses and depolarized light as well. However the most limiting effects concerning the isolation of the FI are the non linear effects that appears into the crystal because of mechanical and thermal constraints. These two points are of great importance for high power FI and we will dedicate two sections to explain the relevant mechanism that lower the isolation in those cases (respectively section 5.3 and section 5.2).

5.2 High power induced non-linear effects in Faraday Isolators

5.2.1 Heating of the crystal by absorption of laser radiation

While a Gaussian laser beam is propagating into a magneto-optic crystal, a part of its optical power is transferred into thermal power because of the relatively high absorption of those crystals. This results in an increase of the temperature inside the crystal, and because of the Gaussian shape of the beam the heating is not uniform: the medium is hotter on the beam

axis than in the outer region and this create a radial gradient of temperature.

Let us consider a TGG rod having a radius r, a length l, an absorption coefficient α and a thermal conductivity coefficient κ. This crystal is heated up by a Gaussian laser beam whose radius is r_0 and having a power P_0. In most cases we have $\alpha \ll 1/L$ and we can consider that there is no temperature gradient on the longitudinal axis, dT/dz=0. So the temperature gradient is only transverse and can be defined by the thermal diffusion equation :

$$\frac{dT}{dr} = -\frac{\alpha P_0}{2\pi\kappa}\left(\frac{1-\exp(-r^2/r_0^2)}{r}\right) \tag{5.5}$$

This non uniform temperature distribution leads to the three following thermal effects that will be detailed in the coming sections:

- A non uniform change in the Verdet constant which leads to a non uniform rotation angle over the transverse cross section of the crystal. Moreover a global error in the rotation angle can also arise from the thermal expansion of the crystal.
- A thermal lensing, mainly caused by the temperature dependence of the refractive index that non uniformly modifies the phase of the beam.
- A radial linear birefringence cause by the mechanical constraints that arises from the photoelastic effects inside the heated crystal.

In the next sections, we will define a Jones matrix model used to described these effects and especially how they affect the performance of high power FI. This will lead us to detail the work that has been done on the designs in order to reduce or suppress these effects. However before considering reducing or suppressing one could think about decreasing the temperature by dissipating the heat out of the crystal. In the equilibirum state, the global temperature of the crystal is lower without impacting too much on the temperature gradient. To do dissipate the heat, several methods are possible, first of all, the material of the crystal holder has to be chosen with a good thermal conductivity such as copper in order to dissipate the heat from the crystal. This holder can then also be cooled down either by a peltier module [129] or by a water cooling system [130]. This problem is particularly relevant for the high power FI that are working under vacuum conditions since there is no convection to cool the crystal down. In the Virgo collaboration and particularly in the optics group of EGO, many works have been done to characterize [131] and to try to mitigate this problem, especially concerning the FI that will be needed for the coming squeezing light injection in the interferometer [132].

Many works have also been carried out to built cryogenic FI. It allows to reduce the temperature of the crystal and thus to keep the thermal effects low. But the other very interesting effect that appears while cooling the TGG crystal down is that its main characteristics are improved. Its Verdet constant increase as 1/T [133], its anistotropic thermo-optical constant

Q (eq 5.14) can be reduced by a factor 5.7, its istotropic thermo-optical constant P (eq 5.8) by 6.8 [134]. This leads to a length L that can be 3.8 times shorter while cooling the crystal down to 77K.

5.2.2 Jones matrix model of a heated magneto-optic crystal

A pratical way to represent these effects is to use the Jones matrix formalism (appendix C). The material can be considered as a plate of length L, refractive index n_0, having both a circular birefringence δ_c due to the Faraday effect and a linear birefringence δ_l due to the photoelastic effect. In [135], starting from the Maxwell equations and by analyzing the electromagnetic propagation of the electric field inside such a material, Tabor and Chen gave the expression of the Jones Matrix. This matrix is widely used in the studies of magnetooptical materials. Khazanov et al in [128] gave its expression in our case, using the notation of figure 5.3 :

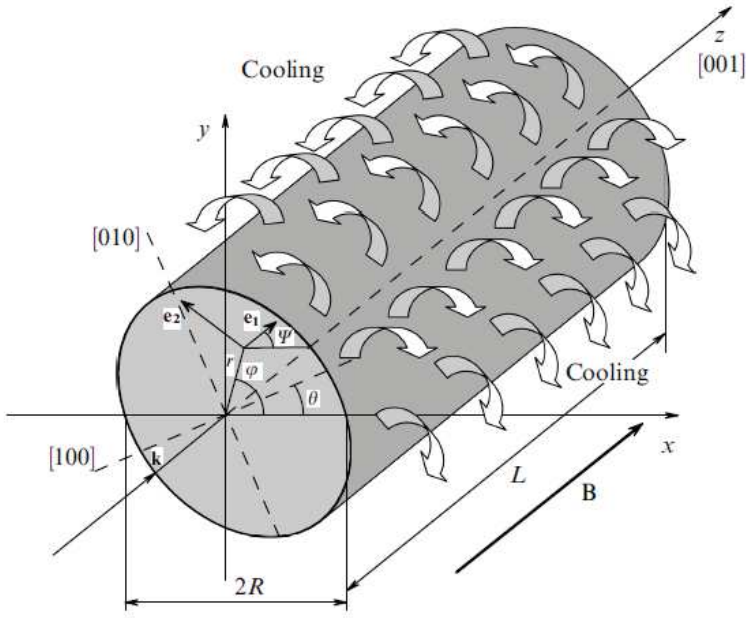

Figure 5.3: Scheme of a magneto-optic crystal with the parameters of the Jones matrix used to desribe it (equation 5.6). (figure from [128])

$$F(\delta_c, \delta_l, \Psi) = \exp(ikLn_0)\exp(ikLP(T(r) - T(0))) \times \begin{pmatrix} \cos\frac{\delta}{2} - i\frac{\delta_l}{\delta}\sin\frac{\delta}{2}\cos(2\Psi) & -\frac{\delta_c}{\delta}\sin\frac{\delta}{2} - i\frac{\delta_l}{\delta}\sin\frac{\delta}{2}\sin(2\Psi) \\ \frac{\delta_c}{\delta}\sin\frac{\delta}{2} - i\frac{\delta_l}{\delta}\sin\frac{\delta}{2}\sin(2\Psi) & \cos\frac{\delta}{2} + i\frac{\delta_l}{\delta}\sin\frac{\delta}{2}\cos(2\Psi) \end{pmatrix} \tag{5.6}$$

Where $\delta^2 = \delta_c^2 + \delta_l^2$. The linear birefringence of the material δ_l will be explicitly studied in following section. The circular birefringence δ_c is two times the angle of rotation of the polarization plane defined in equation 5.1, $\delta_c = 2\beta$. By taking into account the variation of the Verdet constant due to the radial temperature change, we have:

$$\delta_c(r) = \delta_{c0}\left(1 + \frac{1}{V}\frac{dV}{dT}(T(r) - T(r^*))\right) \tag{5.7}$$

Where r^* is the radius at which we have $\delta_{c0} = 2\beta$. In order to minimize the effect of the variation of the Verdet constant, it has been proven [136] that one has to choose a magnetic field such $\beta = \pi/4$ at $r^* = 0.92r_0$. However, we will see in section 5.2.3 that in practice the variation of the Verdet constant can be neglected in most of the cases.

The parameter P that appear in the definition of the matrix is the isotropic thermo-optical constant that we will use in the further developments. It is defined with ν the Poisson coefficient of the material and p_{ij} its photo-elastic coefficients :

$$P = \frac{dn}{dT} - \frac{1}{L}\frac{dL}{dT}\frac{n_0^3}{4}\frac{1+\nu}{1-\nu}(p_{11} + p_{12}) \tag{5.8}$$

5.2.3 Thermal dependence of the rotation angle

We saw in equation 5.1 that the rotation angle β induced by the Faraday rotator depends on the magnetic field, the length of the crystal and its Verdet constant. In the following paragraphs, we are explaining how the modification of these parameters by a temperature change is modifying the angle.

In practice the temperature of the permanent magnets surrounding the crystal is barely affected by the increase of the temperature inside the crystal and do not bring any modification in its magnetic field. However this is not true anymore when using cryogenic FI. The magnets are part of the whole design and are cooled down to low temperature as well and this influences its magnetic field. The temperature dependence is not monotonic, for example the magnetic field of the generally used Nd-Fe-B magnets increases while cooling down till a value T=160K [137] [138] and then it decreases and reaches its room temperature value again at T=77K.

In the development hereafter, we are discussing the influence of the temperature dependence of the parameters L and V. To do so, at each point of the crystal, the global

depolarization γ is separated into two components: $\gamma = \gamma_p + \gamma_V$. γ_V is the contribution coming from the changes for V whereas γ_p is the depolarization due to photo-elastic effects. This depolarization γ_p takes into account the variation of the length of the crystal, and will be fully studied in section 5.2.5. To compute the depolarization in the backward direction, one can start with a linear polarization, compute the depolarization at each point of the cross section of the crystal, using the matrix of the crystal defined in equation 5.6, and analyzed the transmission through the input polarizer. Then by integrating over the whole cross section of the crystal we can make appear the two contributions γ_p and γ_V. For γ_p two cases have to be considered depending on the value of the optical anisotropy of the crystal ξ (eq 5.11) defined thanks to its photoelastic coefficients.

$$\begin{aligned} \gamma_p &= A_p p^2, \quad \text{if } |\,\xi\,| \geqslant 1 \\ &= A_p p^2 \xi^2, \quad \text{if } |\,\xi\,| < 1 \end{aligned} \tag{5.9}$$

$$\gamma_V = A_V p_V^2 \tag{5.10}$$

$$\xi = \frac{2p_{44}}{p_{11} - p_{12}} \tag{5.11}$$

A_p and A_V are constants that depend on the shape of the beam. Their litteral expression and values can be found in [128] and in our case, for a Gaussian beam, we have $A_p = 0.0139$ and $A_V = 0.067$. The parameter p and p_V are defined as follow:

$$p_V = \frac{\alpha P_0}{8\kappa}\left(\frac{1}{V}\frac{dV}{dT}\right) \tag{5.12}$$

$$p = \frac{L}{\lambda}\frac{\alpha Q}{\kappa}P_0 \tag{5.13}$$

Where Q is the anisotropic thermo-optical constant of the crystal:

$$Q = \frac{1}{L}\frac{dL}{dT}\frac{n_0^3}{4}\frac{1+\nu}{1-\nu}(p_{11} - p_{12}) \tag{5.14}$$

An equal contribution of both components can be obtained by giving a condition on the length of the crystal:

$$\gamma_V = \gamma_p \Leftrightarrow A_V p_V^2 = A_p p^2 \Leftrightarrow A_V \left(\frac{\alpha P_0}{8\kappa}\frac{1}{V}\frac{dV}{dT}\right)^2 = A_p \left(\frac{L^*}{\lambda}\frac{\alpha Q}{\kappa}P_0\right)^2 \tag{5.15}$$

$$L^* = \sqrt{\frac{A_v}{A_P}}\frac{\lambda}{8Q}\left(\frac{1}{V}\frac{dV}{dT}\right), \mid \xi \mid \geqslant 1 \tag{5.16}$$

$$L^* = \sqrt{\frac{A_v}{A_P}}\frac{\lambda}{8Q\xi}\left(\frac{1}{V}\frac{dV}{dT}\right), \mid \xi \mid < 1 \tag{5.17}$$

In practice the characteristic values for a TGG crystal can slightly vary from one crystal to another one but we can take the following values to compute an approximative critical length in a worst case: $\xi = 1$ for a [111] cut, $Q = -17 \times 10^{-7} K^{-1}$ with $\kappa = 5 W K^{-1} m^{-1}$ [139], $V^{-1}dV/dT = 3.5 \times 10^{-3} K^{-1}$ [133]. With such parameters the numerical evaluation of the critical length is approximately 6×10^{-4} m, which is much shorter than the length of the crystal that are generally used in FI. So the dominating depolarization contribution is the one coming from the photo-elastic effect and there is no need for compensating the change of the Verdet constant. However this is not valid anymore in the cryogenic FIs that we detailed in section 5.2.1. At lower temperature there is indeed an increase in the term $V^{-1}dV/dT$ and at 77 K the numerical evaluation of the critical length L* is 13 mm which is of the same order of magnitude than the length of the crystals that are used.

5.2.4 Beam distorsion and thermal lensing

Thermal lensing is an effect that arises from the non-linear heating of the material. It appears in every material but can be neglected in general. In our case however since we are working with high power beam and crystals that have a relatively high absorption, it is of particular importance as it has been highlighted in [140] where they studied its effect in interferometric gravitational waves detectors.

Formally the effects of beam distortion can be computed by taking the difference from unity of the overlapping between the actual beam and a perfect one using the equation 2.19. It gives a value γ_h that have 2 contributions, an isotropic one γ_i and the anisotropic one that has already been defined before γ_p (equation 5.9) [128]:

$$\gamma_h = \gamma_a + \gamma_i \tag{5.18}$$

$$\gamma_i = A_i p_i^2 \tag{5.19}$$

$$p_i = \frac{L}{\lambda}\frac{\alpha P}{\kappa} P_0 \tag{5.20}$$

Where A_i=0.067 is the case of a Gaussian beam [128]. The isotropic contribution is the non-parabolic thermal lens that comes from the phase shift induced by the radial gradient of

refractive index. The anisotropic contribution is coming from the spatial depolarization of the beam (see section 5.2.5) which modifies both its phase and its amplitude while passing through a polarizer. This value of γ_h gives the information on the beam distortion, however the most usual and convenient way to approximate the effects is to define an equivalent ideal lens whose focal length is given in the case of a Gaussian beam by [128]:

$$f = \frac{4\pi\kappa w^2}{L\alpha P_0 P} \tag{5.21}$$

Where w is the width of the beam, P_0 is its power, L is the length of the crystal, α is its absorption, κ is its thermal conductivity and P is the isotropic thermo-optical constant that we defined in equation 5.8. The values for the TGG crystal can slightly vary from one crystal to another, from one manufacturer to another. They have been reviewed in [128] and here are the values that we took to compute the thermal lens in a general: $\alpha = 1.5 \times 10^{-3} cm^{-1}$, $\kappa = 7.4 W/m/K$ $P = 17 \times 10^{-6}$. With these values we have a thermal lens of about 300 m at 1 W and it is getting down to 2 m for 200 W. So this effect is also of particular importance while considering the fibering of the FI since it modifies the Gaussian propagation and thus the mode matching into the fiber. It also introduces HOM that do not propagate in the fiber.

5.2.5 Thermal depolarization due to photo-elastic effects

As we highlighted in the previous section, in most cases the main contribution of depolarization in FI is coming from the thermally induced photo-elastic effects. In this section we are detailing this photo-elastic depolarization ratio γ_p (eq 5.9) that we used in section 5.2.3.

5.2.5.1 Thermally induced linear birefringence

The photoelastic effects that arises in the crystal due to its heating is described by both the value of its linear birefringence $\delta_l(r, \varphi)$ (equation 5.22) and the direction of its eigenpolarization axis given by the angle $\Psi(r, \varphi)$ (equation 5.23). The angle φ and θ that appear in this equation are respectively the angle of the cylindrical coordinates system and the angle of the crystal axis as defined in figure 5.3. The parameter ξ is the optical anisotropy of the crystal defined in the equation 5.11.

$$\delta_l(r, \varphi) = 2kLQ\sqrt{\cos^2(2\varphi - 2\theta) + \xi^2 \sin^2(2\varphi - 2\theta)} \times \left(\frac{1}{r^2}\int_0^r r^2 \frac{dT}{dr} dr\right) \tag{5.22}$$

$$\tan(2\Psi - 2\theta) = \xi \tan(2\varphi - 2\theta) \tag{5.23}$$

By substituting the thermal gradient induced by a Gaussian beam defined in equation 5.5, the integration of the equation 5.22 gives us:

$$\delta_l(r,\varphi) = p\frac{r^2/r_0^2 + \exp(-r^2/r_0^2) - 1}{r^2/r_0^2} \times \sqrt{\cos^2(2\varphi - 2\theta) + \xi^2 \sin^2(2\varphi - 2\theta)} \tag{5.24}$$

5.2.5.2 Effects on the depolarization without magnetic field

With this definition of the depolarization induced by linear birefringence, we can estimate its contribution in the depolarization of the FI. This depolarization will deteriorate both the throughput on the forward direction and the isolation in the backward direction, the most critical parameter being the isolation. Let us consider two cases to better understand this depolarization effect: a TGG rod with and without magnetic field.

For each point (r,φ) the Jones matrix $F_{OM}(r,\varphi)$ of the element can be defined by the matrix of a phase retarder rotated by the angle Ψ :

$$\begin{aligned} F_{OM}(r,\varphi) &= \begin{pmatrix} \cos(\Psi) & -\sin(\Psi) \\ \sin(\Psi) & \cos(\Psi) \end{pmatrix} \begin{pmatrix} e^{-i\delta_l(r,\varphi)} & 0 \\ 0 & e^{i\delta_l(r,\varphi)} \end{pmatrix} \begin{pmatrix} \cos(\Psi) & \sin(\Psi) \\ -\sin(\Psi) & \cos(\Psi) \end{pmatrix} \\ &= \sin\left(\frac{\delta_l(r,\varphi)}{2}\right) \begin{pmatrix} \cot\left(\frac{\delta_l(r,\varphi)}{2}\right) - i\cos(2\Psi) & -i\sin(2\Psi) \\ -i\sin(2\Psi) & \cot\left(\frac{\delta_l(r,\varphi)}{2}\right) - i\cos(2\Psi) \end{pmatrix} \end{aligned} \tag{5.25}$$

One could notice that this matrix could also be obtained by evaluating the general Jones matrix of a heated magneto-optical element given in equation 5.6, with δ_c=0 (i.e. without magnetic field) and by neglecting the phase retardation terms $\exp(ikLn_0)$ and $\exp(ikLP(T(r) - T(0)))$.

Let us consider the crystal between crossed polarizers, with a Gaussian input beam polarized on the horizontal axis: $\boldsymbol{E_0} = E_0(r)(1,0)$. The beam at the output can be computed thanks to the Jones matrix defined previously:

$$\begin{aligned} \boldsymbol{E_{out}} &= F_{OM}(r,\varphi)\boldsymbol{E_0} \\ &= \cos\left(\frac{\delta_l(r,\varphi)}{2}\right)\boldsymbol{E_0} - i\sin\left(\frac{\delta_l(r,\varphi)}{2}\right) E_0(r)[\cos(2\Psi)\boldsymbol{E_x} + \sin(2\Psi)\boldsymbol{E_y}] \end{aligned} \tag{5.26}$$

Through the second polarizer we get :

$$\begin{aligned} \boldsymbol{E_{depol}} &= \begin{pmatrix} 0 & 0 \\ 0 & 1 \end{pmatrix} \boldsymbol{E_{out}} \\ \boldsymbol{E_{depol}} &= \sin\left(\frac{\delta_l(r,\varphi)}{2}\right) E_0(r)\sin(2\Psi)\boldsymbol{E_y} \end{aligned} \tag{5.27}$$

From this equation of the depolarized electric field we can get the intensity of the depolarized light :

$$I_{depol}(r,\varphi) = \boldsymbol{E_{depol}}\boldsymbol{E^*_{depol}} = \sin^2\left(\frac{\delta_l(r,\varphi)}{2}\right) E_0^2(r)\sin^2(2\varphi) \tag{5.28}$$

Thanks to this equation we can plot the depolarization figure as a function of r and φ. It presents a characteristic shamrock shape (figure 5.4). Qualitatively this shape can be understood by noticing that when the eigen axis of the linear birefringence is oriented along or perpendicular to the output polarizer axis, the introduced phase shift does not have any effect. On the contrary the effect is maximum when the eigen axis of the linear birefringence form a $\pi/4$ angle with the axis of the polarizer.

The global depolarization ratio γ_0 is finally obtained by integrating the local depolarized intensity $I_{depol}(r,\varphi)$ over the cross section of the crystal, and normalizing it by the average input power: $P_0 = E_0^2 \times \pi r_0^2$:

$$\gamma_0 = \frac{P_{depol}}{P_0} = \frac{1}{E_0^2 \times \pi r_0^2}\int_0^r \int_0^{2\pi} I_{depol}(r,\varphi) r dr d\varphi \tag{5.29}$$

Khazanov et al give an analytic expression for this depolarization ratio without magnetic field [141]:

$$\gamma_0 = p^2 \frac{A_1}{8}(1 + (\xi - 1)\cos(2\theta)) \tag{5.30}$$

Where θ is the angle between the crystal axis and the horizontal axis as defined in figure 5.3. $A_1 = 0.137$ is obtained by numerically evaluate the following integral that appears in the calculus:

$$A_1 = \int_0^\infty \exp(-y) \left(\frac{1}{y} - \frac{\exp(-y)}{y-1} \right)^2 dy \tag{5.31}$$

5.2.5.3 Effects on the depolarization with magnetic field

The calculations while considering the crystal with and without magnetic field are globally the same but one has to use the matrix $F(r, \varphi)$ defined in equation 5.6 that makes appear the circular birefringence. Moreover, since the laser beam polarization is rotated by an angle of $\pi/4$ while passing through the crystal, we are also considering a half waveplate set at $3\pi/8$ used to realign the beam on the output polarizer. This finally lead to the following equation:

$$\boldsymbol{E_{depol}} = \begin{pmatrix} 0 & 0 \\ 0 & 1 \end{pmatrix} R(\frac{3\pi}{8}) F(\delta_c, \delta_l) \boldsymbol{E_0} \tag{5.32}$$

By making the assumption, true in practice, that $\delta_l \ll 1$, and that $\delta_c(r) - \delta_{c0} \ll \delta_{c0}$ we can find the local depolarization ratio [128]:

$$\Gamma_p(r, \varphi) = \frac{2\delta_l^2}{\pi^2} \sin^2(2\Psi(r, \varphi) - \frac{\pi}{4}) \tag{5.33}$$

And by integrating over the cross section of the crystal we get the global depolarization:

$$\gamma_p = A_p p^2 \left(1 + (\xi^2 - 1) \cos^2(\frac{\pi}{4} - 2\theta) \right) \tag{5.34}$$

So thanks to this development we found back the equation of γ_p (eq 5.9) that we used in the development of the section 5.2.3. From this equation we can clearly see that by setting the axis of the crystal such as $\theta = \pi/8$ when $\mid \xi \mid < 1$ and $\theta = 3\pi/8$ when $\mid \xi \mid > 1$, the non decoupling is minimized.

The second point to notice is that the depolarization figure is turned by an angle of $\pi/8$ (see figure 5.4). Mathematically we can see it in the equation of the local depolarization ratio 5.33, considering for example a crystal with $\xi > 1$ with its axis set at $3\pi/8$. On this axis according to equation 5.23, we have $\Psi = \varphi = 3\pi/8$. By reinjecting it in formula 5.34 we have indeed a maximum as it can be seen on the depolarization figure.

This rotation of the depolarization figure can also be understood in terms of mode coupling. Indeed another approach is to consider the depolarized light along the crystal layer by layer, in a model similar to the one that we used to described the behavior of PM fiber in section 2.2.3.2. In such a model for each layer of crystal the incident electric field will be

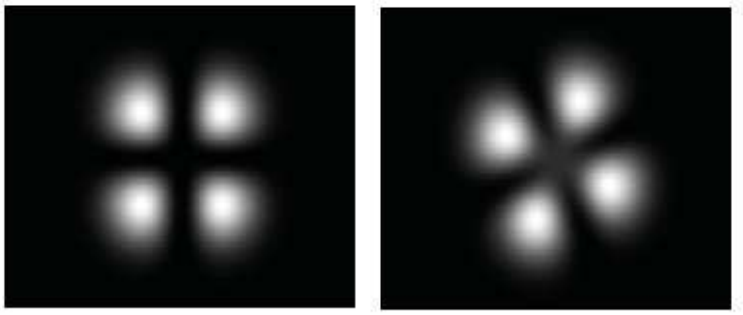

Figure 5.4: Figures of depolarization of a magneto-optic crystal heated by a laser beam with a magnetic field (left) and without magnetic field (right). The figure is rotated by an angle of $\pi/8$.

decomposed in the basis of the eigen axes, it will experience a phase shift due to the linear birefringence, and will be then rotated by the Faraday effect. In the following layer, these two rotated components of the electric field are decomposed again on the eigen axes of the birefringence. Thus one can define an equivalent birefrigence $\delta_l^*(r,\varphi)$ with a direction and value that is an average over the rotation angle of the Faraday rotator.

$$\begin{aligned}
\delta_l^*(r,\varphi) &= \int_{\varphi}^{\varphi+\pi/4} \cos(\alpha)\delta_l(r,\varphi)d\alpha\ \boldsymbol{ex} + \int_{\varphi}^{\varphi+\pi/4} \sin(\alpha)\delta_l(r,\varphi)d\alpha\ \boldsymbol{ey} \\
&= [\sin(\varphi+\pi/4) - \sin(\varphi)]\delta_l(r,\varphi)\ \boldsymbol{ex} - [\cos(\varphi+\pi/4) - \cos(\varphi)]\delta_l(r,\varphi)\ \boldsymbol{ey} \\
&= 2\cos(\varphi+\pi/8)\sin(\pi/8)\delta_l(r,\varphi)\ \boldsymbol{ex} + 2\sin(\varphi+\pi/8)\sin(\pi/8)\delta_l(r,\varphi)\ \boldsymbol{ey} \\
&= 2\sin(\pi/8)\delta_l(r,\varphi)[\cos(\varphi+\pi/8)\ \boldsymbol{ex} + \sin(\varphi+\pi/8)\ \boldsymbol{ey}] \\
&\simeq 0.77\ \delta_l(r,\varphi)\ \boldsymbol{e_{\varphi+\pi/8}}
\end{aligned} \tag{5.35}$$

For example if we consider a point at $\varphi = 3\pi/8$, where the depolarized light is maximum. The equivalent birefringence δ_l^* that is seen by an electric field at that point will be given by:

$$\begin{aligned}
\delta_l^*(r,\frac{3\pi}{8}) &= \int_{3\pi/8}^{5\pi/8} \cos(\alpha)\delta_l(r,\frac{3\pi}{8})d\alpha\ \boldsymbol{ex} + \int_{3\pi/8}^{5\pi/8} \sin(\alpha)\delta_l(r,\frac{3\pi}{8})d\alpha\ \boldsymbol{ey} \\
&= \int_{3\pi/8}^{5\pi/8} \sin(\alpha)\delta_l(r,\frac{3\pi}{8})d\alpha\ \boldsymbol{ey} \\
&\simeq 0.77\ \delta_l(r,\frac{3\pi}{8})\ \boldsymbol{ey}
\end{aligned} \tag{5.36}$$

The axis of the resulting birefringence is vertical. An input electric field will be decomposed on this two axes and will experience a phase shift proportional to $0.77\delta_l$. It is then rotated by the half waveplate of the set-up set at $3\pi/8$, which finally orientates the eigen axis of the equivalent birefringence at $\pi/4$. This gives indeed a maximum of depolarized light while passing through the output polarizer. So this averaging explains while the depolarization figure is turned by an angle of $\beta/2$. This also highlights a fact which is not explicitly mentioned in papers: the effects of a pure photoelastic depolarization are lower when the crystal is put into the magnet. By comparing the equations of the global depolarization with magnetic field γ_p (5.34) and without magnetic field γ_0 (5.29), it is however possible to get back to a similar value:

$$\frac{\gamma_p}{\gamma_0} = \frac{A_p}{A_0/8} \simeq 0.81 \tag{5.37}$$

While doing matlab simulations, we saw this decrease of the depolarization while putting the crystal in the magnet (see figure 5.5). In practice, however, this improvement can not be observed because it is too small compare to all the other defaults that arise while inserting the crystal inside the magnet, such as the non homogeneity of the magnetic field inside the magnet, that lead to local mistuning of the rotation angle.

5.2.5.4 Investigation on the use of longer crystals

Another idea, considering this averaging of the depolarized light is to consider FI designs having greater rotational angle: $3\pi/4$, $5\pi/4$ or $7\pi/4$. We did not have any magnet and/or crystal long enough to perform some experimental tests, but we did the Matlab simulation of such designs and confirmed the improvement (see figure 5.5).

However, in practice, longer crystal would increase the absorption losses and other non-linear effects such as thermal lensing (sec 5.2.4). Compare to advanced designs that are also compensating for depolarization with good performances by introducing other optical elements (detailed in section 5.2.6), this design as the advantage of its simplicity and to not increase the number of interfaces. A compromise between the length of the crystal and the increase in the isolation that could be of interest is the design having a rotational angle of $3\pi/4$. It enhances the isolation at high power by 10dB by increasing the length by a factor 3. So the focal length of the equivalent lens due to thermal lensing is 3 times shorter (equation 5.21) and the losses due to absorption three times greater. Let us compare the absorption of a design with a crystal 3 times longer and an advanced design using a crystal of usual length (20mm) and two more optical components (figure 5.6 c). With an absorption of $1.3 \times 10^{-3} cm^{-1}$ [134] and a reflection of 0.1% at each interface, we get theoretical losses of 9.8×10^{-3} in the first case and 10.6×10^{-3} in the second case. So the losses in the two designs are of the same order of magnitude. If thermal lensing is not a problem in the application or if one has a good scheme to compensate for it, due to is simplicity the design using a crystal 3 times longer could be of interest.

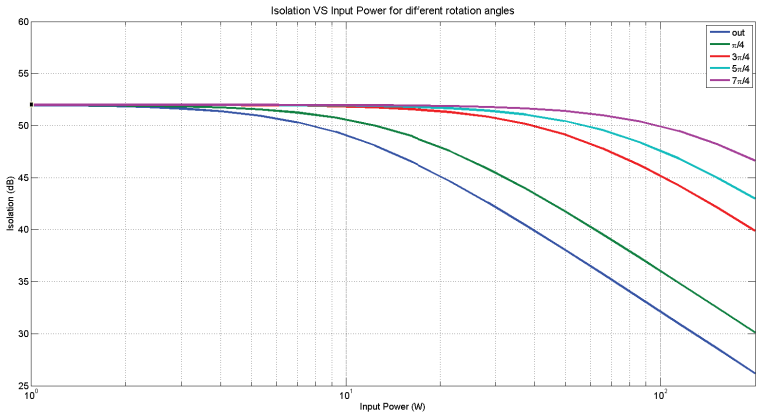

Figure 5.5: Results of the Matlab simulation on the isolation that would have FI having a greater rotation angle. The initial depolarization was set to 52 dB and we plotted it against the optical power heating the crystal.

5.2.6 Advanced designs

Based on the same idea of self cancellation of the depolarized light, some advanced designs have been developed [142]. They are presented in figure 5.6. The idea of the two first ones is to separate the rotation angle of $\pi/4$ into two rotation of $\pi/8$ by using two crystal and to rotate the polarization between the two. By doing this, instead of averaging the depolarization over the rotation angle, they are averaging on two sections and the depolarized light of the first crystal will be canceled by the second one. In the third design, they are using an absorber element having a thermally induced birefringence similar to the one of the crystal.

5.3 Effects of mechanical constraints on the crystal

5.3.1 Observations and motivations

While working with a FI with a TGG having a [111] cut, we noticed some unusual behaviors such as the unbalanced lobes of the depolarization figure that can be seen on figure 5.7, or that despite it [111] cut the crystal had a preferential orientation that was minimizing the isolation (blue curve of the figure 5.10). We investigated it and it appeared that it was coming from the constraints that the holder was applying on the crystal. In this section we are detailing the investigation on those constraints that we did through Matlab simulations and experimental work. We will see how these mechanical constraints affect the depolarization but also how they could be used to decrease the thermal induced depolarization due to photo-elastic effects that we saw in section 5.2.5.

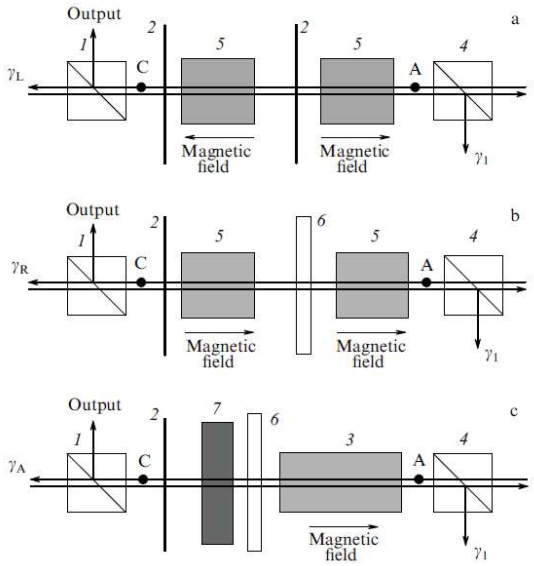

Figure 5.6: Advanced design of FI in order to decrease the depolarized light. (a) design with a half waveplate, (b) design with a reciprocal rotator (c) design with an absorber element. 1,4: polarizers ; 2: half waveplate ; 3: Crystal rotation of $\pi/4$; 5: Crystal rotation of $\pi/8$; 6: 67.5° reciprocal rotator ; 7: optical absorber. (Figure from [128])

5.3.2 Mechanically induced birefingence model

To do the simulation we were considering a TGG rod having characterisitcs close to the ones of the crystals used for the experiments : a [111] cut, a diameter d of 12mm, a length L of 18mm, an absorption $\alpha = 2.3 \times 10^{-3}$ cm^{-1} , a thermal conductivity $\kappa = 7.4$ W/K/m and an anisotropic thermo-optical constant Q = 5.5×10^{-6}. This crystal was heated by a 1mm-radius Gaussian beam of power P_0 and stressed by a force F that was applied on an axis defined by its angle θ (see figure 5.8) The depolarized light was obtained thanks to the formula 5.28 and was integrated over the cross section of the crystal to get the global depolarization (eq 5.2) and the equivalent isolation (eq 5.3). On this crystal we were applying a stress F at an angle θ. We used the model presented in [143] and [144] to compute the effects of this stress on the birefringence of the crystal. This model is for a YAG crystal, however both this YAG crystal and the TGG that we are using have a [111] cut and we will see through the development hereafter that we can use it in a first approach. The resulting changes in the refractive indices are given by the following equations :

$$\begin{cases} n_x = n + C_x\sigma_x + C_y\sigma_y \\ n_y = n + C_x\sigma_y + C_y\sigma_x \end{cases} \tag{5.38}$$

Where C_x and C_y are constants that depend on the crystal, and σ_x and σ_y are the stresses

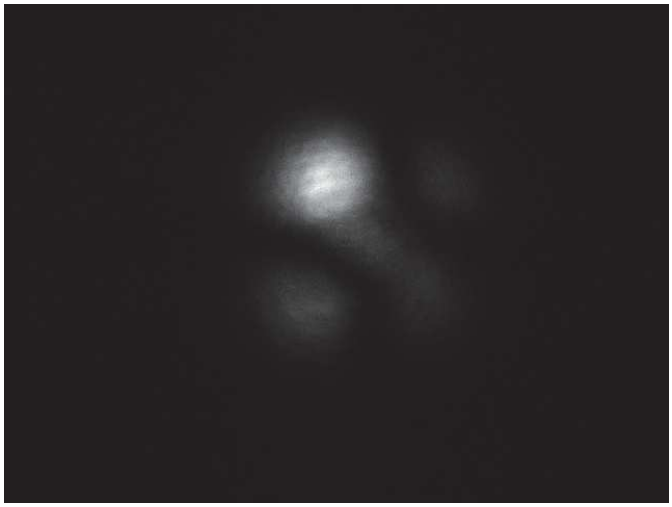

Figure 5.7: Typical unbalanced figure of depolarization that was observed while working with a TGG crystal at high power. The expected one is presented in figure 5.4.

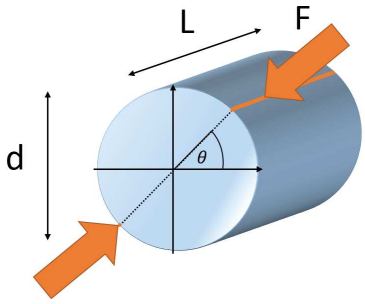

Figure 5.8: TGG rod crystal of length L and diameter d mechanically stressed by applying a force F with an angle θ

on the x and y direction. One can then compute the induced birefringence:

$$\Delta n = n_x - n_y = (C_x - C_y)(\sigma_x - \sigma_y) \tag{5.39}$$

In the model of the YAG on which we based this model they give the following values for the stresses [144]:

$$\begin{cases} \sigma_x = & 2F/\pi Ld \\ \sigma_y = & -6F/\pi Ld \end{cases} \tag{5.40}$$

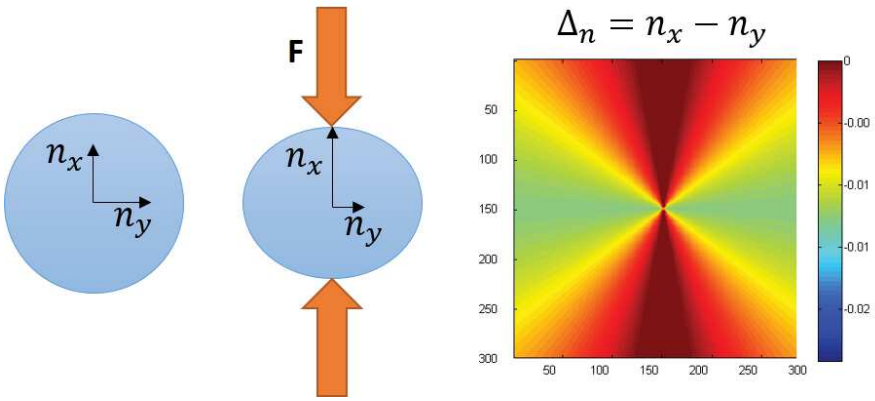

Figure 5.9: Mechanical birefringence arising in the crystal rod while stressing it with a force F on the vertical axis

Where L is the length of the crystal and d its diameter. So we finally get the following expression for the induced birefringence:

$$\Delta n = (C_x - C_y)\frac{8}{\pi dl}F \tag{5.41}$$

This equation can be written under the following form:

$$\Delta n = \frac{d\Delta n}{dF}F \tag{5.42}$$

where $\Delta n/dF = (C_x - C_y)/8\pi dl$ is the variation of birefringence according to the applied force. In the case of the TGG crystal that we are using we do not know the value $d\Delta n/dF$ but in the simulation we fixed an arbitrary value and were making F varying in arbitrary units. In the experimental works that we carried out the intensity of the stress that was applied was also unknown. In figure 5.9, one can see a graphic representation of the effect as well as the resulting birefringence.

We confirmed the behavior that had been experimentally observed: while stressing the crystal there are preferential angles at which the depolarized light is minimum. The experimental and simulated results are presented in figure 5.10. The simulation allowed us to get similar results but does not fully explain the observations, especially the amplitude between the maximum and the minimum of depolarized light. We confirmed also that at a given angle and a given power, the more stress is applied on the crystal, the more depolarized light there is (see figure 5.11). This is an effect that want to be avoid in Faraday Isolator, however we will see in the next paragraph that by carefully choosing the applied stress one can actually partially compensate for the depolarization due to the thermal effects.

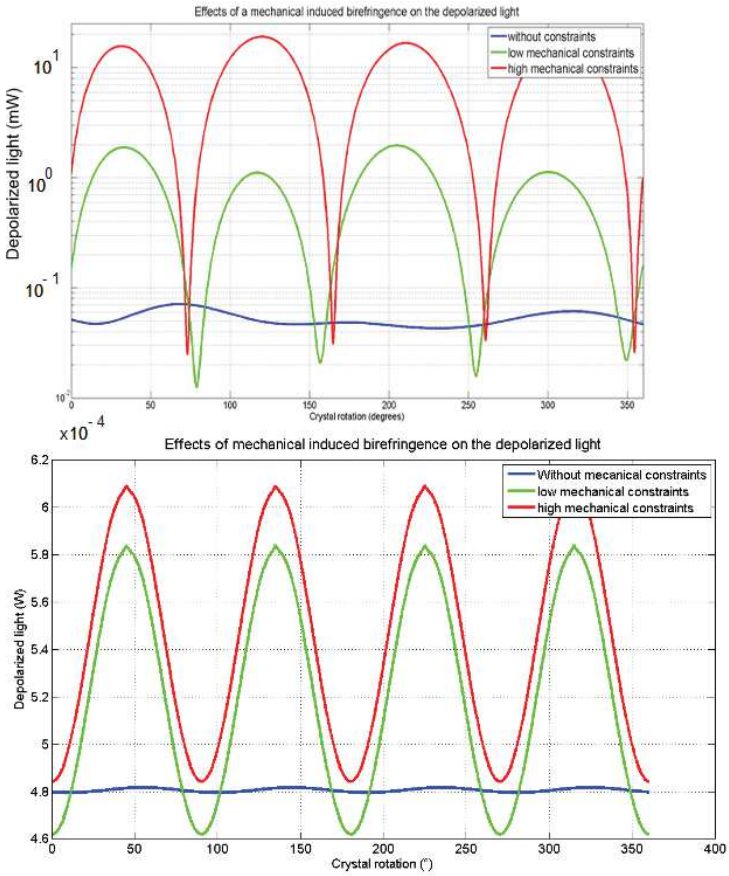

Figure 5.10: Influence of the rotation of the crystal on the depolarized light, without stress (blue), with low stress (green) and with high stress (red). The crystal was not subject to thermal depolarization. Experimental results are shown on the top figure and the simulated one on the bottom. To be noticed that the experimental results are plotted in a logarithmic scale while the simulated one are in a linear one. Even if a similar behavior has been observed, the amplitude of the effects was greater in practice than in theory.

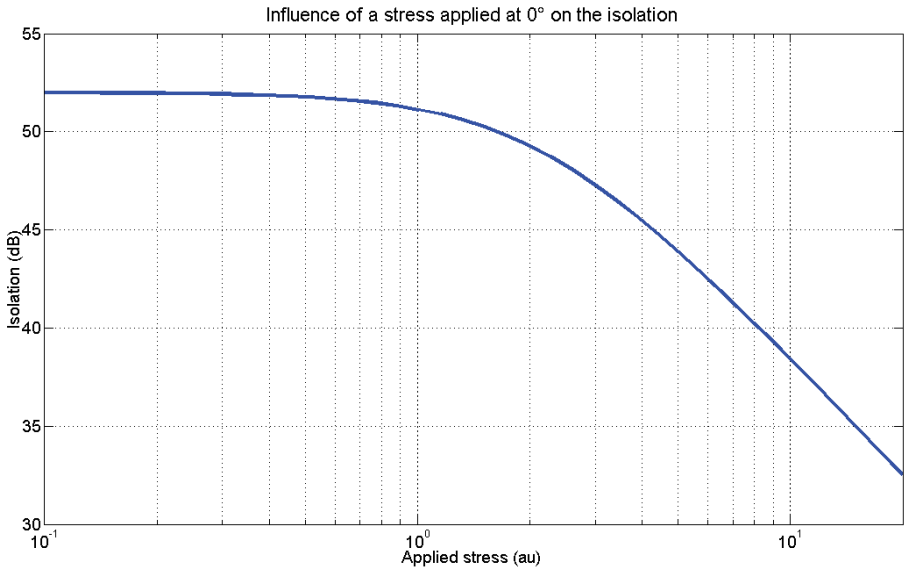

Figure 5.11: Simulation of the isolation dependence on a mechanical stress applied on the vertical axis.

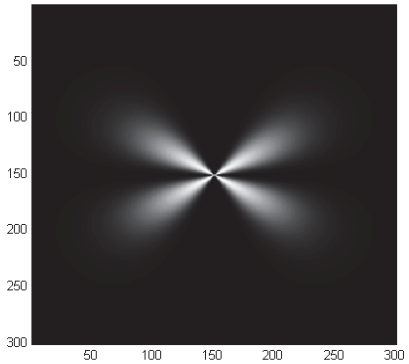

Figure 5.12: Figure of depolarization for a non-heated crystal subject to a mechanical stress on the vertical axis.

5.3.3 Compensation for the thermally induced birefringence

The depolarization figure of a mechanically stressed crystal is presented in figure 5.12. It has been simulated without heating the crystal. One can see that similarly to the heated depolarization figure, this one is presenting a kind of shamrock shape with four lobes on the diagonal axes. However, what is important to notice here, is that this depolarization figure is due to a diminution of the refractive index on the radial direction and not an increase like in the case of the heated crystal. Indeed, due to the coefficients 2 and -6 of the equation 5.40, the effects on the refractive index of the dilatation of the crystal are greater than the ones of the compression (see figure 5.9). The idea is then to use this dilatation on the diagonal axis to compensate for the thermally induced birefringence.

We simulated many different cases to see the improvements that could bring other stress mapping, such as stressing the crystals on two axes (perpendicular or not), applying different level of stress (balanced or unbalanced). The main outcomes of these simulations are presented in figure 5.13. The 0° axis the horizontal axis while 90° is the vertical one. As explain in the previous section, the different levels of stress that are applied are in relative units since the $d\Delta n/dF$ of the unknown and has been arbitrarily fixed. For each case, the different stress parameters are summarized in the table on the left, then we are presenting, from left to right, the mechanical birefringence, the depolarization mechanically induced, the birefringence induced both by the heating and by the stress of the crystal, the depolarized light induced by heating and stress, and finally the associated isolation. The input power was fixed at 40 W and the axes of the analyzing polarizer were horizontal/vertical. For each column there is a common scale that is displayed at the bottom. The birefringence is without unit while the depolarized light is given in microwatt for the considered pixel. There are 1200 × 1200 pixels and each of it has a size of 10 × 10 µm.

In the first case, no stress is applied, it serves as a reference. In the second case we applied a first stress, it also serves as a reference to see the influence of a basic stress. In the third case, we optimized the force F_1 in order to maximize the isolation. In cases 4 5 and 6, we were applying stresses on the vertical and horizontal axis. The fourth one serves as reference, while in the fifth and sixth case we maximized the isolation by respectively increasing F_2 while keeping F_1 fixed and by increasing F_1 and F_2 together. In cases 7 and 8, we were investigating the possibility of applying the stress on different axes than the previous ones. The applied stress in these cases have been increase simultaneously till reaching a maximum of isolation.

As one could intuitively expect the best case is when the stress is applied homogeneously on the vertical and horizontal axes (case 6). It creates the needed negative birefringence on the diagonal axes that balances the birefringence induced by the heating of the crystal. In the rest of the simulations and experiments that we are presenting hereafter we were using this stress mapping.

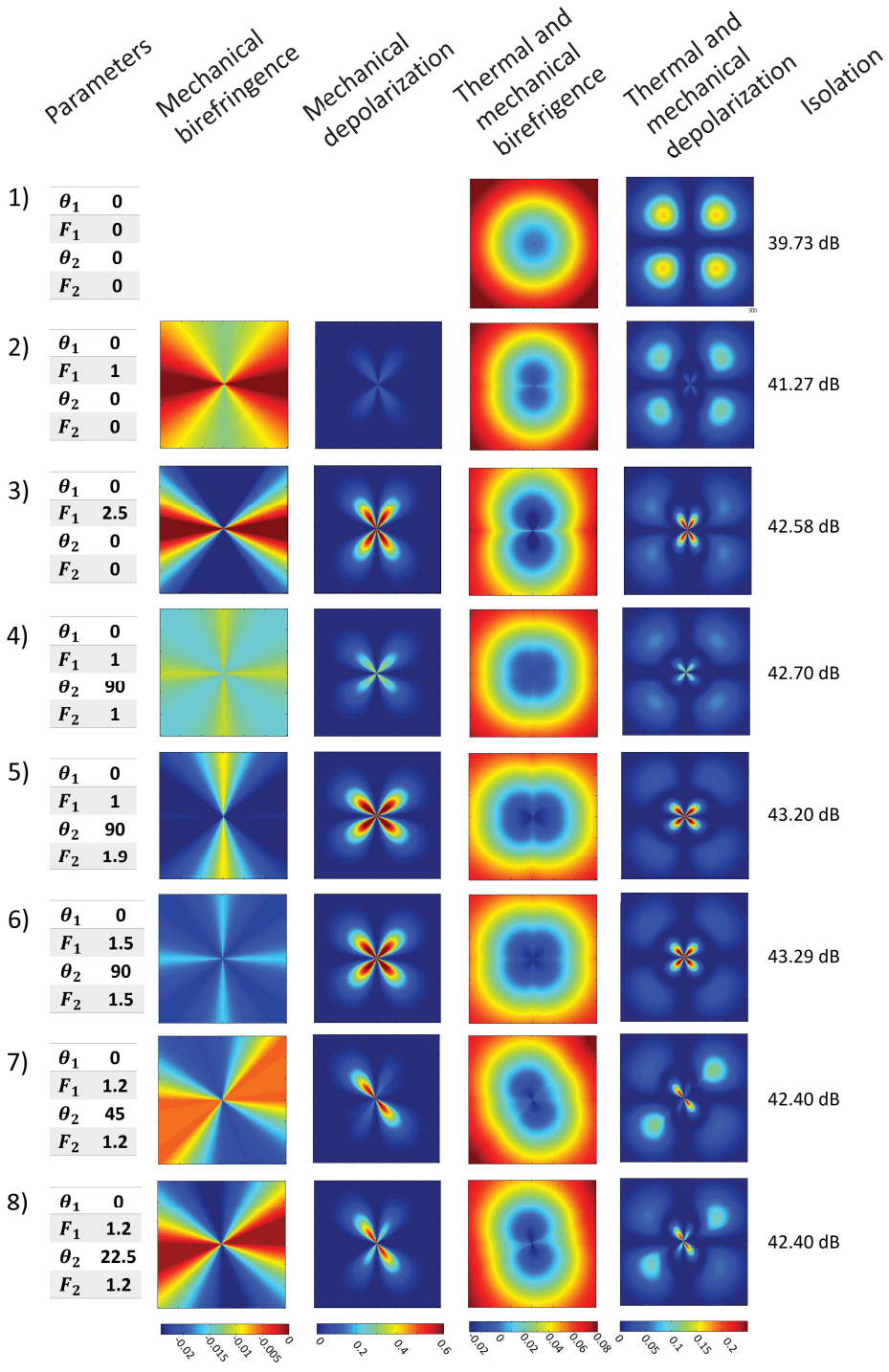

Figure 5.13: Main outcomes of the investigation on the stress mapping of the crystal. The best case is obtained while stressing on the vertical and horizontal axis with a similar stress.

In figure 5.14, we set a stress and were making the power varying. At low power the mechanical stress is deteriorating the performances, while at high power the depolarized light has it usual $1/P^2$ behavior that comes from the heating of the crystal. But the interesting point lies in between, around 17W of input power, when the mechanical stress is compensating for the thermal depolarization. These simulated results have been experimentally confirmed and the results of the experiments are presented in figure 5.15. On this figure one can also see the different depolarization figure, the lobes of the shamrock shape are unbalanced, but it can be seen that the depolarization mainly depend on the mechanical stress at low power and to the thermal one at high power.

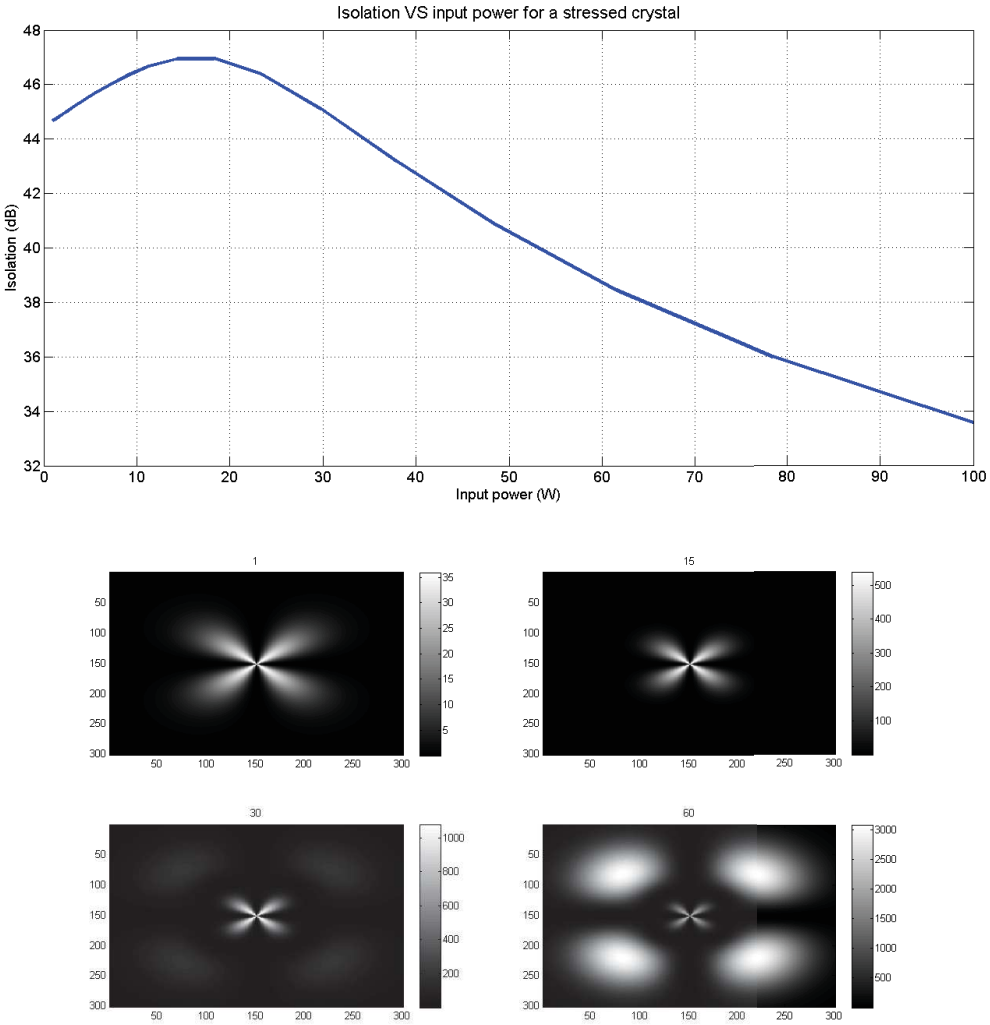

Figure 5.14: Simulated results of the isolation at different power for a given stress and the associated figures of depolarization for 1 W 15 W 30 W and 60 W.

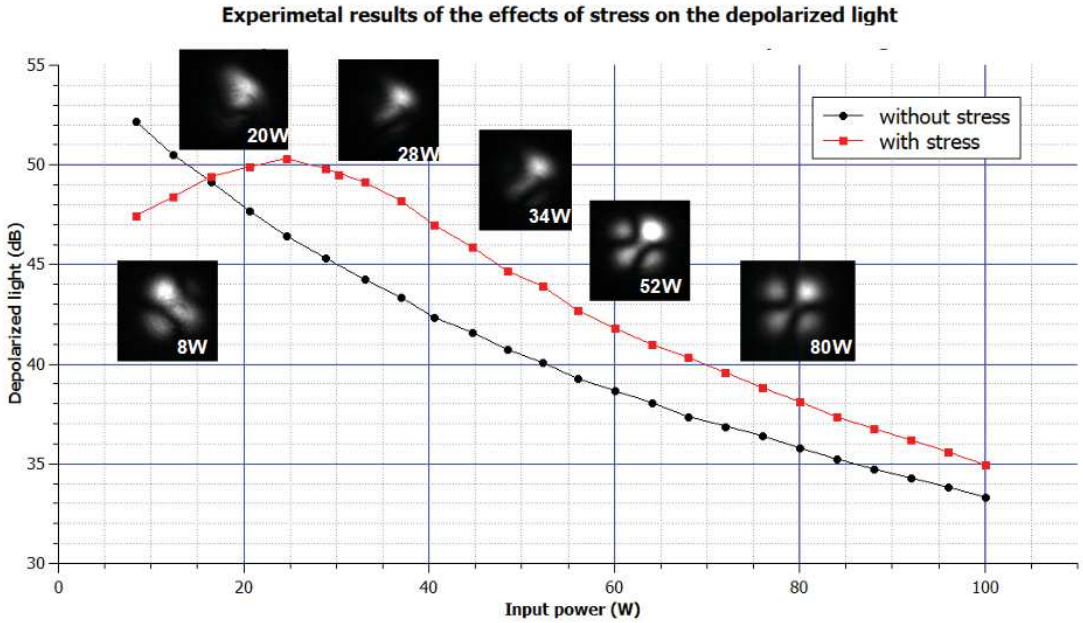

Figure 5.15: Experimental results of the effect of mechanical stress on the depolarized light and the associated figures of depolarization

We confirmed these results for different applied stress. On figure 5.16 you can see both the experimental results and the simulated one. A higher stress deteriorates the depolarized light at low power but is leading to an optimum at higher power. The experimental results are actually giving better improvement than the simulated ones.

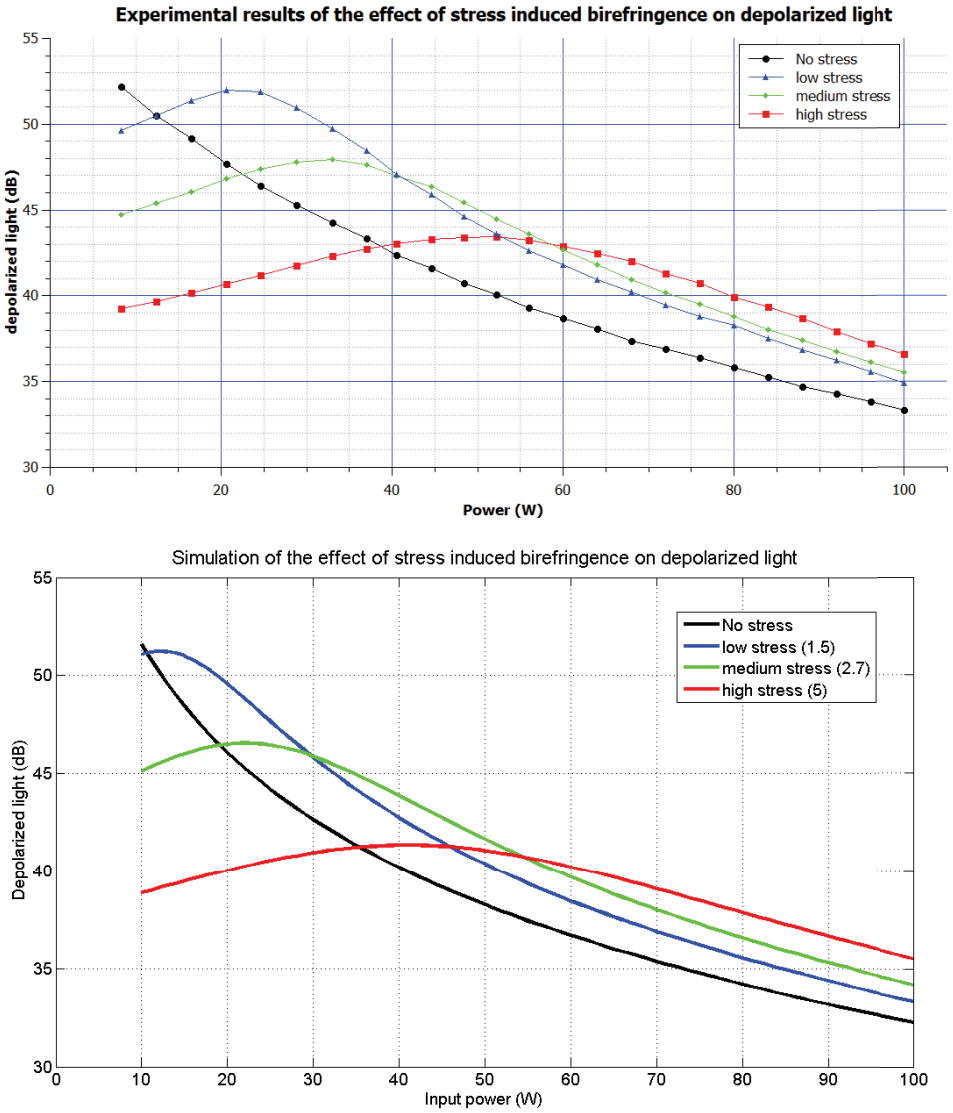

Figure 5.16: Experimental (top) and simulated (bottom) results of the effect on the depolarized light of four different stresses applied on the crystal

Another point that we investigated was the HOM induced by both the heating of the fiber and the stress of the crystal. To do that we computed the overlapping integral between the input Gaussian beam and the output beam whose phase has locally changed because of the birefringence of the crystal. The results are presented in figure 5.17 in which we plotted

the results of this simulation. We were making the power varying between 0.1 W and 200 W while the applied stress was varying between 0 and 100. From this simulation we can see that the introduced HOM are dominated by the thermal lensing due to the heating of the crystal (when F=0). A noticeable effect of the stress can only be seen for values that are much higher than the one that was used during the previous simulations ($\approx$ 0-10). Thermal lensing can be compensated thanks to a lens, the remaining HOM content is only of about 0.01% on the range of stress that we apply. This is not critical for the injection into the fiber.

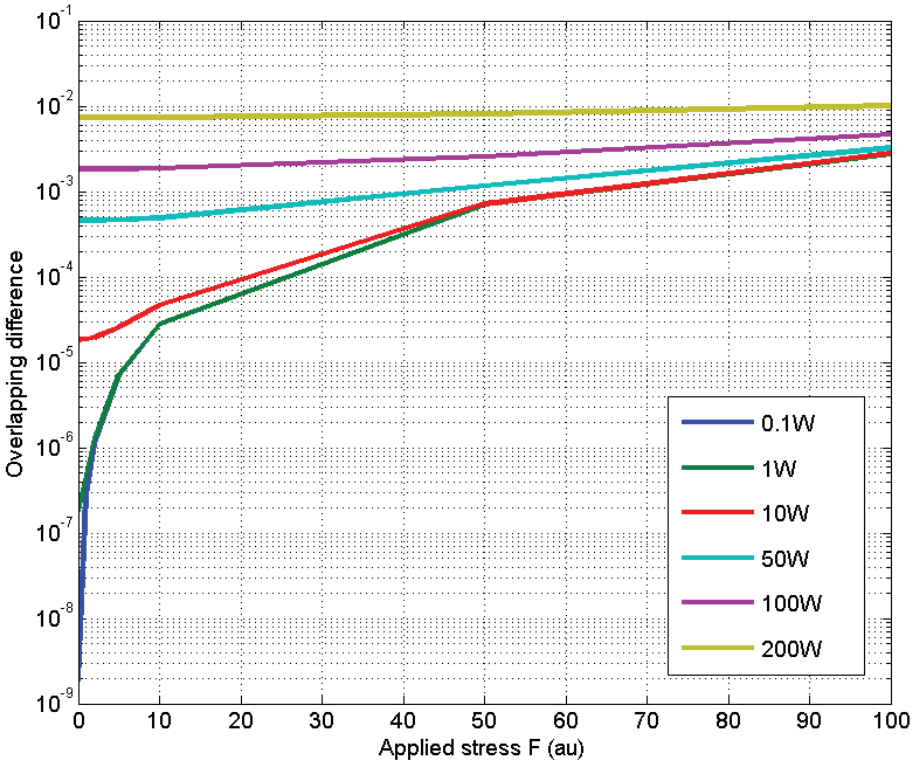

Figure 5.17: Overlapping difference between an input Gaussian beam and the output beam whose phase has been locally changed by the birefringence. It has been computed thanks to equation 2.19

From these investigations, we can get two conclusions. On one hand if one wants to improve the performance of the FI by applying a mechanical stress, we could imagine a mechanism such as PZT around the crystal that would apply the stress that minimizes the depolarized light at each power. Such a mechanism would be difficult to realize in practice. A better idea is to set the stress according to the power at which we want the depolarized light to be minimum. And this even if the isolation while setting it at low power is deteriorate.

On the other one, one could be tempted to let the crystal free of any holder to avoid constraints and the difficulties related to its set-up. However,in order to evacuate the heat of the crystal, there is a compromise to be found between a good thermal contact between

and the applied stress. That is why we developed a new holder. We present it in figure 5.18, it has a conic outer diameter so that the stress applied on the crystal can be monitored by screwing the locking ring. With this holder the stress is applied uniformly and the thermal contact is insured.

Figure 5.18: New holder for the magneto-optical crystal. Its conic outer diameter allows to control the stress applied on the crystal while screwing the ring

5.4 Design of a fibered version

5.4.1 Commercial FI and prototypes

Faraday isolator is one of the key components while using high power lasers. A back reflection which would be reinjected into the laser, would indeed be amplified again and would lead to even higher power that can destroy everything. So lots of work have been done on high power FI and especially those used for fiber laser or in set-ups where fibers are used to deliver high power beam. However the FI in these case are often half fibered: there is a fiber at the input but it is a free space propagation at the output. Moreover in the case of the high power beam delivery, there is no strong restrictions on the quality of the beam at the output, which makes the propagation in the fiber, with multimode fibers for example, much more easier than in our case.

In table 5.1 we are reviewing the properties of some available FI to show that none of them fulfill the characteristics that we detailled in the previous section. The IO-K-1064 (1) and IO-10-1064 (2), respectively fibered and free space, are two FI with the best properties that can be purchased from Thorlabs. One can find some other FI on the market with slightly better characteristics but the performance would be on the same order of magnitude (Pavos series from EOT [145] for example). The (3) that we are comparing in the table is a prototype that has been developed at the Fraunhofer Institute for Laser Technology. It has been designed to protect high power fiber laser used for material processing. It is fibered with multimode fibers and can handle power up to 1 kW. In figure 5.19 you can see these three FI. The (4) is a prototype that has been developed at the Institute of Applied Physics of the Russian Academy of Sciences in collaboration with optics group of EGO [146]. They are developing FI for high power applications and especially for gravitational waves detectors.

	(1)	(2)	(3)	(4)	desired characteristics
Isolation (dB)	39	40	20	40	40
Throughput (%)	80	92	80	>95	>95
Max power CW (W)	10	200*	1000	>200	200
Propagation	fibered	free space	fibered	free space	fibered

*for the combined forward and backward directions.

Table 5.1: different FI

What comes out of this comparison is that there is no FI available that would fulfill our needs. The fibered ones that would handle high power are designed with fibers that do not keep the quality of the beam. The free space ones, commercially available, have characteristics that are not high enough for our application. So the idea of the fibered version that we will develop is to fiber an improved version of a FI similar to the one that is already used in Advanced Virgo. In particular, the mount that we presented in figure 5.18 can be used in order to decrease the losses due to the mechanical constraints inside the crystal.

Figure 5.19: Three (1,2,3) of the four FI that are compared in table 5.1

5.4.2 Optical layout

Using the experience that we get through the handling of high power FI and LMA fibers we designed a version of a fibered FI that try to minimize the undesirable effect of each component that can lower the performance of the other one. Further works will be conducted to characterize its performances. Since we are using the LMA-PM-40-FUD fibers that we presented in section 3.3, it is quite unlikely that the overall performance in terms of losses could be reached. The connectors of these fibers are cooled down and the beam collimated thanks to the home made collimators presented in chapter 3 (figure3.4). The pick-off on PD1 through the first mirror is used to monitor the coupling through the input fiber, especially to be able to use the automatic alignment on the core of the fiber that we presented in section 3.1.4. The HWP1 is used to tune the output polarization of the fiber to the TFP. Indeed, during the manufacturing of the end facets there has been a difference of about 15° between the tilt angle of the end facet and the actual plane of propagation of the output beam. So one has to choose either to have a beam horizontally polarized at the output or a beam that propagates in the plane parallel to the optical bench. We chose the second option to avoid alignment issues, especially on the lens of the collimator. The beam is then going through the Faraday rotator. The HWP2 allows to correct for a possible mistuning of the angle of rotation and to re-orientate the polarization (±45°) to keep the reflections on TFP2 in an horizontal plane. L1, L2 and L3 are three converging lenses placed in a 4F configuration that can correct the thermal lensing induced in the crystal (see section 5.2.4). Depending on the power inside the crystal, one can use either L1 or L2 to correct for the thermal lensing. L3 is placed on a translation stage in order to finely tune the matching into the fiber. The pick-off on PD2 allows to monitor the losses and the eventual problems that could appear in the FI. The PZT is used to automatically keep the beam aligned on the core of the fiber. Finally the PBS is set in a rotational mount to perfectly align it with the propagation axis of the fiber. The HWP3 with this PBS are used as an IPC. The idea is, as much as possible, to avoid the power variation inside the set-up. Such variations could require a realignment of the beam, but they would especially require a re-tuning of the telescope used for compensating the thermal lensing.

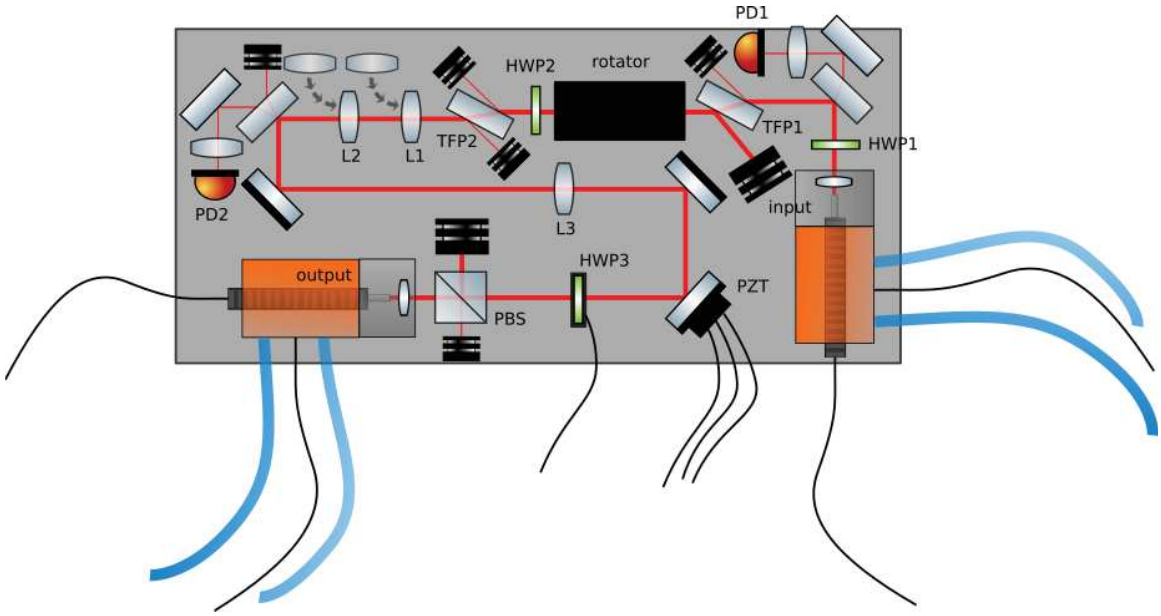

Figure 5.20: Scheme of the design of the fibered Faraday Isolator

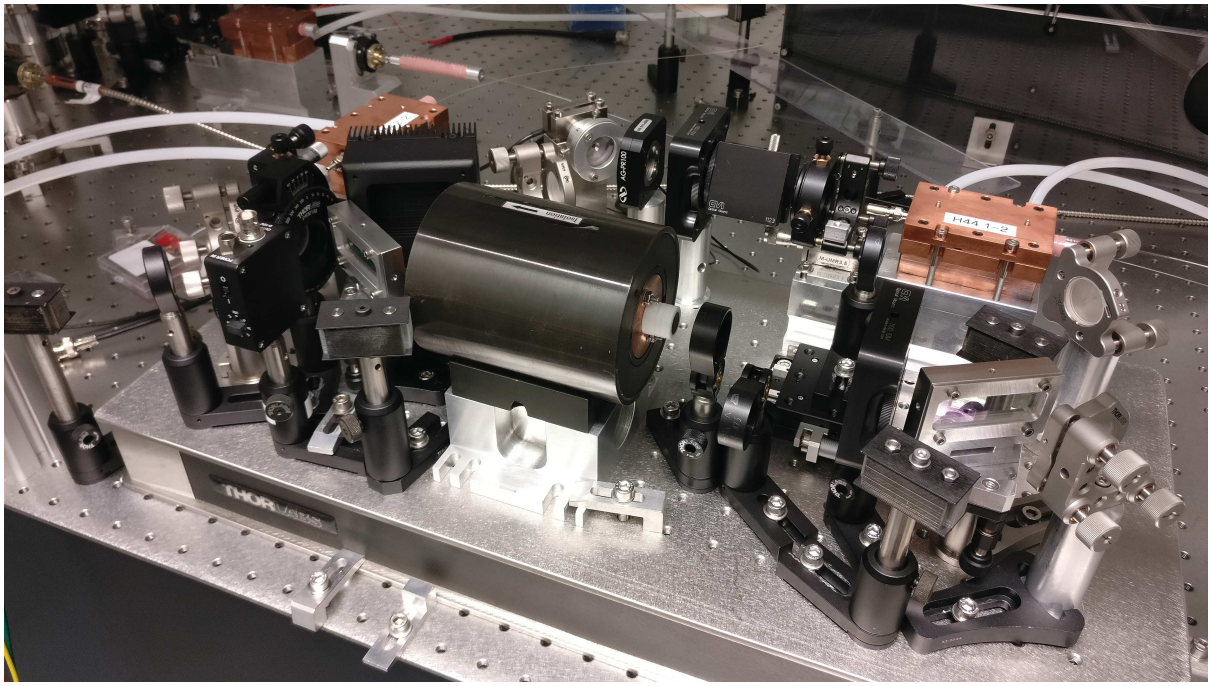

Figure 5.21: Picture of the fibered Faraday Isolator

5.5 Conclusion

After having described the working principle of a FI, we went through the main problems that one has to face while working with high power FI: the non-linear effects due to the heat of the crystal. By detailing the principles and understanding them, we suggested some possible improvement and especially we highlighted the importance of the mechanical constraints that are applied on the crystal, how they could deteriorate the isolation of a FI but also how they could be used to improve it. Finally using the experience that we had with the optical fibers and the non-linear effects that appear in magneto-optical crystals, we set-up a fibered version of a FI for high power single frequency laser. This version is under tests and the future work will be to validate its good functioning.

Conclusion and perspectives

By detailing the working principle of the Advanced Virgo detector in the first chapter, we saw the importance of all the subsystems in order to detect GWs. We especially detailed the laser and injection system and saw how it could be improved and simplified by using optical fibers.
However, as we saw in the second chapter, the laser beam that is used exhibits very specific characteristics that have to be kept while propagating into the fiber. This makes the use of optical fibers particularly difficult in this frame. In particular, we highlighted that the main issues are due to the very high densities of power that are involved. On one hand the fibers (in particular its ends) can easily be damaged and, on the other hand, there is a non-linear effect called Stimulated Brillouin Scattering that arises in the fiber. This effect prevents the fiber from guiding high power single frequency laser by imposing a threshold above which the light is not propagating anymore. However depending on their design some fibers are less sensitive to this effect.
In the third chapter, we presented the experimental works that have been done to test two of those fibers: the LMA-PM-15 and the LMA-PM-40-FUD from NKT Photonics. The first one was easy to handle and allows us to reach power up to 19 W single frequency at the output of a 5 meters patchcord with 1% of power losses due to non-linear effects **95.5 W.m**. The second one, however, is a fiber that is still under development, it was particularly difficult to set up but it showed better performance in terms of power handling. We were limited by the power available to test it but we showed that power up to 26 W single frequency at the output of a 10 meters patchcord was possible without having to deal with non linear effect (**260 W.m**). The main issue linked to these fibers is the introduced losses due to their attenuation and their HOM content. One can find the overall results about these two fibers in the conclusion of the dedicated chapter (section 3.4)
Using the LMA-PM-15 fiber, we designed and characterized a fibered electro-optic modulator for high power laser. It has been tested for power up to 50 W with a broadband laser. The maximum theoretical coupling at low power that could be reached with this fibered version is 88.5%. This is a quite good performance but makes it, in this state, unsuitable for Gravitational Waves detector since the losses associated to the free space EOMs installed in the injection subsystem are about 0.1% per modulator.
Finally, in the last chapter, we presented the issues that have to be faced in a high power Faraday isolator. We studied both theoretically and experimentally how the mechanical constraints on the magneto-optic crystal affect its behavior. The depolarization that arises because of those constraints can deteriorate the isolation. But we showed that in some cases it can also improve the isolation ratio of the Faraday Isolator. We also proposed the optical

layout of a fibered version of a high power single frequency Faraday isolator, that has been set up but not tested yet.

The aim of this PhD was a prospective work towards a more challenging objective which is to fiber the whole injection system. Through the work that has been presented in this thesis, we gained experience in handling optical fibers able to withstand a high power single frequency laser beam. It has not been tested yet, because of an issue with the AR coating on the end facets of the fibers, but we have fibered versions using 1.5 meter long fibers of an EOM and a FI that could theoretically withstand 200 W single frequency laser. However, as things stand, these fibers are introducing some losses, some of them can be lowered (mode matching, AR coating) but some other can not (attenuation, HOM content). Those losses make the use of fibered optical components difficult in the frame of the injection subsystem of Gravitational Waves detectors. Moreover, the more global objective of fibering the whole injection seems difficult to reach since it requires a 20 meters long fiber to go through the suspension system. We are at the cutting edge of the technology concerning the fibers that could at the same time withstand a very high single frequency laser beam and keep its properties unchanged over that length. That is why in parallel of this work we are discussing with fiber manufacturers in order to develop a fiber that could exhibit better performances as it has been discussed in section 3.4.

The work that we presented on the EOM and the FI can also be used for the free space version of these components, but the main efforts for the further works will be devoted on the fibers. Indeed, we are considering fibering only some parts of the injection subsystem that would require much shorter fibers: between the laser bench and the external injection bench, in order to decrease the misalignment due to the fact that one is suspended and not the other, and between the external injection bench and a viewport of the vacuum vessel of the Suspended Injection Bench 1. This would not avoid the misalignment issues between the two benches, but it will avoid the beam jitter due to the in-air propagation of the beam.

Appendices

Appendix A

Acronym

AC: Alternating Current
AdV: Advanced Virgo
AOI: Angle Of Incidence
AR: Anti Reflective
BBH: Binary Black Holes
BNS: Binary Neutron Star
BPC: Beam Pointing Control
BS: Beam Splitter
CW: Continouous Wave
DC: Direct Current
EGO: European Gravitational Observatory
EIB: External Injection Bench
EOM: Electro-Optic Modulator
FI: Faraday Isolator
FP: Fabry-Pérot
FSM: Fundamental Space-filling Mode
FSR: Free Spectral Range
FWHM: Full Width at Half Maximum
GW: Gravitational Waves
GWD: Gravitational Waves Detector
HOM: Higer Order Modes
HP: High Power
HR: High Reflective
HWP: Half WavePlate
IMC: Input Mode Cleaner
IPC: Input Power Control
LIDT: Laser Induced Damage Threshold
LMA: Large Mode Area
LP: Low Power
MFD: Mode Field Diameter
MZI: Mach Zender Interferometer
NA: Numerical Aperture

NPRO: Non-Planar Ring Oscillator
NS: Neutron Star
PBFL: Positive Best Form Lens
PBS: Polarized Beam Splitter
PCF: Photonic Crystal Fiber
PD: PhotoDiode
PDH: Pound Drever Hall
PER: Polarization Extinction Ratio
PM: Phase Modulation
PMF: Polarization Maintening Fiber
PR: Power Recycling
PSL: Pre-Stabilized Laser
PZT: Piezo Electric Transductor
QPD: Quadrant PhotoDiode
QWP: Quarter WavePlate
SIF: Step-Index Fiber
SBS: Stimulated Brillouin Scaterring
SBST: Stimulated Brillouin Scaterring Threshold
SIB: Suspended Injection Bench
SNR: Signal to Noise Ration
SR: Signal Recycling
SRS: Stimulated Raman Scattering
SFP: Scanning Fabry-Pérot
TDR: Technical Design Report
TFP: Thin Film Polarizers
TGG: Terbium Gallium Garnet

Appendix B

Optical cavities and Pound-Drever-Hall locking technique

The developement that are presented hereafter are based on the works done by Fritz Riehle, for a more detailed development one can refer to his book [115].

Optical cavities are arrangements of two or several mirrors that have the particularity of having a transmission response to an input beam that depends on its characteristics. Thus it behaves as a spatial and frequency filter and can be used either to clean the mode or to stabilize the frequency of lasers.

In order to understand the behavior of optical cavities, let us consider a basic one: the Fabry-Perot cavity. It consists in two parallel mirrors M_1 and M_2 having respectively a transmission coefficient t_1 and t_2 and a reflection coefficient r_1 and r_2. Such a cavity is represented in figure B.1. As shown in that figure, an incident wave $E_0 e^{i(\omega t - \vec{k}.\vec{r})}$ will experience different transmissions and reflections. By summing all the contributions, one obtains a mathematical series and can show that the transmitted electric field E_t is given by the following formula:

$$E_t = E_0 \frac{t_1 t_2 \exp(-i\omega L/c)}{1 - r_1 r_2 \exp(-i\omega 2L/c)} \tag{B.1}$$

which leads to a transmitted power:

$$P_t = E_t \, E_t^* = E_0^2 \frac{t_1^2 t_2^2}{1 + r_1^2 r_2^2 - 2 r_1 r_2 \cos(\omega 2L/c)} \tag{B.2}$$

This is a periodic function that depends on the phase shift between the different contributions: $\Delta\Phi = \omega 2L/c$. This function is represented in figure B.2, it has a maximum whenever $\Delta\Phi = 2\pi$. In these cases, all the contributions are constructively interfering. From this condition we can define the Free Spectral Range (FSR) of the cavity which is the interval

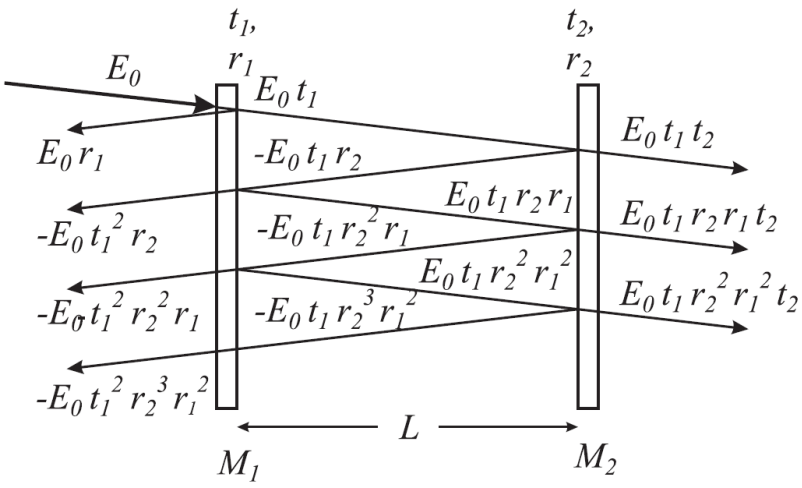

Figure B.1: Different reflection in a FP cavity. A tilt has been added to the input beam on the drawing to ease the understanding (figure from [115])

between two maxima. It is given by the formula:

$$FSR = \frac{c}{2L} \tag{B.3}$$

Another parameter of interest of the cavity is the Full Width at Half Maximum (FWHM) $2\pi\delta\nu$ of the transmitted peaks. By doing the approximation that the phase shifts are small in the equation of the transmitted power (eq B.2), it can be shown that the transmitted peaks have a Lorenzian shape whose linewidth is given by:

$$\delta\nu = \frac{(1 - r_1 r_2)}{\pi\sqrt{r_1 r_2}} \frac{c}{2L} \tag{B.4}$$

Thanks to these two parameters, we can define the Finesse of the cavity:

$$\mathcal{F} = \frac{FSR}{\delta\nu} = \frac{\pi\sqrt{r_1 r_2}}{(1 - r_1 r_2)} \tag{B.5}$$

By a similar reasoning than for the transmitted power, one can calculate the refractive power from the different contributions and get :

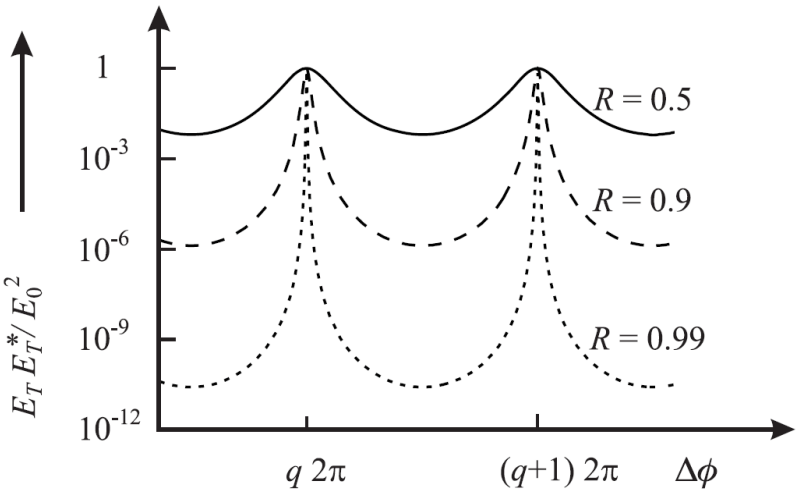

Figure B.2: Transmitted power through a FP cavity (figure from [115])

$$E_R = E_0 r_1 \; - \; \frac{t_1^2 r_2 \exp(-i\omega 2L/c)}{1 - r_1 r_2 \exp(-i\omega 2L/c)} \tag{B.6}$$

This reflected electromagnetic wave normalized by the input one give us the reflection coefficient of the cavity:

$$r_{FP} = \frac{E_R}{E_0} = \frac{r_1 - r_2(r_1^2 + t_1^2)\exp(-i\omega 2L/c)}{1 - r_1 r_2 \exp(-i\omega 2L/c)} \tag{B.7}$$

This is a complex number, that can be used to compute the reflective factor for the optical power ($R_{FP} = r_{FP} r_{FP}^*$) and the phase of the reflected signal ($tan(\Phi_R) = \mathrm{Im}(r_{FP})/\mathrm{Re}(r_{FP})$). They are represented in figure B.3. These two parameters are of particular interest for the interferometer, especially for the Pound-Drever-Hall technique used to lock the cavities. One can indeed clearly see that the transmitted and reflected power from the cavities directly depends on the phase shift $\Delta\Phi = \omega 2L/c$. A cavity is said to be locked when this factor ωL is kept constant. To do so one can either modify the length of the cavity or modify the frequency of the input beam. However giving the fact that the transmitted and reflected power by an optical cavity are symmetric for a phase change, one does not have the information about the sense of the correction to apply just by looking at it. The solution comes from the PDH technique whose scheme is presented in figure B.4 and that we are explaining the principle hereafter.

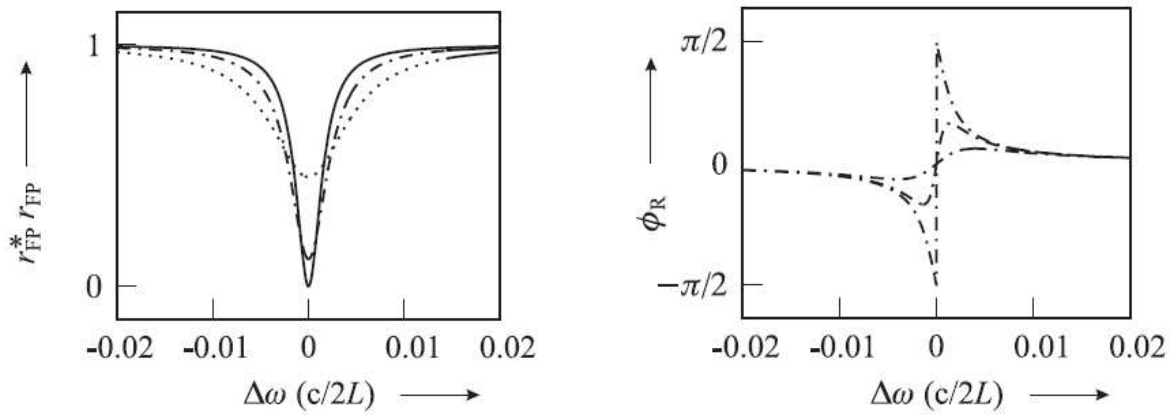

Figure B.3: Reflections coefficients for both the phase and the amplitude at the input of a FP cavity (figure from [115])

Pound Drever Hall locking technique

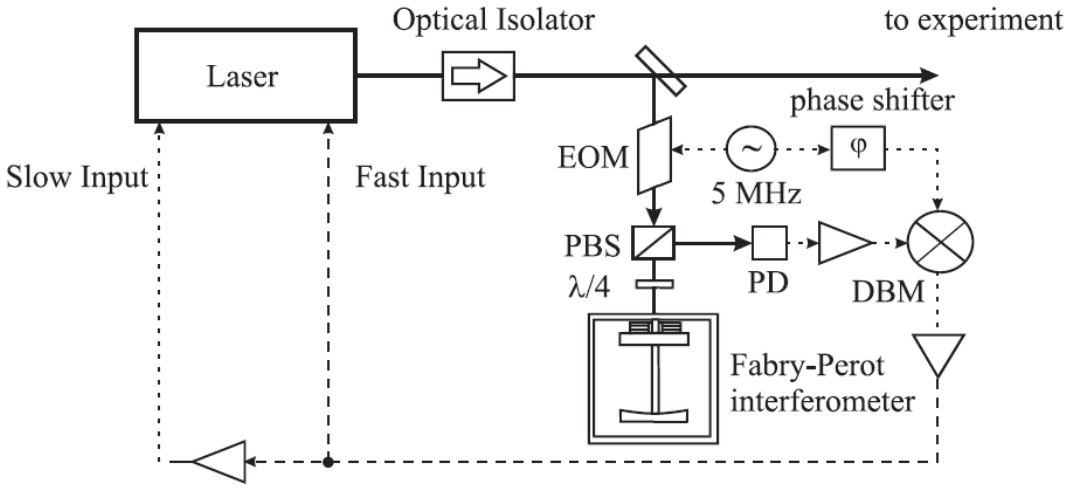

Figure B.4: PDH locking system (figure from [115])

The input beam is modulated by an EOM at a modulation frequency ω_m with a modulation depth m which leads to the following expression for the electric field of the light at the input of the cavity:

$$E_{FM}(\omega) = E_0 \left[J_0(m) e^{i\omega t} + J_1(m) e^{i(\omega+\omega_m)t} - J_1(m) e^{i(\omega-\omega_m)t} \right] \tag{B.8}$$

By using the reflection coefficients B.7 that we computed before we have the following expression for the reflected electric field:

$$E_r(\omega) = \frac{E_0}{2} \left[r_{FP}(\omega) J_0(m) e^{i\omega t} + r_{FP}(\omega+\omega_m) J_1(m) e^{i(\omega+\omega_m)t} - r_{FP}(\omega-\omega_m) J_1(m) e^{i(\omega-\omega_m)t} \right] \tag{B.9}$$

The quarter waveplate and the PBS of the set-up are acting as an isolator, thus this reflected beam will be read by the photodiode. Its electric response is proportional to the optical power:

$$V_{PD} \propto E_r E_r^* \tag{B.10}$$

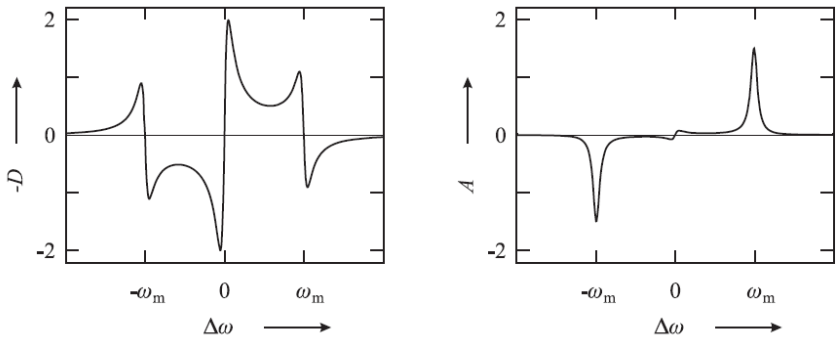

Figure B.5: $A(\Delta_\omega)$ and $D(\Delta_\omega)$ coefficients that appear in the development of the PDH locking system. They are plotted against the pahse shift. The asymmetrie around the working point $\Delta_\omega = 0$ allows to get the sign of the phase shift. (figure from [115])

By developing this expression we can make appear a DC voltage as well as terms in $\pm\omega_m$ and $\pm 2\omega_m$. For our application we are especially interested in the term in ω_m, it can be written under the form:

$$V_{PD}^{\omega_m} \propto J_0(\delta)J_1(\delta)(A(\Delta_\omega)\ \cos(\omega_m t) + D(\Delta_\omega)\ \sin(\omega_m t)) \tag{B.11}$$

where $A(\Delta_\omega)$ and $D(\Delta_\omega)$ are coefficients that can be analytically computed (see [115]), they are plotted in figure B.5. By carefully choosing the phase shift with the phase shifter while demodulating the signal, one can get only the contribution of this coefficient $D(\Delta_\omega)$. Given its asymmetry around the working point $\Delta_\omega = 0$, the sign of the demodulated signal is giving the sign of the phase shift. Thus it can be used as an error signal to lock the cavity by either correcting the length of the cavity or the frequency of the laser.

Appendix C

Jones matrix formalism

The Jones matrix formalism is an easy and piratical way to describe the evolution of the polarization while propagating into an optical set-up. As described in section 2.1.4, the polarization state is described by the values E_{0x}, Φ_x, E_{0y}, Φ_y of the electric field vector $\vec{\boldsymbol{E}}$ in the ($\vec{\boldsymbol{x}}$,$\vec{\boldsymbol{y}}$) base :

$$\vec{\boldsymbol{E}} = \begin{pmatrix} E_{0x}e^{i\Phi_x} \\ E_{0y}e^{i\Phi_y} \end{pmatrix} \tag{C.1}$$

In the Jones Matrix formalism, the modification of the polarization state of an input electric field through an optical element can simply be computed by multiplying the (1×2) matrix representing the input state of the polarization by the (2×2) Jones matrix of the optical element. The result of this calculation is a (1×2) matrix that give the information on the polarization state of the output field. Here below we are reviewing the matrix of the main states of polarization as well as the matrix of the main optical components:

- Horizontal state of polarization :
$$\begin{pmatrix} 1 \\ 0 \end{pmatrix} \tag{C.2}$$
- Vertical state of polarization:
$$\begin{pmatrix} 0 \\ 1 \end{pmatrix} \tag{C.3}$$
- Linear state of polarization at 45° from the horizontal axis :
$$\frac{1}{\sqrt{2}}\begin{pmatrix} 1 \\ 1 \end{pmatrix} \tag{C.4}$$
- Linear state of polarization at -45° from the horizontal axis :
$$\frac{1}{\sqrt{2}}\begin{pmatrix} 1 \\ -1 \end{pmatrix} \tag{C.5}$$

- Right handed circular polarization :

$$\frac{1}{\sqrt{2}}\begin{pmatrix}1\\-i\end{pmatrix} \tag{C.6}$$

- Left handed circular polarization :

$$\frac{1}{\sqrt{2}}\begin{pmatrix}1\\i\end{pmatrix} \tag{C.7}$$

- Half waveplate:

$$\begin{pmatrix}-i & 0\\0 & i\end{pmatrix} \tag{C.8}$$

- Quarter waveplate:

$$e^{-i\pi/4}\begin{pmatrix}1 & 0\\0 & i\end{pmatrix} \tag{C.9}$$

- Polarizer horizontal :

$$\begin{pmatrix}1 & 0\\0 & 0\end{pmatrix} \tag{C.10}$$

- Polarizer vertical :

$$\begin{pmatrix}0 & 0\\0 & 1\end{pmatrix} \tag{C.11}$$

- Arbitrary phase retarder of birefringence $\eta = \phi_x - \phi_y$ rotated by an angle θ from the horizontal axis and having a circular birefringence ϕ :

$$\begin{pmatrix}e^{i\eta/2}\cos^2(\theta) + e^{-i\eta/2}\sin^2(\theta) & (e^{i\eta/2} - e^{-i\eta/2})e^{-i\phi}\cos(\theta)\sin(\theta)\\e^{i\eta/2} - e^{-i\eta/2})e^{i\phi}\cos(\theta)\sin(\theta & e^{-i\eta/2}\cos^2(\theta) + e^{i\eta/2}\sin^2(\theta)\end{pmatrix} \tag{C.12}$$

All this elements are given in the ($\vec{\boldsymbol{x}}$,$\vec{\boldsymbol{y}}$) base, but they can be rotated of an angle θ thanks to the rotation matrix $R(\theta)$ by using the formula $M(\theta) = R(\theta)MR(-\theta)$ with :

$$R(\theta) = \begin{pmatrix}\cos(\theta) & -\sin(\theta)\\\sin(\theta) & \cos(\theta)\end{pmatrix} \tag{C.13}$$

Bibliography

[1] B. P. et al Abbott. "Observation of Gravitational Waves from a Binary Black Hole Merger". In: *Phys. Rev. Lett.* 116 (6 2016), p. 061102. DOI: 10.1103/PhysRevLett.116.061102. URL: https://link.aps.org/doi/10.1103/PhysRevLett.116.061102.

[2] B. Canuel et al. "Sub-nanoradiant beam pointing monitoring and stabilization system for controlling input beam jitter in gravitational wave interferometers". In: *Appl. Opt.* 53.13 (2014), pp. 2906–2916. DOI: 10.1364/AO.53.002906. URL: http://ao.osa.org/abstract.cfm?URI=ao-53-13-2906.

[3] Steven Weinberg. *Gravitation and Cosmology: principles and applications of the General Theory of Relativity*. John Wiley and sons, 1972. ISBN: 10 : 0471925675.

[4] Francois Bondu. "Etude du bruit thermique et stabilisation en frequence du laser du detecteur interferometrique d'ondes gravitationnelles VIRGO". PhD thesis. Universite Paris Sud - Paris XI, 1996.

[5] J. et al Abadie. "Directional Limits on Persistent Gravitational Waves Using LIGO S5 Science Data". In: ().

[6] J. H. Taylor. "DISCOVERY OF A PULSAR IN A BINARY SYSTEM". In: *Annals of the New York Academy of Sciences* 262.1 (1975), pp. 490–492. ISSN: 1749-6632. DOI: 10.1111/j.1749-6632.1975.tb31467.x. URL: http://dx.doi.org/10.1111/j.1749-6632.1975.tb31467.x.

[7] J. H. Taylor and J. M. Weisberg. "A new test of general relativity: Gravitational radiation and the binary pulsar PS R 1913+16". In: *Astrophys. J.* 253 (1982), pp. 908–920. DOI: 10.1086/159690.

[8] B. P. et al Abbott. "GW151226: Observation of Gravitational Waves from a 22-Solar-Mass Binary Black Hole Coalescence". In: ().

[9] B. P et al Abbott. "GW170104: Observation of a 50-Solar-Mass Binary Black Hole Coalescence at Redshift 0.2". In: *Phys. Rev. Lett.* 118 (22 2017), p. 221101. DOI: 10.1103/PhysRevLett.118.221101. URL: https://link.aps.org/doi/10.1103/PhysRevLett.118.221101.

[10] B. P. et al Abbott. "GW170814: A Three-Detector Observation of Gravitational Waves from a Binary Black Hole Coalescence". In: *Phys. Rev. Lett.* 119 (14 2017), p. 141101. DOI: 10.1103/PhysRevLett.119.141101. URL: https://link.aps.org/doi/10.1103/PhysRevLett.119.141101.

[11] B. P. et al Abbott. "GW170817: Observation of Gravitational Waves from a Binary Neutron Star Inspiral". In: *Phys. Rev. Lett.* 119 (16 2017), p. 161101. DOI: 10.1103/PhysRevLett.119.161101. URL: https://link.aps.org/doi/10.1103/PhysRevLett.119.161101.

[12] A. Goldstein et al. "An Ordinary Short Gamma-Ray Burst with Extraordinary Implications: Fermi -GBM Detection of GRB 170817A". In: *The Astrophysical Journal Letters* 848.2 (2017), p. L14. URL: http://stacks.iop.org/2041-8205/848/i=2/a=L14.

[13] B. P. Abbott et al. "Gravitational Waves and Gamma-Rays from a Binary Neutron Star Merger: GW170817 and GRB 170817A". In: *The Astrophysical Journal Letters* 848.2 (2017), p. L13. URL: http://stacks.iop.org/2041-8205/848/i=2/a=L13.

[14] B. P. Abbott et al. "Multi-messenger Observations of a Binary Neutron Star Merger". In: *The Astrophysical Journal Letters* 848.2 (2017), p. L12. URL: http://stacks.iop.org/2041-8205/848/i=2/a=L12.

[15] The LIGO Scientific Collaboration Collaboration et al. "A gravitational-wave standard siren measurement of the Hubble constant". In: *Nature* advance online publication (2017). Letter. ISSN: 1476-4687. URL: http://dx.doi.org/10.1038/nature24471.

[16] J. Weber. "Detection and Generation of Gravitational Waves". In: *Phys. Rev.* 117 (1 1960), pp. 306–313. DOI: 10.1103/PhysRev.117.306. URL: https://link.aps.org/doi/10.1103/PhysRev.117.306.

[17] PUSTOVOIT V.I. GERSTENSHTEIN M.E. "On the detection of low frequency gravitational waves". In: *Sov. Phys.* 16 (1962), p. 433.

[18] R. Weiss. "Electromagnetically coupled broadband gravitational antenna". In: *Techreport* 105 (1972).

[19] A. Giazotto A.Brillet. "Virgo Project Technical Report". In: *Techreport* (1989).

[20] R.W.P Drever et al. "Laser Interferometer Gravitational waves Observatory (LIGO) Technical Report". In: *Techreport* (1989).

[21] Tomotada Akutsu and KAGRA collaboration. "Large-scale cryogenic gravitational-wave telescope in Japan: KAGRA". In: *Journal of Physics: Conference Series* 610.1 (2015), p. 012016. URL: http://stacks.iop.org/1742-6596/610/i=1/a=012016.

[22] Pablo Barriga et al. "Optical design of the proposed Australian International Gravitational Observatory". In: *Opt. Express* 17.4 (2009), pp. 2149–2165. DOI: 10.1364/OE.17.002149. URL: http://www.opticsexpress.org/abstract.cfm?URI=oe-17-4-2149.

[23] B Sathyaprakash et al. "Scientific objectives of Einstein Telescope". In: *Classical and Quantum Gravity* 29.12 (2012), p. 124013. URL: http://stacks.iop.org/0264-9381/29/i=12/a=124013.

[24] Karsten Danzmann and the LISA study team. "LISA: laser interferometer space antenna for gravitational wave measurements". In: *Classical and Quantum Gravity* 13.11A (1996), A247. URL: http://stacks.iop.org/0264-9381/13/i=11A/a=033.

[25] Seiji Kawamura et al. “The Japanese space gravitational wave antennaDECIGO”. In: *Classical and Quantum Gravity* 23.8 (2006), S125. URL: http://stacks.iop.org/0264-9381/23/i=8/a=S17.

[26] G. M. Harry et al. “The Big Bang Observer: High Laser Power for Gravitational Wave Astrophysics”. In: *Conference on Lasers and Electro-Optics/Quantum Electronics and Laser Science Conference and Photonic Applications Systems Technologies*. Optical Society of America, 2007, PThB2. DOI: 10.1364/PHAST.2007.PThB2. URL: http://www.osapublishing.org/abstract.cfm?URI=PhAST-2007-PThB2.

[27] G. Vajente. “Analysis of sensitivity and noise sources for the Virgo gravitational wave interferometer”. PhD thesis. Universita di Pisa, 2008.

[28] Stefan Hild. *Power recycling, signal recycling, classical quantum noise*. GraWIToN Lecture. 2015.

[29] Virgo Collaboration. “Advanced Virgo Technical Design Report, VIR0128A12”. In: (2012). URL: https://tds.ego-gw.it/ql/?c=8940.

[30] G. Ballardin et al. “Measurement of the VIRGO superattenuator performance for seismic noise suppression”. In: *Review of Scientific Instruments* 72.9 (2001), pp. 3643–3652. DOI: 10.1063/1.1392338.

[31] A. Einstein. “Zur Quantentheorie der Strahlung (On the Quantum Theory of Radiation)”. In: *Physika Zeitschrift* 18 (1917), pp. 121–128.

[32] Christopher C. Davis. *Lasers and Electro-optics: Fundamentals and Engineering*. 2nd ed. Cambridge University Press, 2014. ISBN: 978-0-521-86029.

[33] T. H. MAIMAN. “Stimulated Optical Radiation in Ruby”. In: *Nature* 187.4736 (1960), pp. 493–494. DOI: 10.1038/187493a0. URL: http://dx.doi.org/10.1038/187493a0.

[34] Coherent. *White paper on NPRO: Ultra-Low Noise and Narrow Linewidth*. URL: https://www.coherent.com/assets/literature/white_papers/WP1_MephistoNPRO_Final.pdf#page=1.

[35] Thomas J. Kane and Robert L. Byer. “Monolithic, unidirectional single-mode Nd:YAG ring laser”. In: *Opt. Lett.* 10.2 (1985), pp. 65–67. DOI: 10.1364/OL.10.000065. URL: http://ol.osa.org/abstract.cfm?URI=ol-10-2-65.

[36] A. C. Nilsson, E. K. Gustafson, and R. L. Byer. “Eigenpolarization theory of monolithic nonplanar ring oscillators”. In: *IEEE Journal of Quantum Electronics* 25.4 (1989), pp. 767–790. ISSN: 0018-9197. DOI: 10.1109/3.17343.

[37] neoLASE GmbH. *neoLASE Factsheet OEM Amplifier*. 2017. URL: https://neolase.com/wp-content/uploads/2017/03/neoLASE_Factsheet_OEM_Amplifier.pdf.

[38] *Lasers and laser-related equipment Test methods for laser beam widths, divergence angles and beam propagation ratios*. Standard. Geneva, CH: International Organization for Standardization, Feb. 2005.

[39] J.D. Colladon. “Sur les réflexions d’un rayon de lumière l’intérieur d’une veine liquide parabolique”. In: *Compte-rendus de l’Académie des Sciences* 15 (1842), p. 800.

[40] J. Babinet. “Note sur la transmission de la lumière par des canaux sinueux”. In: *Compte-rendus de l’Académie des Sciences* 15 (1842), p. 803.

[41] H.C. Saint-René. “Sur une solution du problème de la vision à distance”. Pli cachet. 1895.

[42] Ray Tricker. “1 - The history of fiber optics”. In: *Optoelectronics and Fiber Optic Technology*. Ed. by Ray Tricker. Oxford: Newnes, 2002, pp. 1 –35. ISBN: 978-0-7506-5370-1. DOI: https://doi.org/10.1016/B978-075065370-1/50003-9. URL: http://www.sciencedirect.com/science/article/pii/B9780750653701500039.

[43] Gilles Poupon. *Traitement des puces lectroniques et nouveaux procds d’interconnexion*. Hermes Science Publicationsr, Sept. 2011. ISBN: 978-2-746-22085-0.

[44] D. L. HUTT, K. J. SNELL, and P. A. BÉLANGER. “Alexander Graham Bell’s PHOTOPHONE”. In: *Opt. Photon. News* 4.6 (1993), pp. 20–25. DOI: 10.1364/OPN.4.6.000020. URL: http://www.osa-opn.org/abstract.cfm?URI=opn-4-6-20.

[45] G.A. Hockhan C.K. Kao. “Dielectric-fibre surface waveguides for optical frequencies”. In: *Proceedings of the Institution of Electrical Engineers* 113 (1966), p. 1151.

[46] F. Beier et al. “Narrow linewidth, single mode 3 kW average power from a directly diode pumped ytterbium-doped low NA fiber amplifier”. In: *Opt. Express* 24.6 (2016), pp. 6011–6020. DOI: 10.1364/OE.24.006011. URL: http://www.opticsexpress.org/abstract.cfm?URI=oe-24-6-6011.

[47] Mark Wuilpart. *Phenomenes de polarisation dans les fibres optiques*. Reseaux de transmission photoniques. URL: http://slideplayer.fr/slide/3333213/.

[48] V. Ramaswamy and W. G. French. “Influence of noncircular core on the polarisation performance of single mode fibres”. In: *Electronics Letters* 14.5 (1978), pp. 143–144. ISSN: 0013-5194. DOI: 10.1049/el:19780096.

[49] Philip Russell. “History and Future of Photonic Crystal Fibers”. In: *Optical Fiber Communication Conference and National Fiber Optic Engineers Conference*. Optical Society of America, 2009, OTuC1. DOI: 10.1364/OFC.2009.OTuC1. URL: http://www.osapublishing.org/abstract.cfm?URI=OFC-2009-OTuC1.

[50] J. C. Knight et al. “All-silica single-mode optical fiber with photonic crystal cladding”. In: *Opt. Lett.* 21.19 (1996), pp. 1547–1549. DOI: 10.1364/OL.21.001547. URL: http://ol.osa.org/abstract.cfm?URI=ol-21-19-1547.

[51] K. R. Hansen, J. Lgsgaard, and J. Broeng. “Transverse mode instability in high-power ytterbium doped fiber ampliers”. PhD thesis. Technical University of Denmark, 2013.

[52] Masanori Koshiba and Kunimasa Saitoh. “Applicability of classical optical fiber theories to holey fibers”. In: *Opt. Lett.* 29.15 (2004), pp. 1739–1741. DOI: 10.1364/OL.29.001739. URL: http://ol.osa.org/abstract.cfm?URI=ol-29-15-1739.

[53] Niels Asger Mortensen. “Effective area of photonic crystal fibers”. In: *Opt. Express* 10.7 (2002), pp. 341–348. DOI: 10.1364/OE.10.000341. URL: http://www.opticsexpress.org/abstract.cfm?URI=oe-10-7-341.

[54] M. D. Nielsen et al. “Predicting macrobending loss for large-mode area photonic crystal fibers”. In: *Opt. Express* 12.8 (2004), pp. 1775–1779. DOI: 10.1364/OPEX.12.001775. URL: http://www.opticsexpress.org/abstract.cfm?URI=oe-12-8-1775.

[55] Pochi Yeh, Amnon Yariv, and Emanuel Marom. “Theory of Bragg fiber∗”. In: *J. Opt. Soc. Am.* 68.9 (1978), pp. 1196–1201. DOI: 10.1364/JOSA.68.001196. URL: http://www.osapublishing.org/abstract.cfm?URI=josa-68-9-1196.

[56] T.A. Birks et al. “Full 2-D photonic bandgaps in silica/air structures”. In: *Electronics Letters* 31.5121497 (1995), pp. 1941 –1943. DOI: 10.1049/el:19951306. URL: http://ieeexplore.ieee.org/document/490675/.

[57] R. F. Cregan et al. “Single-Mode Photonic Band Gap Guidance of Light in Air”. In: *Science* 285.5433 (1999), pp. 1537–1539. ISSN: 0036-8075. DOI: 10.1126/science.285.5433.1537. eprint: http://science.sciencemag.org/content/285/5433/1537.full.pdf. URL: http://science.sciencemag.org/content/285/5433/1537.

[58] F. Couny, F. Benabid, and P. S. Light. “Sub-Watt Threshold CW Raman Fiber-Gas-Laser Based on H2-Filled Hollow-Core Photonic Crystal Fiber”. In: *33rd European Conference and Exhibition of Optical Communication - Post-Deadline Papers (published 2008)*. 2007, pp. 1–2.

[59] O. H. Heckl et al. “High harmonic generation in a gas-filled hollow-core photonic crystal fiber”. In: *Applied Physics B* 97.2 (2009), p. 369. ISSN: 1432-0649. DOI: 10.1007/s00340-009-3771-x. URL: https://doi.org/10.1007/s00340-009-3771-x.

[60] Fàtima Domingues Paulo André Ana Rocha and Margarida Facão. “Thermal Effects in Optical Fibres, Developments in Heat Transfer”. In: *Developments in Heat Transfer*. Ed. by Marco Aurelio Dos Santos Bernardes. InTech, 2011. DOI: 10.5772/22812. URL: https://www.intechopen.com/books/developments-in-heat-transfer/thermal-effects-in-optical-fibres.

[61] Fiberguide. *High Power Laser assemblies*. 2012.

[62] Holoor. *Laser Damage Treshold - application note*. last checked: 14/06/17. 2014. URL: http://www.holoor.co.il/Diffractive_Optics_Publications/Laser_Damage_Threshold.pdf.

[63] Troy Alley; Peter Allard; Rod Schuster; David Collier; Arlee V. Smith; Binh T. Do; Alice C. Kilgo. “How to polish fused silica to obtain the surface damage threshold equals to the bulk damage threshold”. In: *Proceedings of SPIE - The International Society for Optical Engineering* 7842 (2010). DOI: 10.1117/12.868416.

[64] I. H. Malitson. “Interspecimen Comparison of the Refractive Index of Fused Silica∗,”. In: *J. Opt. Soc. Am.* 55.10 (1965), pp. 1205–1209. DOI: 10.1364/JOSA.55.001205. URL: http://www.osapublishing.org/abstract.cfm?URI=josa-55-10-1205.

[65] S. Höfer et al. “Single-frequency master-oscillator fiber power amplifier system emitting 20 W of power”. In: *Opt. Lett.* 26.17 (2001), pp. 1326–1328. DOI: 10.1364/OL.26.001326. URL: http://ol.osa.org/abstract.cfm?URI=ol-26-17-1326.

[66] S. P. Singh and N. Singh. “Nonlinear effects in optical fibers: origin, management and applications”. In: *Progress In Electromagnetics Research* 73 (2007), pp. 249–275. DOI: 10.2528/PIER07040201. URL: http://www.jpier.org/pier/pier.php?paper=07040201.

[67] David Milam. “Review and assessment of measured values of the nonlinear refractive-index coefficient of fused silica”. In: *Appl. Opt.* 37.3 (1998), pp. 546–550. DOI: 10.1364/AO.37.000546. URL: http://ao.osa.org/abstract.cfm?URI=ao-37-3-546.

[68] Gadi Fibich and Alexander L. Gaeta. “Critical power for self-focusing in bulk media and in hollow waveguides”. In: *Opt. Lett.* 25.5 (2000), pp. 335–337. DOI: 10.1364/OL.25.000335. URL: http://ol.osa.org/abstract.cfm?URI=ol-25-5-335.

[69] Richard L. Lindstrom Ronald R. Krueger Jonathan H. Talamo. *Textbook of Refractive Laser Assisted Cataract Surgery (ReLACS)*. Springer Dordrecht Heidelberg London New York, 2012. ISBN: 978-1-4614-1009-6. DOI: 10.1007/978-1-4614-1010-2.

[70] A. Smekal. “Zur Quantentheorie der Dispersion”. In: *Naturwissenschaften* 11 (Oct. 1923), pp. 873–875. DOI: 10.1007/BF01576902.

[71] C. V. Raman. “A new radiation [Reproduced from Indian J. Phys., 1928, 2, 387398]”. In: *Current Science* 74.4 (1998), pp. 382–386. ISSN: 00113891. URL: http://www.jstor.org/stable/24101519.

[72] “Eine neue Erscheinung bei der Lichtzerstreuung in Krystallen”. In: *Naturwissenschaften* 16 (July 1928), pp. 557–558. DOI: 10.1007/BF01506807.

[73] R. Gangwar S. P. Singh and N. Singh. *Nonlinear scattering effects in optical fibers*. Vol. 74. 2007, pp. 379–405. DOI: http://dx.doi:10.2528/PIER07040201. URL: http://www.jpier.org/pier/pier.php?paper=07051102.

[74] Brillouin, Leon. “Diffusion de la lumiere et des rayons X par un corps transparent homogene - Influence de l’agitation thermique”. In: *Ann. Phys.* 9.17 (1922), pp. 88–122. DOI: 10.1051/anphys/192209170088. URL: https://doi.org/10.1051/anphys/192209170088.

[75] R. Y. Chiao, C. H. Townes, and B. P. Stoicheff. “Stimulated Brillouin Scattering and Coherent Generation of Intense Hypersonic Waves”. In: *Phys. Rev. Lett.* 12 (21 1964), pp. 592–595. DOI: 10.1103/PhysRevLett.12.592. URL: https://link.aps.org/doi/10.1103/PhysRevLett.12.592.

[76] Andrey Kobyakov, Michael Sauer, and Dipak Chowdhury. “Stimulated Brillouin scattering in optical fibers”. In: *Adv. Opt. Photon.* 2.1 (2010), pp. 1–59. DOI: 10.1364/AOP.2.000001. URL: http://aop.osa.org/abstract.cfm?URI=aop-2-1-1.

[77] A. H. McCurdy. “Modeling of stimulated Brillouin scattering in optical fibers with arbitrary radial index profile”. In: *Journal of Lightwave Technology* 23.11 (2005), pp. 3509–3516. ISSN: 0733-8724. DOI: 10.1109/JLT.2005.855876.

[78] Andrey Kobyakov et al. “Design concept for optical fibers with enhanced SBS threshold”. In: *Opt. Express* 13.14 (2005), pp. 5338–5346. DOI: 10.1364/OPEX.13.005338. URL: http://www.opticsexpress.org/abstract.cfm?URI=oe-13-14-5338.

[79] A. Boh Ruffin et al. “Brillouin gain analysis for fibers with different refractive indices”. In: *Opt. Lett.* 30.23 (2005), pp. 3123–3125. DOI: 10.1364/OL.30.003123. URL: http://ol.osa.org/abstract.cfm?URI=ol-30-23-3123.

[80] S. Chi et al. “Measurement of stimulated-Brillouin-scattering thresholds for various types of fibers using Brillouin optical time-domain reflectometer”. In: *Conference on Lasers and Electro-Optics*. Optical Society of America, 2000, CWK24. URL: http://www.osapublishing.org/abstract.cfm?URI=CLEO-2000-CWK24.

[81] M. O. van Deventer and A. J. Boot. “Polarization properties of stimulated Brillouin scattering in single-mode fibers”. In: *Journal of Lightwave Technology* 12.4 (1994), pp. 585–590. ISSN: 0733-8724. DOI: 10.1109/50.285349.

[82] Matthias Hildebrandt et al. “Brillouin scattering spectra in high-power singlefrequency ytterbium doped fiber amplifiers”. In: *Opt. Express* 16.20 (2008), pp. 15970–15979. DOI: 10.1364/OE.16.015970. URL: http://www.opticsexpress.org/abstract.cfm?URI=oe-16-20-15970.

[83] Michael Steinke. *Fiber amplifiers: Laser sources for next generation GW detectors*. GraWIToN Lecture. 2016. URL: http://moodle.grawiton-gw.eu/.

[84] NKT photonics. *LMA-PM-15 datasheet*. 2016. URL: https://www.nktphotonics.com/wp-content/uploads/sites/3/2015/01/lma-pm-15.pdf.

[85] P. Dainese et al. “Stimulated Brillouin scattering from multi-GHz-guided acoustic phonons in nanostructured photonic crystal fibres”. In: *Nat Phys* 2.6 (2006), pp. 388–392. ISSN: 1745-2473. DOI: 10.1038/nphys315. URL: https://www.nature.com/articles/nphys315.

[86] J.-C. Beugnot et al. “Complete experimental characterxization of stimulated Brillouin scattering in photonic crystal fiber”. In: *Opt. Express* 15.23 (2007), pp. 15517–15522. DOI: 10.1364/OE.15.015517. URL: https://www.osapublishing.org/oe/abstract.cfm?URI=oe-15-23-15517.

[87] C. Fortier et al. “Experimental investigation of Brillouin and Raman scattering in a 2SG sulfide glass microstructured chalcogenide fiber”. In: *Opt. Express* 16.13 (2008), pp. 9398–9404. DOI: 10.1364/OE.16.009398. URL: http://www.opticsexpress.org/abstract.cfm?URI=oe-16-13-9398.

[88] J. McElhenny, R. Pattnaik, and J. Toulouse. “Polarization dependence of SBS in small-core PCFs”. In: *2008 Conference on Lasers and Electro-Optics and 2008 Conference on Quantum Electronics and Laser Science*. 2008, pp. 1–2. DOI: 10.1109/CLEO.2008.4551583.

[89] Justin B. Spring et al. *Comparison of stimulated Brillouin scattering thresholds and spectra in nonpolarization-maintaining and polarization-maintaining passive fibers*. 2005. DOI: 10.1117/12.591035. URL: http://dx.doi.org/10.1117/12.591035.

[90] Matthias Hildebrandt et al. “Brillouin scattering spectra in high-power singlefrequency ytterbium doped fiber amplifiers”. In: *Opt. Express* 16.20 (2008), pp. 15970–15979. DOI: 10.1364/OE.16.015970. URL: http://www.opticsexpress.org/abstract.cfm?URI=oe-16-20-15970.

[91] T. Theeg et al. “All-Fiber Counter-Propagation Pumped Single Frequency Amplifier Stage With 300-W Output Power”. In: *IEEE Photonics Technology Letters* 24.20 (2012), pp. 1864–1867. ISSN: 1041-1135. DOI: 10.1109/LPT.2012.2217487.

[92] H. Tnnermann et al. “SBS mitigation via phase modulation and demodulation”. In: *2014 Conference on Lasers and Electro-Optics (CLEO) - Laser Science to Photonic Applications*. 2014, pp. 1–2. DOI: 10.1364/CLEO_SI.2014.SW3N.2.

[93] P. D. Dragic et al. “Brillouin scattering properties of lanthano–aluminosilicate optical fiber”. In: *Appl. Opt.* 53.25 (2014), pp. 5660–5671. DOI: 10.1364/AO.53.005660. URL: http://ao.osa.org/abstract.cfm?URI=ao-53-25-5660.

[94] W. H. Renninger et al. “Forward Brillouin scattering in hollow-core photonic bandgap fibers”. In: *New Journal of Physics* 18.2, 025008 (Feb. 2016), p. 025008. DOI: 10.1088/1367-2630/18/2/025008.

[95] W. H. Renninger et al. “Guided acoustic wave Brillouin scattering in air”. In: *2016 Conference on Lasers and Electro-Optics (CLEO)*. 2016, pp. 1–2.

[96] Alphanov NKT photoncics. *Photonic Crystal Fiber Interfacing and fiber laser components catalogue*. 2016. URL: http://www.alphanov.com/client/document/catalogue_composants-fibres_2016_212.pdf?PHPSESSID=92d88dcd6b6803eb803f5a26988afea

[97] Tem-messtechnik.de. *FiberLock*. 2016. URL: http://www.tem-messtechnik.de/EN/fiberlock.htm.

[98] Martin R. Fuchs. “A High-Field / High-Frequency Electron Paramagnetic Resonance Spectrometer (360 GHz / 14 T)”. PhD thesis. Freie Universitat Berlin, 1999.

[99] Toptica Photonics. *Falc110*. 2016. URL: http://www.toptica.com/products/research_grade_diode_lasers/analog_control_electronics/falc_110_fast_analog_linewidth_control_module.html.

[100] Oliver A. Schmidt et al. *Measurement of local polarization for multi-mode photonic crystal fibers*. 2011. DOI: 10.1117/12.874596. URL: http://dx.doi.org/10.1117/12.874596.

[101] Michael Hohmann et al. “Neutral impurities in a Bose-Einstein condensate for simulation of the Fröhlich-polaron”. In: *EPJ Quantum Technology* 2.1 (2015), p. 23. ISSN: 2196-0763. DOI: 10.1140/epjqt/s40507-015-0036-y. URL: https://doi.org/10.1140/epjqt/s40507-015-0036-y.

[102] Nelson Darkwah Oppong and Jun Ye. “Towards a Degenerate Fermi Gas of Strontium-87 in a 3d Optical Lattice”. In: 2016.

[103] Radoslaw Uberna et al. “Coherent combination of high power fiber amplifiers in a two-dimensional re-imaging waveguide”. In: *Opt. Express* 18.13 (2010), pp. 13547–13553. DOI: 10.1364/OE.18.013547. URL: http://www.opticsexpress.org/abstract.cfm?URI=oe-18-13-13547.

[104] C.Nary Man Matteo Barsuglia Henrich Heitmann. *Mode spectrum of a ring Fabry-Perot cavity*. 1998. URL: https://tds.ego-gw.it/?call_file=VIR-NOT-LAS-1390-120.pdf.

[105] F. Cleva. *Pre Mode Cleaner datasheet*. 2008. URL: https://scientists.virgo-gw.eu/ISYS/AdV_ISYS/ISYS/Documentation/Optics/PMC_datasheet_270208.pdf.

[106] NKT Photonics. *Koheras BOOSTIK, High Power Low Noise Single-frequency Fiber Laser*. 2017. URL: http://www.nktphotonics.com/wp-content/uploads/sites/3/2015/03/koheras-boostik.pdf.

[107] Schafter und Kirchhoff. *Fiber optic catalog*. 2018. URL: https://www.sukhamburg.com/download/fiberopt-cat_e.pdf.

[108] IPG Photonics Corporation. *YLR-LP, 200-500 W datasheet*. 2017. URL: http://www.ipgphotonics.com/en/products/lasers/mid-power-cw-fiber-lasers/1-micron/ylr-lp-200-500-w.

[109] E Genin F Paoletti F Nocera B Canuel R Day. "High power input optics R&D for Advanced Virgo Final Report". In: (2010). URL: https://tds.ego-gw.it/ql/?c=7438.

[110] B Canuel et al. "High power input optics R&D for Advanced Virgo Final Report". In: (2010). URL: https://tds.ego-gw.it/ql/?c=7438.

[111] NKT photonics. *Koheras ADJUSTIK, Low noise, single frequency fiber laser benchtop systems*. 2017. URL: http://www.nktphotonics.com/wp-content/uploads/sites/3/2015/04/koheras-adjustik-all.pdf.

[112] NKT photonics. *HC-1060-02 datasheet*. 2015. URL: https://www.nktphotonics.com/wp-content/uploads/sites/3/2015/01/HC-1060.pdf.

[113] John M. Fini et al. "Low-loss hollow-core fibers with improved single-modedness". In: *Opt. Express* 21.5 (2013), pp. 6233–6242. DOI: 10.1364/OE.21.006233. URL: http://www.opticsexpress.org/abstract.cfm?URI=oe-21-5-6233.

[114] F. Pockels. In: *Lehrbuch der Kristalloptik*. B. Teubner, 1906.

[115] F. Riehle. *Frequency Standards: Basics and Applications*. Wiley-VCH, 2005. ISBN: 3527402306. DOI: 10.1002/3527605991.

[116] G. Pillant. "Assemblage et caracterisation des modulateurs electro optiques pour Advanced VIRGO (rapport de stage Master 2 (Aout 2013))". In: (2013). URL: https://tds.ego-gw.it/ql/?c=11708.

[117] David Walsh. *Nonlinear Optics: KTP fiber-coupled phase modulators advance atom interferometry*. Nov. 2016. URL: http://www.laserfocusworld.com/articles/print/volume-52/issue-07/features/nonlinear-optics-ktp-fiber-coupled-phase-modulators-advance-atom-interferometry.html.

[118] AdvR Inc. *High Power Fiber Coupled Optical Phase Modulators*. 2017. URL: http://advr-inc.com/modulators.html.

[119] qioptiq. *The LINOS Laser Modulators and Pockels Cells*. 2017. URL: https://www.qioptiq-shop.com/en/Precision-Optics/LINOS-Laser-Modulators-Pockels-Cells/LINOS-Laser-Modulators/Phase-Modulators-PM-C-BB.html.

[120] https://www.photonics.com. *Photonics Buyers' Guide / Nova Write Inc.* 2017. URL: https://www.photonics.com/Company.aspx?CompanyID=19424.

[121] Edward A. Whittaker, Manfred Gehrtz, and Gary C. Bjorklund. "Residual amplitude modulation in laser electro-optic phase modulation". In: *J. Opt. Soc. Am. B* 2.8 (1985), pp. 1320–1326. DOI: 10.1364/JOSAB.2.001320. URL: http://josab.osa.org/abstract.cfm?URI=josab-2-8-1320.

[122] Toptica Photonics. *FPI100*. 2016. URL: https://www.toptica.com/products/wavemeters-laser-diodes/photonicals/fpi-100-fabry-perot-interferometer/.

[123] Keiko Kokeyama et al. "Residual amplitude modulation in interferometric gravitational wave detectors". In: *J. Opt. Soc. Am. A* 31.1 (2014), pp. 81–88. DOI: 10.1364/JOSAA.31.000081. URL: http://josaa.osa.org/abstract.cfm?URI=josaa-31-1-81.

[124] Wan Wu. "Instrumentation of the next generation gravitational wave detector: triple pendulum suspension andelectro-optic modulator". PhD thesis. University of Florida, 2007. URL: http://etd.fcla.edu/UF/UFE0021385/wu_w.pdf.

[125] N. C. Wong and J. L. Hall. "Servo control of amplitude modulation in frequency-modulation spectroscopy: demonstration of shot-noise-limited detection". In: *J. Opt. Soc. Am. B* 2.9 (1985), pp. 1527–1533. DOI: 10.1364/JOSAB.2.001527. URL: http://josab.osa.org/abstract.cfm?URI=josab-2-9-1527.

[126] Liufeng Li et al. "Measurement and control of residual amplitude modulation in optical phase modulation". In: *Review of Scientific Instruments* 4.83 (2012). DOI: http://dx.doi.org/10.1063/1.4704084.

[127] Richard Fitzpatrick. *Faraday Rotation*. 2006. URL: http://farside.ph.utexas.edu/teaching/em/lectures/node101.html.

[128] E A Khazanov. "Thermooptics of magnetoactive media: Faraday isolators for high average power lasers". In: *Physics-Uspekhi* 59.9 (2016), p. 886. URL: http://stacks.iop.org/1063-7869/59/i=9/a=886.

[129] O V Palashov et al. "Cooling and thermal stabilisation of Faraday rotators in the temperature range 300 200 K using Peltier elements". In: *Quantum Electronics* 41.9 (2011), p. 858. URL: http://stacks.iop.org/1063-7818/41/i=9/a=A18.

[130] E. A. Mironov et al. "Large-aperture Faraday isolator based on a terbium gallium garnet crystal". In: *Opt. Lett.* 40.12 (2015), pp. 2794–2797. DOI: 10.1364/OL.40.002794. URL: https://www.osapublishing.org/ol/abstract.cfm?URI=ol-40-12-2794.

[131] The Virgo Collaboration. "In-vacuum optical isolation changes by heating in a Faraday isolator". In: *Appl. Opt.* 47.31 (2008), pp. 5853–5861. DOI: 10.1364/AO.47.005853. URL: http://ao.osa.org/abstract.cfm?URI=ao-47-31-5853.

[132] The AEI-AdV squeezing working group. "Integration of the AEI squeezer in the Advanced Virgo detector Technical Design Report, VIR-0761A-17". In: (2017). URL: https://tds.ego-gw.it/?content=3&r=13720.

[133] Norman P. Barnes and Larry B. Petway. "Variation of the Verdet constant with temperature of terbium gallium garnet". In: *J. Opt. Soc. Am. B* 9.10 (1992), pp. 1912–1915. DOI: 10.1364/JOSAB.9.001912. URL: http://josab.osa.org/abstract.cfm?URI=josab-9-10-1912.

[134] Dmitry S. Zheleznov et al. "Cryogenic Faraday isolator with a disk-shaped magneto-optical element". In: *J. Opt. Soc. Am. B* 29.4 (2012), pp. 786–792. DOI: 10.1364/JOSAB.29.000786. URL: http://josab.osa.org/abstract.cfm?URI=josab-29-4-786.

[135] W J. Tabor and F S. Chen. "Electromagnetic Propagation through Materials Possessing Both Faraday Rotation and Birefringence: Experiments with Ytterbium Orthoferrite". In: 40 (July 1969), pp. 2760 –2765.

[136] W C. Scott and Melissa de wit. "Birefringence compensation and tem00 mode enhancement in a Nd: Yag laser". In: 18 (Jan. 1971), pp. 3–4.

[137] D. S. Zheleznov et al. "Faraday Rotators With Short Magneto-Optical Elements for 50-kW Laser Power". In: *IEEE Journal of Quantum Electronics* 43.6 (2007), pp. 451–457. ISSN: 0018-9197. DOI: 10.1109/JQE.2007.895668.

[138] D S Zheleznov et al. "Cryogenic Faraday isolator". In: *Quantum Electronics* 40.3 (2010), p. 276. URL: http://stacks.iop.org/1063-7818/40/i=3/a=A19.

[139] E. Khazanov et al. "Compensation of thermally induced modal distortions in Faraday isolators". In: *IEEE Journal of Quantum Electronics* 40.10 (2004), pp. 1500–1510. ISSN: 0018-9197. DOI: 10.1109/JQE.2004.834766.

[140] Joe Gleason and David H. Reitze. "Methods of compensation for thermal lensing effects in gravitational wave detectors". In: (). URL: http://www.phys.ufl.edu/REU/2003/reports/leidel.pdf.

[141] E. A. Khazanov et al. "Investigation of self-induced depolarization of laser radiation in terbium gallium garnet". In: *IEEE Journal of Quantum Electronics* 35.8 (1999), pp. 1116–1122. ISSN: 0018-9197. DOI: 10.1109/3.777210.

[142] Ilya Snetkov et al. "Compensation of thermally induced depolarization in Faraday isolators for high average power lasers". In: *Opt. Express* 19.7 (2011), pp. 6366–6376. DOI: 10.1364/OE.19.006366. URL: http://www.opticsexpress.org/abstract.cfm?URI=oe-19-7-6366.

[143] Naceur-Eddine Khelifa. "Small-Force Measurement by Photo-Elastic Transducer". In: *Optics and Photonics Journal* 4.1 (2014), p. 7. DOI: 10.4236/opj.2014.41003. URL: www.scirp.org/journal/PaperInformation.aspx?PaperID=42232.

[144] M. Ohmi et al. "High-sensitivity two-dimensional thermal- and mechanical-stress-induced birefringence measurements in a Nd:YAG rod". In: *Appl Opt.* 33 (Sept. 1994), pp. 6368–6372. DOI: 10.1364/AO.33.006368.

[145] Electro-Optics Technology. *EOT Pavos series*. 2015. URL: http://www.photonicsolutions.co.uk/upfiles/1010-1080nmFaradayRotatorsandIsolators-LargeAperture.pdf.

[146] Oleg V. Palashov et al. “High-vacuum-compatible high-power Faraday isolators for gravitational-wave interferometers”. In: *J. Opt. Soc. Am. B* 29.7 (2012), pp. 1784–1792. DOI: 10.1364/JOSAB.29.001784. URL: http://josab.osa.org/abstract.cfm?URI=josab-29-7-1784.